Spring 1-1-2016

Solar Eruptive Events: Coronal Dimming and a New CubeSat Mission

James Paul Mason
University of Colorado at Boulder, james.mason@lasp.colorado.edu

Solar Eruptive Events:

Coronal Dimming and a New CubeSat Mission

by

James Paul Mason

B.S., University of California at Santa Cruz, 2009

M.S., University of Colorado at Boulder, 2012

A thesis submitted to the

Faculty of the Graduate School of the

University of Colorado in partial fulfillment

of the requirements for the degree of

Doctor of Philosophy

Department of Aerospace Engineering Sciences

2016

This thesis entitled:

Solar Eruptive Events:

Coronal Dimming and a New CubeSat Mission

written by James Paul Mason

has been approved for the Department of Aerospace Engineering Sciences

Dr. Thomas Woods

Prof. Xinlin Li

Prof. Scott Palo

Dr. Amir Caspi

Prof. Jeffrey Forbes

Date _____

The final copy of this thesis has been examined by the signatories, and we find that both the content and the form meet acceptable presentation standards of scholarly work in the above mentioned discipline.

Mason, James Paul (Ph.D., Aerospace Engineering Sciences)

Solar Eruptive Events:

Coronal Dimming and a New CubeSat Mission

Thesis directed by Dr. Thomas Woods

Coronal mass ejections (CMEs) and solar flares are among the most energetic events in the solar system. As such, they power numerous physical processes in environments that push the limits of theory, observation, data analysis, and laboratory experiments. When these eruptive events are directed toward Earth, their interaction with the earth's upper atmosphere and magnetosphere results in numerous impacts on technology. Thus, solar eruptive events provide a field ripe for scientific study to deepen our understanding of fundamental physics and provide a practical motivation for the development of predictive capabilities.

When CMEs depart from the solar corona, they leave behind a temporary void. These "coronal dimmings" can be characterized to gain information about the CME that produced them. This dissertation presents a new theoretical and observational framework to describe coronal dimmings. Additionally, a new method for deconvolving thermal and mass-loss influences on extreme ultraviolet irradiance is developed. Correlations between coronal dimming irradiance light curve parameters (slope and depth) and CME parameters (speed and mass), driven by the physical theory, is also established. Focus is then turned from CMEs to solar flares in the development of a new, low-cost CubeSat mission – the Miniature X-ray Solar Spectrometer (MinXSS). The science instruments onboard MinXSS will provide, for the first time, measurements of the solar soft x-rays with moderate spectral resolution across most of the band. An outline of the scientific objectives, spacecraft development, and lessons learned is provided. The primary science instrument on MinXSS – the X123 silicon drift detector – has a thermal electric cooler (TEC) to keep the detector at -50 °C, which reduces thermal noise such that the source signal is not lost. The TEC requires its heat sink to remain below +35 °C. A thermal model and thermal balance testing were performed in order to

ensure that this and other temperature requirements will be met on orbit. This forward-modeling process and results are finally described.

Dedication

To my late father, who inspired me from an early age to come this far.

Acknowledgements

First and foremost, my deepest thanks to Tom Woods. Through the projects he's introduced me to – in solar physics, in sounding rockets, and in small satellites – I've discovered a career path that excites me and that provides continuous opportunities to learn and contribute. Moreover, he's an excellent role model: enthusiastic about his work, effortlessly patient with everyone, and exceptionally reliable. All of the above combined has made my time in graduate school likely to be, upon reflection long from now, one of the highlights of my life. Thank you to my committee for guidance and support, most of whom I've been fortunate to work with closely: Xinlin Li, Scott Palo, Amir Caspi, and Jeff Forbes. I'm especially grateful for their most important nugget of wisdom: to not hinge my dissertation on the deployment of spaceflight hardware, which is prone to delay and risk. Many thanks to Bret Lamprecht, who taught me the more advanced ropes of thermal modeling. Without him, I don't think I'd believe anything my models predicted. Finally, my peers have turned what could have been a struggle, instead, into an adventure. In particular, Allison Youngblood's work ethic inspires me and I've been extremely lucky to find her. Oh, and the three walks per day that my dog, Nessie von Braun, requires has provided me with the periods of relaxation away from a screen that have aided in my comprehension of the work herein.

Contents

Tables

Table

Figures

Figure

Chapter 1

Introduction

Solar eruptive events are among the most energetic phenomena in the solar system. As such, they power myriad physical processes that make the sun a highly dynamic environment – an excellent natural laboratory for the study of high-energy and plasma physics, as well as for pushing the boundaries of remote sensing. The various processes are often cotemporal, which makes sorting out their influence on the solar electromagnetic spectrum nontrivial. Instruments with spatial resolution can alleviate some of this confusion, but those instruments often have relatively broad spectral resolution, which convolves the temperatures that are another critical piece of information for analyzing the solar events. The task before us requires creativity, thoroughness, and a good understanding of the advances already made. There is a practical motivation for studying solar eruptive events as well: sometimes they are directed toward the earth where they can have numerous impacts from the beautiful (e.g., the aurora) to the detrimental (e.g., satellite damage, radio communications interference, massive power disruption). The impacted industries have a strong desire for advanced warning of these events so that they can mitigate the impacts. An informative warning must include both an expected time of the disturbance and the expected magnitude (geoeffectiveness) of the event.

The three basic types of solar eruptive events are solar flares, coronal mass ejections (CMEs), and solar energetic particles; all of which are manifestations of rapid energy release from the coronal magnetic field. This dissertation focuses on CMEs and flares, which can be observed directly in the solar atmosphere with remote-sensing instruments. Their emissions span the electromagnetic

spectrum, but much of the signal is in extreme ultraviolet (EUV) and soft x-ray (SXR) bands – wavelengths that don't reach the surface of Earth because they are absorbed by Earth's atmosphere. Hence, space-based observations are necessary. CMEs are the departure of plasma from the corona, which necessarily results in a decrease in emission from their local source region (provided that the timescale for plasma replenishment with a similar ionization profile is longer than than the CME departure rate). Observations of localized, transient (hours long) holes in the corona are known as coronal dimming. These were first observed in 1976 (Rust and Hildner 1976) and have since been characterized in numerous energy bands with imager data (e.g., Hudson et al. 1996; Thompson et al. 2000; Reinard and Biesecker 2008; Aschwanden et al. 2009b). The 2010 launch of the Solar Dynamics Observatory with the EUV Variability Experiment (EVE) onboard has now enabled the study of coronal dimming in terms of EUV irradiance due to its relatively high (1 Å) resolution which can be used to more accurately probe temperature space in the solar corona. Several key questions are addressed in the work herein. Can coronal dimming be detected in EUV irradiance data, given sufficiently high spectral resolution and only one eruption happening at a time? In other words, is spatial resolution necessary for the identification of coronal dimming? Plasma temperature in the corona is related to its location, so could that be used in lieu of spatial resolution for isolation of events? Do dimming emission-line time-series have a characteristic shape in irradiance data? Can that shape be parameterized in some way? Do such parameters have a quantitative relationship to the CME speed (related to expected arrival time) and mass (related to the expected geoeffectiveness)? Should such a relationship be expected to exist and why? This research herein is the first to explore EUV dimmings with irradiance measurements.

Just as the new measurements from EVE have enabled further coronal dimming and CME research, we anticipate new measurements from the Miniature X-ray Solar Spectrometer (MinXSS) CubeSat will do the same for solar flare research. These forthcoming measurements will be used to study coronal heating and improve Earth-atmospheric models as well. The largest increase in emission during solar flares is expected to occur in the SXR part of the spectrum, precisely where MinXSS will be looking. Prior solar SXR measurements have either been broadband or

high resolution in a band much narrower than the full SXR range. MinXSS will provide, for the first time, moderate spectral resolution across most of the SXR band. MinXSS data can then be used to address questions relevant to the physics of solar flares and their influence in the Earth's upper atmosphere. For example, how is energy distributed in the SXRs during a flare? How does that fit into the context of flare energy distribution provided by other instruments observing in other parts of the electromagnetic spectrum (e.g., hard x-ray, EUV)? What physical processes are underway at particular times during a flare? Is there significant variation between flares in terms of the SXR energy distribution? What does that imply about the universally adopted Geostationary Operational Environmental Satellites (GOES) SXR broadband measurement for classifying flares? Is the quiescent corona heated by nanoflares? How is the earth's ionosphere impacted by the SXRs and how does it change with SXR energy distribution variation? Can SXR energy distribution be parameterized and tied to geoeffectiveness in a manner useful for the space weather forecasting community? Before any of these questions can be answered, we first need to prove that a CubeSat-class mission is capable of taking such observations. Critically, the signal of the SXR measurement must dominate any noise, including thermal noise in the system. The detector has a thermal electric cooler to keep it cold, but can we expect that the heat sink of the cooler will be below its upper-temperature limit when on orbit? Similarly, will all other subsystems of the spacecraft be within their temperature limits on orbit? As MinXSS has yet to deploy, it is not yet possible to address these science questions with its data. However, this dissertation presents new analysis that brings closure to the engineering questions posed here.

Chapter 2 is dedicated to providing the context for the work in subsequent chapters. It first provides a tour of the sun from the core to the heliosphere, outlining the physics in each zone. Particular emphasis is placed on anything that can produce or influence photons because light is the observable that much of our understanding of the sun relies on, and the small contribution to that understanding made herein certainly relies on the interpretation of spectra. The chapter then delves deeper into the physics of solar eruptive events. In the broadest description, they consist of a long period of energy storage into the coronal magnetic field followed by the sudden and rapid

release of that energy. The various pathways for energy release are particularly relevant for the later chapters and so solar flares and coronal mass ejections have dedicated subsections to provide more detail about them. Next, some of the space weather implications are described. The final section provides description of the instruments that are critical to the analyses of later chapters.

Data from those instruments are turned to the purpose of characterizing the relationship between coronal mass ejections and the void they leave behind in the solar corona. That relationship and the physics surrounding it are the subject of Chapter 3. Here, the various physical processes that can lead to the observation of a transient, localized dimming are described. Coronal mass ejections, i.e., mass loss, are only one possible way that coronal dimming could occur but the one most relevant for space weather. Competing thermal effects play an important role in the coronal irradiance. Obscuration of bright plasma by dark filaments, wave propagation, and Doppler effects can also have observational identifiers that potentially conflict with those from a departing coronal mass ejection. Fortunately, each identifier is somewhat unique, provided sufficient instrument spectral and/or spatial resolution.

Chapter 4 applies the understanding of dimming gained from Chapter 3 to two event case studies. One was chosen for its relative simplicity: it only showed significant observational signatures from mass-loss dimming and thermal evolution. The other event was chosen for its complexity. It showed nearly all of the types of dimming described in Chapter 3. In each case, the chapter first lays out the observations from a variety of instruments. A physically-motivated, empirical method is then developed for isolating and removing the influence of thermal evolution from the irradiance light curve such that mass-loss dimming can be more accurately measured with an irradiance (i.e., no spatial resolution) instrument. The light curves are then parameterized with the expectation that the slope of the light curve corresponds to the velocity of the coronal mass ejection and the depth of the dimming corresponds to the mass of the CME. These case studies do not provide the statistics necessary to establish whether or not those correlations exist.

Chapter 5 analyzes approximately 30 dimming events with associated coronal mass ejections in order to establish a relationship between their respective parameterizations. The process of event

selection is detailed. Additionally, a study of the best functional fit to the dimming light curves is presented followed by further discussion of the parameterization method. Finally, the positive correlations between dimming and coronal mass ejection parameterizations are described.

The topic of solar flares is picked up again briefly in Chapter 6. This chapter provides an overview of the MinXSS CubeSat mission, including science motivation, system overview, and lessons learned. MinXSS is designed to measure the soft x-ray emission from the sun, much of which comes from the various physical processes that take place as part of a solar flare. My own contributions to this mission were varied, but at the time of writing MinXSS Flight Model 1 (FM-1) is still awaiting deployment from the International Space Station and FM-2 has yet to be delivered. Thus, this chapter and the next have a stronger engineering tilt than the science focus of prior chapters.

Chapter 7 delves into the details of thermal modeling, thermal balance testing, and model validation for MinXSS. Most CubeSat programs are not required to do thermal vacuum testing, which stresses the system to its operational and survival limits to ensure the spacecraft doesn't break under the extreme conditions that it may experience on orbit. Thermal balance goes a step further and is correspondingly even less common in the CubeSat community. Its purpose is to validate the thermal model by putting the spacecraft in an environment that is as flight-like as possible. For example, one side of the vacuum chamber is hot while the rest of the chamber is cold. For a sun-pointing satellite like MinXSS, this is a good approximation of the sun on one side and deep space on all others. The chamber and measured conditions can be input into the thermal model, where the spacecraft thermal parameters can be tuned such that the predicted temperatures match measured temperatures. In the case of MinXSS, the thermal performance is critical to the science because the sensor must be kept at -50 °C to prevent noise in the science data from drowning out the solar signal.

Finally, Chapter 8 provides a summary of all results and makes suggestions for next steps. Of particular excitement to me, the work on coronal dimming suggests the possibility of new low-cost instruments to measure irradiance in a few key wavelengths, allowing the characterization

of coronal mass ejections without the traditional coronagraph observations. Such an instrument could be leveraged in space weather forecasting to complement existing data for monitoring CMEs and/or to provide a new and unique method of characterizing the coronal mass ejections of other stars.

Chapter 2

Relevant Background

This chapter first introduces the fundamental physics that subsequent sections and chapters rely on. Where citations are not provided, further detail can be found in Zirker (2004); Lang (2001); Mihalas (1970); Eddy (2009); Mariska (1993). Remote sensing is a critical tool for probing the various layers of the sun due to the tie between physical processes and their influence on light. In particular, several atomic and charged-particle processes that generate electromagnetic radiation are described because they are the dominate source of photons that the instruments of interest here observe. Additionally, the conditions required for thermodynamic equilibrium are discussed because not all regimes of the sun obey the corresponding mathematical descriptions and drastically different methods of interpretation must be employed in such cases. It turns out that non-local thermodynamic equilibrium processes do not strongly influence the results of later chapters, but care must be taken and assumptions made explicit.

Next, Section 2.2 provides a brief tour of the sun – from its center to the heliosphere that encompasses the solar system. The basic physics previously outlined underly much of the discussion here. Section 2.3 delves deeper into the physics of solar eruptive events whose basic lifecycle is a long period of magnetic energy storage followed by a rapid release of those enormous energies. Particular attention is paid to two manifestations of this: solar flares and coronal mass ejections. Section 2.4 briefly discusses the practical implications of solar eruptive events, namely space weather and its detrimental influences on human technology. Finally, Section 2.5 provides descriptions of the instruments that are critical components of the analyses in later chapters.

2.1 Relevant Basic Physics

2.1.1 Electromagnetic Radiation From Atoms and Charged Particles

There are three basic types of electromagnetic radiation that are emitted by electron interaction with atoms: bound-bound, free-bound, and free-free. Additionally, excited nuclei can emit photons. Figure 2.1 shows examples of each in the solar spectrum.

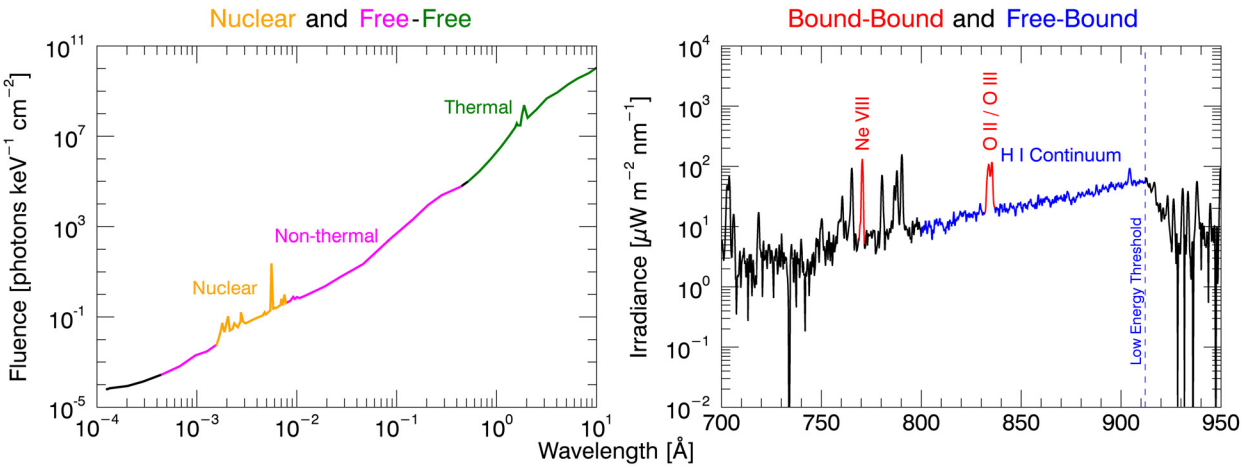

Figure 2.1: Examples of electromagnetic radiation process as observed in the actual solar spectrum.

Bound-bound When an electron transitions from one discrete (quantized) orbital energy of an atom to a lower one, a photon is emitted with energy equal to that of the transition. Downward energy transitions can occur spontaneously or through collisional de-excitation, where the atom impacts another particle and transfers some of its energy to the other particle. Upward energy transitions can also occur through collision or by absorption of a photon. The wavelength of an emitted photon is primarily determined by the electronic energy transition but can also be influenced by numerous other processes. For example, the strength of the surrounding magnetic field (Zeeman splitting), collisions during the energy transition, and the relative line-of-sight velocity of the atom with respect to the observer (Doppler) all influence the final wavelength of a photon emitted from a bound-bound transition. These and other effects result in line broadening, sometimes to the point of splitting the line.

Free-bound Also known as radiative recombination, free-bound transitions are those where an atom captures a free electron. A photon is then emitted with energy equal to the difference between the kinetic energy of the free electron and the energy of the bound atomic state it is captured into. The orbitals of the atom have quantized energy values but the kinetic energy of free electrons exists on a continuum. Thus light from free-bound transitions is also a continuum in wavelength though it has a lower limit defined by the energy of the bound state it is captured into. The reverse process (bound-free) is ionization and occurs when a photon is absorbed by an atom and an electron is liberated.

Free-free Also known as Bremsstrahlung ("braking radiation"), any accelerating charged particle emits photons according to Maxwell's equations. The resultant emission is on a continuum because there are no quantum constraints on the kinetic energy of free particles before or after an acceleration event. Because electrons are much less massive than nuclei, they tend to experience many changes in direction and speed in a dynamic plasma. Even the lightest nucleus – that of hydrogen, which is just a proton – is 1836 times heavier than an electron. So, while the nucleus will also experience a change in kinetic energy, it is negligible compared to the electron's. The acceleration in this case is mediated through the powerful electromagnetic force between these oppositely charged particles. It is also possible for similarly charged particles to accelerate each other, but these events are not responsible for the dominant observed emission in the sun.

Nuclear decay Nuclei can also be excited into a higher energy state through powerful collisions. When they return to a lower energy state, a photon is emitted and is typically in the gamma range of the spectrum.

Spectral band definitions This dissertation will refer frequently to different bands of light by common names. The International Organization for Standardization (ISO) has defined specific values for these ranges, and the relevant subset of them are included in Table 2.1.

Table 2.1: Selected formal spectral band definitions adapted from ISO document 21348.

Common name	Wavelength range (Å)
Gamma-ray	$1.00 \times 10^{-4} \leq \lambda < 1.00 \times 10^{-2}$
Hard X-ray (HXR)	$0.01 \leq \lambda < 1.0$
Soft X-rays (SXR)	$1.0 \leq \lambda < 100$
Extreme Ultraviolet (EUV)	$100 \leq \lambda < 1210$
Visible	$3800 \leq \lambda < 7600$
Ultra High Frequency (UHF)	$1.00 \times 10^{9} \leq \lambda < 1.00 \times 10^{10}$

2.1.2 Thermodynamic Equilibrium

The simplest definition of thermodynamic equilibrium is that there is one characteristic temperature in the volume of interest and there is no net flow of energy or mass. For a plasma, this implies that the radiation field is strongly coupled with the matter in the volume. A large, dynamic body such as the sun shouldn't be expected to be in thermodynamic equilibrium everywhere. The term "local thermodynamic equilibrium (LTE)" appreciates this. There are many volumes of the sun where the laws and conveniences of thermodynamic equilibrium can be applied. LTE is a good assumption when three basic criteria are met: the electron and ion velocity distributions are Maxwellian, the plasma is only weakly ionized such that the Saha equation holds, and collisional excitation dominates radiative such that the Boltzmann equation can be applied.

The Maxwell-Boltzmann equation describes the velocity distribution of a population of particles:

$$f(v) = \sqrt{\left(\frac{m}{2\pi k_B T}\right)^3} 4\pi v^2 e^{-\frac{mv^2}{2k_B T}} \tag{2.1}$$

where f is the probability density function, v is velocity, m is particle mass, k_B is Boltmann's constant, and T is temperature. This is a valid description for processes involving only continuum emission (free-free and free-bound) and is usually valid for atoms and ions in the sun. Particle acceleration during solar flares can push a population of electrons and ions outside of the Maxwellian

distribution. The Saha equation describes the ionization state of a plasma as a function of temperature and pressure:

$$\frac{n_{i+1}n_e}{n_i} = \frac{2g_{i+1}}{\Lambda^3 g_i} e^{-\frac{\epsilon_{i+1}-\epsilon_i}{k_B T}} \tag{2.2}$$

where n_i is the number density of ions in the *i-th* ionization state, n_e is the number density of electrons, Λ is the deBroglie wavelength (characteristic wavelength of the matter), g_i is the degeneracy of states for the i-ions, ϵ_i is the energy to remove i ions from the neutral atom, and all other terms are as defined previously. In the solar atmosphere, the low-lying atomic levels are dominated by radiative ionization while the high levels are dominated by collisional ionization when the temperature and density are high. The Saha equation is valid when collisions dominate the overall plasma or when the radiation field is Planckian (i.e. corresponds to a blackbody, see Equation 2.4). The Boltzmann equation (not to be confused with the Maxwell-Boltzmann equation) describes the excitation distribution of electrons in an atom:

$$f(i) = \frac{e^{-\epsilon_i/k_B T}}{\sum_{i=1}^{M} e^{-\epsilon_i/k_B T}} \tag{2.3}$$

where M is the number of all states accessible to the system and all other terms are as defined previously. The Boltzmann equation is valid when collisions dominate excitation as compared to radiative excitation. The inherent simplifying assumption is that the excitation state depends only on the temperature and density of the plasma. This is not true in general so the assumption of LTE must be applied carefully. When LTE does hold, the distribution of thermally emitted photons is described by the Planck equation (Equation 2.4). Non-LTE analyses must account for the fact that the radiation field also impacts the population of electrons in atomic energy states.

Planck's law describes blackbody emission:

$$S_\lambda = \frac{8\pi hc}{\lambda^5} \frac{1}{e^{hc/\lambda k_B T} - 1} \tag{2.4}$$

where S is the spectral radiance of a body at a particular temperature, λ is wavelength, h is

Planck's constant, c is the speed of light, and other terms are as previously defined. This equation can be interpreted simply as a lower temperature resulting in lower energy emission (i.e., longer wavelength) and lower intensity (see Figure 2.2). Figure 2.2 also shows the spectrum that actually arrives at earth, which has distinct deviations from the blackbody spectrum. The absorption features are known as Fraunhofer lines and suggest that the sun is not a simple body.

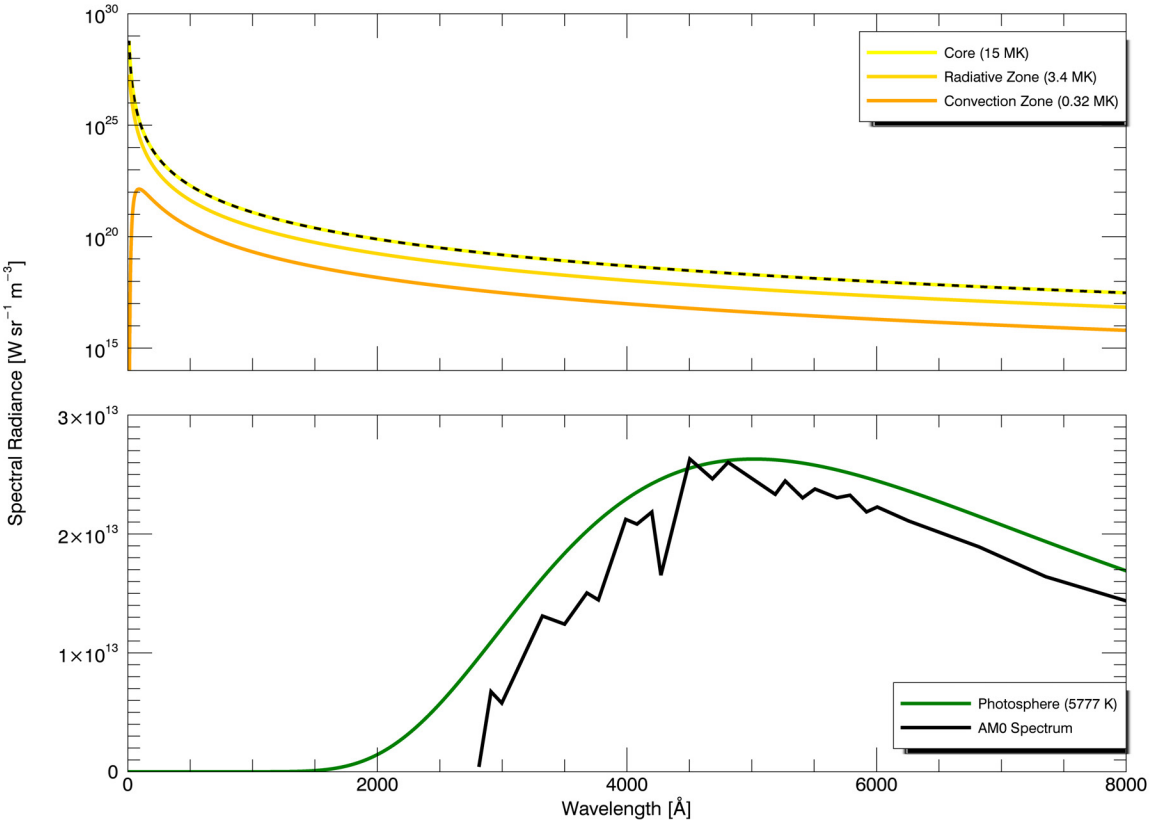

Figure 2.2: Blackbody curves at various temperatures throughout the sun. The colors correspond to those used in Figure 2.4 but a black dashed line overlies the yellow curve to improve clarity. The radiative and convection zone temperatures used correspond to the mean temperature value in those zones. The air mass zero (AM0) spectrum represents measurements and models of the solar spectrum above the earth's atmosphere (American Society for Testing and Materials 2000). The spectral units are Watts (W) per steradian (sr) per meter-cubed (m^3).

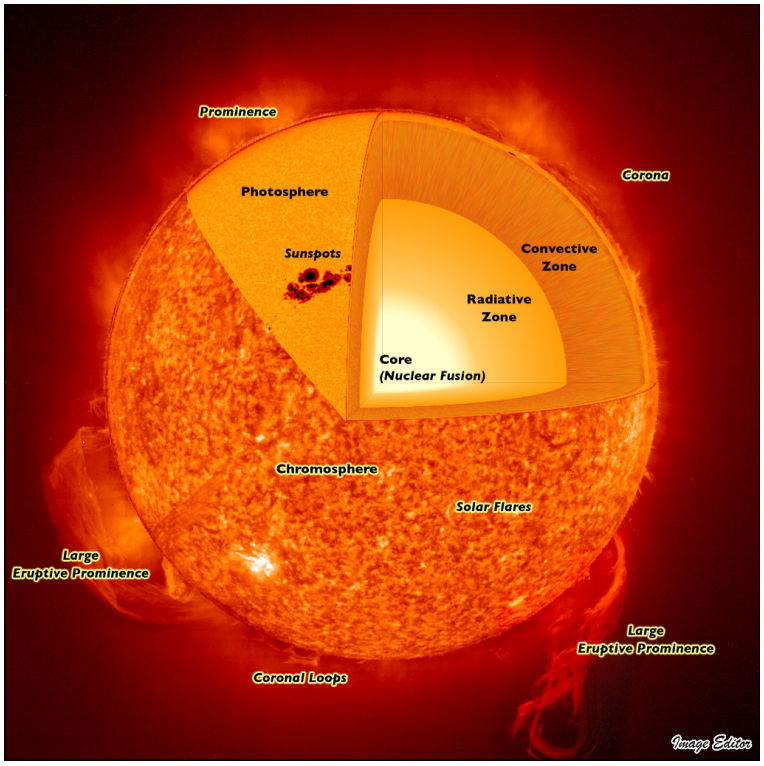

Figure 2.3: Sectional cutaway diagram of the sun to show basic structure. Figure courtesy of Image Editor on flickr.

2.2 Brief Tour of the Sun

Figure 2.3 shows the basic structure of the sun. Nuclear fusion occurs in the core and produces high-energy photons that slowly travel outward through the radiative zone. In every spherical surface centered on the core, the net energy flux outward must be positive or there would be a steady build-up of energy that would eventually cause the sun to explode. In the convection zone, the dominant form of heat transport becomes mass plasma motion that circulates hot matter upward where it cools and sinks back down. At the photosphere, the opacity drops rapidly and photons are free to fly. The undulating chromosphere lies just above the photosphere; it is vastly out-shined by the photosphere except in a few special wavelengths corresponding to dark absorption lines in the photospheric spectrum. The transition region is so named for the dramatic and unintuitive temperature increase from the chromosphere to the corona. Through the interior

of the sun, the temperature and density steadily drop (see Figure 2.4), as one would expect, with increasing distance from the heat-generating core. Nevertheless, the transition region escalates the temperature, bringing the corona to ∼1 MK.

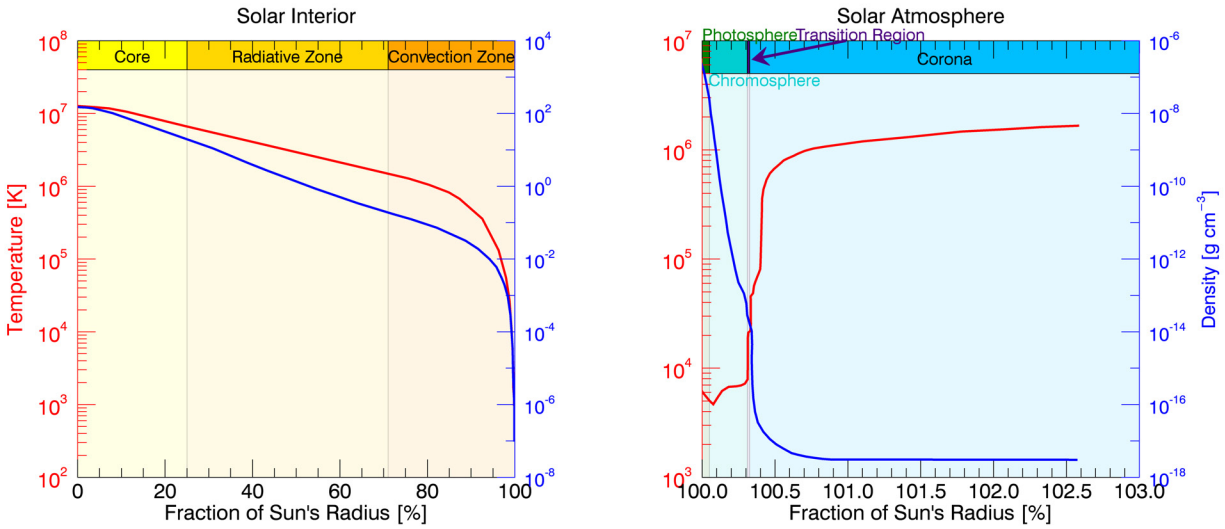

Figure 2.4: Solar temperature and density versus height from the core to the corona. Data adapted from various sources. Atmospheric temperature and density from Eddy (1979), interior temperature from Lang (2001), and interior density from Christensen-Dalsgaard et al. (1996).

Where the solar plasma below, and far above, the corona are dominated by gas dynamics, the corona itself is dominated by magnetic fields. The ratio of gas to magnetic pressure is known as the plasma β parameter:

$$\beta = \frac{p_{gas}}{p_{mag}} = \frac{nk_BT}{B^2/(2\mu_0)} \tag{2.5}$$

where p_{gas} is the pressure of a gas (or plasma in this case), p_{mag} is the magnetic pressure, B is the strength of the magnetic field, μ_0 is the permeability of free space, and all other terms are as previously defined. When $\beta > 1$, normal gas pressure dominates and when $\beta < 1$, magnetic pressure dominates. Because the plasma in the sun is highly conductive, the plasma and magnetic field (where it exists) are inextricably linked. This is often referred to as the "frozen in flux

condition". The transition from $\beta > 1$ to $\beta < 1$ is an important one for understanding how vast amounts of energy can be stored in the solar atmosphere, providing the necessary power to drive solar eruptive events. β as a function of height above the photosphere is shown in Figure 2.5.

The following sections will step through each layer of the sun with descriptive detail proportional to their relevance to the work to be presented in later chapters.

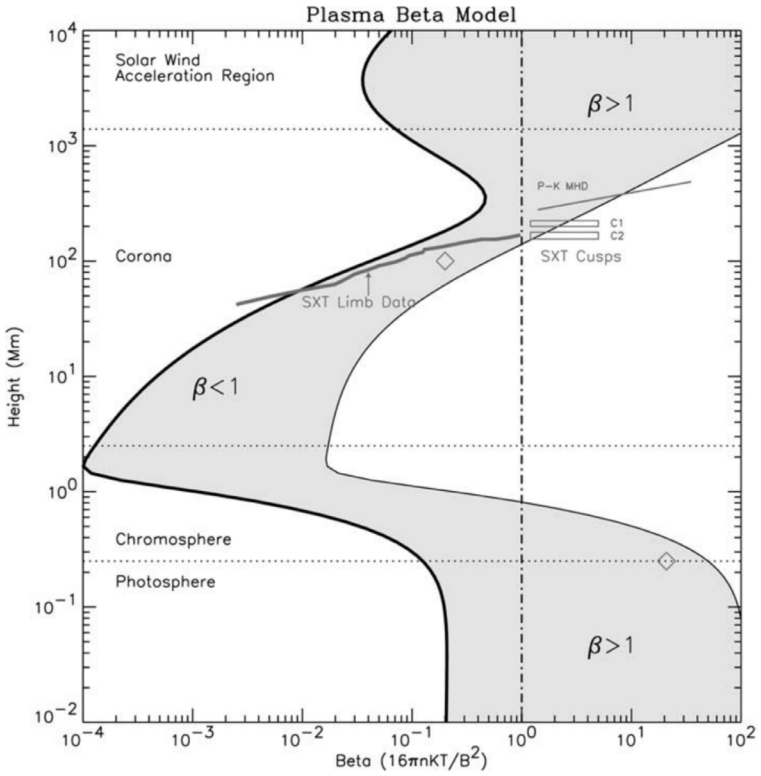

Figure 2.5: Model of solar plasma β versus height from the photosphere through the corona. The shaded region represents the open and closed field lines originating between an active region of 2500 G and a plage region of 150 G. (The plage curve can also represent older, decaying active regions that have no umbral features.) Various data indicate that β approaches unity at relatively low heights in the mid-corona. Figure courtesy of Gary (2001).

2.2.1 Core

The gravitational pressure and density in the core of stars is sufficient to ignite nuclear fusion. In a main sequence star at the midpoint of its life, like the sun, the primary fusion reaction is the conversion of hydrogen to helium. The majority of the sun is made of hydrogen (see Figure 2.6) – a

reflection of its relative abundance in the universe at large. Fusion in the core of stars is responsible for producing elements up to iron; the fusion process for elements heavier than iron is endothermic and thus cannot be used by the star to support itself against gravity. Instead, heavier elements are produced during supernovae. Supernovae also spread the source star's fusion products far away where they are incorporated into newly forming stars. Thus, the sun has observable metals[1] such as Fe even though it has not reached the point in its life where it produces them itself. The metals in these second and third generation stars are not confined to the core; rather, they can be found even in the corona. In subsequent sections it will become clear that having various elemental species at different stages of ionization in the directly observable solar atmosphere provides a means of determining temperature and structure. The core itself – in fact, everything below the photosphere – is not directly observable. However, the field of helioseismology has developed methods for inferring many properties of the solar interior.

Helioseismology takes advantage of the fact that the roiling "bubbles" at the photosphere are the result of mass fluid-like motion through the entire sun – oscillations due to resonant sound waves. By measuring Doppler shifts in the light, it is possible to derive velocities of the plasma and get an indication of interior plasma properties such as hydrogen abundance in the core (Gough and Kosovichev 1990), the depth of the convection zone (Christensen-Dalsgaard et al. 1991), helium abundance in the convection zone (Basu and Antia 1995), the age of the sun (Guenther 1989), and more. Additionally, models of stars are critical to our understanding of the solar interior and entire textbooks have been written on the subject (e.g., Chandrasekhar 1939; Kippenhahn et al. 2012). Further details are beyond the scope of this dissertation, so we continue our tour of the sun and turn to the radiative zone.

2.2.2 Radiative Zone

Every nuclear reaction in the core generates high-energy photons. It takes thousands to hundreds of thousands of years for these photons to reach the photosphere because the incredible

[1] "metals" here is in the astrophysical sense of all elements heavier than helium

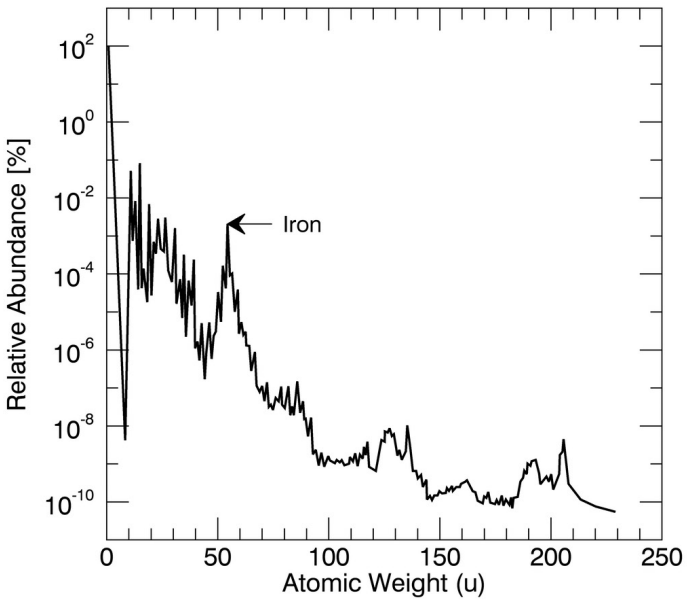

Element	Symbol	Atomic #	Abundance [%]
Hydrogen	H	1	91.2
Helium	He	2	8.7
Carbon	C	6	0.033
Nitrogen	N	7	0.010
Oxygen	O	8	0.078
Neon	Ne	10	0.011
Sodium	Na	11	1.9×10^{-4}
Magnesium	Mg	12	3.5×10^{-3}
Aluminum	Al	13	2.8×10^{-4}
Silicon	Si	14	3.3×10^{-3}
Phosphorus	P	15	3.4×10^{-5}
Sulfer	S	16	1.7×10^{-3}
Chlorine	Cl	17	1.7×10^{-5}
Argon	Ar	18	3.3×10^{-4}
Potassium	K	19	1.2×10^{-5}
Calcium	Ca	20	2.0×10^{-4}
Chromium	Cr	24	4.4×10^{-5}
Manganese	Mn	25	3.1×10^{-5}
Iron	Fe	26	2.9×10^{-3}
Nickel	Ni	28	1.6×10^{-4}

Figure 2.6: (Left) A plot of the abundance of all elements in the sun relative to the total number of particles in the sun. (Right) A corresponding table of the 20 most abundant elements. Plot and table are adapted from Lang (2001) with normalization conversion based on data from Chaisson and McMillan (1999).

density of the solar interior results in a mean free path for photons on the order of centimeters. Because the density decreases with radial distance from the center (blue line in Figure 2.4), there is a subtle bias in the mean free path of the photons that causes the net direction to be outward. This is the physical process that characterizes the radiative zone. Additionally, temperature decreases with distance from the center (red line in Figure 2.4). When in thermodynamic equilibrium, as the solar interior is, atomic emission of photons obeys Planck's law. Thus, as photons move outward from the core, they are absorbed by atoms at lower temperature and reemitted at longer wavelengths. In order to conserve energy, multiple photons of lower energy must be emitted. All sunlight is essentially modified radiation from the fusing core.

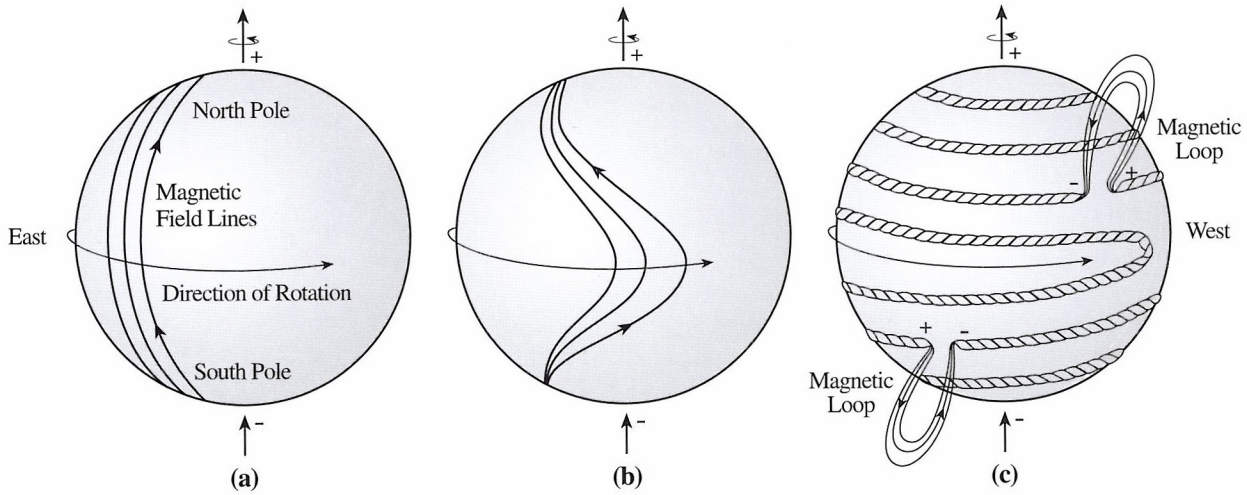

Figure 2.7: (Left) Once the solar dynamo generates a magnetic field vertically around the sun, (middle) differential rotation of the sun causes the field to wrap around the sun, (right) and any small kinks in the field are lifted by their buoyancy in an Ω loop. Figure courtesy of Lang (2001).

2.2.3 Convection Zone

At approximately 70% of the sun's radius, the dominant outward heat transport mechanism changes from radiation to convection. This is because the temperature drops sufficiently for atoms to form, the plasma becomes opaque, and heat cannot be radiated away faster than it is absorbed. Plasma stores heat near the base of the zone and its buoyancy causes it to rise to a point where its heat can be rapidly dissipated (this point is the photosphere where radiative cooling becomes highly effective). The cooled plasma then sinks back down where it will again be heated at the base of the convection zone, establishing the cycle of outward heat transport. The observed convective cells at the photosphere are known as granules and supergranules. The difference between them is size and that supergranules have much slower horizontal plasma flow. Additionally, the convection zone is responsible for many of the dynamics observed in the corona (to be described in subsequent sections), which are due to the strong magnetic field and $\beta < 1$ in the corona. The magnetic field is thought to be generated at the base of the convection zone. The precise mechanism of the solar dynamo is not yet well understood, but is widely accepted to be the result of shear between the the plasma of the solidly-rotating radiative zone and the differentially rotating convection zone. The

surfacing of the field is likely described by slight kinks in the field being lifted by plasma buoyancy (see Figure 2.7). β is large in the convection zone, so the magnetic field generated at the base is subject to the upward plasma motion just described. Once it reaches the solar atmosphere, the magnetic field dominates and so is not pulled back down with the sinking plasma.

2.2.4 Photosphere

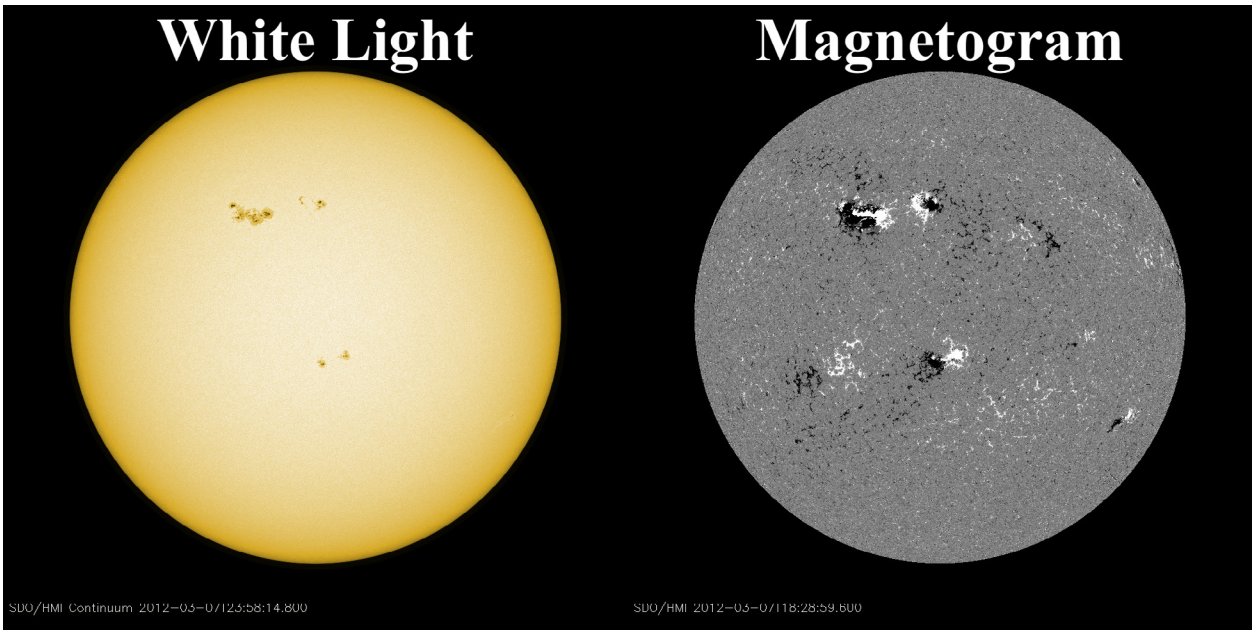

Figure 2.8: (Left) White light image of the solar photosphere on 2012 March 5. (Right) The corresponding photospheric line-of-sight magnetic field. Black indicates field into the page and white indicates field out of the page. These data come from the Helioseismic Magnetic Imager onboard the Solar Dynamics Observatory spacecraft.

The photosphere is a thin ($\sim$300 km or 0.05% $R_\odot$) layer where the opacity suddenly drops (i.e., the optical depth is unity) and photons can escape to space more or less unscathed. It is often referred to as the "surface" of the sun but this label can be misleading since the density at the photosphere is $\sim$2500 times more rarefied than the air on top Mount Everest. The photosphere is constantly roiling; the lifetime of a granule is only about 8 minutes while supergranules last about 24 hours. In each granule, hot plasma rises at the center and sinks at the edges. Magnetic field is collected at the edges of the supergranules as plasma motion can move magnetic field in the

photosphere. Sunspots, dark regions in photospheric white light[2] (Figure 2.8, left), correspond to regions of concentrated magnetic field. In these locations, magnetic pressure alleviates some of the gas pressure (due to the pressure balance), which lowers the temperature (see numerator of Equation 2.5), and thus the emission peak wavelength and intensity decrease according to Planck's law (Equation 2.4 and Figure 2.2). These areas are known as active regions when viewed in magnetogram data (Figure 2.8, right) and are the primary source for solar eruptive events (see Section 2.3).

2.2.5 Chromosphere

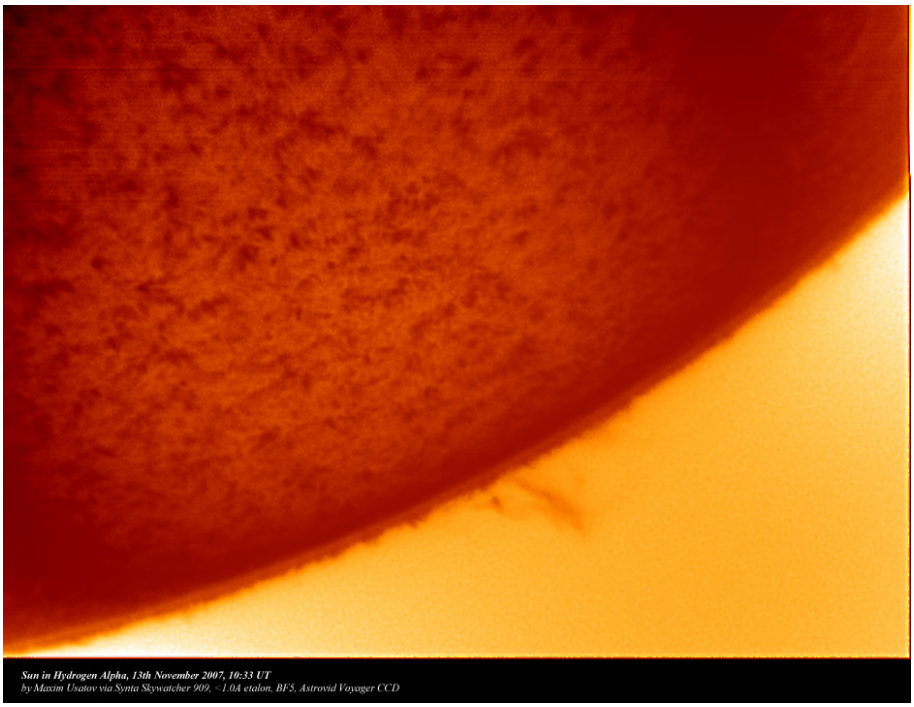

Figure 2.9: Chromospheric spicules visible on the limb (edge) of the sun, imaged in Hα. This photo was taken by an amateur astronomer from the ground, Maxim Usatov.

The chromosphere is an irregular layer of the sun that mostly consists of small jets known as spicules (Figure 2.9). The chromosphere was initially discovered – and only observable – during natural solar eclipses for a few seconds around totality when the bright photosphere was blocked.

[2] "white light" refers to the integrated visible spectrum emission

The layer has a dominant red color, which guided the selection of its name ("chromo" comes from the Greek word for color). The red light is primarily Hα emission, which is the results of the $n = 3 \rightarrow 2$ (bound-bound) transition of hydrogen (Figure 2.10). Instruments can now use filters that isolate this particular wavelength, making observation of the chromosphere routine and independent of solar eclipses.

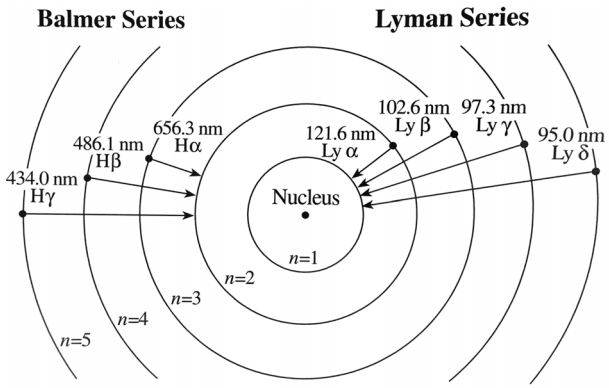

Figure 2.10: Diagram of the hydrogen atom, with electron shells labeled (n). Two important transition series are identified: the Balmer series which includes transitions ending at n = 2 and the Lyman series with transitions ending at n = 1. The wavelength and common name for the resultant photon emission are also labeled.

2.2.6 Transition Region

The transition region is defined by the rapid increase in temperature between the chromosphere and corona (see Figure 2.4). It is only ~100 km thick and is ill defined spatially. Is it in the spicules of the chromosphere? In the loops of active regions? Its location is not obvious and its existence seems to defy the laws of thermodynamics. The early discovery of how hot the corona was and that the transition region existed was controversial. It depended on temperature-sensitive observations, which have now become routine and widely accepted.

There are several means by which temperature of the solar atmosphere can be inferred. The simplest is the observation of an emission line that has been identified in the laboratory, which specifies the corresponding ion and bound-bound transition. Additional laboratory measurements

and theory provide the ionization fraction of each element as a function of temperature (e.g., see Figure 2.11 for Fe ions). A higher temperature results in greater ionization. Thus, observation of an emission line known to correspond to a particular ion is an indicator of that ion's existence in the remote plasma and an approximate temperature can be inferred. Table 2.2 provides some examples for ionization state, corresponding temperature, and a known emission line, which will be used extensively in later chapters.

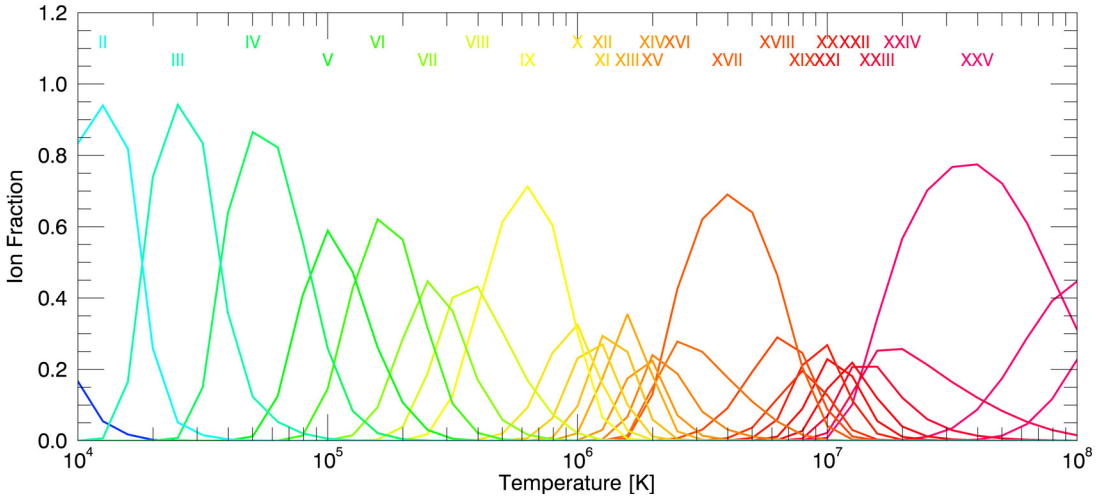

Figure 2.11: Ionization fraction for Fe as a function of temperature. Figure based on data from Mazzotta et al. (1998).

The next most common method for temperature determination uses the ratio of two emission lines. The flux in each line is dependent on the energy of the bound-bound transition, ΔE, and the collision rates for that transition. The ratio of the line fluxes is temperature sensitive if $\Delta E > k_B T$. This method can handle non-isothermal plasmas by integrating the collision rates over volume. This method fails if the lines used have source regions that are distant from each other so care must be taken when the source plasma contains spatial variations in density and temperature, as is the case with the sun. Additionally, this method depends on the relative ion abundances, so if ionization balance varies with time, that time variation must be taken into account. Line ratios are not used for temperature determination in this dissertation.

Table 2.2: Selected emission lines

Ion	Wavelength (Å)	Peak formation temperature (MK)
Fe IX	171	0.63
Fe X	177	0.93
Fe XI	180	1.15
Fe XII	195	1.26
Fe XIII	202	1.58
Fe XIV	211	1.86
Fe XV	284	2.19
Fe XVI	335	2.69
Fe XVIII	94	6.46
Fe XX	132	9.33

The mechanism responsible for the rapid temperature change through the transition region remains poorly understood and is one of the biggest problems in solar physics. Theories abound to explain it but are beyond the scope of this dissertation. Here, we simply accept that the transition region *does* lead to a much hotter corona – an observational fact that has long been established.

2.2.7 Corona

The corona is the highly dynamic, tenuous upper atmosphere of the sun. Its lower boundary is defined by the transition region at approximately 2.45×10^3 km above the photosphere ($1.0035\ R_\odot$). Its outer boundary is determined by the Alfvén surface where information can no longer be propagated inward and has recently been discovered to be at a much higher altitude than previously thought: 8.35×10^6 km ($12\ R_\odot$) above polar coronal holes and 1.04×10^7 km ($15\ R_\odot$) at lower latitudes (DeForest et al. 2014). The average temperature of the corona is about 1.5 MK (Figure 2.4) but it ranges from roughly 0.6 MK to 50 MK. As mentioned in earlier sections, the ratio of gas to magnetic pressure, β, is less than 1 in the corona. This is why we see structure in the corona. The magnetic field contorts, compresses, and opens dynamically to produce regions of

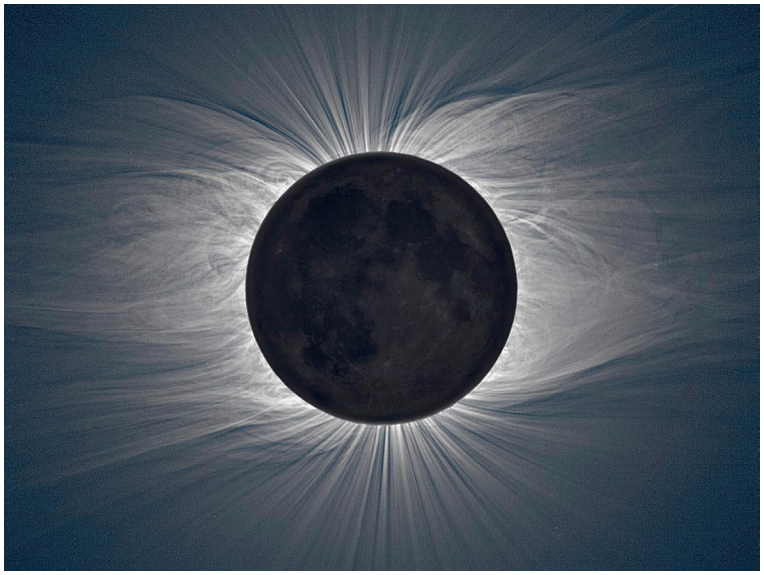

Figure 2.12: Composite white-light image of the corona from a total solar eclipse in the Marshall Islands in 2009 July. Features on the moon can be seen in the foreground and a great deal of structure appears in the corona. Image courtesy of Miloslav Druckmuller.

varying plasma density and temperature (Figure 2.12). Those changes in the plasma impact the electromagnetic emission, which can be observed in Thomson scattering as in Figure 2.12 or in terms of the emission line flux and differential emission measure (DEM):

$$F = \frac{2.2 \times 10^{-15}}{4\pi R^2} f A_{el} \int g G(T) Q(T) dT \tag{2.6}$$

$$G(T) = \frac{n_{ion}}{n_{el}} \frac{e^{\frac{-h\nu}{k_B T}}}{\sqrt{T}} \tag{2.7}$$

$$Q(T) = \sum_{i=1}^{N} \left(\iint_{S_T} \frac{n_e n_i}{|\nabla T|} dS_T \right)_i \tag{2.8}$$

where F is the emission line flux, $G(T)$ is the contribution function, $Q(T)$ is the DEM; R is the distance between the emission source and the observer, f is the oscillator strength (probability of absorption/emission between two atomic energy levels), A_{el} is the elemental abundance, g is the Gaunt factor (a correction for absorption/emission to account for quantum effects), ν is photon frequency, S_T is a constant temperature surface, the summation in $Q(T)$ runs across all regions

along the line of sight in the temperature range T to $T + \Delta T$, and all other variables are as defined previously. The DEM, and hence the line flux, is strongly dependent on density and moderately dependent on temperature. All of this is to say that where the coronal magnetic field increases the density or temperature of the plasma, the intensity of the emission goes up. Thus, the bright structures in coronal images provide an indicator of magnetic topology and intensity. It is important to note that in the forthcoming coronal dimming discussions, the emission lines used in analysis are collisionally excited and are proportional to n_e^2. The corona is about 90% hydrogen, which means that it mostly consists of equal numbers of protons and electrons. Thus, the widely accepted practice is to set the n_{ion} term of Equation 2.6 equal to n_e to simplify the expressions. Hence, emission intensity goes as the square of electron density.

The corona is optically thin and as such is not in LTE, i.e., the plasma is not strongly coupled to the locally-generated radiation field. In yet simpler terms, this means that photons generated from a very distant region can stream directly to a plasma parcel of interest and interact there. This makes modeling of the solar atmosphere a nontrivial task. There should be different temperatures defined for photons, electrons, protons, and ions. Their velocities need not be Maxwellian, making the definition of temperature at all somewhat murky. However, many of the emission lines in the corona are emitted by collisionally excited, moderately ionized atoms (e.g., Fe IX 171 Å) and these lines can only be formed in sufficient quantities to be measurable between certain temperatures. In regions of the corona that are relatively quiescent, the assumption of a Maxwellian distribution remains a good one, so temperature carries some meaning. Thus, observations of particular emission lines still provide a decent indicator of approximate plasma temperature. Herein, "peak formation temperature" or simply "temperature" will be used as a convenient shorthand that implies the caveats provided above.

2.2.8 Heliosphere

The heliosphere stretches from the end of the corona and encompasses the solar system. It is the region where solar influences dominate the interstellar. Solar wind, a tenuous plasma constantly

streaming out from the sun, applies a subtle outward pressure. There are similar breezes coming from the stars. The heliopause is defined as the point of equilibrium between these pressures. The solar wind flows outward at about 400 km/s with a pressure at 1 astronomical unit (AU[3]) in the range of $1 - 6 \times 10^{-9}$ N/m^2. However, this gentle wind is periodically disturbed by spasms in the sun known as solar eruptive events. These events can impact the earth and cause various problems with technology, health, and safety. The physics of solar eruptive events is the subject of Section 2.3 and the impacts and forecasting of space weather is the subject of Section 2.4.

2.3 Physics of Solar Eruptive Events

Solar eruptive events are some of the most energetic phenomena in the solar system. Solar flares can release 10^{25} J in minutes to hours (Woods et al. 2006) – an energy that is hard to fathom. The total world energy consumption over the last 42 years was 1.17×10^{22} J[4] . A powerful flare has nearly 1000 times that energy. Coronal mass ejections (CMEs) have a similar amount of energy: up to 10^{25} J of kinetic energy (Vourlidas et al. 2010). The general process for solar eruptive events is a long period (days or more) of energy storage and then a rapid release of that energy through numerous physical processes. The following subsections provide further detail into energy storage and release.

2.3.1 Magnetic Energy Storage

The energy to power a solar eruptive event comes from stored energy in the coronal magnetic field. A "potential" field is defined such that the field is smooth, i.e., it has no field lines twisting around each other and instead they nest alongside each other in an orderly way. This is the lowest possible energy configuration of the field, meaning there is no energy to power an eruptive event. When field lines are packed closely together, become braided, shear, or single ropes twist, energy is stored into the field (Figure 2.13). As described earlier, the convective motions at and below the

[3] 1 AU is the average distance between the sun and earth, 1.50×10^8 km
[4] Analysis based on 1971-2013 data from International Energy Agency (2015)

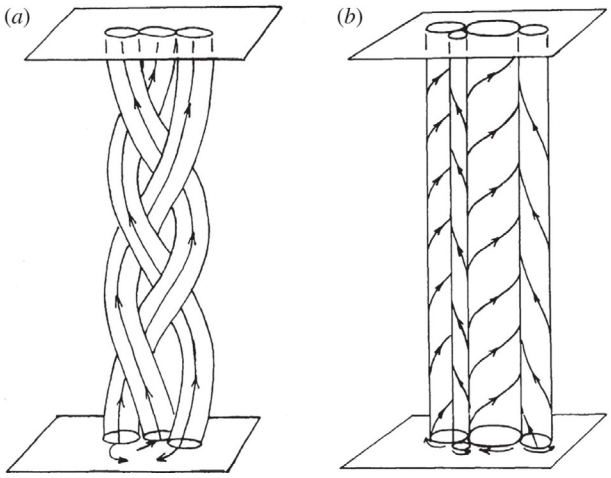

Figure 2.13: Schematic depiction of magnetic energy storage. (Left) Translation of magnetic fields/ropes/strands leads to braiding and tangling and (right) the field lines/ropes/strands can themselves be twisted. Figure courtesy of Klimchuk (2015).

photosphere are one important source of these motions. Additionally, a complex of magnetic fields such as an active region can be influenced by distant eruptive events through energy propagation via the coronal magnetic field, such as Alfvén waves (Schrijver and Title 2011). Gentler disturbances in the large-scale coronal magnetic field likely occur frequently and could contribute to localized energy concentration.

2.3.2 Energy Release Overview

The rapid energy release of a solar eruptive event is no small topic. As mentioned earlier, worldwide energy consumption pales in comparison to the energy release of a single solar eruptive event and as such, a large number of physical processes are powered. Magnetic reconnection is the widely accepted catalyst of sudden energy release, though the microphysics remain poorly understood. We do know, however, that it requires antiparallel magnetic fields to be forced close to each other. The plasma is has a nonzero resistivity, which allows field annihilation and the connection of one line to another. Magnetic reconnection also occurs in planetary magnetospheres and laboratory experiments have sought to cause it, but the details of this active area of research are beyond the scope of the relevant background to this dissertation. Magnetic energy storage

and reconnection is somewhat analogous to the sudden shifting of tectonic plates (earthquakes), avalanches on a ski slope, the snapping of a rubber band that has been twisted too tightly, and the sudden flash and crack of a lightning bolt (Lang 2001).

As energy continues to build in the coronal magnetic field, eventually somewhere in the complex of loops, a particular strand is stressed beyond a critical limit. Because it can no longer adjust to the additional stress, it suddenly snaps into a new lower-energy configuration as it finds the path of least resistance, like a stream of water working its way through rough downhill terrain. This sudden change to the local field configuration causes the neighboring loops to adjust rapidly as well; in this way the disturbance propagates. Within seconds, all loops in the region are relieving their strain by reducing their twists, shear, and other complexity as they strive toward the potential field configuration. Eventually, a region of loops that are not near their critical stress limit is reached and the propagation ceases. The field configuration after the disturbance contains less energy than before. All of that energy has to go somewhere! It turns out that particle acceleration is one of the key processes powered by this energy release. A comparative few particles can be accelerated to relativistic velocities and/or a huge mass of particles can be accelerated to a few hundred km/s. The former is strongly associated with solar flares (Section 2.3.3) and solar energetic particles (SEPs; not discussed in detail here) while the latter is a simple description of coronal mass ejections (Section 2.3.4). Both are manifestations of magnetic energy release and they can occur together. Flares are often categorized by the amount of soft x-ray emission they release as measured by the Geostationary Operational Environmental Satellites (GOES) where each letter (A, B, C, M, X) indicates an increased order of magnitude. ∼30% of C-class, ∼56% of M-class, and ∼90% of X-class flares occur with CMEs (Yashiro et al. 2005; Wang and Zhang 2007). In other words, larger magnitude flares tend to occur with CMEs. The reverse is also true: 90% of the fastest CMEs (>1500 km/s) are associated with flares but the association rate drops for slower CMEs (Wang and Zhang 2008).

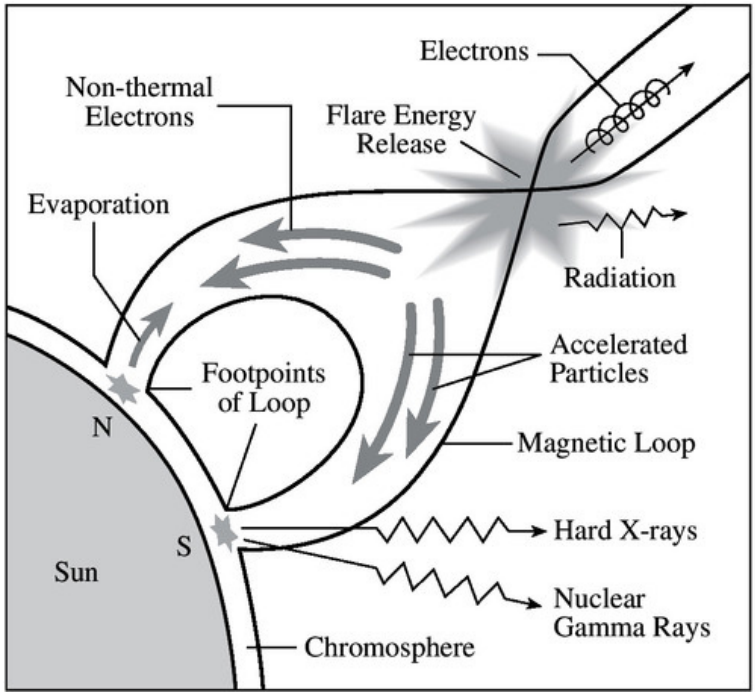

Figure 2.14: Schematic depiction of solar flare energy release processes. Figure courtesy of Lang (2001).

2.3.3 Solar Flares

"Solar flare" is a somewhat vague term that broadly encompasses all of the rapid magnetic energy release processes that result in additional electromagnetic radiation (Figure 2.14, see also review by Fletcher et al. 2011). One natural place for some of the energy to go is Joule heating. This is a process where electrons are accelerated by an electric field and collide with relatively stationary ions causing them to scatter randomly (though still in a Maxwellian distribution), thus increasing the average kinetic energy of the system (i.e., heating). Particle acceleration in flares is poorly understood but there are numerous proposed mechanisms that could produce electron and ion beams. Each proposed mechanism has issues and the existing observations have not placed sufficient constraints to determine which mechanism dominates for various physical conditions (Kontar et al. 2011; Zharkova et al. 2011). The observations do tell us that acceleration occurs near or above the top of the coronal loops. Some particles are accelerated outward (SEPs) and others are accelerated

downward.

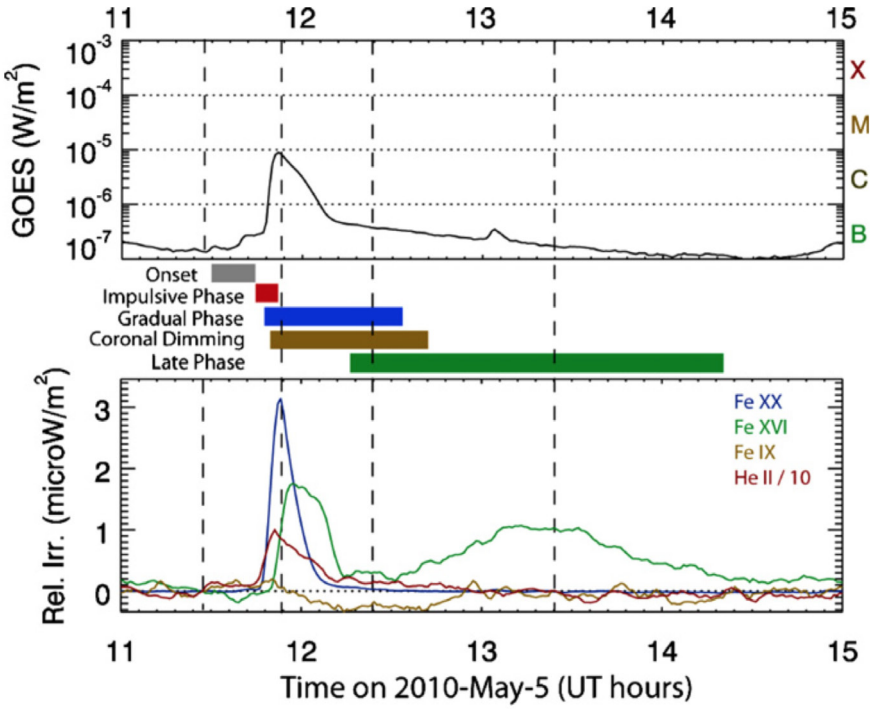

Figure 2.15: Flare variations for a flare on 2010 May 5. Relative irradiance (Rel. Irr.) subtracts a pre-flare spectrum at each point in the time series. The transition region He II 304 Å emission highlights the impulsive phase. The GOES X-ray defines the gradual phase, and the hot corona Fe XX / Fe XXIII 133 Å emission behaves almost identically to the X-ray. The cool corona Fe IX 171 Å emission is the EUV emission with the largest amount of coronal dimming. The warm corona Fe XVI 335 Å emission has its first peak a few minutes after the X-ray gradual phase peak and then has a second peak many minutes later. The change in slope of the GOES X-ray during the gradual phase is indicative of the late phase contribution (second Fe XVI peak). The four vertical dashed lines can be ignored as they correspond to other figures in Woods et al. (2011), the source of this figure.

Electrons and ions that are accelerated downward are trapped by the magnetic field because $\beta < 1$, so they run down the legs of the coronal loops until they reach the relatively dense chromosphere. At this point, numerous physical processes ignite. Figure 2.15 shows the characteristic spectral light curves of these processes. As the non-thermal[5] charged particles in the beam approach the plasma in the chromosphere, their electromagnetic attraction/repulsion causes acceleration, which results in bremsstrahlung (free-free) continuum radiation. Sometimes the particles

[5] Non-thermal implies that the velocity distribution is not Maxwellian

in the beam collide with the chromospheric particles, which results in direct heating, ionization, atomic excitation of electrons, and atomic excitation of the nucleus. Electrons that become excited but remain bound may then spontaneously decay in a bound-bound transition by emitting a photon (often in SXR or EUV). Alternatively, the excited atom may collisionally de-excite – another heating mechanism. Heating in the chromosphere causes the plasma to rapidly expand and because $\beta < 1$, it expands up the legs of the coronal loops. Those loops then appear bright in SXR and EUV wavelengths (Figure 2.16). These processes tend to generate a multitude of high energy emission, from UV to gamma, and also microwave emission at the characteristic plasma frequency as the electron beam causes a small oscillation in the elements of the target plasma. Because the corona is optically thin, we are able to directly observe these emissions.

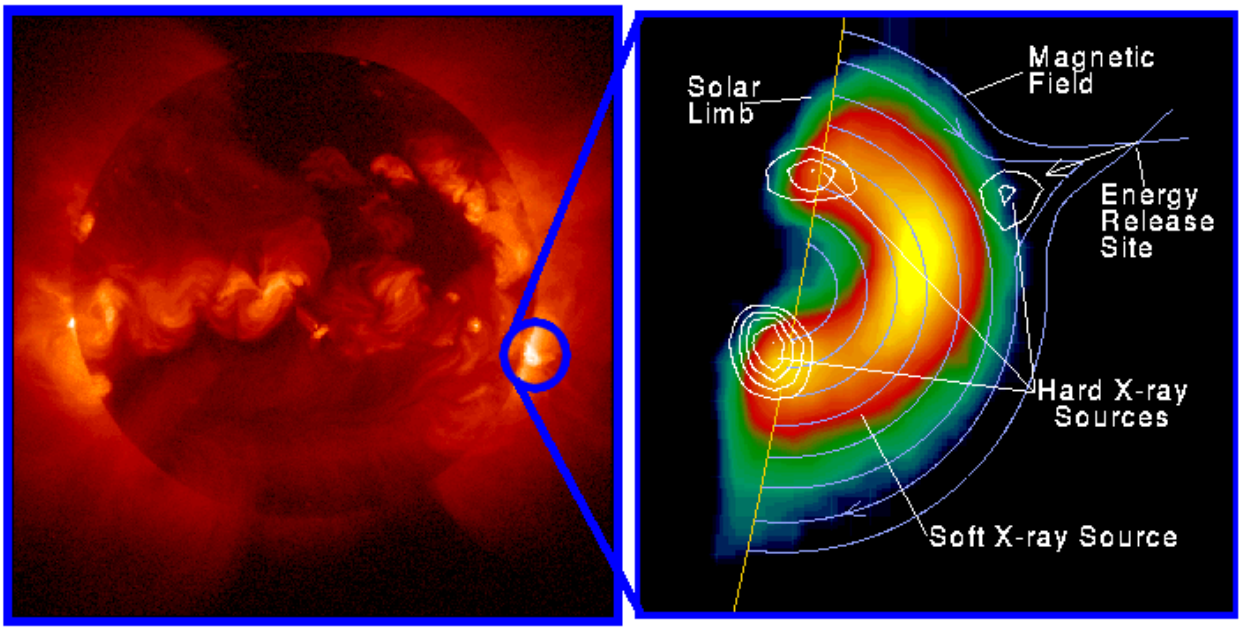

Figure 2.16: (Left) SXR image of the sun during a flare on 1992 January 13. (Right) The flaring loops in SXR and HXR wavelengths. Images from instruments onboard the Yohkoh spacecraft. Figure courtesy of Holman (2008).

The HXRs and microwave emission tend to cease within minutes as the electron beam ceases. The period that these emissions persist is known as the impulsive phase of the flare (Figure 2.15). The gradual phase is essentially the atmospheric response to the disturbance of the impulsive phase;

the hot plasma (up to 50 MK in the most intense events, e.g., Caspi et al. 2014a) cools and lower ionization states are enhanced. Those lower ionization states radiate, which makes them observable and contributes to the cooling of the plasma. Highly relevant to the following chapters, many of the gradual phase emission lines are in the EUV.

2.3.4 Coronal Mass Ejections

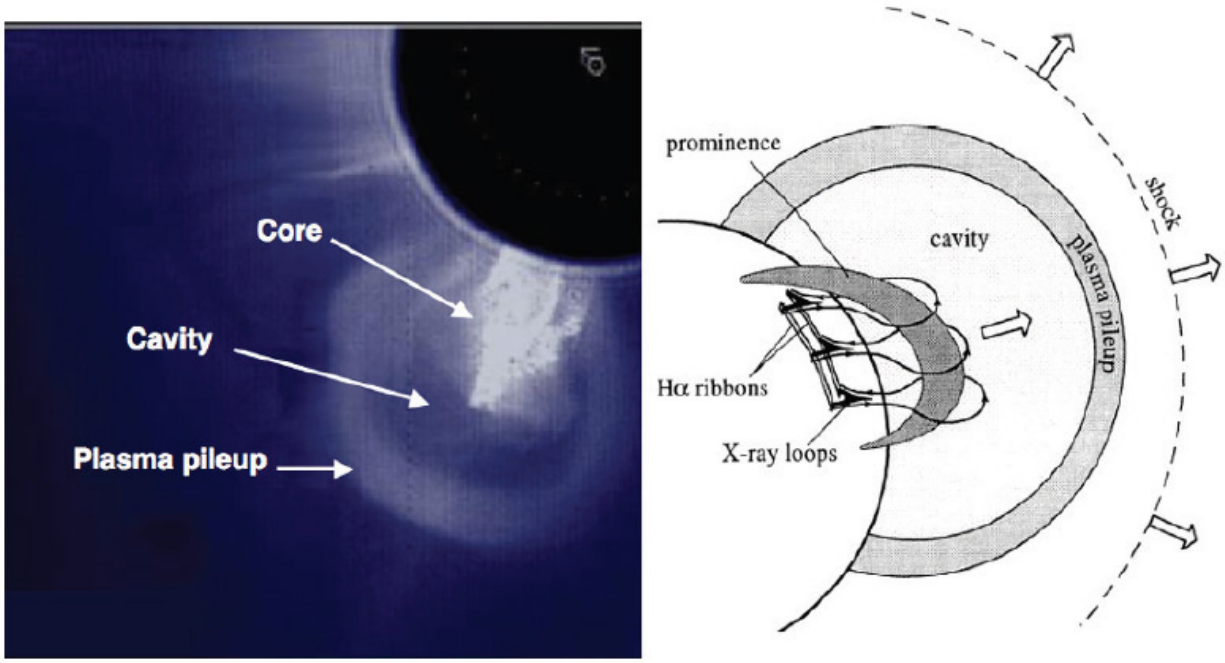

Figure 2.17: (Left) Typical observation of a CME. (Right) Schematic depiction of filament eruption CME. Figure courtesy of Forbes (2000).

Energy stored in the coronal magnetic field can also be directed into accelerating a great mass out of the corona and into the heliosphere. Prior to the eruption, the strong magnetic fields of the active region in a low β environment can prevent a great mass of plasma from escaping, despite strong outward plasma pressure. The sudden reconfiguration of the magnetic field changes that situation: the restraining magnetic field can be disconnected from lower down, effectively pinching off a magnetic bubble (Figure 2.17). Often times, highly-stable plasma features can be found resting in regions of strong magnetic field, which tend to be in and near active regions (Figure 2.17). These

features are called filaments when seen on disk because they appear dark, and prominences when viewed towering over the solar limb. Filaments/prominences have orders of magnitude higher density than their surroundings but are at orders of magnitude lower temperature. They should sink like a brick in water or evaporate like an ice cube in an oven but they are supported and protected by the strong magnetic fields encapsulating them. When a CME departs, often times a filament/prominence that was a part of the local magnetic structure will be torn away with it. This adds to the mass of the CME and can make for beautiful images (Figure 2.18). Here too, the precise mechanism for accelerating the CME is poorly understood. It is particularly perplexing because the average speed of a CME is 400 km/s but the escape velocity here is about 600 km/s.

For space weather, the most useful piece of information is predicted time of the CME to reach Earth. Fortunately, the CME properties are set in the low corona, i.e., their speed and acceleration don't change much through interplanetary space (Temmer 2016). This means that observations of the low corona can yield accurate predictions of Earth-arrival time. What is relevant for this dissertation is that as the CME leaves, it brings its magnetic field and associated plasma with it, leaving a temporary void in the corona. These voids were first known as "transient coronal holes" but are now more commonly referred to as coronal dimmings. The relationship of CME and coronal dimming observations is the focus of Chapters 3-5 in this dissertation.

2.4 Space Weather

If solar eruptive events are directed toward Earth, there can be myriad negative consequences (National Research Council 2008), which provides some practical motivation to study the responsible events beyond their merits as scientific curiosities. The National Research Council (2008) report is the definitive source for space weather impacts so only a few examples will be listed here. The electromagnetic radiation from solar flares is absorbed by the earth's atmosphere, which can cause it to expand. Satellites at a particular altitude will then see a greater number of particles in their path and thus experience a small but non-negligible increase to their drag. The gross effect is that the orbital lifetime of satellites in low Earth orbit is reduced, unless they have the capability to

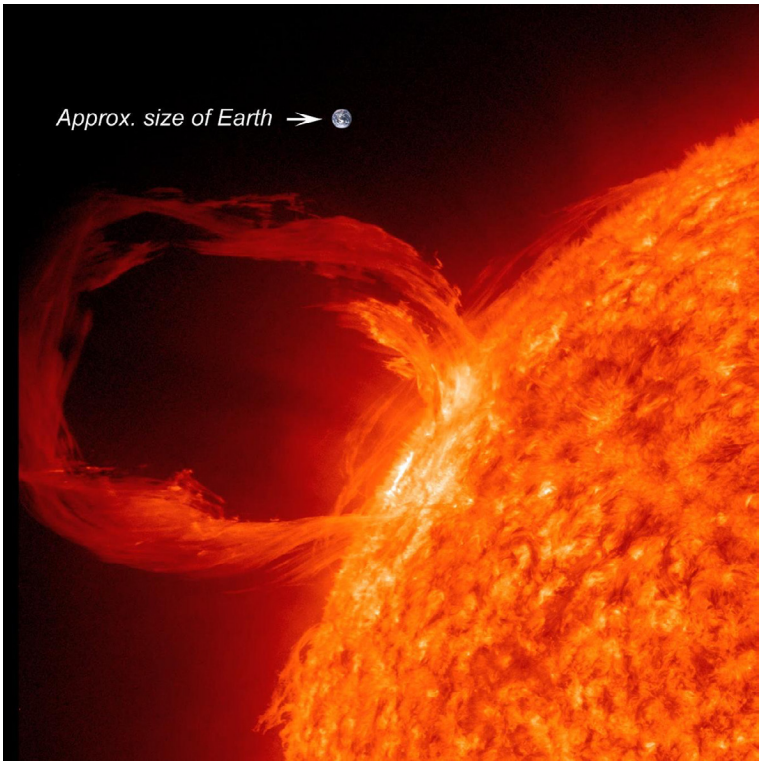

Figure 2.18: Prominence eruption as viewed from the Solar Dynamics Observatory's Atmospheric Imaging Assembly. Image credit: NASA.

boost themselves; the International Space Station does this periodically. Additionally, high-energy photons, electrons, and protons can be directly absorbed by satellites or humans in space. This can cause numerous problems with electronics and health. In particular, solar storms can cause disruptions to the global positioning satellite (GPS) system. This is an inconvenience to people on travel in unfamiliar places, but has serious implications for the agricultural and oil drilling industries that increasingly rely on GPS for precise positioning in their automated systems. Coronal mass ejections are clouds of electrically charged plasma that influence the earth's magnetosphere. According to Maxwell's equations, a changing magnetic field induces a current. Long oil pipelines and power lines are particularly susceptible to this because they are good electrical conductors. In the case of power lines, the surges in current can exceed the tolerance of large transformers and blow them out. These transformers are expensive and have long lead times to replace; thus large populations can be left without power for extended periods of time, as was the case in Quebec in

1989. Finally, the earth's ionosphere can be influenced by solar eruptive events, causing disruptions in radio communication that rely on the ionosphere to bounce signals over long distances. This has important implications for the airline industry because airplanes are required to maintain constant contact with the ground. In relatively inaccessible areas like the poles and the oceans, they rely on the ionosphere to maintain contact. Thus, when ionospheric disturbances disrupt an airline's ability to maintain contact, they are forced to reroute flights. Many of the human implications of space weather can be mitigated with warning. For example, astronauts can take shelter, satellites can be temporarily powered down or put into safe mode, and transformers can be protected from current surges. In the United States, the National Oceanic and Atmospheric Administration's Space Weather Prediction Center (NOAA/SWPC) is responsible for providing those warnings for the space-weather-sensitive industries and to the general public.

It remains difficult to predict when solar eruptive events will occur. One popular method uses photospheric magnetic field measurements to derive parameters tied to field complexity (e.g., emerging flux, polarity inversion line length, magnetic field gradients), which are proxies for the amount of stored energy in the magnetic field. These data are then used to make forecasts of solar flares, but while they show a positive correlation to solar flare occurrence and magnitude, they have not proven particularly effective for real-time prediction (Mason and Hoeksema 2010). Fortunately, CMEs are the more geoeffective type of solar eruptive event and they take several hours to a few days to reach 1 AU. This makes nowcasting possible because the light from CMEs only takes 8 minutes to reach the same distance. An industry has sprung up around the monitoring of real-time data from various space-weather assets, and they issue alerts to other industries that may be impacted. The true test of any science is its ability to make accurate and precise predictions. The sun may be the most well studied star in the universe, but there remains ample room for improvement in our understanding of its details and our observations of it.

2.5 Instrument Descriptions

The following subsections are broken into instrument types. Only instruments that are important for this dissertation are described. Of primary importance is the Solar Dynamics Observatory's Extreme Ultraviolet Variability Experiment spectrograph, so it will be described first.

2.5.1 Spectrographs

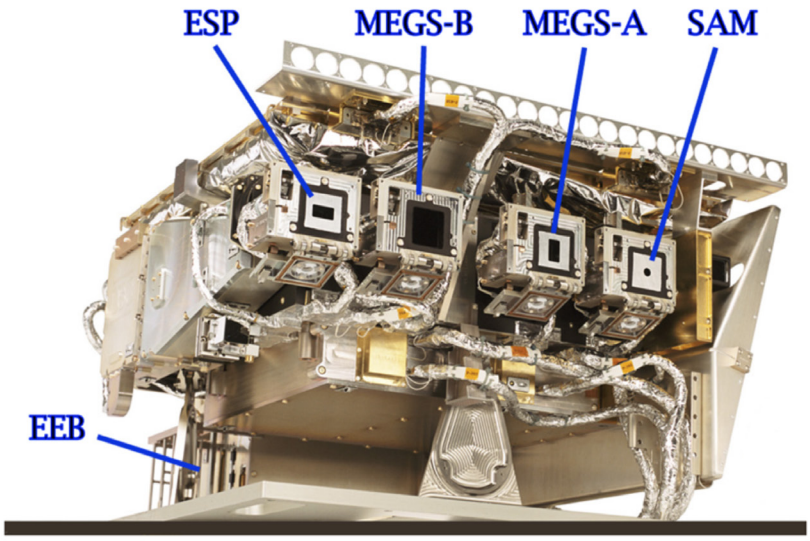

Figure 2.19: The EVE instrument suite (ESP, MEGS-B, MEGS-A, and SAM). The EVE Electronics Box (EEB) provides the electrical interface to the SDO spacecraft. The entrance baffle in the door mechansisms are indicated for the various instruments. Figure courtesy of Woods et al. (2012).

The Extreme Ultraviolet (EUV) Variability Experiment (EVE; Woods et al. 2012) onboard the Solar Dynamics Observatory (SDO; Pesnell et al. 2012) was launched on 2010 February 11 into a geosynchronous orbit that has a view of the sun that is only occasionally obstructed by the earth. EVE is a suite of instruments that measure EUV emission from the sun (Figure 2.19). Multiple EUV Grating Spectrographs (MEGS)-A is a grazing incidence spectrograph that measures the solar EUV irradiance from 50 to 370 Å with 1 Å resolution. MEGS-B is a normal-incidence, dual-pass spectrograph that extends the MEGS-A spectrum from 350 to 1050 Å with the same resolution; the 20 Å of overlap between the two primary components of MEGS allows for cross-

calibration. The MEGS-Photometer (MEGS-P) measures solar Lyman α (Lyα) at 1216 Å. The EUV SpectroPhotometer (ESP) obtains broadband measurements between 1 and 390 Å that are used to provide in-flight calibration. Finally, the Solar Aspect Monitor (SAM) is a pinhole camera to provide alignment information for EVE in visible light and also to measure individual X-ray photon events to generate X-ray images. Of primary interest to this dissertation is MEGS-A, which encompasses emission lines from many of the ionization states of Fe between IX and XX and the He II 304 Å chromospheric line (Table 2.2). MEGS-A images are read from two back-illuminated, 2048 x 1024 charge coupled devices (CCDs) every 10 seconds. Once received on the ground, data processing converts the raw images into spectra (e.g., Figure 2.21) – a nontrivial task that requires continuous tracking of and correction for on-orbit instrument degradation. The next level of data processing converts the spectra into a data structure that contains the extracted emission lines, which are the product used in this dissertation. Additionally, herein, the 10-second data are averaged to one or two minutes to reduce noise. The spectral resolution of MEGS-A is sufficiently high that emission-line blends are few and do not impact the analyses to come in the following chapters. However, as an irradiance instrument, EVE has no spatial resolution across the solar disk.

The modified Amptek X123 silicon drift detector onboard MinXSS is a spectrometer to observe SXRs. It will be described in Chapter 6.

2.5.2 Spectral Imagers

Also onboard SDO is the Atmospheric Imaging Assembly (AIA; Lemen et al. 2012). AIA consists of seven EUV channels from four telescopes. The full solar disk is observed and the light is imaged onto 4096 x 4096 CCDs every 12 seconds. The spatial resolution of 1.5 arcsec translates to about 1000 km at the sun. AIA uses filters to select bandpasses, most of which are in the EUV and complement EVE data (Figure 2.20). The 304 Å bandpass contains the He II 304 Å emission line, which is primarily formed in the chromosphere of the sun. When filaments are present, they appear in this bandpass as long, dark strips, as can be seen in in the 304 Å image of Figure 2.20.

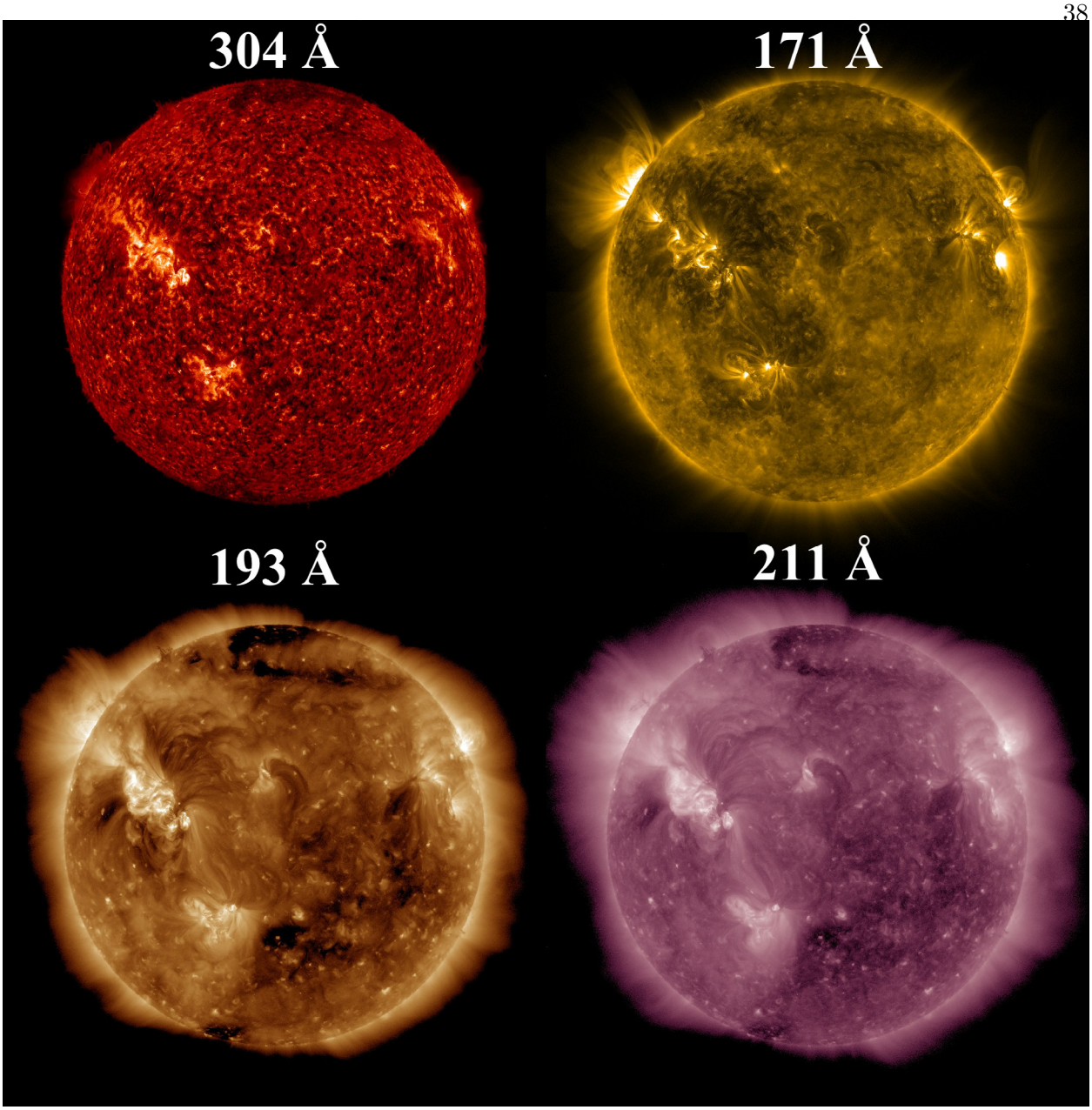

Figure 2.20: AIA images through four of the bandpass-filters that contain important emission lines used in the analyses of later chapters. These images were all taken within 12 seconds of each other on 2010 August 7 at 23:32 UT.

Prominences also appear in this bandpass as large structures hanging above the limb. Thus, this bandpass is ideal for identifying obscuration dimming (e.g., dark filament moves in front of bright flare loops) as will be described in Chapter 3. The 171 Å bandpass (Figure 2.20 upper-right)

contains the coronal Fe IX 171 Å emission line and can show coronal dimming from mass-loss (see Chapter 3) and heat waves (Robbrecht and Wang 2010). The 193 Å bandpass, which contains the Fe XII 195 Å emission line, is particularly good for identifying dimming due to its high contrast. The filament structure previously identified and several coronal holes can be seen in the 193 Å image of Figure 2.20. Finally, the 211 Å bandpass, which contains the Fe XIV 211 Å emission line, shows much of the same structure as the 193 Å bandpass but at lower contrast.

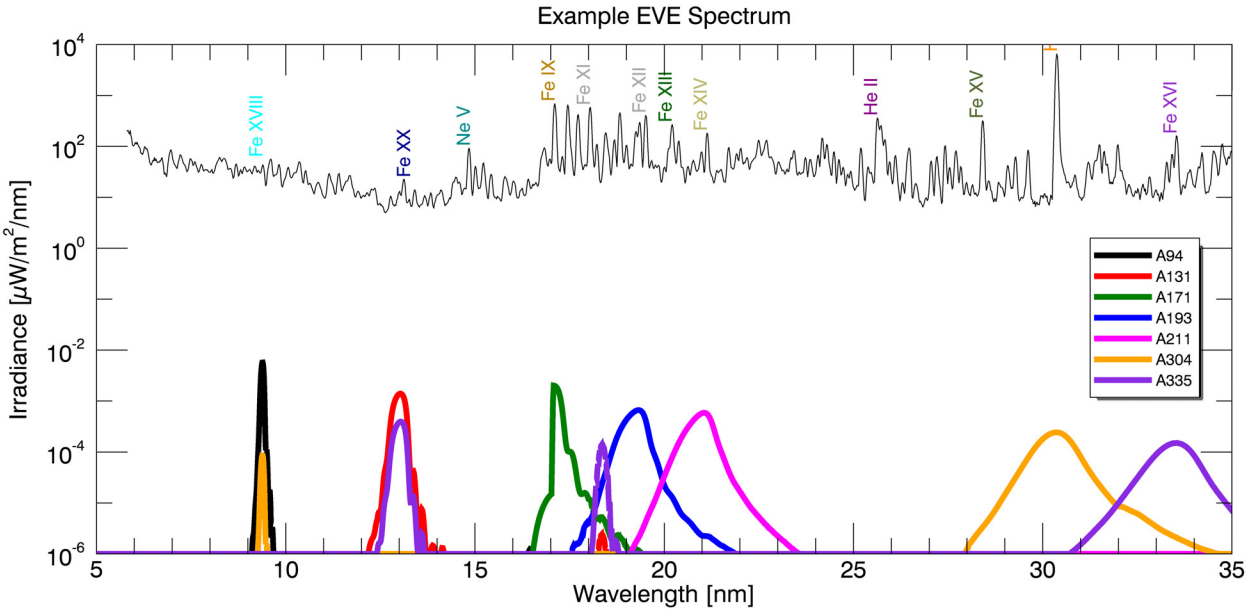

Figure 2.21: The AIA bandpasses with an example EVE solar spectrum to provide an idea of the amount of blending. Some emission lines are labeled with their corresponding ion. The cooler corona lines, such as Fe IX through Fe XII, are the better ones for coronal dimming analysis.

The language of the previous paragraph was careful to distinguish between the bandpasses and the emission lines they contain. This is because the filters have bandpasses that are several nanometers wide, which results in spectral-line blending. Spectral-line blends result in degeneracy in temperature space. For example, if a pixel in the 171 Å bandpass becomes bright, it is not known if that is due to an enhancement in Fe IX or Fe X. The sharpness of the 171 Å bandpass helps mitigate this issue, but as can be seen in Figure 2.21, some of the bandpasses cover a wide range of wavelengths, which can make temperature diagnostics difficult. Fortunately, analyses can

leverage AIA and EVE data together to gain an improved understanding of solar plasma in terms of space, time, and temperature. The spectral images of coronal dimming used in this dissertation are from the AIA instrument.

2.5.3 Coronagraphs

Coronagraphs are instruments that block out the bright photosphere to observe the corona, just as rare total solar eclipses do. The Solar and Heliospheric Observatory (SOHO; Domingo et al. 1995) has a coronagraph onboard – the Large Angle Spectroscopic Coronagraph (LASCO; Brueckner et al. 1995). SOHO was launched 1995 December 2 to the Earth-Sun first Lagrange point, which is always between the earth and sun (though still much closer to the earth). LASCO contains three coronagraphs with different fields of view. Only C2 (1.5 - 6 $R_{\odot}$) and C3 (3.7 - 30 $R_{\odot}$) have remained in operation through the present era when SDO data became available. LASCO and other coronagraphs observe white light from the corona that has been Thomson scattered by the numerous electrons in the fully-ionized and hydrogen-dominated corona. This makes them ideal for observing coronal mass ejections.

The Solar Terrestrial Relations Observatory (STEREO; Kaiser et al. 2007) contains an instrument similar to LASCO, two Lyot coronagraphs (COR1 and COR2; Howard et al. 2008). COR1 has a field of view from 1.5 - 4 $R_{\odot}$ and COR2 from 2.5 - 15 $R_{\odot}$. The STEREO mission has two identical spacecraft that were launched on 2006 October 26; one is slightly inside Earth's orbit and thus travels further and further ahead of the earth, and the other is slightly outside Earth's orbit so falls behind the earth. The increasing distance to these spacecraft means the communications bandwidth is always diminishing, so the resolution and cadence of COR and the other instruments could not be as high as the imaging technology at the time could have made them. Nevertheless, the instruments onboard STEREO provide truly unique possibilities for data analysis. In particular, the geometry of CMEs can be better determined by using STEREO/COR in conjunction with each other and/or with LASCO. This means that CME direction can be determined less ambiguously and thus a "true-space" velocity computed.

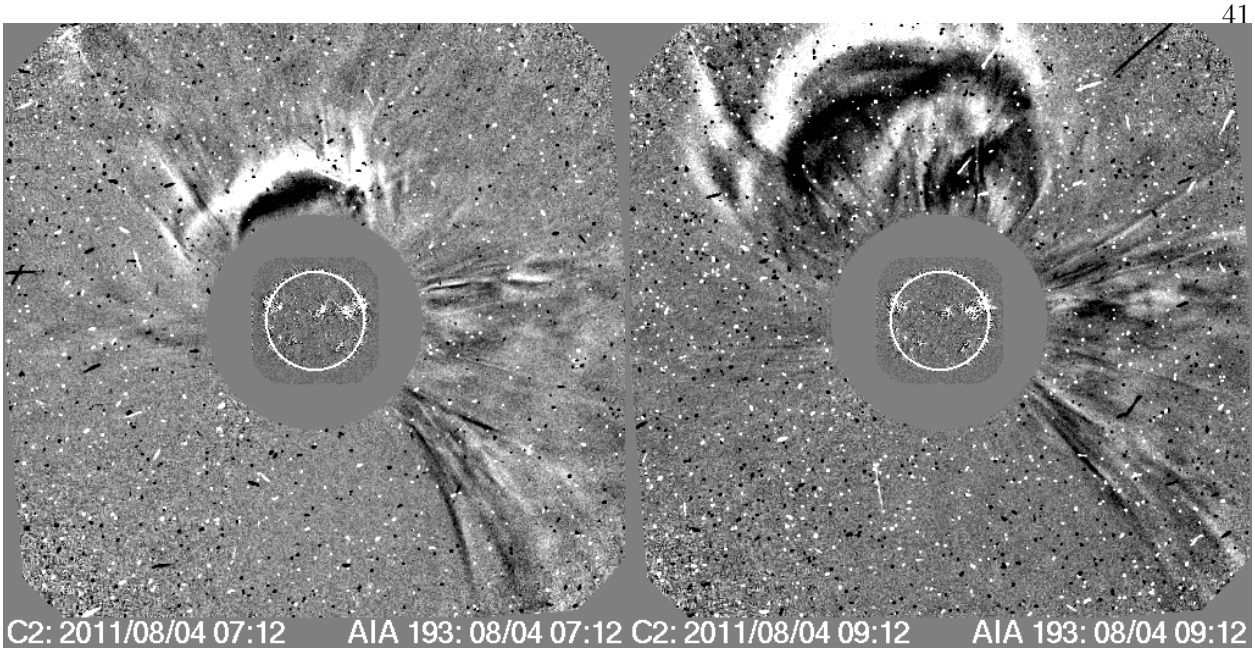

Figure 2.22: LASCO C2 coronagraph running-difference images two hours apart showing the propagation of a CME on 2011 August 4. "Running difference" means that each image subtracts the previous image, so that small changes can be more readily identified. The white front indicates the leading edge of the CME, which expands as it moves outward.

CME speed from coronagraphs is determined by tracking the bright leading edge of the CME through a series of coronagraph images (Figure 2.22). Combining the measured distance from the sun and the time of each observation, a speed and acceleration can be determined. There are caveats, however. The case is simpler if propagation is radial, which may or may not be true and should be evaluated on a case-by-case basis. Also, additional information is needed to estimate the direction of the CME. Only a small percentage of CMEs will have directions that are near 90° from the line-of-sight, so in most cases there is an error associated with that angle. This is where the multiple view angles provided by STEREO can be used to mitigate error.

CME mass is computed by selecting the area of the CME in the coronagraph image, assuming that all particles (electrons) are in the plane-of-sky, summing up the bright pixels, and applying a conversion factor to obtain mass. Again, having multiple view angles helps in determining the volume of the CME. df

Chapter 3

Mechanisms and Observational Signatures of Coronal Dimming

This chapter details the physics of coronal dimming and the observational signatures that result. There are theoretically many physical processes that can lead to an observer identifying "dimming", but some physical processes have little to do with coronal mass ejections (CMEs). Traditionally, the term "coronal dimming" has been assumed to refer to the void left in the corona after a CME departs. This is one cause of a transient hole in the corona and is of the greatest concern to space weather forecasters. However, changing temperatures (common during solar eruptive events) cause ionization fraction shifting, resulting in some emissions dimming while others brighten. Additionally, dark material (e.g., a filament) can pass between a lower bright region (e.g., flaring loops) and the observer, causing a transient dip in emission. Third, solar eruptive events sometimes have associated waves that propagate across the solar disk. These waves are observed as narrow bright fronts with a trailing dark region. The trailing dark region is another way to achieve a transient dimming of emission. Next, there are two ways that Doppler effects can cause transient dips in emission. The first is called Doppler dimming and results from fast moving plasma being sufficiently Doppler-shifted to reduce resonant fluorescence from the solar emission line sources; a phenomenon which is independent of the observation angle. The second occurs if eruptive plasma is moving fast enough in the line-of-sight to shift its emissions outside the bandpass of an observing instrument, which we have named "bandpass dimming". The physics and instrumental identifiers for each of these types of theoretically observable dimming are summarized in Table 3.1 and are discussed in detail in the sections that follow.

Table 3.1: Summary of physical processes that can manifest as observed dimming

Short Name	Physical Process	EVE Full-Disk Observational Identifiers	AIA Imaging Observational Identifiers
Mass loss (Fig. 3.1)	Ejection of emitting plasma from corona	Simultaneous intensity decrease in multiple coronal emission lines, with percentage decrease indicative of percentage mass lost	Area over and near the erupting active region (AR) darkens
Thermal (Fig. 3.2)	Heating raises ionization states (e.g., a fraction of Fe IX becomes Fe X); cooling does the opposite	Heating: Emission loss in lines with lower peak formation temperatures and near simultaneous emission gain in lines with higher peak formation temperatures; vice versa for cooling	Heating: Area near AR darkens in channels with lower peak formation temperature and near simultaneous brightening in channels with higher peak formation temperatures; vice versa for cooling
Obscuration (Fig. 3.5)	Dim feature (e.g., filament material) moves into line-of-sight over a bright feature (e.g., flare arcade)	Drop of emission lines proportional to their absorption cross section in the obscuring material	Direct observation of this obscuration process
Wave (Fig. 3.7)	Wave disturbance propagates globally, causing compression/rarefaction of plasma as wave passes by	No effects have been clearly identified	Direct observation of this wave process, especially apparent with difference movies
Doppler (Fig. 3.8)	Fast moving plasma Doppler shifts away from resonant fluorescence with solar emission lines	Doppler wavelength shift of emission lines and change in intensity, possibly also observed as line broadening	Change in intensity of moving plasma as its velocity changes
Bandpass (Fig. 3.9)	Emissions from fast moving plasma have Doppler wavelength shift	Emission line shifts in wavelength or has broadening	Doppler shift convolves with band-pass sensitivity to cause apparent reduction in emission

3.1 Mass-loss Dimming

The physical process in mass-loss dimming is the eruption of emitting plasma (see Figure 3.1; Harrison and Lyons 2000; Harra and Sterling 2001). It can be a CME (i.e., plasma leaves the sun) or a failed ejection (i.e., plasma rises and then falls back onto the sun), the latter of which still manifests locally as a mass-loss dimming, but does not result in the appearance of a CME in coronagraph data and may not appear in a disk-integrated spectrograph like EVE. The eruption physics model is the standard CME initiation discussed in Section 2.3.4. However, where most CME discussions will then follow the CME as it transitions away from the sun into an interplanetary CME, in mass-loss dimming we are instead interested in the details of the void left behind in the corona. The mass of an average CME and a typical active region are of the same order of magnitude: 10^{15} g, meaning that a departing CME can "blow out" a large part of the active region with it (Aschwanden et al. 2009a). This is the physical process assumed to be the main contributor to observed dimming in many recent studies (Sterling and Hudson 1997; Reinard and Biesecker 2008, 2009; Aschwanden et al. 2009a). Harrison et al. (2003) showed that dimmings can account for a large percentage of CME mass. Thus, mass-loss dimming is very relevant for the space weather community, who study and forecast CMEs.

Observationally, mass-loss dimming appears in EVE as multiple emission lines dropping nearly simultaneously. In the case of a failed ejection, the dimming area and the ejected material are likely to maintain a total emission that is close enough to constant that it will not be apparent in EVE data. For space weather, this is of little concern since CMEs have far greater geoeffectiveness than short-lived holes in the corona of small spatial extent. However, AIA data allow the identification of mass-loss dimming even if the event is a failed ejection. In either case, mass-loss dimming appears in AIA as a relatively compact area near an active region becoming darker, sometimes with a dark cloud visibly moving off-disk. Assuming the dimmings in Reinard and Biesecker (2008) to all be due to mass loss, the timescale of the process is 3 – 12 hr and rarely persists longer than a day. Additional observations from the Hinode spacecraft have confirmed

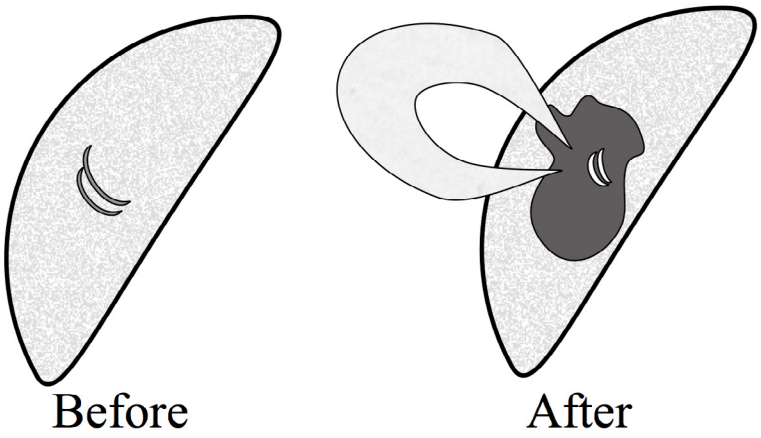

Figure 3.1: Schematic depicting the process of mass-loss dimming. Prior to the eruption (left), coronal loops in an active region are relatively quiescent. During and after the eruption (right), the loops become brighter and reconfigure, a CME is ejected, and a void forms in the coronal plasma. The post-flare coronal loops usually reform in much the same as the original configuration.

density decreases with accompanying outflows (Attrill et al. 2010; Harra et al. 2010; Tian et al. 2012).

3.2 Thermal Dimming

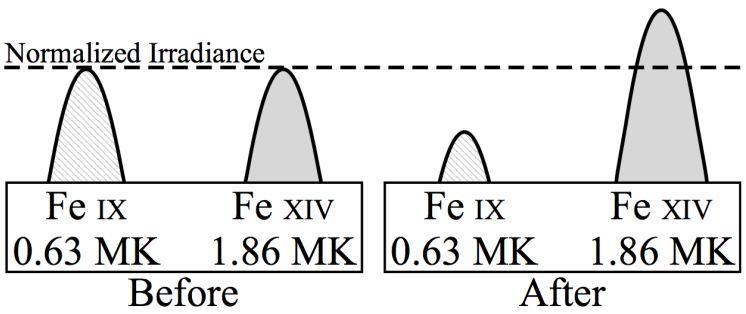

Figure 3.2: Schematic depicting the observational behavior for the thermal dimming effect. Relative to a pre-eruption time (left), the cooler Fe IX emission drops while the warmer Fe XIV emission increases (right) due to heating of the plasma and redistribution of ionization states.

Temperature evolution of emission lines is only interpreted as observed dimming if one is not careful to observe co-spatial emission lines at different peak formation temperatures. As plasma is heated or cooled, the ionization fraction changes, necessarily causing the emission intensity to

change (Figure 3.2). For example, heating causes some Fe IX to become Fe X and thus, in the absence of competing physical processes, Fe IX 171 Å emission drops while Fe X 177 Å emission rises. This pattern was identified observationally in Figure 6 of Woods et al. (2011) using SDO/EVE data, Robbrecht and Wang (2010) using STEREO/EUVI, and Jin et al. (2009) and Imada et al. (2007) with Hinode/EIS. It can also be observed in the standard composite (multi-wavelength) movies produced by the AIA team; indeed, this is one of the prime purposes for the composites. The initiation time and duration of temperature evolution tends to be quite similar to mass-loss dimming, as they are typically both responses to the rapid release of magnetic field energy in active regions and require several hours of recovery time. Thus, thermal processes could be mistaken for mass loss if only a single spectral line was observed. Ideally, unblended emission lines from an entire coronal ionization sequence (e.g., Fe I to Fe XVIII) could be used to mitigate this convolution of dimming observations. However, as we will show in Section 4.3, it may be sufficient to have observations of two sufficiently separated ionizations states to differentiate between thermal evolution and mass-loss dimming. This is due, in part, to the fact that hotter lines (e.g., Fe XV and above) are primarily emitted from confined loops near the flare and are thus not strongly impacted by mass-loss dimming.

Multi-wavelength Doppler studies have shown that while all measured emission lines become blue-shifted (indicating an outflow), the magnitude of the shift is strongly proportional to the lines peak formation temperature (Imada et al. 2007; Jin et al. 2009). Figure 3.3 shows this dependence for a plage region with a dimming event during an X-class flare. Note that Imada et al. (2007) state that these outflows are only "possibly" a part of the CME. Part of the explanation for this phenomenon is that as a population of ions is accelerated outward as part of the CME, it is simultaneously experiencing heating as part of the eruptive process. This causes the ionization fraction to shift upward to the point where there may be little low ionization states left e.g., Fe IX. Tracking a single ion, one would see the same nuclei accelerating outward while having electrons stripped away. This explains why lower ionization states seem to have relatively little outflow velocity. Additionally, Fe IX 171 Å emission can be depressed further after open magnetic field

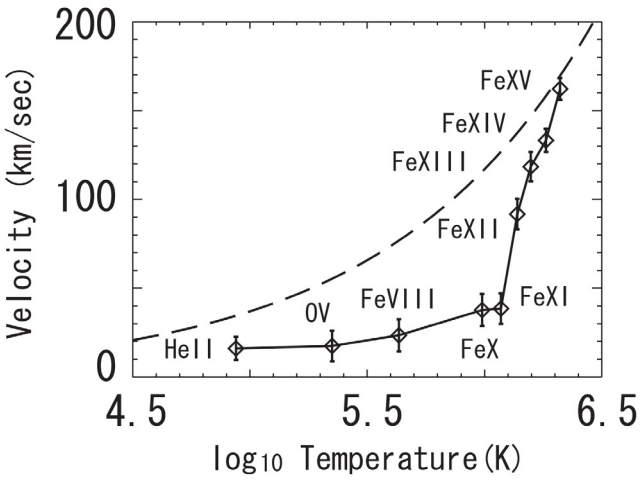

Figure 3.3: Outflow velocity vs emission line peak formation temperature for a dimming region near a plage. Adapted from Imada et al. (2007).

lines from the departing CME close down and cause another bout of heating; causing e.g., Fe IX to become Fe X and beyond, which propagates outward as a "heat wave dimming" (Robbrecht and Wang 2010). However, Mason et al. (2014) found that the onset time, slope, and duration of dimming are comparable in SDO/AIA 171 Å and 193 Å[1] and in SDO/EVE 171Å and 195 Å (described in Chapter 4). It should also be noted that EUV images tend to provide higher contrast for dimming in Fe XII 195 Å than Fe IX 171 Å. This is because there is much less Fe XII in the quiescent corona than Fe IX. Therefore, the background in 171 Å images is much brighter, making dimming (which are typically less than a 5% reduction of full-disk emission) more difficult to identify. Nevertheless, we find that for full-disk emission (i.e., irradiance from EVE) the 171 Å emission shows stronger dimming than the 195 Å emission as shown in 3.4.

It is important to note that, in general, the magnitude of total observed dimming in a given line in EVE spectra is inversely proportional to its peak formation temperature, which can be inferred from Figure 3.4. This figure was generated using a simple algorithm that searched all EVE/MEGS-A data for relative irradiance decreases greater than a specified threshold (1%, 2%,

[1] Note that the SDO/AIA 193 Å band encompasses 195 Å

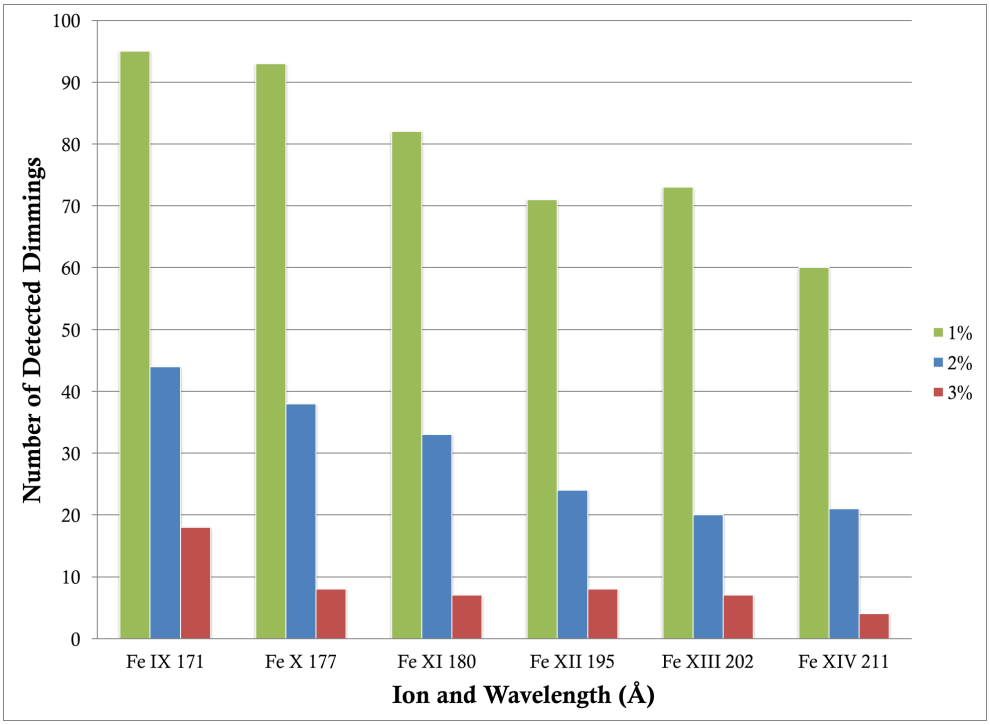

Figure 3.4: Number of identified dimmings in EVE for six spectral lines using different percentage dimming depths as the threshold for a detection. There were 302 flares ($\geq$ M1.0 GOES class) used to trigger an automated search for dimming in EVE. Note the decrease in detections with increasing ionization state (i.e. peak formation temperature).

3%) of flares exceeding GOES X-ray class of M1. The window of time searched was bounded by the GOES event start time and the sooner of either 4 hours after the start time or the next GOES event start time. This algorithm was applied to all EVE data from mission start (2010 May 1) to the failure of the MEGS-A detector (due to a shorted capacitor on 2014 May 26). MEGS-A takes the measurements of all wavelengths studied here. Figure 3.4 shows that the number of dimmings dramatically decreases as the magnitude threshold is increased, and decreases slightly with higher peak formation temperature. This latter effect is partially due to flare heating adding emission in the higher temperature, higher ionization state, lines that partially offsets the mass-loss dimming. Additionally, these trends indicate that at sufficiently high peak formation temperature, no dimming may be observed at all, even at the lowest detection threshold, which is consistent with the hotter lines being restricted to the confined flare loops and hence experiencing no mass loss. In

other words, the higher the peak formation temperature, the greater the relative contribution of more confined loops to the measured emission.

An instrument with spatial resolution like AIA can be used to isolate the confined flaring loops and create a time series of just the dimming region, and then the sum of those dimming regions can be compared to the EVE full-disk (irradiance) dimming trend. This type of analysis and comparison between AIA and EVE dimming is provided in Chapter 4. AIA too has its own limitations; relevant in this case is the relatively lower spectral resolution that blends together emission from several ionization states of Fe. With EVE and AIA combined, it is possible to analyze thermal dimming but the ideal instrument for fully characterizing this phenomenon would be a high spectral resolution hyperspectral imager in the EUV.

3.3 Obscuration Dimming

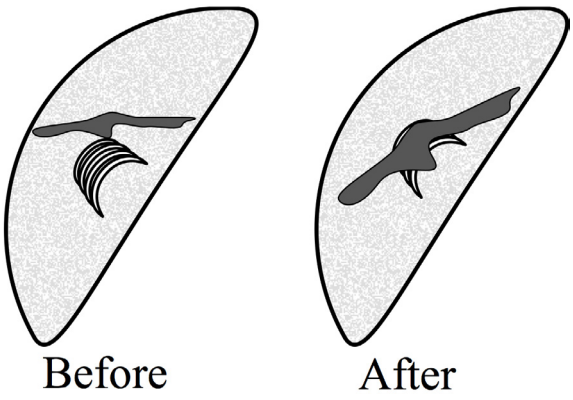

Figure 3.5: Schematic depicting the process of obscuration dimming. A filament previously obscuring only the quiet sun (left) expands and moves in front of a flare arcade (right). This results in a decreased observed emission from the flare arcade in wavelengths where the filament is optically thick.

The physical process that results in apparent dimming here is material that is dark in a particular wavelength (e.g., a filament) moving between lower-down bright material (e.g., flare arcade) and the observer (Figure 3.5). In optically thick wavelengths, the dark plasma absorbs some of the bright emission, resulting in an apparent decrease in emission. The slow draining of plasma

back to the corona can obscure underlying emission for hours, and absorption can be observed in both coronal and chromospheric lines (e.g., Gilbert et al. 2013). Although obscuration dimmings can exhibit time and spatial scales comparable to the more short-lived mass-loss dimmings, it is fairly straightforward to identify absorption signatures in the EUV images. It may also be possible to identify this phenomenon with EVE using the He II 256 Å and 304 Å chromospheric emission lines and knowledge of the absorption cross-section through filamentary plasma.

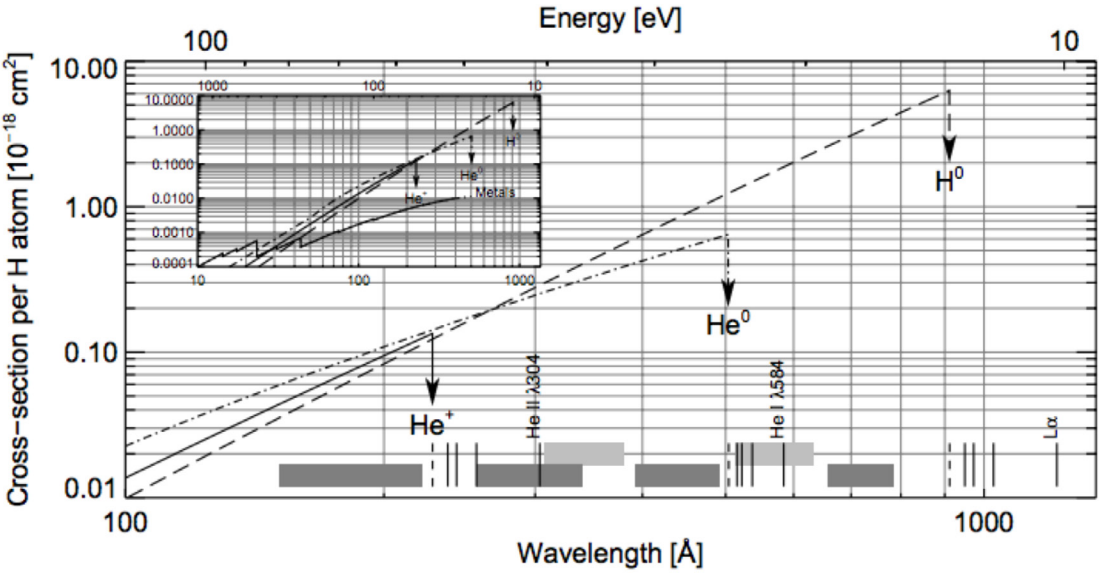

Figure 3.6: Photoionization cross-sections for He I (dot-dashed line), He II (solid line), and H (dashed line) per hydrogen atom. The inset shows a wider wavelength range of the same data but with metals shown for comparison. The dashed vertical bars at the bottom indicate the edges of respective continua. The grey regions at the bottom are not pertinent here as they correspond to specifics of the SOHO/CDS instrument. Adapted from Andretta et al. (2003).

Figure 3.6 shows the photoionization cross-sections of the dominant species in the solar corona. Hydrogen and helium contribute an order-of-magnitude more absorption than metals[2] , and thus the effect of metals can be ignored. The cross-sections are quite steep in the wavelength range of interest here (roughly 150-310 Å). This means that approximately twice as much He II 256 Å than He II 304 Å emission will come through a filament. Furthermore, the mass-loss dimming sensitive lines (e.g., Fe IX 171 Å and 195Å) will be less affected by this obscuration, but a 1%

[2] "Metals" in the astrophysical sense

effect would be sufficient to cause a "false" detection. It may be possible to identify obscuration dimming with EVE's 256 Å and 304 Å measurements and determine that an obscuration dimming has occurred. However, further analysis of this type of dimming is required before any conclusions can be drawn.

3.4 Wave Dimming

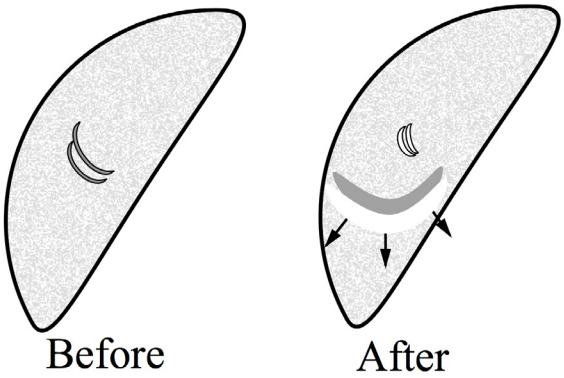

Figure 3.7: Similar to Figure 3.5, but depicting the process of wave dimming. After an eruptive event, a wave propagates and expands through the corona. The compressed plasma of the wavefront results in enhanced emission, while the rarefied trailing region is dimmed.

The debate about the physics of coronal EUV waves continues (e.g., Zhukov and Auchère 2004; Muhr et al. 2011; Liu and Ofman 2014) but one of the simplest explanations of the observations is that plasma is compressed as a longitudinal wave passes through the medium. Traveling (i.e., not static) rarefactions are sometimes observed following the compression (Muhr et al. 2011), the compressed regions having higher densities resulting in increased emission, and vice versa (Figure 3.7). Alternatively, some models suggest that the observed phenomenon is not a wave at all, but rather the impact of the CME departing on the global magnetic field (Chen et al. 2002, 2005). Regardless of the physical process responsible, the observation is the same. The EUV waves emanating from an eruption can be seen to cause dimmings and brightenings elsewhere in the solar EUV images, often starting at the eruption site and then seen later very far from the original eruption site, particularly near other active regions. We refer to these dimmings that are non-local

to the erupting site as sympathetic dimmings (Schrijver and Higgins 2015). This is quite likely to occur if a distant active region has significant potential energy stored when the disturbance reaches it – the wave propagating across the magnetic field lines acts as a catalyst.

It is important to distinguish between the wave-caused dimmings and other causes of remote dimming, such as large-scale disappearing loops that are visible in soft X-ray images but only have visible EUV changes at their footpoints (Pohjolainen et al. 2005). EUV wave dimmings are unlikely to be easily identified in full-disk spatially-integrated instruments like EVE because the enhanced emission nearly cancels out the dimmed emission when summed.

3.5 Doppler and Bandpass Dimming

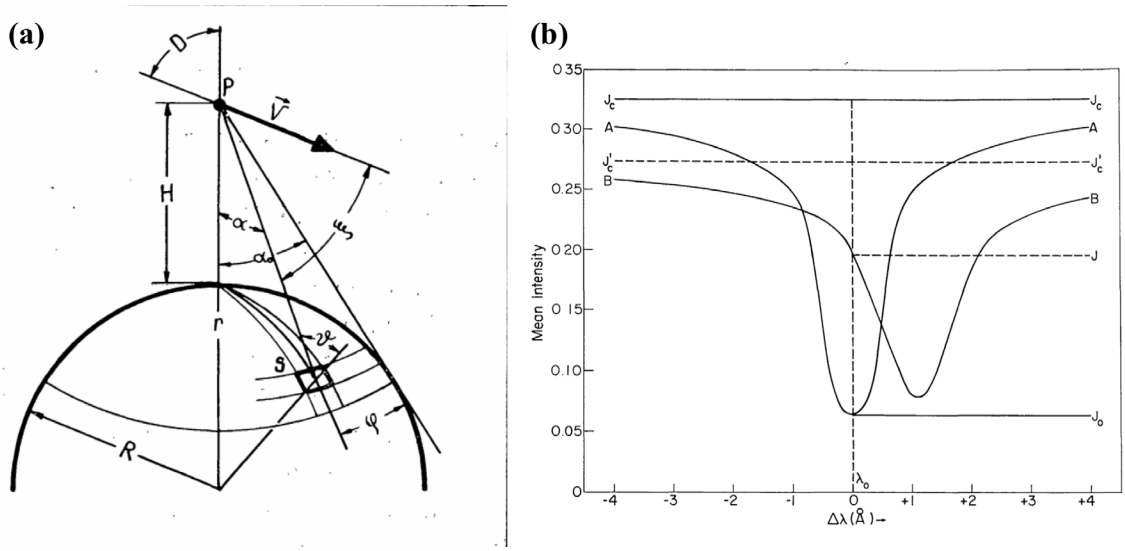

Figure 3.8: (a) Geometry of Doppler dimming. The large circle at the bottom represents the sun, the point P represents the position of mass that has erupted e.g., a CME. The vector V is the velocity of the CME. The square patch on the sun represents an area of source emission. Adapted from Rompolt (1967). (b) The Hα profiles seen by (A) a stationary observer at a height of 5600 km above the photosphere; and (B) an observer at a height of 30,000 km moving radially outward at 75 $km\ s^{-1}$. The mean intensity (as seen by the scattering medium) is measured in units of the intensity of the nearby continuum at the center of the disk. It can be seen that the Doppler shift also causes an intensity decrease. Adapted from Hyder and Lites (1970).

Two additional processes can theoretically lead to the observation of dimming in a limited wavelength range and both result from Doppler effects. The first has been given the name "Doppler

dimming". In this type of dimming, resonant fluorescence of a high-velocity, remote cloud of plasma (e.g., CME) by a source population (solar emission lines) can decrease as the resultant Doppler shift becomes sufficiently large (see Figure 3.8; Hyder and Lites 1970). Here, Doppler takes effect due to the relative velocity between the source (the sun) and the scattering medium (the CME) and is thus independent of observer angle. This phenomenon has been known for decades for cometary emissions (Swings 1941; Greenstein 1958) and has been documented in chromospheric lines associated with eruptions (Labrosse and Mcglinchey 2012) as well as in coronal lines such as O VI for polar coronal hole outflows (Giordano et al. 2000). However, the majority of EUV emission lines in the corona are collisionally dominated i.e. not resonantly excited, and will not exhibit this effect. Furthermore, the dimming region is the CME itself, which is likely to be outside the field of view of EUV instruments observing the solar disk. Therefore, it is possible to diagnose this type of dimming when it is pronounced in resonantly excited lines but does not manifest in the lines of interest studied herein.

The second type of dimming that results from a Doppler effect is one we call "bandpass dimming". This physical process is tied to the observer's location similarly to obscuration dimming (see Section 3.5). Mass ejected toward the observer will have emissions that are necessarily blue-shifted. If the velocity is high enough, it can shift emission lines outside of an imager's bandpass, causing an apparent dimming in the data. Most imagers use filters that tend to have bandpasses on the order of nanometers but can have sharp edges (Figure 3.9). CMEs typically have speeds ranging from a few hundred to a couple thousand $km\ s^{-1}$. However, a CME only accounts for a small fraction of the total emission from the solar disk. As noted in Hudson et al. (2011), these Doppler shifts tend to be on the order of picometers. Additionally, a CME moving fast enough to shift emission outside the bandpass would be outside the field-of-view of the instrument in a very short time. Thus, this type of apparent dimming is not expected in EUV images, but we include it for completeness and note that this may be a consideration for designing future instruments.

In a spectrograph like EVE, the Doppler shifts would instead simply cause a wavelength shift of the emission line from the ejected material, which is how Hudson et al. (2011) performed

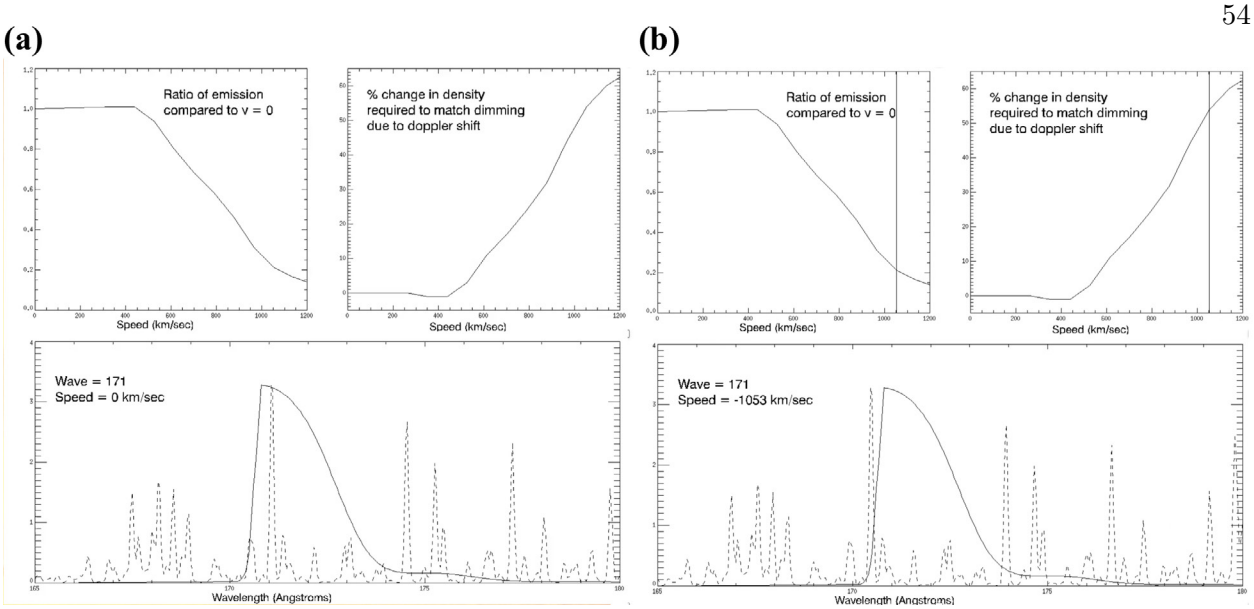

Figure 3.9: Spectra to illustrate bandpass dimming, taken as snapshots from a movie produced by Barbara Thompson. (a) Bottom: The dashed line shows a modeled solar spectrum and the solid line shows the AIA 171 Å bandpass. Top left: The ratio of emission relative to plasma with no line-of-sight velocity as a function of velocity. Top right: The amount of density decrease (in %) that would be required to achieve the same amount of dimming as bandpass dimming at each velocity. (b) Same as (a) but at a velocity of 1053 $km\ s^{-1}$, which is an example of the 171 Å emission Doppler shifting outside the associated AIA bandpass.

their Doppler analysis of the EVE data. When this Doppler-shifted emission is convolved with the relatively static plasma remaining on the sun, a small Doppler shift from the ejected material manifests as line-broadening in the integrated irradiance while a large shift would result in a line splitting. It should be noted that the EVE extracted lines data product applies a static mask to the spectra so a sufficiently large Doppler shift could cause an apparent dimming in this product. Again, the observed shifts are far too small to impact the EVE data analysis.

3.6 Dimming Physics and Observations Summary

The physics for most of these types of dimming is relatively simple and well-understood, with the exception of global waves. Mass-loss dimming is simply the direct result of a CME removing a significant quantity of emitting material from the solar corona. The coronal dimming amount

increases as the CME pulls away, reaches a maximum dimming depth, and then the emission begins to return to the original pre-flare level after a few hours as post-flare loops begin to replace the lost plasma from the surrounding corona and transition region. Instrumentally, even though EUV measurements select specific temperature ranges, mass-estimates based on them appear consistent with white-light coronagraph derived masses (Aschwanden et al. 2009a).

Thermal dimming is a major concern in nearly all of the citations above for its potential to interfere with mass-loss dimming analysis and the resultant estimated CME masses. The physics here is also simple: eruptive events result in various forms of heating (see Section 2.3) that shift upward the ionization fraction of dominant EUV emitters (e.g., Fe). Instrumentally, this effect can be compensated for by measuring emission lines from multiple ionization states of the same ion (e.g., Fe IX-XV).

Obscuration dimming physics are also simple, essentially a result of extinction, as light passes through a medium with nonzero opacity. Instrumentally, this is easily identified with imagers and we believe it may be possible to identify with a spectrograph, provided some chromospheric helium emission lines are measured (e.g., 256 Å and/or 304 Å).

The physics of global waves is highly contested but the observations are well established. For a disk-integrating spectrograph like EVE, which is the primary source of data analysis herein, we believe that wave dimming will be negated by wave brightening. Indeed, to our knowledge, no observations of waves have been detected from EVE observations.

Doppler dimming physics are well understood and long standing. A CME may fluoresce due to stimulation from the sun, but the wavelengths will be Doppler shifted according to the relative velocity of the CME from the sun. This shift reduces the efficacy of the stimulation, resulting in less fluorescence. However, the dimming region in this case is the CME itself, which is likely to be outside the field of view of instruments like AIA and EVE. Additionally, the emission lines of interest in this study are collisionally dominated. Thus, Doppler dimming is an interesting phenomenon but is not expected to dramatically impact analyses of the other types of dimming.

The physics of bandpass dimming is simple Doppler shifting of an emitting plasma. Potential

dimming in this case is primarily an instrumental effect, as the Doppler shift could push important emission lines outside the instruments bandpass or data processing line-selection masks. However, studies have shown that the actual Doppler shifts are orders of magnitude too small to cause this type of dimming.

Chapter 4

Coronal Dimming Case Studies

This chapter focuses on the detailed analysis of two coronal dimming events. One was selected for its relative simplicity, involving only mass-loss dimming and some thermal effects, while the other was selected for its complexity, involving nearly all of the types of dimming as described in Chapter 3. Observations and analysis of the EUV irradiance and images of these events as well as the related coronagraphs are first described in Section 4.1. A new method for deconvolving flare emission from dimming irradiance measurements is developed in Section 4.2 while Section 4.3 contains the associated error propagation. Finally, Section 4.4 provides analyses spanning the observations of these two coronal dimming events and parameterizes dimming into depth and slope. We find that the new flare-dimming deconvolution method for irradiance successfully matches the dimming profile extracted from the spatially-isolated dimming as obtained from EUV image time series for the simpler dimming case. Thus, we show that it is possible to accurately characterize dimming in a localized area even with no spatial resolution, i.e., with irradiance. The preliminary analysis of the more complex dimming case is provided here, but further analysis of the complex dimming case for the full-range of cotemporal dimming processes will be a topic of postdoctoral research.

4.1 Observations and Analysis

4.1.1 Simple Dimming Case

This event occurred on 2010 August 7 at approximately 18:24 UT. The eruptive event consisted of an M1.0 flare, dimming in the region around the flare, and a coronal mass ejection (CME). Other, relatively distant, active regions were also on disk but did not have any significant sympathetic eruptive responses as is sometimes seen. Mass-loss dimming and flare-related thermal effects were found to be important, while the other types of dimming (see Chapter 3) were negligible.

Coronagraph Observations

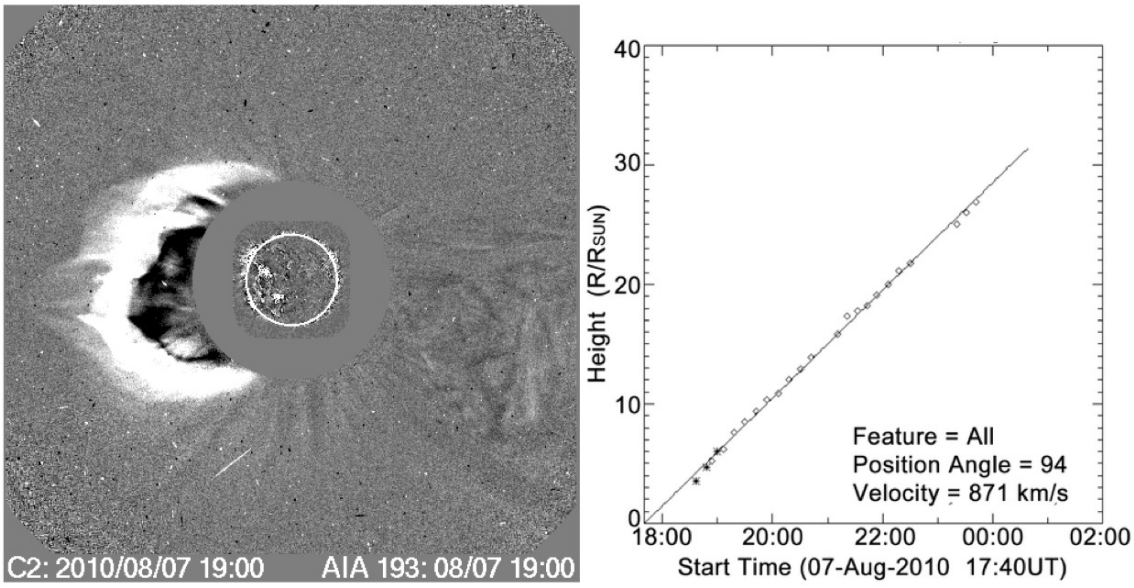

Figure 4.1: CME event at 19:00 on 2010 August 7. Left: difference image from LASCO C2 and AIA 193 Å channel. Right: CME height versus time shows nearly linear velocity of 871 km s^{-1}. Figure adapted from CDAW CME Catalog, courtesy of S. Yashiro and N. Gopalswamy.

The Coordinated Data Analysis Workshops (CDAW) LASCO CME catalog (herein referred to simply as the CDAW catalog) is an extensive database of all CMEs observed by the SOHO/LASCO coronagraphs with related quantities such as date, time, computed velocity, and sometimes mass (Gopalswamy et al. 2009). The CDAW catalog has seven CME events listed for 2010 August 7. All but two of them occur prior to the M1.0 flare at 18:24 UT that is of primary interest for the

simple dimming case study. This rules out all but those two to be CMEs associated with the M1.0 flare. The CME shown in Figure 4.1 is flagged as a halo event with a time of 18:36 UT in CDAW, while the next event occurred with a central position angle of 116° at 22:24 UT. The timing and location of the flare and associated dimming region suggest that the halo CME is the one associated with the dimming. The plane-of-sky velocity estimate for this CME is 871 km s^{-1} as indicated in Figure 4.1. No mass is listed for this CME in CDAW, but using LASCO and STEREO data and the techniques outlined in Colaninno and Vourlidas (2009), a mass of 6.4×10^{15} g was computed for this CME event (A. Vourlidas 2014, private communication). A "true space" velocity was also computed as 850 km s^{-1} at 9 $R_{\odot}$ with a deceleration of 6.84 m s^{-2} (Figure 4.2). True space in this context means that the viewpoints from multiple angles were used to determine the actual 3-D vector of propagation; a single viewpoint has inherent uncertainty in the propagation angle because there are too many free parameters to fully constrain it. Based on these estimates for mass and velocity, this CME is considered be of modest size.

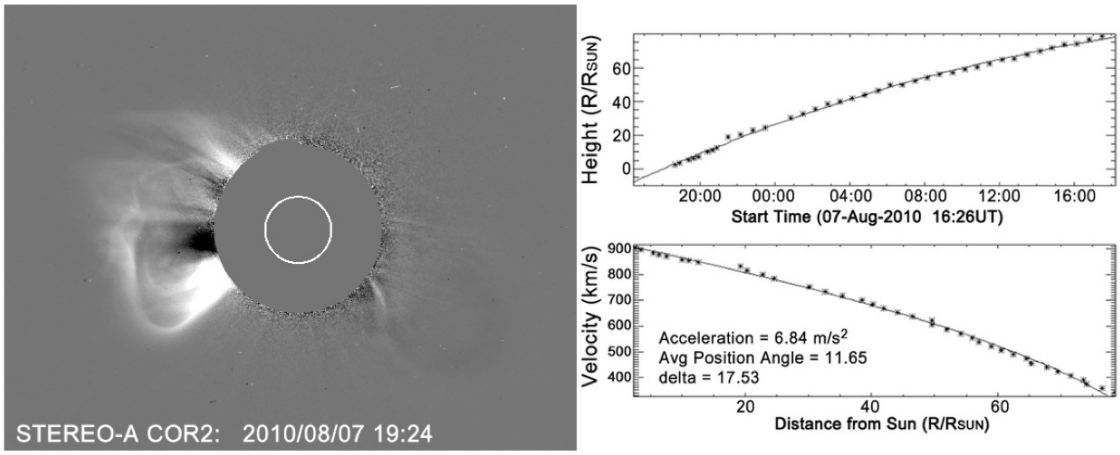

Figure 4.2: Left: STEREO-A COR2 difference image at 19:24 UT. Right: CME height vs. time calculated from STEREO and shows a deceleration of 6.84 m s^{-2}. Figure courtesy of Barbara Thompson.

SDO/AIA EUV Image Observations The relative simplicity of this event is why it was chosen for a case study. The observations in AIA do not suggest that obscuration, waves, or Doppler shift contributed to the observed dimming. The area in the red contour of Figure 4.3 was

selected manually (by eye) to represent the region of mass loss. Pixel values inside each contour were summed and a time series of these sums created with successive images in multiple AIA wavelength bands. These light curves are shown on the right of Figure 4.3. The light curve for the red contour shows clear dimming in 193 Å and 171 Å. In fact, the dimming from this region accounts for nearly all of the observed dimming throughout the entire event. This contour was selected after several iterations that indicated slight deviations in the contour had minimal impact on the light curve, as long as the dark region was fully encompassed. In other words, the result is fairly insensitive to the precise contour selection. The other contours were also selected manually to isolate regions of potential dimming e.g., as a sympathetic response from the solar eruptive event of interest. The exception is the magenta contour surrounding the flare loops that brightens dramatically but does not ever dim.

The He II 304 Å light curves are included to provide a contrast to the dimming effects seen in the coronal Fe lines. This He II wavelength is generated primarily in the chromosphere and transition region, as opposed to the coronal source of the other EUV wavelengths. Mass loss occurs primarily in the corona, as the term coronal mass ejection suggests. This is reflected in the lack of dimming observed in the non-coronal He II 304 Å emission line.

Thermal effects may play a role in this event but may be difficult to quantify using only AIA because the relatively wide spectral bands of AIA channels mean many emission lines and continuum are blended together (see Figure 2.21 and Table 2.2), which makes specifying a well-defined temperature difficult. Nevertheless, some indication of temperature is given by AIA and multi-wavelength composites can aid in this analysis. Figure 4.4 shows AIA composite images (211 & 193 & 171 Å) before the solar eruptive event and during the dimming. All of these bands correspond primarily to the cool corona and transition region. If an area is dark, that means that there is little emission in all three of these wavelengths. Because these three bands span a broad range of temperatures from 0.6 MK to 1.86 MK, having all three dim at the same time means it is not a thermal dimming case but is instead indicative of mass loss dimming. In areas where temperature effects are very strong, e.g., heating in the confined flare loops, it can be seen that

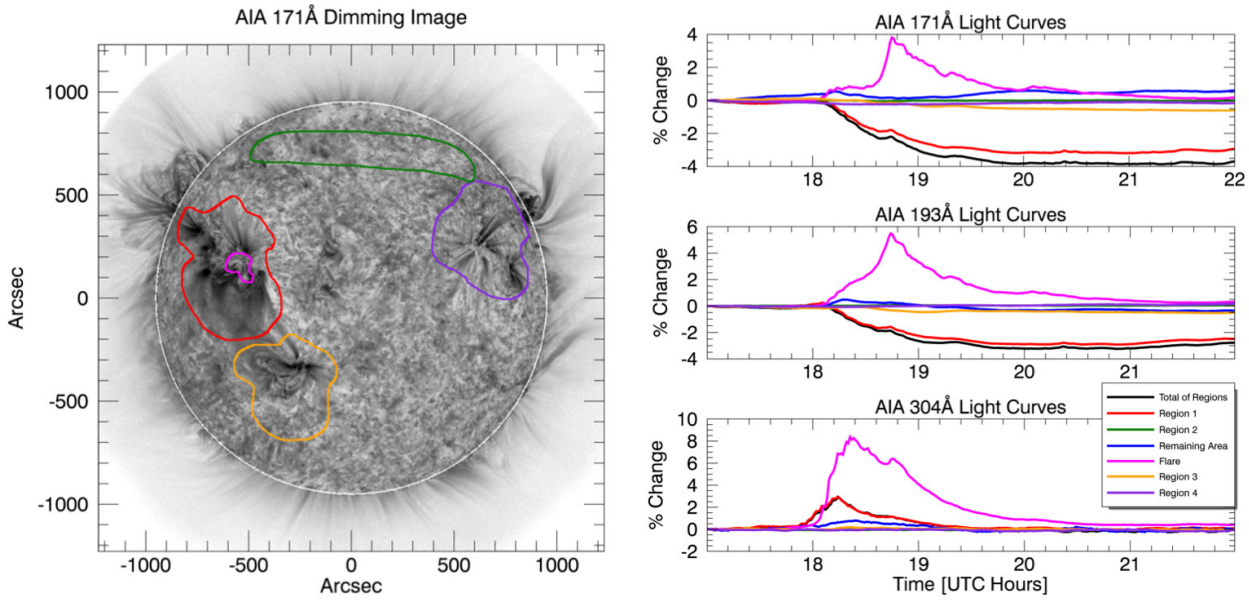

Figure 4.3: AIA results for the M1.0 Flare on 2010 August 7. Images improved by using point spread function to compensate for instrument "blurring" of light. Left: AIA 171 Å channel difference image with subjectively selected region contours overlaid. The red contour outlines what is thought to be the region of mass loss. The orange and purple contours outline other active regions on the disk, which have the potential to have sympathetic eruption/dimming. The green contour outlines a filament, which also has the potential to sympathetically dim based on its behavior during the M flare on 2010 August 5. The magenta contour isolates the flaring coronal loops. The white line around the solar limb is an artifact of the solarsoft de-rotation method. Right three plots: light curves of AIA 171 Å, 193 Å, and 304 Å channels for the color-corresponding contours on the AIA image. The blue line is the light curve for all on-disk area not enclosed by a contour. The black line is the sum of all contoured regions (excluding the magenta flaring region) and acts as a proxy for total dimming. All percent changes are calculated from the band's pre-flare value at 17:00 UT. The transition region He 304 Å emission does not show dimming; both cool corona Fe emissions (171 Å and 193 Å) show dimming.

emission is strong in all three of these bands resulting in the composite being white near the active region. Even though the flare loop region is also where the highest ionization states and their emissions can be found, there is still ample emission in these relatively low ionization states of Fe. Thus, it's unlikely that a region in these composites would become dark purely from a temperature change. EVE is less sensitive than AIA to blending in temperature space due to its higher spectral resolution and plethora of emission lines from Fe at different ionization states. A future study using the differential emission measure techniques of Caspi et al. (2014b) to study the temperature

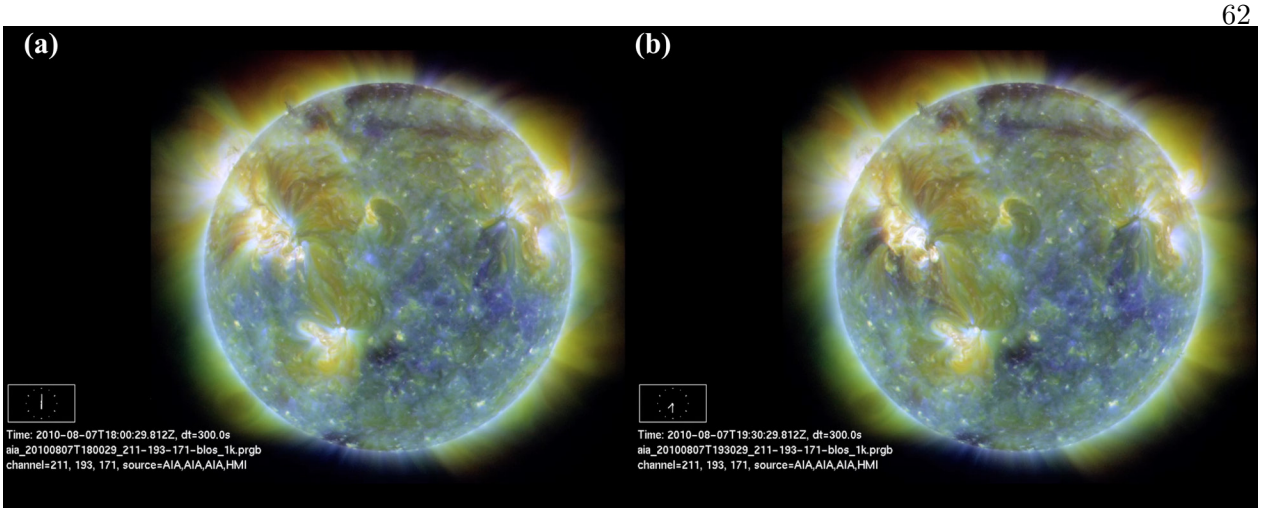

Figure 4.4: AIA composite images (a) prior to solar eruptive event and (b) during deep dimming. In these images, purple is 211 Å, brownish-gold is 193 Å, and yellow is 171 Å. These static images show dimming in the region as outlined in Figure 4.3, though the change is much more dramatic and obvious when viewed as a movie (link).

evolution could help to quantify this effect.

SDO/EVE EUV Irradiance Observations Figure 4.5 shows a trend that is consistent with the findings from Figure 3.4: that an ion's peak formation temperature is inversely proportional to magnitude of dimming. The transition from an ionization state that shows dimming to ones that only show brightening occurs at Fe XIV 211 Å, which itself shows dimming in some events but not others. The transition for where the Fe emission shows dimming varies by solar eruptive event. For example, the Fe XVI 335 Å emission has shown dimming for larger CME events (Woods et al. 2011). Herein, we will refer to Fe IX 171 Å through Fe XIV 211 Å as "dimming lines" and Fe XIV 211 Å through Fe XXIV 192 Å as "non-dimming lines" based on examining many dimming events. Note that 211 Å emission line is included in both descriptions to reflect its ambiguity for different eruptive events.

It is also important to note in Figure 4.5 that the onset of dimming in the dimming lines is nearly simultaneous. Meanwhile, the gradual-phase flare peak is delayed in lower ionizations of Fe, which is due to a cooling effect. The primary source of energy release in a flare is near the point of magnetic reconnection, typically far above the footpoints of the magnetic loops involved,

in the corona. Some of the energy goes into the acceleration of particles downward. When these particles impact the denser chromosphere, they cause heating and chromospheric evaporation. As that thermal plasma enters the corona it cools (Fletcher et al. 2011), and highly ionized Fe gains electrons (radiative recombination) as the primary primary cooling process. Thus, the peak is later for lower ionization states as the hot, highly-ionized Fe ions cascade down to cooler Fe ions for this case (see Figure 4.5). This process is typical for most flare events. The Fe IX 171 Å irradiance, in particular, shows the competing effects of this gradual phase flare peak and coronal dimming: it's irradiance begins to drop at the same onset as the other emission lines, then has a positive peak of about +2%, and drops to a dimmed condition again. Images with spatial resolution can isolate the flaring region responsible for this peak, as is shown with the magenta contour in Figure 4.3. Alternatively, we have developed a method for isolating and removing this peak in dimming lines with the spatially-integrated irradiance from EVE, which will be detailed in Section 4.2.

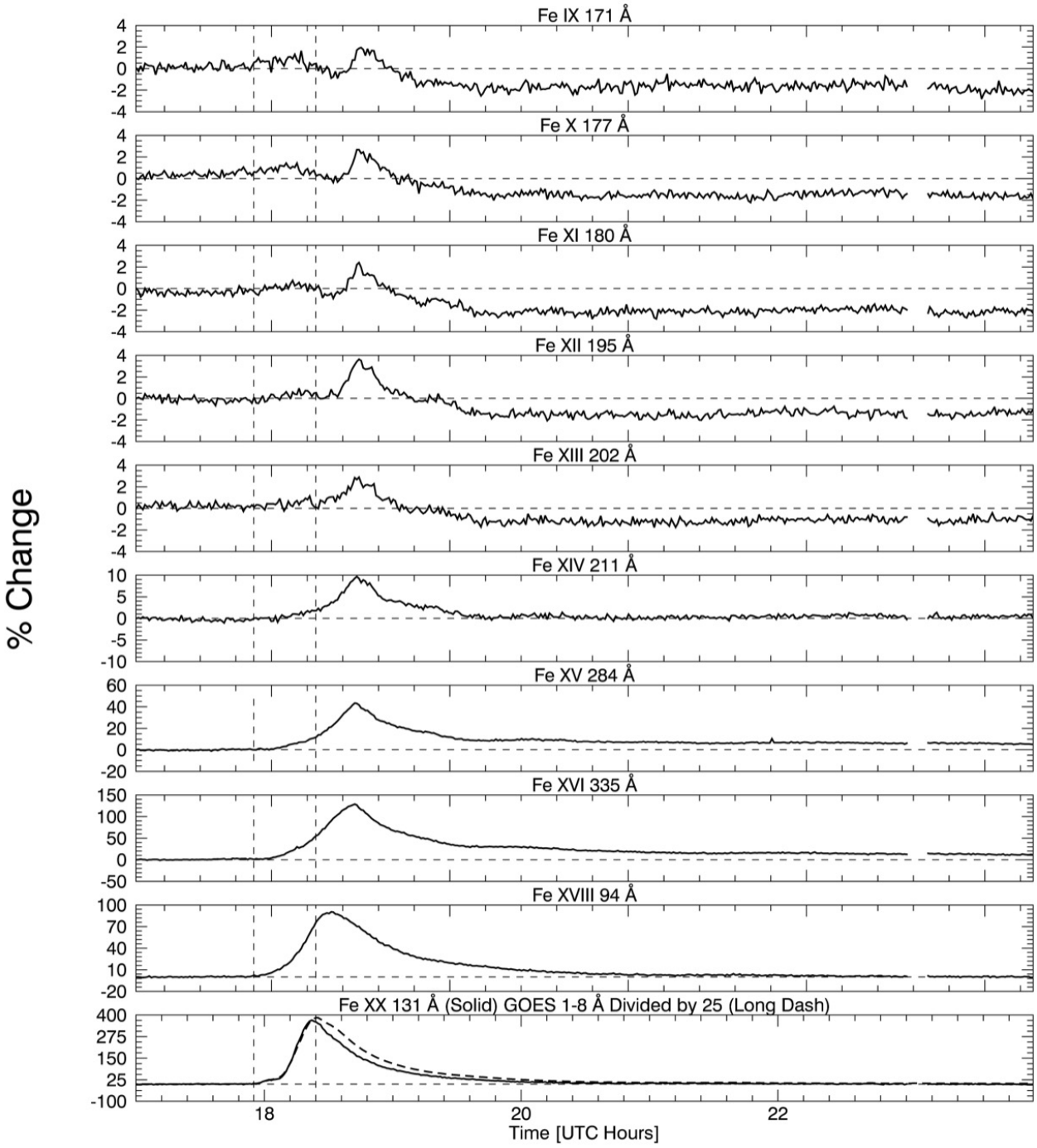

Figure 4.5: One minute average EVE light curves of the 2010 August 7 coronal dimming event for most of the spectral lines listed in Table 2.2, as well as the GOES 1-8 Å channel light curve. The leftmost vertical dashed line indicates the GOES event start time, while the other vertical dashed line indicates the GOES event peak time. Peak formation temperature of the EVE spectral lines increases from top to bottom plot. Fe IX to Fe XIII show clear dimming, Fe XIV is borderline, and Fe XV to Fe XX show smooth brightening with no dimming. The Fe XX 131 Å profile is very similar to GOES 1-8 Å, indicating that this line in EVE is a good proxy for gradual phase timing. Also note the vertical axes: dimming is on the order of a few percent for the cooler Fe emissions while the hotter Fe emissions have bright peaks in the hundreds of percent. All percent changes are calculated relative to the pre-flare irradiance at 17:00 UT.

4.1.2 Complex Dimming Case

This event occurred on 2011 August 4 at approximately 3:47 UT. It spawned from NOAA active region 11261 at location N19W36. The eruptive event consisted of an M9.3 flare, a large and fast CME, and nearly all of the types of dimming discussed in Chapter 3: mass-loss and thermal dimming, a global wave that then triggered a sympathetic filament eruption, and an obscuration dimming from the nearby filament. No bandpass or Doppler dimming were identified even in this relatively energetic event. This event was chosen specifically for presenting so many types of dimming and related physical processes in a single case.

Coronagraph Observations

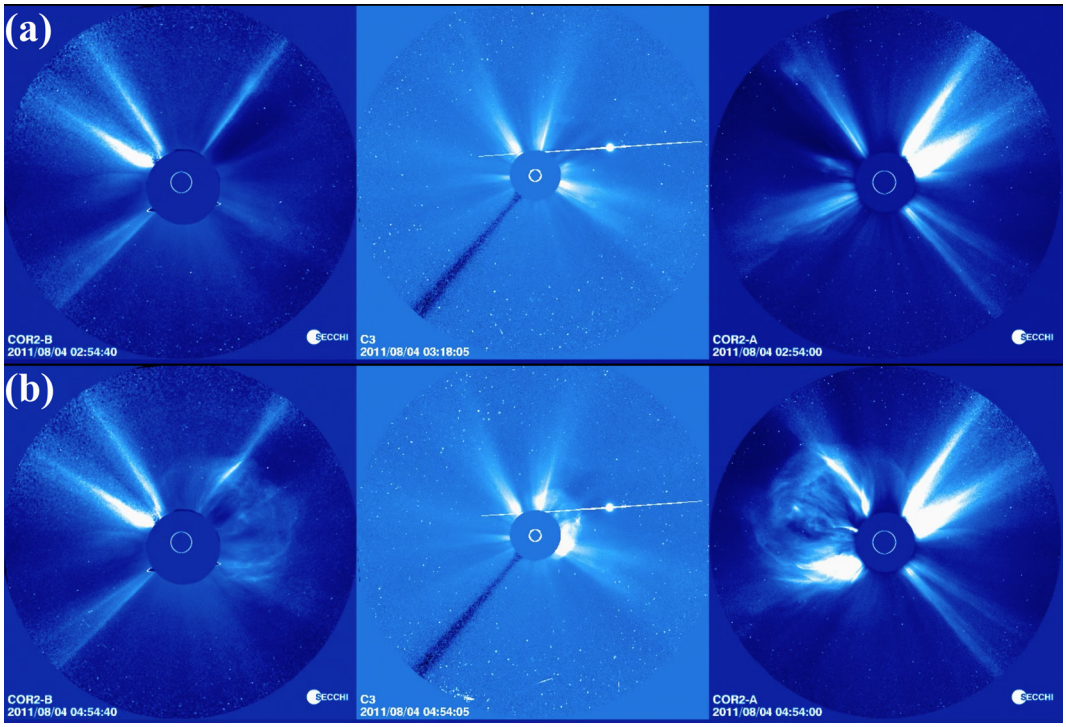

Figure 4.6: Coronagraph images of CME associated with 2011 August 4 dimming event. From left to right the coronagraphs are STEREO Behind C2, LASCO C3, and STEREO Ahead C2. Top: Images prior to CME. Bottom: Images during CME.

Images from the three coronagraphs are shown in Figure 4.6. The CME in Figure 4.6 (b) can be seen in STEREO-B (behind) on the right of the solar disk, in LASCO as the start of a

halo CME offset to the upper-right of the disk, and in STEREO-A (ahead) on the left of the disk. Additionally, bright streamers can be seen inside the CME and on the opposite side of the Sun, signifying that the outer corona of the Sun was also in a more complex configuration than the 2010 August 7 case.

The CDAW catalog for this event lists it as a halo CME with a velocity of 1315 km s^{-1}, relatively fast for a CME (faster than 99.03% of other CMEs, see Figure 4.7), and a mass of 1.16×10^{16} g. However, halo CMEs present a strong challenge for obtaining accurate mass, and the catalog flags it as a poor mass estimate. Mass estimates based on the three coronagraphs are 8.6×10^{15} g for LASCO C3 (35% lower than the CDAW value), $7 - 8 \times 10^{15}$ g for STEREO-A COR2, and 4.3×10^{15} g for STEREO-B COR2 (A. Vourlidas 2013, private communication). A deprojected, 3-D analysis has not been performed for this CME.

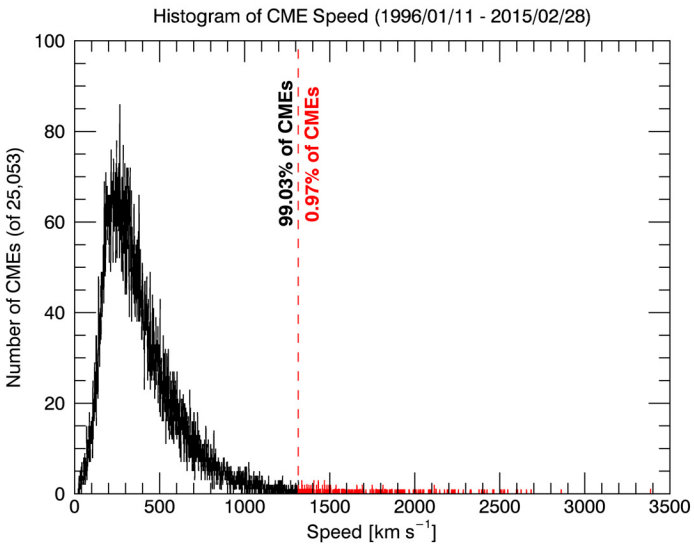

Figure 4.7: Histogram of CME speed from 1995 to 2015 based on the CDAW LASCO CME catalog's 25,053 CMEs with listed speeds. The red vertical line is at 1315 km s^{-1}, the listed speed of the 2011 August 4 event.

SDO/AIA EUV Image Observations

The complexities of this eruptive event are quite apparent in AIA observations. Figure 4.8 is

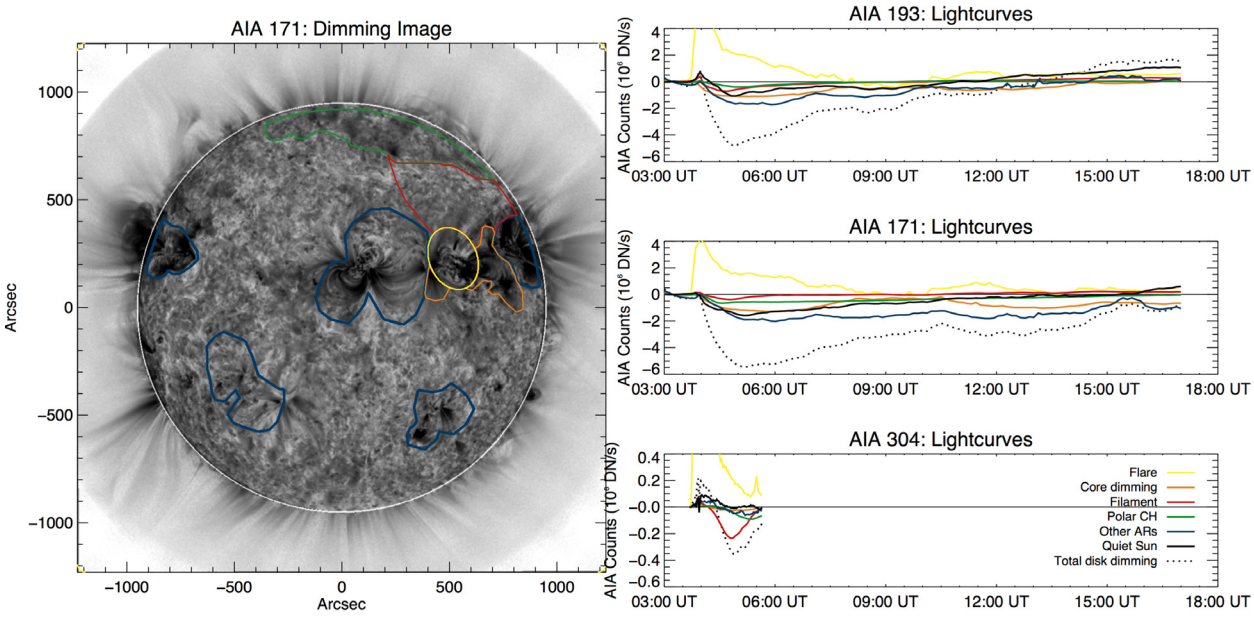

Figure 4.8: Same as Figure 4.3 but for 2010 August 7 event. Colored contours and lines in plots correspond according to legend, but are different from Figure 4.3. An additional difference is that the He II 304 Å line now shows dimming. Not all 304 Å data were available at the time of processing, which is why the time series ends at 6:00 UT. Figure courtesy of Rachel Hock.

in the same format as Figure 4.3 but is for the 2011 August 4 event. Dimming is seen in numerous locations for this event, indicating the far-reaching influence of this eruption. In particular, even though 304 Å data were not processed to the end of the dimming window[1] , the main phase of obscuration dimming is clearly visible. Additionally, 193 Å and 171 Å show dimming in every region outside of the flare-isolating contour (yellow). The primary region thought to be associated with mass-loss dimming is labeled "core dimming" (orange) here. It corresponds to an area immediately surrounding the active region where the flare took place and is bounded by quiet-Sun on top and bottom and other active region loops to the left and right. All other active regions visible on disk are contained in blue contours and eventually show even greater dimming than the core region (orange). Note that for the first several minutes, the core dimming dominates the other active regions. Also, the dotted black dash line is the disk signal excluding the flare region (yellow),

[1] Figure 4.9 shows these data in full, though for differently selected contours

effectively the sum of all plotted lines except yellow. It can be seen that the relative contribution of each region to the total dimming is nonzero. Table 4.1 details these contributions.

The overall structure of Table 4.1 is wavelength and feature (vertical) and contribution at maximum dimming (i.e. minimum count), maximum dimming contribution, and the range of contributions. It can be seen that in 193 Å and 171 Å, peak dimming is dominated by the non-flaring active regions. As will be shown later, this is mainly a reflection of dimming from the nearby active region. It is also worth noting that core dimming reaches its maximum dimming 36 minutes earlier than the dimming from non-flaring active regions. This suggests that the latter is either a sympathetic response to the primary dimming catalyzed by the global wave or additional mass being ejected that becomes the tail side of the CME. As expected, in 304 Å, the minimum count is dominated by obscuration from the nearby filament (red). This is consistent with the physical theory for obscuration dimming detailed in Section 3.5. The dominant region changes when looking at the maximum contribution. Here, the core dimming region dominates for 193 Å but the non-flaring active regions dominate the dimming in 171 Å. Again, we will soon show that the most nearby active region contributes greatly to the dimming and may have contributed to the outgoing mass of the CME. The 304 Å dimming is similar in timing to the core dimming region evolution, and AIA 304 Å movies confirm that the maximum dimming is coming from the filament eruption and resultant obscuration for the 304 Å emission. In summary, different spectral emissions have maximum dimming at different times because their main contributions are from different dimming regions. In particular, the 193 Å emission is primarily from the core dimming region; the 171 Å emission has greater contributions from non-flaring active regions and the quiet-Sun; and the 304 Å emission is very clearly dominated by obscuration from the filament.

Figure 4.9 is the same format as Figure 4.8 but with different regions selected, and does not use images corrected with the point spread function. The latter explains why the total dimming is about 2% less than in Figure 4.8; in other words, the application of the point spread function correction for AIA images is important for dimming studies. Of importance for this comparison is that the red contour, which encompasses the core dimming region from Figure 4.8 and the most

Table 4.1: Statistics for dimming features in Figure 4.8 for 2011 August 4 event. Table courtesy of Rachel Hock.

Dimming Feature	Count Minimum			Contribution Maximum			Range of Contribution (%)
	Time (UT)	Counts (10^6 DN s^{-1})	Contribution (%)	Time (UT)	Counts (10^6 DN s^{-1})	Contribution (%)	
AIA 193:							
Total disk dimming	4:55	-4.81					-
Core dimming	5:17	-1.11	25.3	04:05	-0.63	73.1	18.9- 73.1
Filament eruption	4:41	-0.72	16.2	04:05	-0.23	27.2	1.0- 27.2
Polar coronal hole	5:03	-0.39	8.5	05:17	-0.38	8.7	0.6- 8.7
Non-flaring active regions	5:53	-1.72	43.1	08:04	-1.05	54.6	29.6- 54.6
Quiet Sun	4:55	-1.07	22.3	08:40	-0.57	26.0	8.0- 26.0
AIA 171:							
Total disk dimming	5:10	-5.46					-
Core dimming	5:53	-1.28	24.5	04:05	-0.40	27.3	9.4- 27.3
Filament eruption	4:48	-0.40	8.0	04:41	-0.38	8.1	0.0- 8.1
Polar coronal hole	4:34	-0.66	15.7	04:26	-0.63	16.6	7.5- 16.6
Non-flaring active regions	6:00	-2.02	38.9	08:54	-1.72	53.9	16.6- 53.9
Quiet Sun	5:10	-1.59	29.0	04:05	-0.68	46.7	20.8- 46.7
AIA 304:							
Total disk dimming	4:53	-0.36					-
Core dimming	5:08	-0.03	9.5	04:23	-0.02	62.2	7.4- 62.2
Filament eruption	4:49	-0.24	69.4	04:25	-0.08	304.3	9.4- 304.3
Polar coronal hole	5:22	-0.09	40.0	05:38	-0.06	49.3	1.1- 49.3
Non-flaring active regions	5:11	-0.06	20.6	05:31	-0.05	25.1	2.4- 25.1
Quiet Sun	5:34	-0.02	14.0	05:37	-0.02	14.4	0.1- 14.4

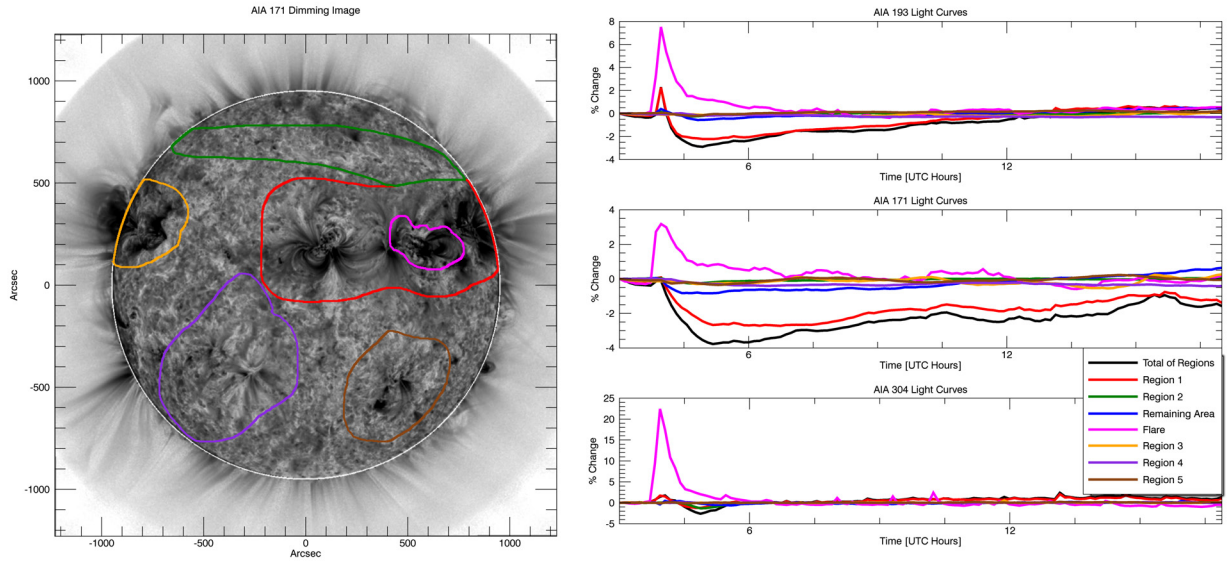

Figure 4.9: Same as Figure 4.8 but with new contours selected and no point spread function correction applied. Also the 304 Å emission time series is now complete in this later analysis using more recent AIA data products.

nearby non-flaring active region, accounts for the majority of total dimming in 193 Å and 171 Å. These two active regions are so close together that it is possible that the CME pulled mass away from a coronal volume encompassing both active regions. It can also be seen that 171 Å has a more prominent dimming in the remaining area (blue), i.e. quiet-Sun, than in 193 Å. This is evidence of heat-wave dimming described in Robbrecht and Wang (2010).

Also note that while the AIA 193 Å band contains the Fe XXIV 192 Å emission line, this high ionization state is only expected in hot plasma such as in flaring loops, which are spatially isolated in the contours of Figures 4.3, 4.8, and 4.9. Thus, for this particular case of spectral blending, the impact on analysis and interpretation is minimized.

Running-difference movies make EUV waves easier to detect by eye but it is difficult get the same clarity with static images. Instead, Figure 4.10 follows a similar format to earlier AIA figures but draws geometric contours propagating from the source active region. The light curves in Figure 4.10 are color coded from dark to light corresponding to increasing distance from the source region.

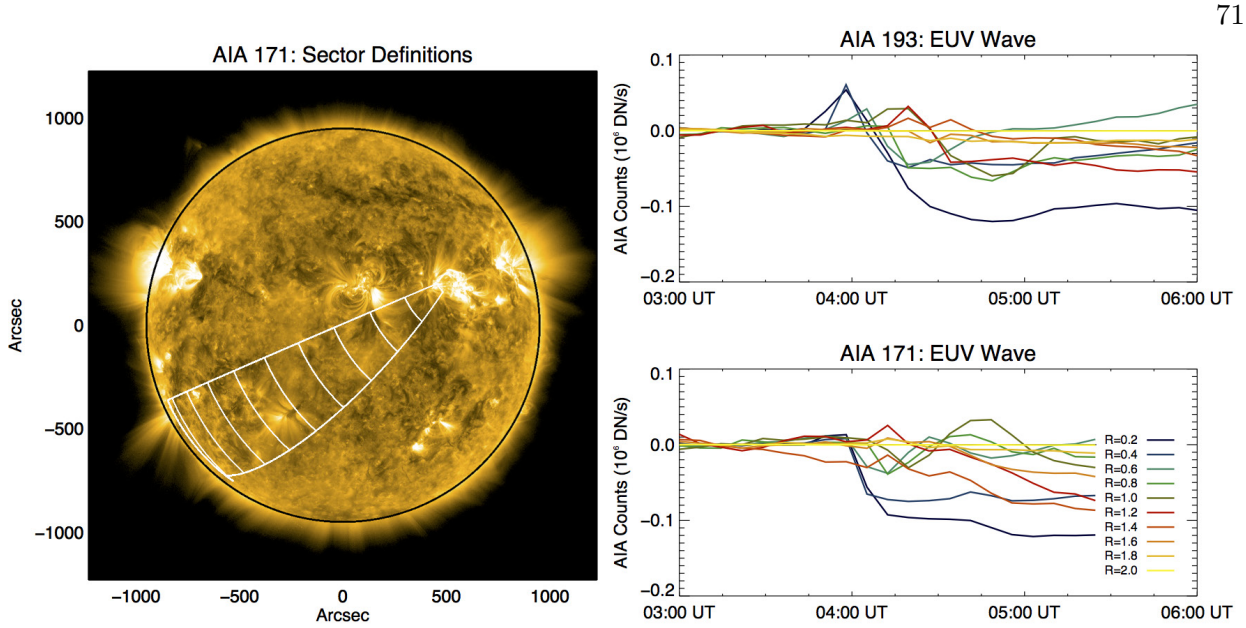

Figure 4.10: Similar format to Figure 4.9, but with geometric contours selected specifically for analysis of propagating wave. In the line plots on the right, distance from the source active region increases with lightness of color. Figure courtesy of Rachel Hock.

There appear to be thermal effects (heating and then cooling) from the wave as the AIA 193 Å and 171 Å light curves peak at different times during this time series. The propagation of the wave can be seen as the darker-color curves reach their minimum earlier with larger magnitude, and the lighter-color curves show only a minor impact from the wave. This is the expected behavior for any impulsive wave phenomenon as energy is dissipated in the surrounding medium.

SDO/EVE EUV Irradiance Observations Figure 4.11 shows selected extracted emission lines from EVE for the 2011 August 7 complex eruptive event. Because obscuration dimming is important for this case, the plot includes two He II lines: 256 Å and 304 Å, both of which show dimming at approximately the same time as what was seen in AIA (Figure 4.8). The irradiance increase from roughly 5:00 to 7:00 UT in Fe XIV 211 Å may relate to the EUV late phase discussed in Woods et al. (2011). Dimming in Fe IX to Fe XIII was significant in this case, roughly twice as large as in the simpler 2010 August 7 event. Furthermore, the peak time versus ionization state trend is reversed compared to the simpler event e.g., Fe IX 171 Å actually peaks just prior to the

GOES event peak time (second vertical dash), and higher ionization states peak later and later. This is indicative that slow heating processes are dominating the overall irradiance time series. In either heating or cooling cases, the flare-dimming deconvolution method discussed in Section 4.2 works equally well.

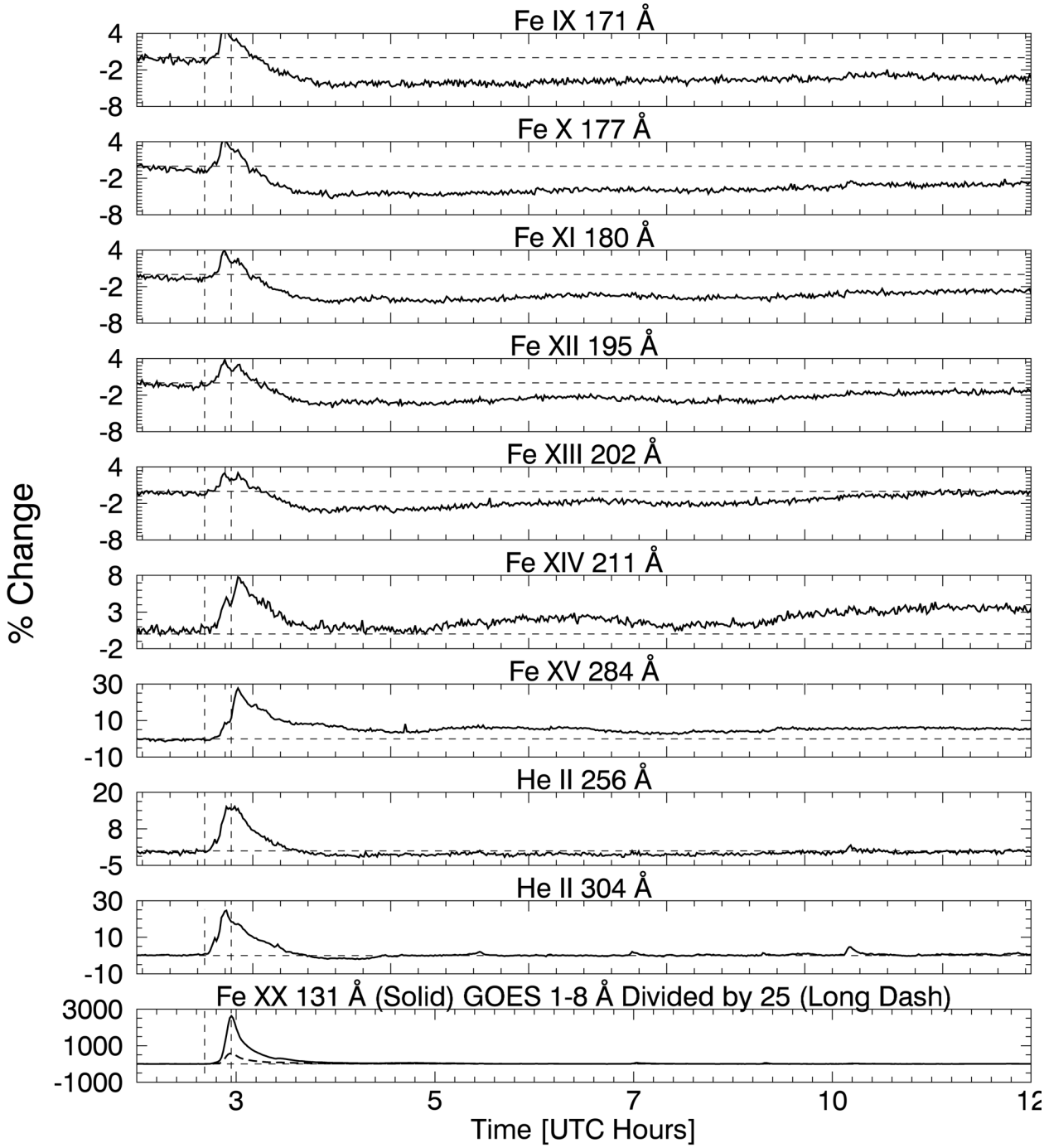

Figure 4.11: Same as Figure 4.5 but for the 2011 August 4 event, and showing He II 256 Å and 304 Å instead of Fe XVI 335 Å and Fe XVIII 94 Å. Just as before, Fe IX to Fe XIII show clear dimming, Fe XIV is borderline, and Fe XV to Fe XX show smooth brightening with no dimming. The Fe XX 131 Å profile is 3x larger than GOES 1-8 Å but still has a similar shape and timing. Also note the vertical axes: dimming is 2x larger than it was for the 2010 August 7 event. The two He II lines show dimming as well, suggestive of obscuration dimming.

4.2 Flare-Dimming Deconvolution Method

Figures 4.5 and 4.11 showed how cooling and heating impact the time of an irradiance peak in each ionization state of Fe: cooling causes the low ionization states to peak later and heating causes the reverse. In either case, it is clear that dimming magnitude decreases with higher ionization states of Fe. Eventually, around Fe XIV at 211 Å, dimming is no longer clear. The next ionization state, Fe XV at 284 Å, shows strong brightening in response to the flare but no dimming. The shape of the flare peak is similar in all wavelengths[2] . Using this observation, we developed a simple algorithm to remove the flare peak in the dimming lines. We make the assumption that the peak in the high ionization states is a good proxy for what *would have* been observed in the low ionization states if there were no dimming. However, the magnitudes and timing are quite different. To account for this, we scale the non-dimming peak down and shift it in time so that they are matched. An example of the process is shown in Figure 4.12, and a flow-chart of the algorithm is shown in Figure 4.13. The ten-second EVE spectra are averaged to two-minutes to reduce noise (see black line in Figure 4.12) and the simple IDL *max* function is applied to find the peak in the light curve for every emission line listed in Table 2.2. Then, the scaled non-dimming emission line is shifted in time such that its peak matches the one in the dimming line (see green line in Figure 4.12). Finally, the scaled and time-shifted non-dimming light curve is subtracted from the dimming emission line to obtain a light curve sensitive primarily to mass-loss dimming (see blue line in Figure 4.12).

The red line in Figure 4.12 is the same red line that was shown in Figure 4.3, which corresponded to the dimming area in AIA thought to be most associated with mass-loss from the corresponding observed CME. It is clear that the deconvolution method applied brings the EVE light curve much closer (from black line to blue line) to the AIA one (red line). The agreement is not perfect, particularly at later times, and the noise in EVE is greater – even with the two-minute averaging – than AIA. However, the agreement during the initial decline is much better

[2] Though the shape of the flare peak appears to become more smooth at higher ionization states because of the significantly larger increase making the small oscillations imperceptible in the plots

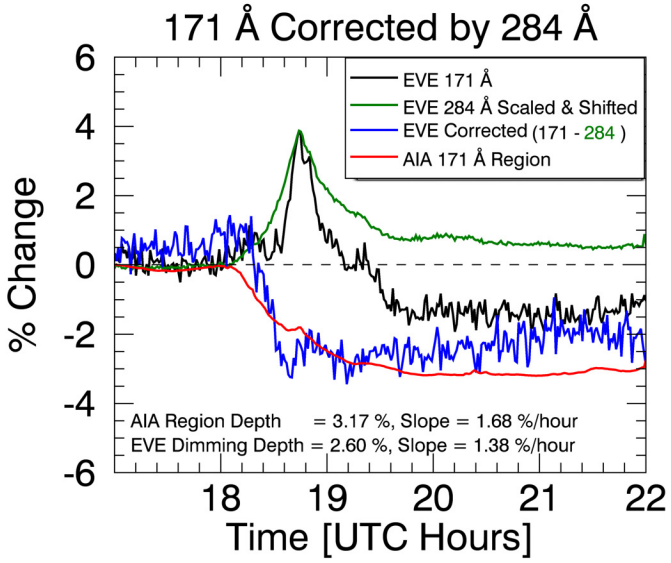

Figure 4.12: Example of the flare-dimming deconvolution method. This particular event is the simple case described in Section 4.1.1. A non-dimming line (e.g., 284 Å) is scaled down and shifted in time such that its flare peak matches the one in a dimming line (green and black, respectively). The scaled and time-shifted non-dimming light curve is then subtracted from the dimming light curve, resulting in a "corrected" or "deconvolved" light curve representative of mass-loss dimming (blue). The red line is the same as the red line in Figure 4.3, indicating the spatially isolated dimming in AIA 171. Dimming depth and slope are shown at the bottom of the plot and were computed at a particular time and time range, respectively.

and is where the slope of dimming is computed, which will be shown to be a critical proxy to CME velocity. The later rise in the corrected EVE line (blue) is due to a slow decrease in the scaled & time-shifted correction line (green). The unaltered dimming line (black) is relatively flat in the later hours of the dimming, consistent with the AIA light curve (red). This behavior varies by event but a "bottomed-out" dimming is common. Typically, the maximum depth is reached quickly and maintained for several hours. It will later be shown that depth is another critical proxy for CMEs; this one for CME mass. In practice, the depth is measured at a point soon after the maximum dimming is reached, so later behavior of the corrected EVE line (blue) is of less importance than the removal of the flare peak. The further in time one goes, the more likely it is for other events or physical processes to occur that would complicate the spatially-integrated EVE analysis. Du-

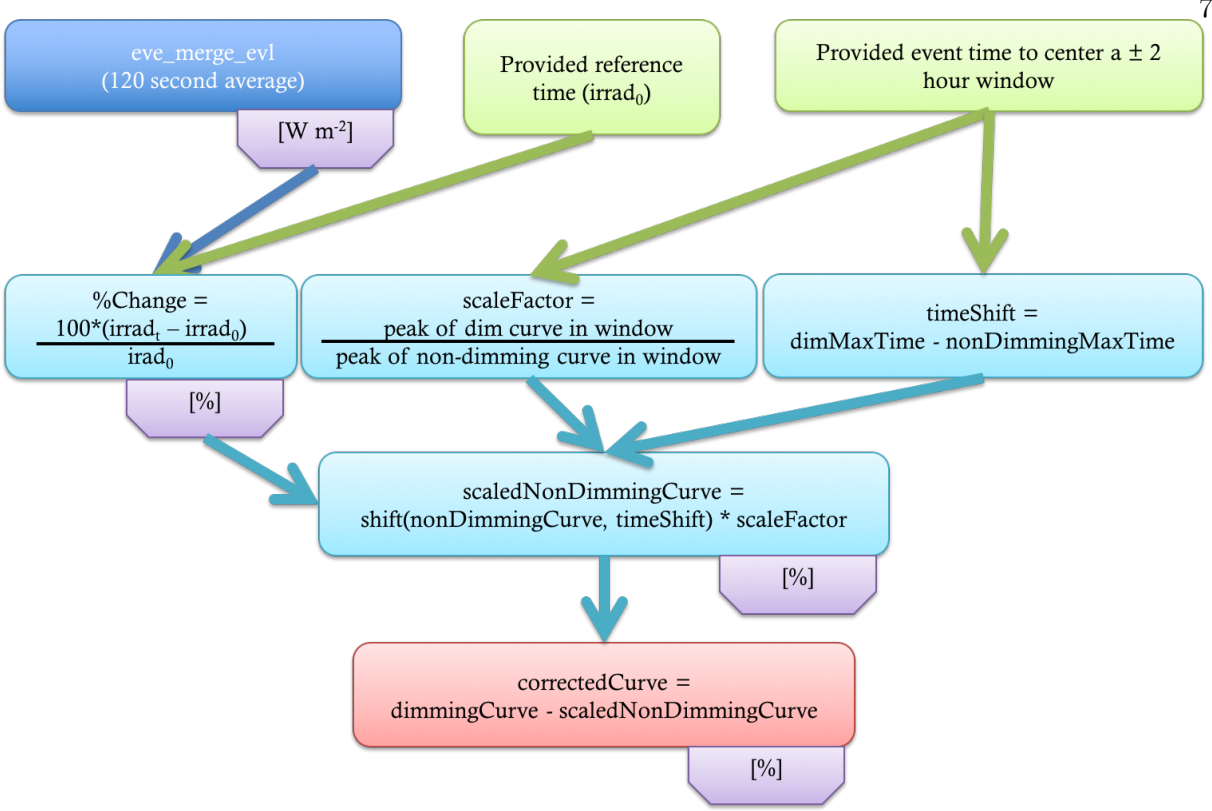

Figure 4.13: Flow-chart for the flare-dimming deconvolution algorithm. Rounded-rectangular boxes describe the steps and the purple boxes indicate the units of the irradiance at that step.

ration of dimming may be an interesting parameter to study, but due to the continuing evolution and dynamics of the sun it is of secondary priority for this study. Additionally, the duration is likely to be most closely linked to the physical processes responsible for filling plasma back into the void, relaxation of the disturbed system, and temperature evolution causing changes to ionization fractions. All of these have a tenuous connection to CME kinetics and thus provide less promise of providing a physical justification for studying dimming proxies for CMEs.

Which combinations of dimming and non-dimming lines make for the best dimming-isolated light curve? In the simple 2010 August 7 event, it was Fe IX 171 Å (dimming) and Fe XV 284 Å, respectively. Similar results were obtained using different combinations of other line pairs, one from the dimming group and one from the non-dimming group. In the 28 other cases studied (see Chapter 5), the same combination of Fe IX 171 Å (dimming) and Fe XV 284 Å (non-dimming)

proved best.

4.3 Error Estimates for Flare-Dimming Deconvolution Method

The error estimates for the dimming parameters of slope and depth will be discussed in Chapter 5. Those errors will depend on the results of the present section.

Coronal dimming is a transient event lasting several hours that is studied in terms of relative change from the initiation time. As such, no long-term degradation of EVE needs to be factored into uncertainties i.e. the absolute accuracy is not important but the measurement precision is. To estimate precision, a period of solar inactivity was analyzed: 2013 January 28 from 00:00 - 01:00 UT. The estimated precision of these 120-second averaged EVE line data was calculated as the variance of the mean (Bevington 2003), i.e., the standard deviation divided by the square root of the number of samples, which was 12 in this analysis. Table 4.2 provides the estimated precision for each emission line used in this study, and provides a sense of how well we can detect EVE dimmings that typically have depths less than 5% of the pre-flight irradiance level.

Table 4.2: Estimated precision for selected emission lines in EVE spectra. The Fe IX 171 Å and Fe XV 284 Å emission lines are the choice lines for dimming analysis with EVE data.

Ion	Wavelength (Å)	Estimated Precision (%)
Fe IX	171	0.25
Fe X	177	0.21
Fe XI	180	0.16
Fe XII	195	0.20
Fe XIII	202	0.21
Fe XIV	211	0.32
Fe XV	284	0.35
Fe XVI	335	0.86
Fe XVIII	94	0.42
Fe XX	132	1.00

These base uncertainties were propagated through each step of the EVE dimming correction method described in Section 4.2. First, the line precisions are combined with the provided reference

time to compute percent change (see Figure 4.13, Equation 4.1).

$$\%change = 100 \times \frac{(irrad_t - irrad_0)}{irrad_0} \tag{4.1}$$

where $irrad_t$ is the irradiance at each time and $irrad_0$ is the irradiance at the provided pre-flare reference time. In practice, the latter is a manually selected pre-flare point that appears to correspond well to a quiet or well-behaved period. All of the uncertainty derivations to follow are based on the basic uncertainty propagation equation,

$$F = f(X, Y) \tag{4.2}$$

$$\sigma_F^2 = \sigma_x^2(\frac{\partial F}{\partial X})^2 + \sigma_Y^2(\frac{\partial F}{\partial Y})^2 \tag{4.3}$$

where F is a generic function that will be specified for each of the steps of the deconvolution method. The first step of computing percent change (i.e. where F = Equation 4.1) has the corresponding uncertainty derivation:

$$\frac{\partial F}{\partial X} = \frac{100}{irrad_0} \implies (\frac{\partial F}{\partial X})^2 = (\frac{100}{irrad_0})^2$$

$$\frac{\partial F}{\partial Y} = -\frac{100 \times irrad_t}{irrad_0^2} \implies (\frac{\partial F}{\partial Y})^2 = (-\frac{100 \times irrad_t}{irrad_0^2})^2$$

$$\therefore \sigma_F^2 = \sigma_x^2(\frac{100}{irrad_0})^2 + \sigma_y^2(-\frac{100 \times irrad_t}{irrad_0^2})^2$$

$$\implies \sigma_F = \sqrt{\sigma_x^2(\frac{100}{irrad_0})^2 + \sigma_y^2(-\frac{100 \times irrad_t}{irrad_0^2})^2} \tag{4.4}$$

where σ_x is the precision of $irrad_t$ and σ_y is the precision of $irrad_0$, which will be identical in this case since Equation 4.1 refers to a single emission line. This is the uncertainty corresponding to $dimmingCurve$ and $non - dimmingCurve$. The next step in the algorithm (see Figure 4.13) is to scale the $non - dimmingCurve$ irradiance so that the peaks of the dimming and non-dimming line have the same magnitude (both of which are now in % units). The derivation for the corresponding uncertainty is,

$$F = xy$$
$$\frac{\partial F}{\partial x} = y, \frac{\partial F}{\partial y} = x$$

$$\therefore \sigma_F^2 = \sigma_x^2 y^2 + \sigma_y^2 x^2 = \sigma_{scalednon-dimmingCurve}^2 \tag{4.5}$$

where x is the non-dimming light curve, σ_x is the result of Equation 4.4 (i.e. the σ_F in Equation 4.4), y is the scale factor (which is a single value), and σ_y is derived as follows:

$$\text{Let} \frac{d}{b} = \frac{dimCurve_{peak}}{nondimCurve_{peak}} = y$$
$$\sigma_y^2 = \sigma_d^2(\frac{1}{b})^2 + \sigma_b^2(-\frac{d}{b^2})^2$$
$$\therefore \sigma_y^2 = (\frac{\sigma_d}{b})^2 + (\frac{\sigma_b d}{b^2})^2$$

Thus we have the $scalednon - dimmingCurve$ and its associated propagated uncertainty. The final step is to apply the correction to the $dimmingCurve$, which is just a simple subtraction, resulting in the final uncertainty:

$$\sigma_{correctedCurve} = \sqrt{\sigma_{dimmingCurve}^2 + \sigma_{scalednon-dimmingCurve}^2} \tag{4.6}$$

where $\sigma_{dimmingCurve}^2$ comes from Equation 4.4 and $\sigma_{scalednon-dimmingCurve}^2$ comes from Equation 4.5. Evaluation of Equation 4.6 with EVE data results in an uncertainty of $\pm 0.175\%$[3] . Chapter 5 will discuss the passing of the above uncertainty into IDL's *poly_fit* function and the final resultant errors associated with that process.

[3] % here is the same unit as the irradiance, not a percentage of the irradiance value

4.4 Dimming Parameterization Results

4.4.1 Simple Dimming Case

Parameterization of dimming is focused primarily on slope and depth, both of which can be manually selected by eye. The time to select for these parameters is debatable but in this case, we chose depth to be a point soon after the dimming "floor" is reached in AIA Region 1 (red contour and line). Slope was taken to this point, starting from 17:50 UT – the time just before GOES 1-8 Å and EVE 131 Å began to rise. The deconvolution method (Section 4.2) significantly reduces the impact of the flare's gradual phase peak to dimming measurements for EVE. Prior to the correction, EVE would have measured a dimming depth of 1.27% in 171 Å and 0.18% in 195 Å. After the correction, these values are 2.94% and 2.09%, respectively. Similarly, slope was changed from 1 % hr^{-1} (171 Å) and 0% hr^{-1} (195 A) to 2.29% hr^{-1} (171 Å corrected) and 2.09% hr^{-1} (195 Å corrected). The expectation is that all dimming lines should have similar dimming amount and onset time for the mass-loss dimming process, and these results after the flare gradual phase contribution has been removed support this expectation for this simple dimming case. Furthermore, if this event was being observed in real time, the gradual phase peak makes it impossible to estimate the amount and speed (slope) of dimming accurately. This correction method allows the irradiance increase due to the gradual phase contribution to be compensated in the EVE time series that have dimming.

The small difference in time between different emission peaks – Fe XX peaks 21 minutes before Fe IX in this case – is information that can be used to understand the temperature evolution during dimming. In this event, that time difference is significantly shorter than the hours-long duration of the total dimming event. Thus, it is unlikely that thermal dimming is a significant contributor to the total observed dimming. Instead, our correction method uses non-dimming lines as independent measurements of the flare gradual phase profile. Since no dimming is observed in the non-dimming lines, the gradual phase profile is assumed to be pure and can then be used as a proxy to remove only the effect of the gradual phase in the dimming light curve with a minimal

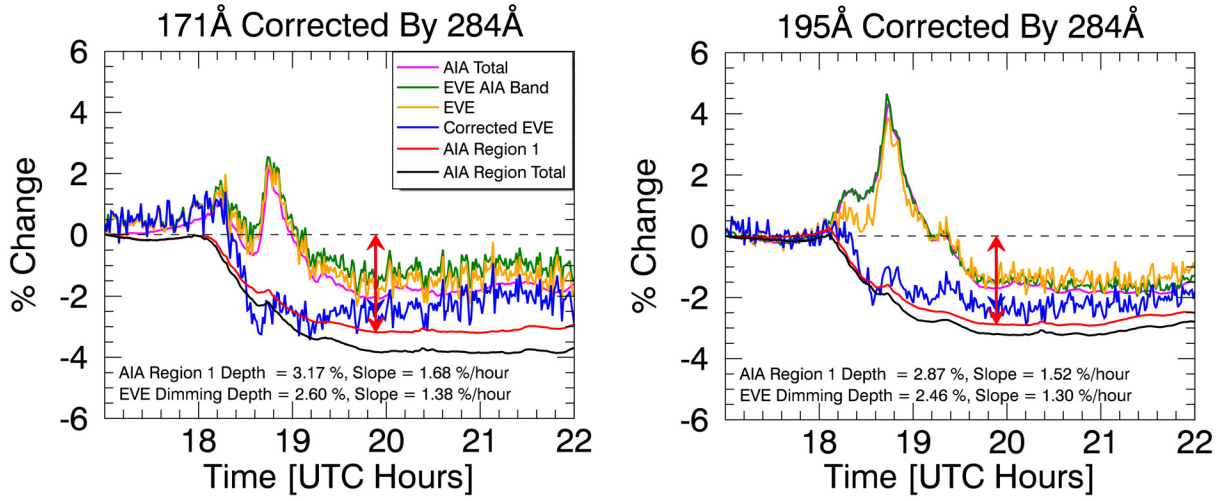

Figure 4.14: Both plots are similar to Figure 4.12 but provide more detail. The left shows results from 171 Å and the right is for 193 Å (AIA) / 195 Å (EVE). The red vertical arrow indicates the point where depth is computed and overlaps a blue vertical arrow indicating the end time of slope computation. The slope range begins at 17:50 UT.

impact on total dimming. In this way, we can effectively match AIA dimming observations, which are capable of isolating the dimming regions.

The expectation is that the EVE-corrected dimming results should have the same amount of dimming as the AIA results and are also independent of Fe ionization level (in the dimming lines). Figure 4.14 shows the comparison of EVE-corrected dimming time series to AIA results in both 171 Å and 193/195 Å, and Table 4.3 lists the dimming results.

AIA Region 1 is considered the reference for mass-loss dimming, so its dimming depth and slope are compared as an estimate of uncertainty for these results from EVE. The differences for the AIA 171 Å and 195 Å dimming depth and slope are 0.3% and 0.16% hr^{-1}, respectively. The relative uncertainty of these is 10% of the mean depth and slope values, being 3.02% and 1.60% hr^{-1}. These differences in the two different AIA bands could reflect the uncertainty that Region 1 is only due to mass-loss dimming and our ability to identify the best Region 1 boundary to encompass the mass-loss dimming phenomena. However, selecting a slightly different boundary did not greatly impact the resultant light curves, so the difference may be real. This would indicate that AIA too

Table 4.3: Key dimming results for 2010 August 7 event. Note that 195 Å in EVE corresponds to the 193 Å band in AIA, which encompasses 195 Å.

Dim line (Å)	AIA Total Depth (%)	AIA Reg. 1 Depth (%)	EVE Depth Corrected (%)	EVE Depth Uncorrected (%)	AIA Total Slope (% hr^{-1})	AIA Rg. 1 slope (% hr^{-1})	EVE Slope Corrected (% hr^{-1})	EVE Slope Uncorrected (% hr^{-1})
171	2.03	3.17	2.60	1.63	1.07	1.68	1.38	0.86
177	–	–	2.79	1.89	–	–	1.48	1.00
180	–	–	2.87	1.98	–	–	1.52	1.05
195	1.68	2.87	2.46	1.52	0.89	1.52	1.30	0.81
202	–	–	2.31	1.60	–	–	1.22	0.85
211	0.52	2.03	2.57	1.60	0.28	1.50	1.36	0.85

sees shallower dimming for higher ionization states if the deconvolution method described in Section 4.2 is not applied. The corrected EVE results for dimming depth and slope have mean values of 2.53% and 1.34% hr^{-1}, and both are 14% less than the AIA Region 1 mean values. The standard deviations for the six EVE lines' corrected dimming depth and slope are 0.21% and 0.11% hr^{-1}, respectively. As expected (intended), the EVE corrected results are much more self-consistent with each other than the uncorrected results. It is also interesting to note that the AIA dimming results from Region 1 are similar to each other and the EVE corrected dimming results, but the AIA total dimming results are less similar to either of these results. The slope tracks the depth variation well; that is, the slope is less when the depth is less. Our expectation is that the dimming slope could represent the CME velocity, and the dimming depth could represent the CME mass loss.

4.4.2 Complex Dimming Case

The dimming parameterization method in this case was the same as in the simple dimming case above. Figure 4.15 shows the analogous plots for this event. While the general trend of EVE follows AIA, it's clear from these plots that applying the same deconvolution methods does not result in as good a match of EVE to AIA. Note that even uncorrected EVE reaches a deeper

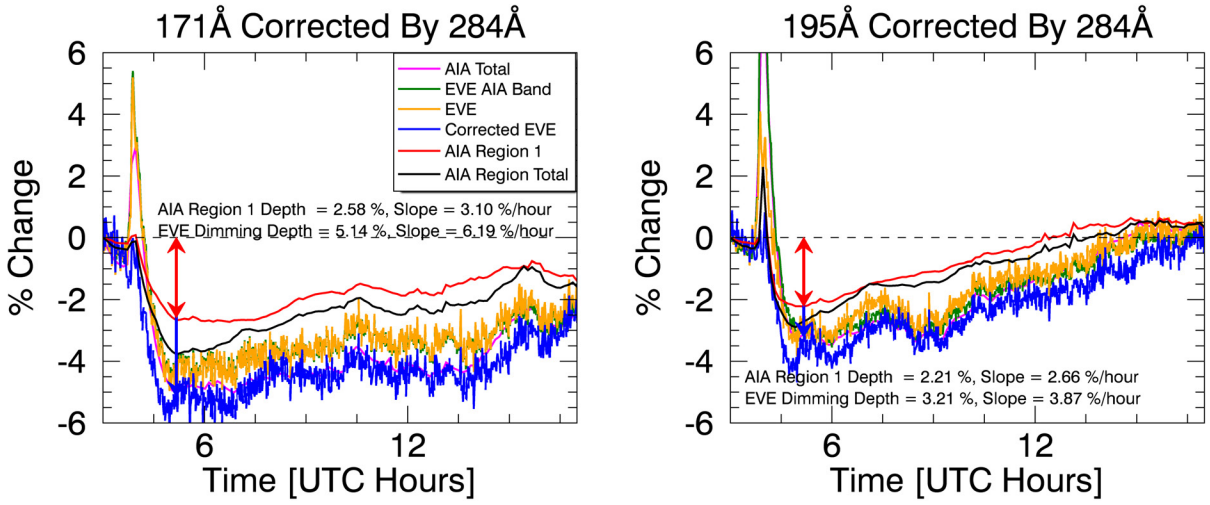

Figure 4.15: Same as Figure 4.14 but for the 2011 August 4, more complex, case. The AIA regions correspond to those selected in Figure 4.9.

minimum than the AIA light curves[4] . The only way for the deconvolution method to raise EVE irradiance would be for the non-dimming line to have dimming, which would violate the definition of it being a non-dimming line. Since this was not the case, all of the corrected/deconvolved EVE light curves (blue) are even lower than the uncorrected EVE dimming line (gold), bringing it further from the AIA "core dimming" light curve (red). The AIA total dimming results, which include all dimming regions but not the flare region, do agree better with the EVE dimming results. Nevertheless, the deconvolution method did successfully remove the flare peak in dimming lines as can be seen in the difference between the raw EVE (gold) and corrected EVE (blue) light curves. AIA showed that the remaining area (i.e. quiet Sun) had non-negligible dimming (black curve in Figure 4.8 and blue in Figure 4.9). Adding that to the AIA total dimming for 171 Å would result in a peak dimming of about 4% – still 1% lower than what is seen in EVE. Doing the same for 195 Å would get the two to match within 1%. The analysis is further complicated by the fact that the AIA bandpasses are several nanometers wide causing blending of many emission lines and continuum that makes direct comparison with EVE difficult, particularly for an event with so many

[4] Remember that the black line is the total inside contoured areas in AIA, not the total disk

simultaneous physical processes involved, each of which has an impact on the different emission lines that can vary differently over time.

The ultimate goal of the dimming analysis is to provide proxies for CME mass and velocity. This event was included in the semi-statistical study to determine the relationship between those CME parameters and the dimming depth and slope that will be discussed in Chapter 5.

4.5 Summary

To summarize the physical processes taking place in the simpler 2010 August 7 event, the plasma and its irradiance have source and sink terms. Near the beginning of the flare, heating is very dominant and causes a rapid increase in high ionization states for the various Fe emissions. Later in the flare, cooling of the plasma causes an increase in lower ionization states, and those cooler lines peak later than the hot lines. Through it all, the mass ejection can act as a sink for most coronal emissions (mass-loss dimming). Early in the flare, before the low ionization states have been strongly affected by the cooling described above, the mass ejection dominates and causes the irradiance to visibly drop for the cool corona lines. Much later in the flare process, as the plasma temperature and post-flare loops begin to return to pre-flare level and loop configurations, the missing plasma again becomes apparent in the irradiance time series as an hours-long, few-percent decrease. Quantitative dimming results for AIA and EVE are summarized in Table 4.3 for this simple dimming case.

The physical interpretation of the more complex 2011 August 4 event is more difficult to obtain. The size of the flare was nearly an order of magnitude larger than in the simpler 2010 August 7 case and the associated CME velocity was 1.5x faster – together, these are a general indicator that the amount of energy involved in the eruptive event was much larger in the more complex event. Additionally, the pre-eruption state of the Sun was more complex for the 2011 August 4 event, as evidenced by the more numerous active regions and polar filament, the coronal streamers, and the proximity of active regions to the one responsible for the eruption itself. All of this means that more energy was released via more mechanisms. The EUV wave was much more prominent

in this case, sympathetic responses were clear, and heating (rather than cooling) dominated the irradiance indicative of energetic processes dominating over relaxing ones. Quantitative dimming results from the analysis of AIA images are summarized in Table 4.1 for this complex dimming case.

Chapter 5

Semi-Statistical Study of Dimming-CME Relationship

Extreme ultraviolet (EUV) coronal dimmings are often observed as part ofew solar eruptive events. These phenomena can be generated via several different physical processes (see Chapter 3). For space weather, the most important of these is the temporary void left behind by a coronal mass ejection (CME). Massive, fast CMEs tend to leave behind a darker void that also usually corresponds to minimum irradiance for the cooler coronal emissions. If the dimming is associated with a solar flare, as is often the case, the flare component of the dimming in the cooler coronal emission can be isolated and removed from the dimming light curve using simultaneous measurements of warmer coronal lines (see Chapter 4). In the present Chapter, we apply this technique to 38 dimming events: the two case studies from Chapter 4 plus 36 additional events taken from two separate two-week periods in 2011. Dimming is then parameterized in terms of depth and slope for each of the events. We provide statistics on which combination of wavelengths worked best for the correction method, describe the fitting methods applied to the dimming light curves, and compare the dimming parameters with corresponding CME parameters of mass and speed. The best linear relationships found with an accuracy of about 20% are that the CME speed is about 630 $km\ s^{-1}$ times the dimming slope (% s^{-1}) and the CME mass is about 1.03×10^{15} g times the dimming depth (%).

5.1 Introduction to Dimming and CME Parameterization and Statistics

Extensive surveys of coronal dimming events and their relation to CMEs have been performed by Reinard and Biesecker (2008, 2009). For their sample of 100 dimming events, Reinard and Biesecker (2008) found a mean lifetime of 8 hours, with most disappearing within a day. Reinard and Biesecker (2009) studied CMEs with and without associated dimmings, finding that those with dimmings tended to be faster and more energetic. Bewsher et al. (2008) found a 55% association rate of dimming events with CMEs, and conversely that 84% of CME events exhibited dimming. Dimming regions occur on a spatial scale similar to CMEs, more so than other CME-associated activity (such as flares and EUV waves). Studies have demonstrated that dimming regions can be a good indicator of the apparent base of the white light CME (Thompson et al. 2000; Harrison et al. 2003; Zhukov and Auchère 2004). Thus, dimmings are usually interpreted as mass depletions due to the loss or rapid expansion of the overlying corona (Hudson et al. 1998; Harrison and Lyons 2000; Zhukov and Auchère 2004). Spectroscopic observations of coronal dimmings (Harra and Sterling 2001; Harrison et al. 2003; Harra and Sterling 2001) found blueshifts in several coronal lines, indicating outflow in dimming regions. When dimmings are present with a CME, they are one of the earliest signatures of the actual mass ejected from the low corona, and provide unique information on the onset time and location of the ejection. Many landmark studies have established that dimmings can contribute a large fraction of the mass to a CME (Harrison and Lyons 2000; Harrison et al. 2003; Zhukov and Auchère 2004; Aschwanden et al. 2009a). There are well-established methods to derive the mass properties of CMEs, but there are still outstanding questions involving the source of the CME mass: how much of the mass comes directly from the erupting region, how much comes from the surrounding or overlying large-scale corona, and how much is "swept up" as the CME propagates (Bein et al. 2013).

An Earth-directed CME's potential geoeffectiveness is typically characterized by three values: its velocity, mass, and the magnitude and duration of the southward component of the magnetic field (B_z) at the time of Earth impact. Typical CME forecasts provide a predicted Earth ar-

rival time only. The geomagnetic storm magnitude is strongly linked to the CME momentum and magnetic field orientation while arrival time at Earth is primarily dependent on CME velocity. The current standard process for estimating velocity relies on sequential coronagraph images from SOHO/LASCO and STEREO/SECCHI. There are ground-based white light coronagraph measurements, such as by High Altitude Observatory's K-Cor instrument, but those measurements are limited to the low corona and constrained by the times that the sun is at a sufficiently high elevation as viewed from a fixed-position on Earth's surface (typically <6 hours per day). Analysis of coronagraph images to determine CME velocities and masses results in relatively large uncertainties of 30-50% (Vourlidas et al. 2000, 2010, 2011). The velocity and mass measurements with the most uncertainty are for Earth-directed CMEs that are seen as halos in coronagraphs at or near Earth. For these CMEs, velocity is significantly affected by projection on the plane-of-sky, and a large percentage of the mass can be hidden behind the instrument's occulter. Without observations of these CMEs from another viewpoint, such as STEREO, it is difficult to make an accurate measurement of the CME velocity and mass from the coronagraph observations. However, dimmings associated with these CMEs are very well observed by Earth-based observations. Our studies of coronal dimming events have focused on the possibility of coronal dimming observations providing useful indicators for CME velocity and mass, and can readily be combined with most B_z prediction methods.

While earlier studies showed that dimmings can account for a significant fraction of the mass ejected, multi-viewpoint observations using STEREO data have the advantage of providing independent mass measurements for the same event from two different aspect angles, yielding a better mass accuracy. In a survey of six STEREO events observed as dimming by EUVI and as CMEs by COR2, Aschwanden et al. (2009a) found a clear correspondence between the EUV and white light mass estimates. Colaninno and Vourlidas (2009) developed a triangulation' method to estimate the true (accurate) mass of CMEs from SECCHI observations. More recently, Bein et al. (2013) applied similar methods to a larger CME sample (25 events) and over an extended height range, allowing them to remove the effects of the CME emerging from behind the occulter

and to calculate the mass flux of the CMEs in the lower corona. Standard plane-of-sky velocity estimates are made and cataloged by the Coordinated Data Analysis Workshops (CDAW) CME catalog (Gopalswamy et al. 2009), which use routinely produced LASCO coronagraph images. None of these methods can be used to estimate B_z but velocity is of particular use to space weather forecasters for predicting Earth-arrival times.

In the present chapter, we analyze 38 coronal dimming events – the two from Chapter 4 plus 36 more during two separate two-week periods during 2011 – and search for the relationship between dimming and CME velocity and mass. Of the 38 total events studied, 17 could be parameterized for CME velocity and dimming speed, and 14 could be parameterized for CME mass and dimming depth.

Section 5.2 shows examples of observations, describes the method for selecting this sample of events, and explains why some events identified in AIA could not be analyzed with EVE and/or coronagraphs. Section 5.3 provides further discussion and statistics on the flare-dimming deconvolution method detailed in Section 4.2. Section 5.4 describes the fitting method applied to the deconvolved EVE light curves, including a discussion of uncertainties. Section 5.5 discusses the parameterization of fitted dimming light curves and CMEs observed in coronagraphs, also including a discussion of uncertainty. Section 5.6 shows the correlations between the various combinations of coronal dimming and CME parameters. As usual, the final section, 5.7, provides a summary of the analysis and results in this chapter.

5.2 Observations and Event Selection

In addition to the two cases studied in detail (see Chapter 4), four weeks were selected in 2011 for analysis of coronal dimming events: February 10-24 and August 1-14 (Figure 5.1). These two independent periods about 6 months apart are during the initial rise of solar activity of solar cycle 24. The duration was chosen such that there would be approximately 30 identifiable dimming events. It is also desirable to select a time when the two STEREO spacecraft orbital locations were advantageous for geometric analysis, and when the other space-based instruments used in this

study could be expected to be operating nominally. The periods of study are typical in terms of CME occurrence and solar EUV irradiance variability, both near their respective mean values (see Figure 5.1).

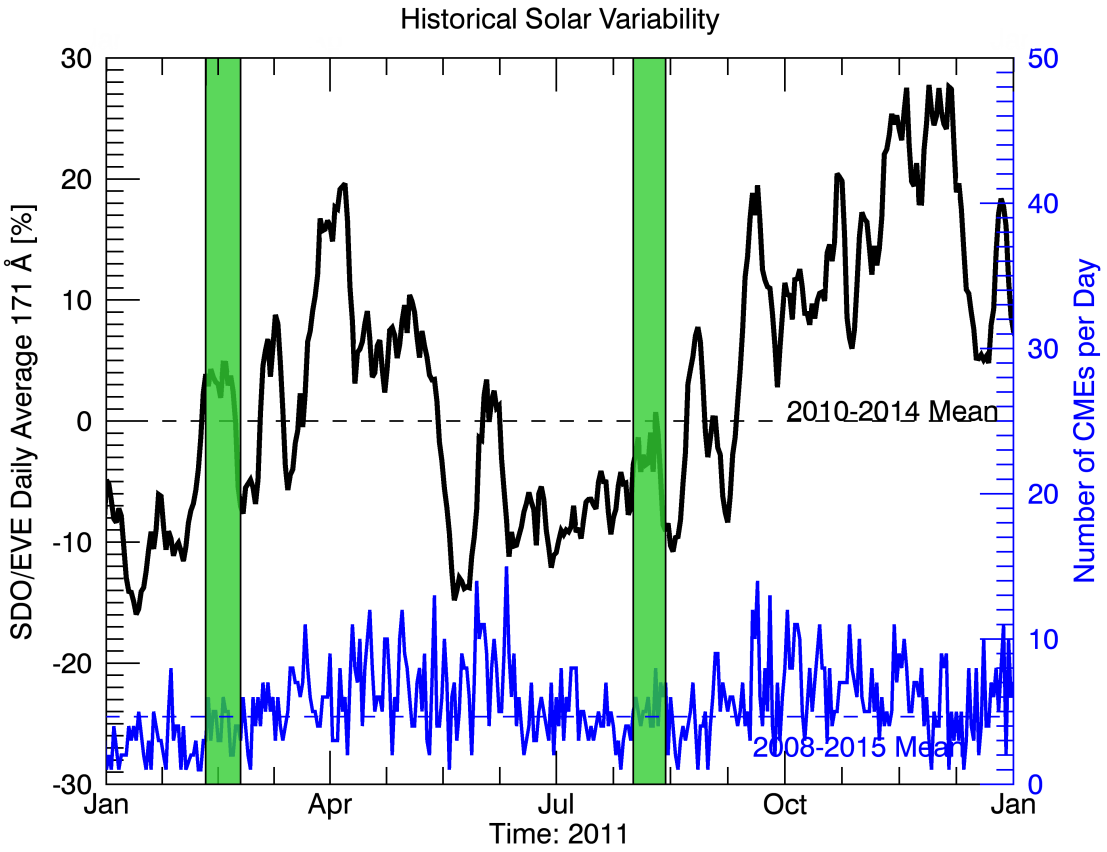

Figure 5.1: Context for the selected periods of study. The black line is the daily averaged EVE Fe IX 171 Å line and the blue line is the daily total CME occurrence. The vertical green bars indicate the selected periods of this study. The mean for EVE (dashed black line) is taken over the first four years of EVE's operations (2010-2014) and the mean for CME occurrence (dashed blue line) is taken for the most recent solar cycle starting in 2008 to the end of 2015. Note that the full range of both of these means is not shown; only 2011 is shown for clarity of the selected periods.

First, images from AIA were used to identify dimming events. Identification was performed manually using daily AIA movies to create a list of candidate events. Two people made the identifications separately, using differently formatted movies. James Mason used the AIA 211-193-171 Å composite movies (e.g., Figure 4.4) and Dave Webb used the 193 Å movies. The primary initial

selection criteria were that 1) the dimming must persist for several hours and 2) the dimming must have non-trivial spatial extent (at least comparable to the size of an active region). The independently identified events were then accumulated, duplicates merged as positively identified events, and disparities investigated by each identifier. Sometimes disparities proved to be questionable events according to the selection criteria above and were removed from the event list. Other times the disparities proved that the independent identification acted as a failsafe – a single observer simply missed an event but the other caught it. Future studies that are more expansive, such as analyzing the entire SDO era, should use the automated AIA dimming detection method developed by Krista and Reinard (2013).

Once the event list was deconflicted, the approximate time of the event was used to search the related observations in other instruments: flares from GOES X-ray flux, CMEs from LASCO and COR, and solar irradiance from EVE. This initial list included 38 events (including the 2010 August 7 simple case from Chapter 4, which was outside the four week period, and the 2011 August 4 complex case from Chapter 4, which happened to fall inside the second two-week range). In some cases, the dimming was not clear in EVE data or the CME was not clearly identified in the coronagraph images; nevertheless these were dimmings identified in AIA and are listed in Table 5.1 and Appendix A for completeness. Appendix A expands the event list with additional ancillary data such as dimming and CME parameterization values and associated uncertainties. Of the 38 total events, 29 could be parameterized with EVE in terms of depth and slope, 21 had measured CME velocities, and 17 had measured CME masses. Six of the CMEs had at least two views so that 3-D analysis could be applied for improved accuracy of the CME kinetic parameters.

Table 5.1: Event list. Times and locations are approximate. The "derived parameter" columns abbreviations are as follows: V = velocity, M = mass, 3V = 3-D velocity, 3M = 3-D mass, D = depth, S = slope. Only 29 of the events have the full complement of parameterizations to allow the study of the relationships between dimmings and CMEs. See Appendix A for event list with additional ancillary data.

Event #	Date	Time [UT]	Location	EVE Derived Parameters	CME Derived Parameters
1	2011 Feb 10	07:40	N20 W-limb	D, S	–
2	2011 Feb 10	13:36	N20 W-limb	D, S	V, M
3	2011 Feb 11	07:46	N20 W-limb	D, S	V, M
4	2011 Feb 11	13:21	N60 W00	D, S	–
5	2011 Feb 11	21:43	N10 E-limb	D, S	V, M
6	2011 Feb 12	06:05	N30 E10	D, S	–
7	2011 Feb 13	14:00	S10 E10	D, S	3V, 3M
8	2011 Feb 14	15:45	S10 W00	D, S	V, M
9	2011 Feb 14	17:36	N30 E20	–	3V, 3M
10	2011 Feb 15	02:07	N00 W00	D, S	3V, 3M
11	2011 Feb 16	14:40	S20 W30	D, S	–
12	2011 Feb 17	00:47	E40 W00	D, S	–
13	2011 Feb 18	11:15	S10 W50	D, S	V, M
14	2011 Feb 17	19:20	N30 W00	D, S	–
15	2011 Feb 24	07:40	N10 E-limb	D, S	–
16	2011 Feb 25	07:00	N45 E60	D, S	V, M
17	2011 Aug 2	05:10	N05 W20	D, S	V, M
18	2011 Aug 2	13:00	N00 E-limb	D, S	–
19	2011 Aug 3	13:43	N05 W48	D, S	V, M
20	2011 Aug 4	04:12	N05 W58	D, S	V, M
21	2011 Aug 4	04:41	N80 W00	–	V
22	2011 Aug 5	07:25	S30 E50	–	–
23	2011 Aug 6	11:50	S14 E10	D, S	–
24	2011 Aug 6	18:25	N05 W25	–	–
25	2011 Aug 6	17:35	N30 W-limb	–	V, M
26	2011 Aug 6	22:40	N10 W25	D, S	–
27	2011 Aug 7	04:00	N10 W55	D, S	V, M
28	2011 Aug 8	01:15	N80 E05	–	–
29	2011 Aug 8	11:00	N15 W70	–	–
30	2011 Aug 8	17:42	N05 W05	D, S	–
31	2011 Aug 8	18:42	N05 W75	–	3V, 3M
32	2011 Aug 9	08:10	N15 W70	D, S	3V, 3M
33	2011 Aug 9	09:12	S30 E-limb	–	–
34	2011 Aug 9	11:26	N05 W00	D, S	V, M
35	2011 Aug 11	10:23	N00 W-limb	D, S	3V, 3M
36	2011 Aug 12	00:09	N45 E80	D, S	V, M
37	2011 Aug 12	11:13	N50 E70	D, S	–
38	2010 Aug 7	18:05	N05 E60	D, S	3V, 3M

Because EVE irradiance observations are spatially integrated, dimmings from distant areas that occur too closely in time overlap in the irradiance time series and cannot be easily separated and parameterized. Thus, such events have a "–" in the EVE Derived Parameters column of Table 5.1 and are excluded from the correlative study in Section 5.6. This was the case for Events 9, 21, 29, 31, and 33. Similarly, Event 22 was a series of small eruptions from an active region with multiple slow CMEs whose analysis would be prohibitively difficult for a statistical study. Secondly, some dimmings identified in AIA were not detectable in the EVE data, making parameterization impossible. Here, "not detectable" simply means that the EVE light curves did not show anything resembling the archetypal dimming near the time that was identified in AIA. This implies the magnitude of the dimming was small ($< 1\%$ impact on irradiance), which would be the case if the dimming itself was not very deep or if evolution elsewhere on the solar disk dominated (e.g., active region evolution). Examples of the former are Event 24, which was a very slight darkening of an active region's coronal loops with no identified CME; Event 28, which was a small occurrence of "coronal rain", also with no identified CME; and Event 25, which was an off-disk dimming event with a narrow CME. In principle, it is possible for off-disk events to generate a large irradiance change, but in this case the change was insufficient to be observable by EVE. In total, these criteria on EVE measurements resulted in 9 of the 38 events being excluded from the correlation analysis, leaving 29 events. These 29 can be processed using the flare-dimming deconvolution method described in Section 4.2. The next section will discuss the results of this process.

5.3 Flare-Dimming Deconvolution Method Statistics

There are 30 permutations of the dimming emission lines (171, 177, 180, 195, 202, 211 Å) and non-dimming emission lines (211[1] , 284, 335, 94, 131 Å) for the correction method. Each one is processed using the same algorithm described in Section 4.2. Figure 5.2 shows an example of all 30 combinations for a single event (Event 20).

It can be seen that the the higher the ionization state of the non-dimming line (blue), the

[1] Recall that 211 Å is included in both dimming and non-dimming categories to reflect its ambiguity

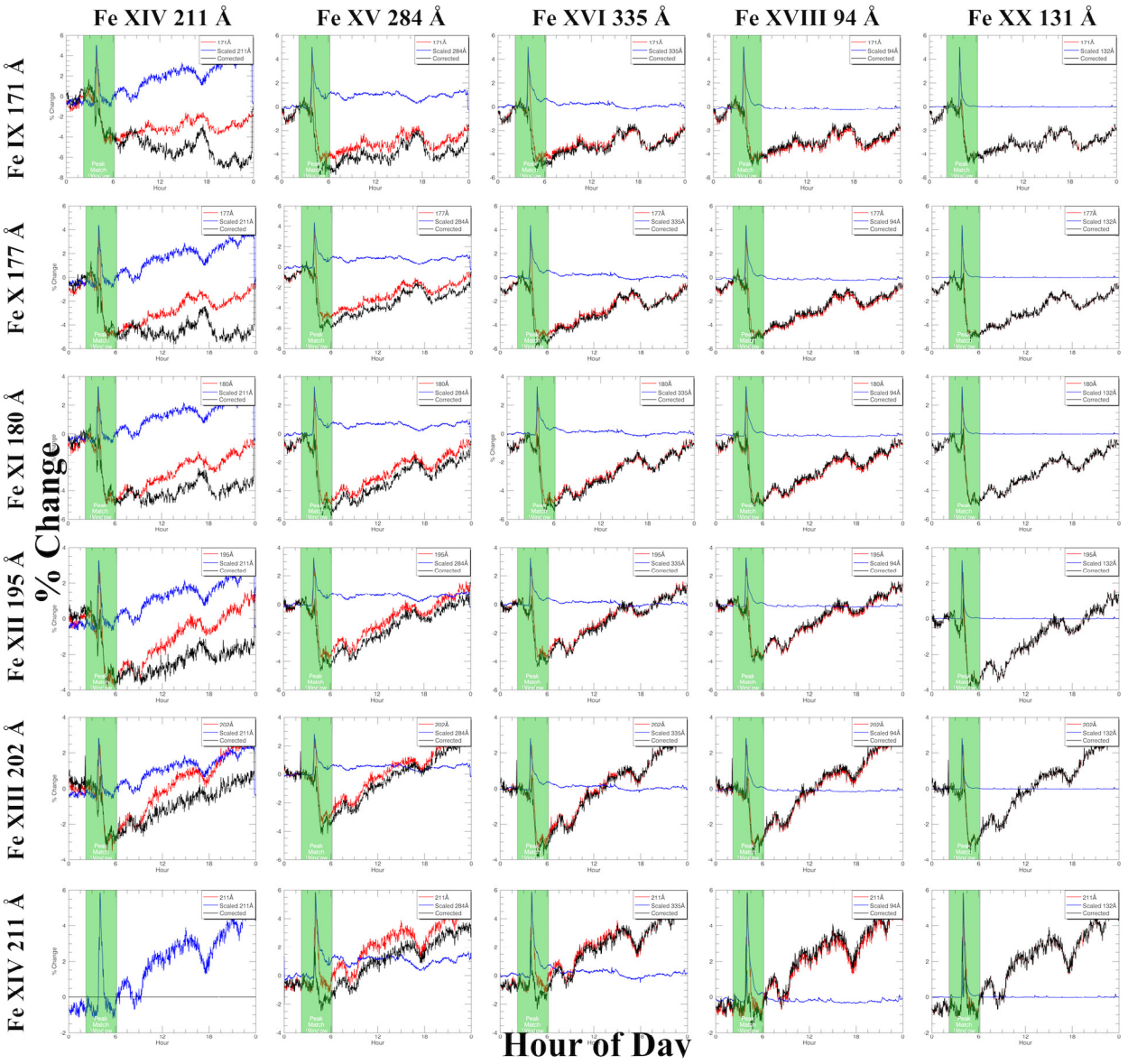

Figure 5.2: Example of every combination of the dimming (rows) and non-dimming (columns) emission lines for the deconvolution method for a single event (Event 20). In each plot, the red is the dimming line, blue is the scaled and time-shifted non-dimming line, and black is the result of the subtraction (red - blue). The vertical transparent green bar indicates the time window the algorithm uses for finding and matching peaks. All emission lines are for Fe. Ionization state increases down for dimming lines and to the right for non-dimming lines.

"purer" the flare light curve, i.e., higher ionization states return almost perfectly back to their pre-flare irradiance level soon after the peak while lower ionization states show some additional post-peak response. Because the most intense heating occurs early in the flare – during the impulsive

phase as observed by GOES or RHESSI HXRs – it's unlikely that the emission from high ionization states disappears due to heating into the next ionization state. Rather, it returns to its pre-flare level because the intense heating supporting its existence is over and cooling has set in. Indeed, the mid-ionization states such as Fe XVI at 335 Å show a slow, hours-long ramp downward in irradiance. The fact that these mid-ionization states don't immediately return back to their pre-flare level indicates that their net cooling rate is lower. The lower net cooling rate is likely due to the higher density of these ions where collisional de-excitation in the plasma competes with radiative cooling. Additionally, the Einstein A coefficient for Fe XVIII 94 Å is 11.4x[2] larger than for Fe XVI 335 Å, indicating that the radiative cooling is even slower for Fe XVI 335 Å. The blue light curve for FeXVI 335 Å indicates that the cooling is ongoing during this hours-long period. In other words, warm ions like Fe XVI are slowly recombining with electrons and acting as a source term for the cooler ionization populations. Critically, this "feeding" of the lower ionization populations, like Fe IX, is a cooling mechanism, not a mass-loss one. By removing this trend as indicated by the irradiance in e.g., Fe XV 284 Å, we obtain a light curve more sensitive to mass-loss than temperature evolution (black curve in Figure 5.2).

In Chapter 4, it was found that for the 2010 August 7 event, the combination of Fe IX 171 (dimming) and Fe XV 284 (non-dimming) in EVE gave the best match to the spatially isolated dimming in AIA 171 Å. The only dimming mechanisms identified to be important in this event were mass-loss and thermal. Thus, it seems that the 171 Å - 284 Å combination can successfully mitigate the impact of thermal processes on the dimming line. If other dimming mechanisms play an important role in the irradiance, as is the case for the 2011 August 4 case in Chapter 4, it may be necessary to account for them, such as by identifying and removing the impact of obscuration dimming. Until such an analysis is performed, we apply the deconvolution method to the additional 28 events with viable EVE data, using the clean removal of the flare peak as the criteria for determining the best combination of dimming-non-dimming line. In other words, the peaks of the dimming and scaled/time-shifted non-dimming lightcurves should be similar in shape.

[2] Determined with the NIST online database

Figure 5.2 shows that many of the combinations would meet this criteria. The next determining factor is depth of dimming. Event 20 had a relatively consistent depth of dimming for all dimming lines, but this is not the case for all events. Generally, we prefer a larger magnitude dimming as its interpretation is less ambiguous and less susceptible to being dominated by other physical processes such as active region evolution. As was shown in Chapter 3, the ionization level is inversely proportional to depth of dimming. Thus, 171 Å is generally preferred as the dimming line but is evaluated on a case by case basis for the events studied here. Finally, we prefer to use 284 Å as the non-dimming line for deconvolution based on the physical motivation provided in the paragraph above.

This methodology has been applied to the 28 unique EVE dimmings found during the four weeks studied. Of these, all 28 were found to be best represented by the 171 Å - 284 Å combination. We will gain additional confidence in the effectiveness of this line pairing for EVE if we find a positive and statistically significant correlation between corrected EVE light curve parameterizations to independently derived CME mass and velocity. The first step in that process is to fit the EVE light curves in preparation for dimming parameterization.

5.4 Dimming Light Curve Fitting Method

5.4.1 Physics Motivation and Fit Types

Recall that the β parameter (Equation 2.5) for a plasma is an indicator of the relative importance of plasma and magnetic pressures. This combined with the frozen-in flux condition tells us whether which will dominate the motion of the plasma. In the solar corona, β is typically < 1, indicating that the magnetic field dominates the flow of plasma, i.e. plasma is confined by magnetic fields. Thus, in the initiation of a CME where magnetic fields are propelled out of the corona and expand as they do so, the plasma in the enclosed bubble of the CME experiences an expansion and density decrease (Figure 5.3).

Dimming – CME mass relationship

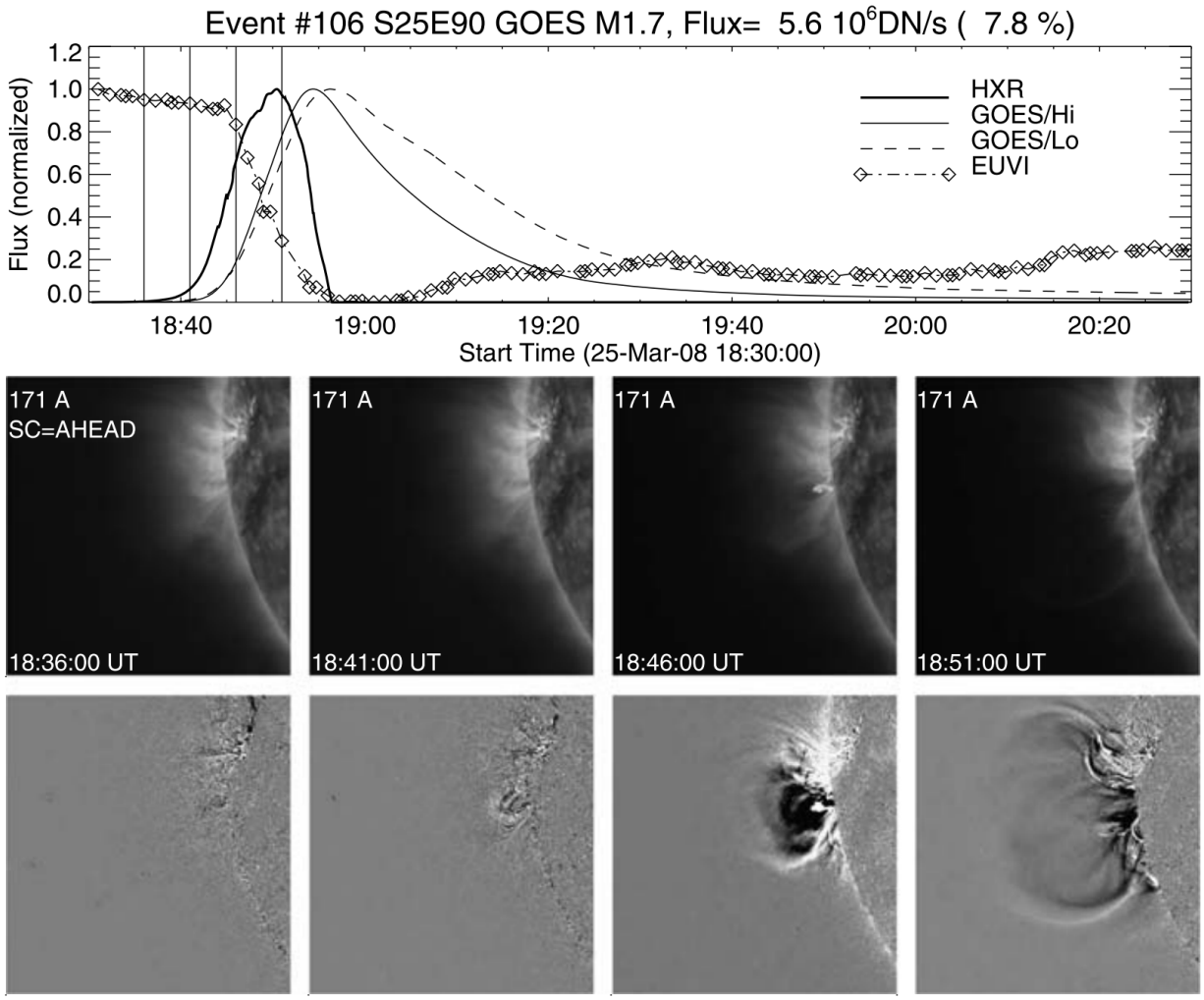

Figure 5.3: Example of CME bubble expansion and associated EUV dimming. (Top) Soft X-ray (GOES/Lo 0.5 4 and 1 8 , thin curves) and EUV (STEREO-A/EUVI, diamonds) light curves and time derivative, dI(t)/dt, of the harder soft X-ray light curve (thick solid line) for the flare/CME event on 2008 March 25 at 18:30 UT. (Bottom) Four STEREO-A/EUVI images (top row) and running-difference images (bottom row). Note the strong dimming in the EUV light curve. The diamond symbols mark the times of the EUV images; the selected images shown below are marked with vertical lines. The peak EUV flux is $F = 5.6 \times 10^6 DNs^1$ (or 7.8% of the total flux). The field of view of the images is 512 EUVI pixels (600 Mm). Adapted from Aschwanden et al. (2009b).

Aschwanden et al. (2009b) described this process and here we adapt it for the variation of intensity in collisionally-excited lines as a function of height for a constant-temperature and expanding volume. As Equation 2.6 described, the emission measure is equal to the square of the density of the emitting material integrated over the emitting volume. The relative change as a

function of time, t, in emission then becomes

$$\frac{n_d(t)}{n_A} = \sqrt{\frac{I_d(t)}{I_A}} \implies n_d(t) = n_A\sqrt{\frac{I_d(t)}{I_A}} \tag{5.1}$$

where $n_d(t)$ is the density in the dimming region as a function of time, n_A is the density of the nearby active region responsible for triggering the dimming, and I is the emission intensity. The volume is assumed to be the void in the corona where the plasma existed before the CME stripped it away, so it falls out of the relative equation. Next, the corona consists primarily of hydrogen (at least 90%) and at the known average temperature (about 1 MK), it can be reasonably assumed to be fully ionized. Because hydrogen consists of a single proton and single electron, the densities of these two populations, n_p and n_e, are equal but the mass is dominated by the protons, m_p. Thus, the mass of the CME, m_{CME}, can be expressed as

$$m_{CME} = m_p n_e V_{CME} \tag{5.2}$$

where V_{CME} is the volume of the CME. The mass of the region in the corona that dims can be similarly expressed as

$$m_d(t,T) = m_p n_d(t) V_d \tag{5.3}$$

where the subscript d indicates the dimming and is a function of temperature, T. We can then substitute Equation 5.1 into Equation 5.3 and obtain

$$m_d(t,T) = m_p \left[n_A\sqrt{\frac{I_d(t)}{I_A}} \right] \frac{\pi}{4} w_d^2 \lambda_T \tag{5.4}$$

where w_d is the width of the dimming region and λ_T is the hydrostatic scale height. Note that these equations as developed by Aschwanden et al. (2009b) are intended for use with EUV imagers. For EVE irradiance, we make the assumption that the temperature response is "pure" as the lines of interest are spectrally resolved. This assumption comes with the caveat that, because EVE is spatially integrated, the temperature evolution of plasma outside of the dimming region can be

ignored. Given the temperature evolution correction method described in Chapter 4, we believe this to be a reasonable assumption. Furthermore, later in this chapter, we will be establishing a correlation between coronagraph-derived and dimming-derived masses. If distribution of ions is assumed to be the same in each event, then it is not necessary for us to compute the dimming at each temperature since this will be captured in the empirical relationship between the two mass-estimation methods. We further assume the constancy of other terms as follows

$$k_A = m_p n_A \frac{\pi}{4} w_d^2 \lambda_T. \tag{5.5}$$

Aschwanden et al. (2009b) makes the assumption that $w_d \approx w_A$, i.e., that the size of the dimming is about the same size as the active region. Active regions that produce large CMEs tend to be of similar size, varying by perhaps a factor of 2. The size of the dimming could of course be measured but our goal is to use irradiance dimming with no additional information and determine a relationship to CME kinetics for use in space weather applications. The assumption that the density of active regions is constant is difficult to assess. Thus, we can simplify the dimming mass equation to

$$m_d(t) = k_A \sqrt{\frac{I_d(t)}{I_A}}. \tag{5.6}$$

As mentioned before, this equation relates the absolute mass to the relative emission intensity. Aschwanden et al. (2009b) used the active region intensity for normalization. With EVE, we use the disk-integrated, pre-flare emission intensity (i.e., pre-flare irradiance), I_{tot}, for normalization. We also desire to parameterize the dimming in terms of a single number to relate to a single CME mass number to be determined with the traditional coronagraph-based methods. This will be herein referred to as dimming depth, or just depth in plots, and is taken at a manually selected time.

$$m_d = k_A \sqrt{\frac{I_d(t = t_{selected})}{I_{tot}}}. \tag{5.7}$$

Finally, we have an equation to estimate dimming mass from irradiance:

$$m_d = k_A \sqrt{depth} \tag{5.8}$$

and we'll make the assumption that $m_d \approx m_{CME}$.

Dimming – CME speed relationship

Again, we start with the emission measure equation but now consider the "standard way to model gravitational stratification of the background corona" using the multi-hydrostatic model in Aschwanden (2004). This provides an equation for the emission measure at a particular altitude, h, which is int he plane of sky and at a particular temperature. It is expressed in terms of the equivalent column depth, z_{eq},

$$EM(h,T) = n_e^2(h_0,T) z_{eq}(h,T). \tag{5.9}$$

Aschwanden goes on to model and compute z_{eq}. We make the simplifying assumption that $z_{eq} = h$ and consider the collisionally excited bound-bound emission for a self-similar, spherical expansion of plasma at constant temperature. Mass is conserved during the expansion:

$$n_0 h_0^3 = n(t) h^3(t) \implies n(t) = \frac{n_0 h_0^3}{h^3(t)} \tag{5.10}$$

which can then be plugged into the simplified emission measure equation, yielding

$$\begin{aligned} EM(t) &= \left[\frac{n_0 h_0^3}{n^3(t)}\right]^2 h(t) \\ &= (n_0^2 h_0) \frac{h_0^5}{h^6(t)} h(t) \\ &= EM_0 \frac{h_0^5}{h^5(t)} \\ \implies \frac{EM(t)}{EM_0} &= \left(\frac{h_0}{h(t)}\right)^5. \end{aligned} \tag{5.11}$$

These equations were also originally developed for usage with EUV spectral imagers. Spatially integrating in the plane-of-sky reduces the exponent by 2, i.e.,

$$\frac{I(t)}{I_0} = \left(\frac{h_0}{h(t)}\right)^3 \tag{5.12}$$

We then assume that when the irradiance has dropped halfway between its initial value and the dimming depth, the CME is at its average velocity. Note that acceleration must occur in the low corona. From the 25,000 (20 years) CMEs in the CDAW catalog, we know that above 2 $R_\odot$ (the approximate lower bound of the LASO C2 coronagraph), the average acceleration is -1.67 m s^{-2} compared to average velocities of 393 km s^{-1}. So the acceleration of the CME from 0 to e.g., 393 km s^{-1} must typically occur below 2 $R_\odot$. As described in Chapter 2, the acceleration mechanism is poorly understood and few observations exist that can be used to determine the CME velocity in the low corona. Future work using the PROBA2/SWAP instrument will do just this. For now, we live with our assumption and its implication:

$$h(t) = h_0 + vt, \tag{5.13}$$

and plug it back into Equation 5.12 to get

$$\begin{aligned}
\frac{I(t)}{I_0} &= \left(\frac{h_0}{h_0 + vt}\right)^3 \\
let\ I\ |_{t=t_{1/2}} &= \frac{I_0}{2} \\
\implies \frac{I_0}{2I_0} &= \left(\frac{h_0}{h_0 + vt_{1/2}}\right)^3 \\
\implies \left(\frac{1}{2}\right)^{1/3} &= \frac{h_0}{h_0 + vt} \\
\implies 2^3(h_0 + vt_{1/2}) &= h_0 \\
\implies v &= \frac{\frac{h_0}{8} - h_0}{t_{1/2}} \\
&= -\frac{7h_0}{8t_{1/2}}
\end{aligned} \tag{5.14}$$

$t_{1/2}$ can be obtained from the light curve of the event assuming the average slope as

$$t_{1/2} = \frac{1}{2}\left(\frac{I_0}{\frac{dI}{dt}}\right) \tag{5.15}$$

where $\frac{dI}{dt}$ is the slope of the light curve while the dimming is in progress. Plugging this back into the final velocity equation in Equation 5.14 results in

$$\begin{aligned} v &= -\frac{7h_0}{8\frac{1}{2}\left(\frac{I_0}{\frac{dI}{dt}}\right)} \\ &= -\frac{7}{4}h_0\frac{\frac{dI}{dt}}{I_0} \\ let\ H &= -\frac{14}{8}h_0 \\ \implies v &= H\frac{\frac{dI}{dt}}{I_0}. \end{aligned} \tag{5.16}$$

H is dependent on the initial size of the CME/dimming region. Herein, we assume that this value is constant but the value could be estimated with image data, just as w_d could be for the mass-depth relationship of the previous section. Again however, we are interested in the development of a correlation between CMEs and dimmings where the dimmings are determined entirely by irradiance. $\frac{dI}{dt}$ is the slope and I_0 is the depth. Thus, the equation that we'll refer to in subsequent sections is

$$v = H\frac{slope}{depth}. \tag{5.17}$$

Note that this method does not include any direction information, so the v indicates speed rather than velocity. Aschwanden (2009) developed a more sophisticated model of dimmings, including adiabatic expansion and gravitational stratification. However, the model contains 14 free parameters and is more suited to a case-by-case study of dimming morphologies. For the purposes of our correlative study, it is reasonable to assume that the decrease in emission due to the volume density is more significant than the thermal and inhomogeneity effects, and that the effective height scale of the CME is the most important parameter.

Light curve fitting Different functions are fitted to the EVE dimming events to explore which functions are more optimal for determining the dimming event parameters of depth and slope. Exponential and power law fits tend to result in $\chi^2 > 20$, meaning they were very poor fits. Polynomial fits up to order five were also computed, with 5th and 3rd orders appearing to best describe the shape of the light curves (see Figures 5.4 and 5.5). The manually-selected best-fit function is used for deriving the dimming slope and depth (see Section 5.5).

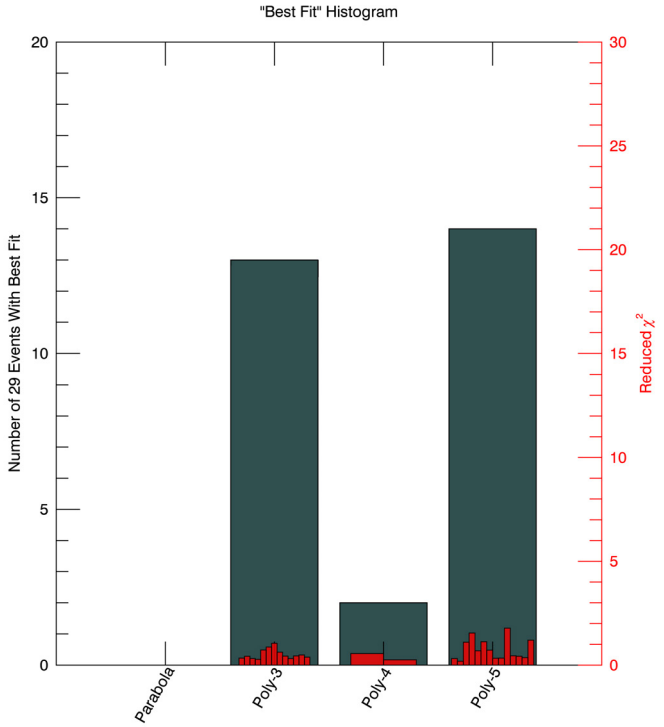

Figure 5.4: (grey) Statistics of manually selected "best fit" for all unique EVE dimming events in 4 weeks studied and (red) the reduced χ^2 for the best fits. The 3rd and 5th order polynomial fits provided the largest number of best fits.

5.4.2 Dimming Fit Uncertainty Computation

The uncertainties from Section 4.3 correspond to the deconvolved/corrected EVE dimming light curve. Those light curves are the input for the fitting function, IDL's *poly_fit*, which also accepts an input *measure_errors* for uncertainties. Figure 5.5 shows polynomial fits from 2 to 5

with the measurement errors and the resultant 1σ uncertainties computed by *poly_fit*. The fits achieve the desired effect of reducing uncertainty even further than 2-minute averaging of the EVE data and providing a smooth function to parameterize. In particular, the fits smooth out any residual bumps in the light curve that the temperature-evolution correction method did not remove or that it introduced. Best fit selection was guided by the desire to have χ^2 near unity and by some flexibility for events where the EVE dimming correction method did not completely remove the flare peak of the cool corona line (Fe IX 171 Å). In such cases, the fits could deviate from the "pure" dimming light curve, but that resulted in a large χ^2 and was obvious upon inspection. Invariably, at least one of the fits performed well. Rather than develop a complicated algorithm to account for this effect autonomously, selection of the best fit was done by manual inspection.

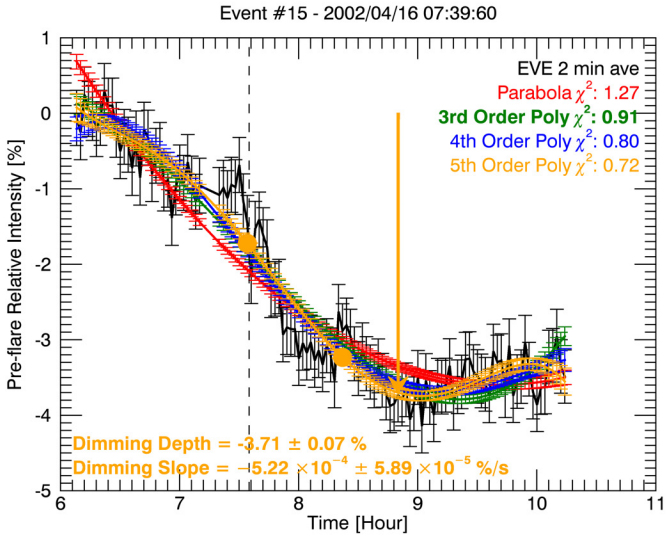

Figure 5.5: A single dimming event (Event 15) showing the reduction in uncertainties of the fits compared to the EVE data. The arrow shows the location of dimming depth parameterization for this event, and the two filled circles indicate the range where slope was computed. Their colors correspond to the fit types in the legend. The lowest χ^2 indicates that the 5th order polynomial was the best fit for this event, but we note that the results from the other polynomial fits are very similar.

5.5 Parameterization Methods

Dimming and CMEs are complex phenomena with complex observations and associated data analysis. Our end goal is to provide simple measures of dimming to act as proxies for CME mass and speed, driven by a physical explanation. Given this, the space weather community would have an independent indicator of CME presence and importance to geospace, and the astronomy community would have a means of detecting and characterizing CMEs on other stars (albeit a first-order characterization). To that end, this section describes the parameter derivations for dimming and CMEs that will be used to establish a correlation in Section 5.6, motivated by the physics in preceding sections.

5.5.1 Dimming Parameterization

Points for the computation of depth and slope are selected manually from the best fit light curve from Section 5.4. The dimming depth parameter is taken from a manually-selected, relatively stable pre-flare value to a point near the beginning of the dimming floor (see arrow in Figure 5.5). Dimming slope was computed across a range: the initial point was typically chosen to be soon after the initial dimming rollover when the slope becomes relatively constant, and the final point was selected just prior to the inverse rollover leading to the relatively flat period in the light curve (see solid circles Figure 5.5).The slope need not be constant between these two points. For each time step within the selected range, the derivative was computed. The single-value slope parameter for each event is the mean of these derivative (slope) values. Ideally, the slope would be constant between these points and the simple mid-point could be selected, consistent with our physical derivation for dimming irradiance slope. The method applied result in a larger uncertainty on the slope parameter than would be obtained selecting a single point. Future work will determine if selection of a single point at $t_{1/2}$ yields better final results.

The uncertainty associated with dimming depth is just the uncertainty of the fitted light curve at the point selected for the depth measure, as exemplified by the error bar at the arrow

in Figure 5.5. The uncertainty for slope requires some additional computation. To compute the derivative of the light curve at each point within the specified time range, IDL's *deriv* function was used; the corresponding *derivsig* function returns the 1σ uncertainty for each point in the derivative array. Collapsing the various derivatives into a single slope parameter via the mean has the corresponding uncertainty,

$$\sigma_{slope} = \frac{1}{N}\sqrt{\sigma_1^2 + \sigma_2^2 + ...\sigma_n^2}$$

where N is the number of points, and $\sigma_1...\sigma_n$ are the uncertainties for each point returned from *derivsig*. Appendix A includes the dimming depth, slope, depth uncertainty, and slope uncertainty for each of the 38 events studied.

5.5.2 CME Parameterization

Detailed 3-D analysis of the velocity and mass was possible for six of the best-observed CMEs, using either or both LASCO and the CORs data. These six events are noted as 3V, 3M in Table 5.1 and shown as solid red symbols in Figure 5.6. Following the method of Colaninno and Vourlidas (2009), the GCS model is fit to the observations to determine the 3-D location and heights of the CMEs. The 3-D heights and longitude of the CME are needed to calculate the "true" 3-D mass of the CME. These heights are also used to calculate the de-projected velocity of the CME. The reported masses are for a height of 15 $R_\odot$, using the fitting method of Bein et al. (2013) for mass increase with height. For the 2011 February 13-15 CMEs the mass was measured in both COR2A and COR2B and then averaged. For the 2011 August 9 and 11 CMEs, the mass was measured in LASCO-C3 only.

The following procedure was used to estimate the uncertainties for the CME kinetic parameters. The LASCO CDAW measurements were used for most of the events to derive the CME velocity and mass, which are based on a single viewpoint observation as opposed to 3-D. The reported linear speed of each CME is obtained by fitting a straight line fit to the height-time measurements at a fixed position angle. If we assume conservatively that the CME axis is 60° from the

sky plane as the worst case (for non-halo CMEs), this results in a factor of 2 (50%) underestimation of the speed. The CDAW catalog also provides the CME span angle, which can be used to provide an estimated error on the CME mass (Figure 4 of Vourlidas et al. 2010). As an example, if we take Event 2 from Table 5.1 above, then using these errors we have speed = 338 ± 345 km s^{-1} and mass = $3.40 \times 10^{14} \pm 4.30 \times 10^{14}$ g.

For the six events with 3-D analysis of the CME measurements, we derive the error in the speed from the linear fit to the data assuming the error in the 3-D height measurements is $\pm 0.48 R_{\odot}$ (Colaninno et al. 2013). Thus, if we take Event 7 as a typical 3-D CME measurement, we get 353 ± 13 $km\ s^{-1}$ for the speed. The mass is still considered an underestimate from the 3-D analysis but is better determined because the plane-of-sky angle and 3-D heights are known from the GCS model fit, so a $\pm 15\%$ error is assumed for the 3-D mass estimates (Bein et al. 2013).

For the purpose of linear-fitting with dimming parameters in Section 5.6, the midpoint between the low and high limits is chosen for each CME speed and mass parameter reported here, and the CME parameter error is the range between the high and low limits divided by two (i.e., $\pm$ error bars in Figure 5.6). The plot of the points themselves does not display this center-point for single-viewpoint derived CME parameters but does for 3-D derived CME parameters. Appendix A includes the CME speed, mass, speed uncertainty, and mass uncertainty for each of the 38 events studied.

5.6 Dimming and CME Parameters Correlation

As described in Chapter 4, we expect direct proportionality between dimming depth and CME mass, and between dimming slope and CME speed. This relationship is intuitive, but Section 5.4.1 derived the functional form of the relationship. Namely, we expect that CME speed goes as dimming slope/depth and CME mass goes as the square root of depth. In other words, there should be a stronger correlation between these parameters than between any other combination of parameters. The analysis of just two events in Chapter 4 does not establish any such possible relationships. This study is a more in-depth examination of such possible relationships with many more events.

While our intention for this study was to have 30 events, it was challenging to obtain coronagraph-based CME velocity and mass for all of the candidate events. At the conclusion of event selection, we had 17 points for comparison. Table 5.2 provides the Pearson correlation coefficients (Pearson 1895) and p-value permutation statistical tests between each combination of the dimming and CME parameters, which confirms our initial expectation. Smaller p-values indicate a lower probability that the correlation could have arisen if no correlation existed at all. There is positive correlation between all of the parameter permutations, which is likely due to the "big flare syndrome" (Kahler 1982, 1992), e.g., a rapid, powerful coronal magnetic field energy release tends to result in a faster, more massive CME.

Table 5.2: Pearson correlation coefficients (PCC) and p-values between dimming and CME parameters.

Parameter 1	Parameter 2	PCC	p-value
Slope/Depth	Speed	0.12	0.65
$\sqrt{\text{Depth}}$	Mass	0.75	4.30×10^{-4}
Slope	Speed	0.78	1.51×10^{-4}
Depth	Mass	0.74	7.80×10^{-4}
Slope	Mass	0.60	0.01
Depth	Speed	0.51	0.04
Mass	Speed	0.64	2.79×10^{-3}
Slope	Depth	0.27	0.15

Our expectation was that we would have the highest correlations between the parameters that had a physical motivation for existing (see the first two rows of Table 5.2). This was accurate for the $\sqrt{\text{depth}}$ – mass relationship, which had the second highest correlation of any two parameters at 0.75. The relationship was effectively just as strong directly between depth and mass, at 0.74. However, the slope/depth – speed relationship performed worse than any other parameter combination, at 0.12. This is likely due to the numerous assumptions that were made during the derivation of that relationship. Those assumptions were made explicit in the derivation and they can be tested in future work. Interestingly, the best performing correlation was between slope and speed. Here,

the implicit assumption is that the functional relationship between the two is a simple linear one. The direct proportionality between the two is intuitive (simply think in terms of limits and you'll see that 0 speed should cause 0 slope and infinite speed should cause a perfectly vertical slope), but that proportionality doesn't indicate whether speed should go as, e.g., the square of the slope. Our derivation based on the physics of the corona was supposed to provide that functional form, but it appears the assumptions made negatively impacted the correlation. The assumption of the initial dimming size, h_0, being about the same for all events is the primary suspect for why the derived CME velocity relationship to slope/depth is not well correlated. Another way of assessing the correlation is through scatterplots and linear fits.

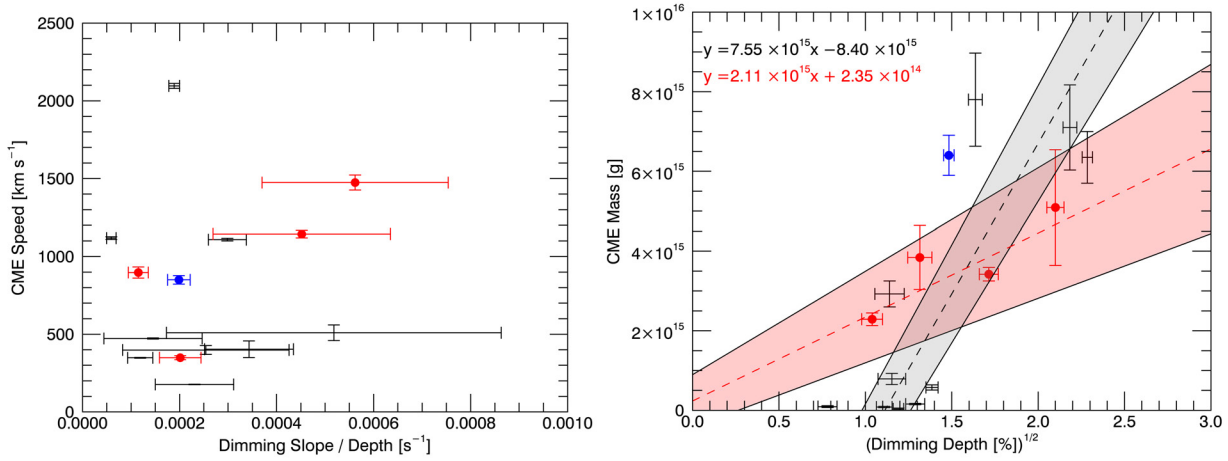

Figure 5.6: Scatterplots of (left) CME speed and dimming slope/depth and (right) CME mass and dimming $\sqrt{\text{depth}}$. Data without a center-point are derived from a single viewpoint of CMEs and are thus presented as a range of possible values rather than a single point with a standard uncertainty. Red symbols, line, and text indicate 3-D computed CME parameters, and the blue symbol indicates data from the simple 2010 August 7 event, which is also 3-D derived. Linear fits are shown as the dashed lines, and the grey/pink region represents the 1σ uncertainty of the linear fits.

Figure 5.6 shows scatterplots of speed vs. slope/depth and mass vs. $\sqrt{\text{depth}}$ with estimated error bars. Linear fits for the latter were computed using IDL's *fitexy*, which can accept input errors in both axes and return the fit parameters with a 1σ uncertainty. The fit uncertainty is then

used to define the grey/pink regions of Figure 5.6. The fit equations are also listed in the Figure 5.6 panels. This process was repeated using only CME values computed from the 3-D methods and are plotted as the red dashed line and pink shaded region. In order to get a nominal fit for the 3-D case with so few data points, a virtual (0, 0) point was added to the fit. The same fitting procedures were also applied to the speed vs. slope/depth plot, but the fits were extremely poor as expected based on the low Pearson correlation coefficient and inspection of the scatter.

The mass vs. $\sqrt{\text{depth}}$ plot (Figure 5.6, right) is linear-linear for clarity of the fits, but several of the data points end up off scale as they are $< 1 \times 10^{15}$ g. These points skew the fit significantly. Figure 5.7 shows the fit applied to high-mass only and low-mass only separately, with the 3-D based fit from Figure 5.6 still shown in red. The high-mass only plot shows very good agreement between the fits for all points and 3-D points, with slopes agreement to 37% of each other, whereas the fit for low-mass only has a fit slope that is 2 orders of magnitude lower than both the 3-D fit and the high-mass fit. Thus, we suspect there may be two statistical families in the data. We examined all of these events individually but did not notice any dimming peculiarities that might cause this separation of high-mass and low-mass families in this comparison. We also verified that the families do not strongly correlate to GOES flare magnitude (or whether there was a flare at all), CME span, or flare type. There may be a systematic error in the mass-estimation method that becomes acute in conditions that result in low masses. Furthermore, the low mass CMEs seem to be out of family when compared to an independently derived relationship between flare energy and CME energy established by Emslie et al. (2012).

Figure 5.8 shows a scatterplot of estimated flare energy versus CME kinetic energy. Flare energy was computed using the method in Woods et al. (2006), which integrates the GOES XRS-B light curve over the period of the flare, multiplies that value by a 1 AU scaling factor and an additional empirically-determined scaling factor. Most, but not all, of the events studied here had associated flares. The coronagraph-determined CME mass and speed were combined to compute CME kinetic energy using the $KE = \frac{1}{2}mv^2$ equation. Figure 5.8 also shows the expectation for the scatter-points based on the results of Emslie et al. (2012), who determined that their 38 flare-CME

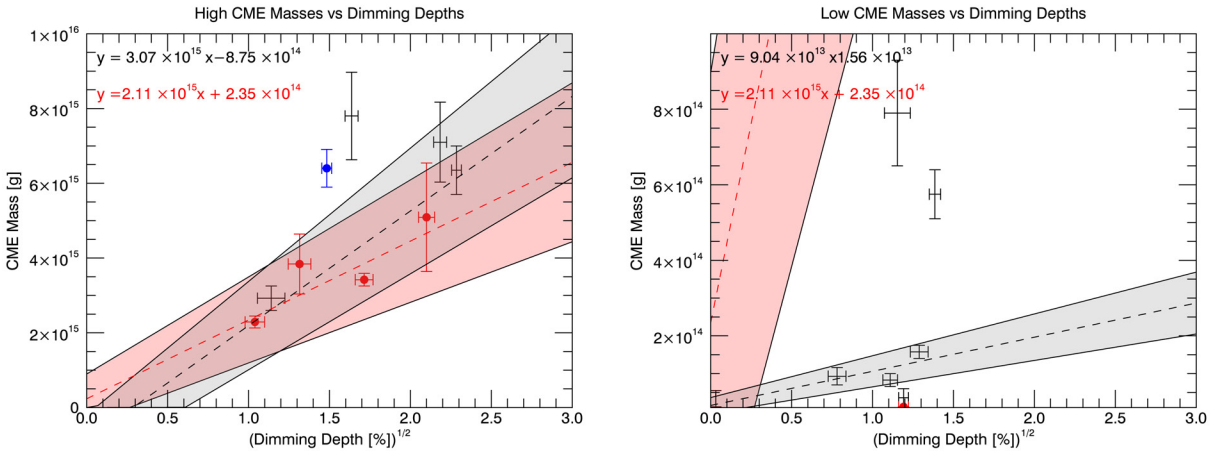

Figure 5.7: Same as Figure 5.6 but for (left) high CME mass ($\geq\ 1 \times 10^{15}\ g$) (right) low CME mass ($< 1 \times 10^{15} g$).

events roughly fell between a 1-1 line and a 0.35-1 line. Our coronagraph-based high-mass results are consistent with Emslie et al. (2012) but the low-mass CMEs are 1-2 orders of magnitude lower than expected. This comparison suggests that the low-mass CME values may just be representative of lower limits for mass. Indeed, this is the qualifier provided by the traditional CME mass estimation community.

We can also compare estimated CME energy through these two independent methods. The flare energies computed for our events (vertical axis of Figure 5.8) can be converted into estimated CME total energy using the relationship from Emslie et al. (2012). The CME kinetic energy can also be estimated by using the relationships between dimming and CMEs established here. The equations of fit in Figure 5.7 for the high-mass and 3-D mass can be averaged to obtain an estimated CME mass based on dimming of

$$m_{CME} = 2.59 \times 10^{15} \sqrt{depth} \tag{5.18}$$

where m_{CME} is in units of g and depth is in relative units of %. Note that the 3-D points are weighted more heavily since they show up in the high-mass as well as the 3-D populations. This

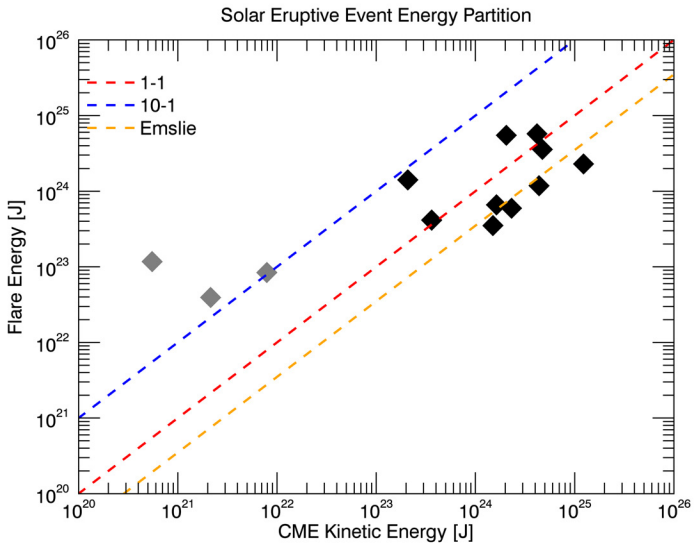

Figure 5.8: Flare-CME energy partition for the events of the semi-statistical study. The grey points are of the "low-mass" family of Figure 5.7 and the black points are from the "high-mass" family. The expectation is that the points should align roughly with the Emslie (0.35-1) line.

is desired because the 3-D derived CME parameters are more trustworthy. We've also dropped the y-intercept, making the assumption that it should be 0 (the average is -3.2×10^{14}, but this value is so small as to be lost in the noise anyway). In order to calculate the kinetic energy of the CME, we also need the estimated speed based on dimming. As described earlier, the physically-motivated relationship did not pan out but the Pearson correlation coefficient between CME speed and dimming slope was the highest of any parameter combination. Figure 5.9 shows a scatterplot of this relationship in the same form as Figure 5.6.

The points here are significantly more linear, though still not perfect. More points are needed to gain greater statistical significance and determine if this relationship is real, but that is future work. For now, we will take the average of the fit to all points and the fit to 3-D points to obtain

$$v_{CME} = 2.36 \times 10^6 slope \tag{5.19}$$

where v_{CME} is in units of km s^{-1} and slope is in units of % s^{-1}. The 3-D points are again

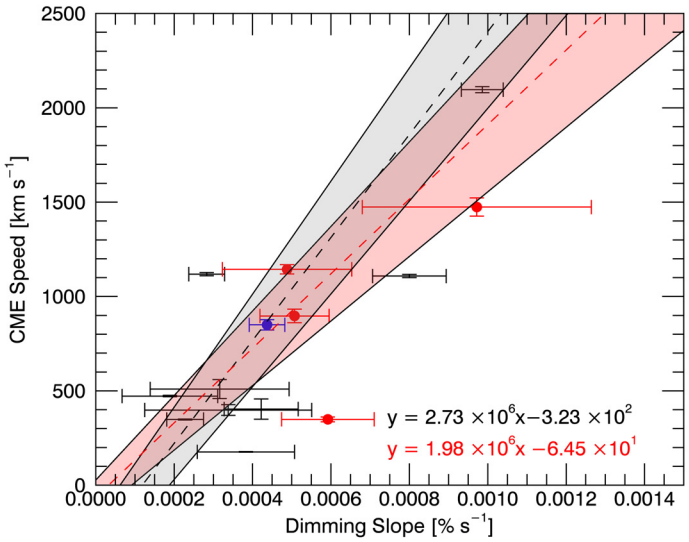

Figure 5.9: Same as Figure 5.6 (right) but the horizontal axis is simply slope rather than slope/depth.

weighted more heavily and the y-intercept is again dropped. Using Equations 5.18 and 5.19, we can compute the kinetic energy of the CME using the $KE = \frac{1}{2}mv^2$ equation again. Combining this with the CME energy estimation based on flare energy discussed above results in Figure 5.10. The Emslie/Woods method (vertical axis) determines the total CME energy i.e. kinetic + potential energy. The dimming-based CME-energy estimation only provides CME kinetic energy. However, gravitational potential energy is comparatively negligible, being only 9% of the kinetic energy on average for the 38 events in Emslie et al. (2012). Most of the points, except for three, cluster around the 1-1 line (red-dashed line). As this comparison relies only on the high-mass CME family, it suggests that the low-mass CME values are not realistic values but instead may represent the lowest limit of the estimation method.

Note that uncertainties are not factored into the Pearson correlation coefficients quoted in Table 5.2. Future work could use additional techniques for correlation that account for uncertainty, e.g., rank order. Such a study could include many more events to maximize the efficacy of the

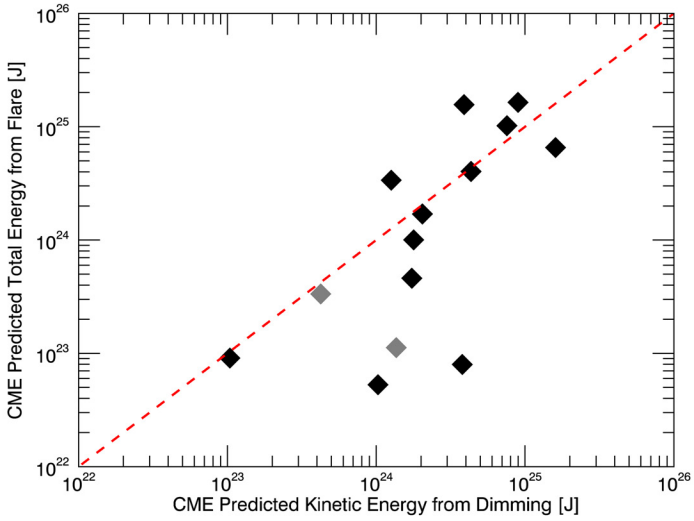

Figure 5.10: Scatterplot comparing CME energy estimation methods. The vertical axis uses the Emslie et al. (2012) result to estimate CME total energy based on total flare energy, which was itself computed using the Woods et al. (2006) method. The horizontal access is also estimated CME energy but based on the relationship established here between dimming depth and CME mass (excluding the low-mass family). The red diagonal line indicates a 1-1 relationship. The grey points are ones that had low CME masses in the coronagraph-based mass estimation.

correlation comparison.

5.7 Summary

Positive correlations with a high degree of significance have been found between coronal dimming and CME parameters. Our physically-motivated hypothesis that the CME mass goes as $\sqrt{\text{depth}}$ had the second highest correlation and the scatterplots looked good when coronagraph-based masses below 10^{15} g were ignored. The second hypothesis, that CME speed should go as dimming slope/depth, was proven incorrect (barring a very unlikely sampling of the statistical space). However, the direct relationship between CME speed and dimming slope had a strong Pearson correlation coefficient and strong significance, though the scatterplot showed that there is a need for more data points. Future work will include hundreds to thousands of events, which should alleviate any concerns about statistical significance. Nevertheless, tentative equations relating CME

mass and speed to dimming depth and slope have been established in Equations 5.18 and 5.19. Additionally, we found that the Fe IX 171 Å dimming corrected for the flare contributions using the Fe XV 284 Å line provides the most accurate dimming results for the EVE data. We note that the uncertainties for coronagraph and dimming parameters are complimentary: there are smaller uncertainties for CME speed than dimming slope, and there are smaller uncertainties for dimming depth than CME mass.

Chapter 6

Overview of MinXSS Solar CubeSat

The Miniature X–ray Solar Spectrometer (MinXSS) is a three–unit (3U) CubeSat developed at the Laboratory for Atmospheric and Space Physics at the University of Colorado, Boulder. Over 40 students contributed to the project with professional mentorship and technical contributions from professors in the Aerospace Engineering Sciences Department at University of Colorado, Boulder and from Laboratory for Atmospheric and Space Physics scientists and engineers. I have personally spent over 4600 hours working on MinXSS at the time of this writing. Over the course of the project I've held numerous roles, including project manager, systems engineer, thermal lead, and mentor to the constant influx of new students. Throughout the project, I have contributed in a variety of ways. For example, I was involved in the development of the proposals to NSF and NASA; assembled most of the solar panels for the two spacecraft and all of the flight battery packs for flight and testing; performed the extensive testing of the batteries to qualify them to the NASA human safety standards; designed part of the mechanical structure and several ground support equipment components; did most of the spacecraft assembly; was heavily involved in subsystem and environmental testing, including taking lead on the thermal balance test setup, procedure, and running the actual test; lead the other students through preparation for major reviews; developed and expanded on numerous ground software applications; helped in shaping the ground station automation and data processing architecture, as well as wrote code for many pieces of the data processing pipeline itself; configured the ground station computers; installed a camera on the roof of LASP to monitor the ground station antenna; and delivered the first spacecraft to NanoRacks in

Houston, TX, which included running the final comprehensive performance test and the mechanical installation into the deployer. The list could continue but it is shorter to simply state that I was involved in nearly every aspect of spacecraft development, integration, testing, and preparation for flight.

The scientific objective of MinXSS is to study processes in the dynamic sun, from quiet sun to solar flares, and to further understand how these changes in the sun influence the Earth's atmosphere by providing unique spectral measurements of solar soft x rays (SXRs). The study of solar eruptive events such as solar flares is the thread tying this chapter and the next together with preceding chapters.

The enabling technology providing the advanced solar SXR spectral measurements is the Amptek X123, a commercial off–the–shelf silicon drift detector. The Amptek X123 has a low mass (324 g after modification), modest power consumption (2.50 W), and small volume (6.86 x 9.91 x 2.54 cm), making it ideal for a CubeSat. This chapter provides an overview of the MinXSS mission: the science objectives, subsystems, and lessons learned.

6.1 Brief CubeSat Introduction

CubeSats are now becoming a viable vehicle for scientific measurements in space. As commercial entities, government laboratories, and universities continue to miniaturize the requisite technologies for satellites, the sophistication and size of space–based scientific instruments increases. The University of Colorado, Boulder (CU) and the Laboratory for Atmospheric and Space Physics (LASP), developed the Colorado Student Space Weather Experiment (CSSWE; Li et al. 2012; Gerhardt et al. 2013) three–unit (3U) CubeSat, which launched in 2012 and operated for approximately two years. The science instrument measured high–energy electrons and protons in low Earth orbit (LEO) and has resulted in many peer–reviewed journal articles. The present work builds on this success and takes advantage of new commercially available precision three–axis attitude determination and control to achieve fine target pointing toward the sun. To date, the majority of CubeSats have been technology demonstrations; their goal is to increase the technology readiness level of

new technologies and old technologies that have been miniaturized for use in CubeSats. MinXSS (shown in Figure 6.1) is a CubeSat with science as its primary mission. So this chapter starts with science.

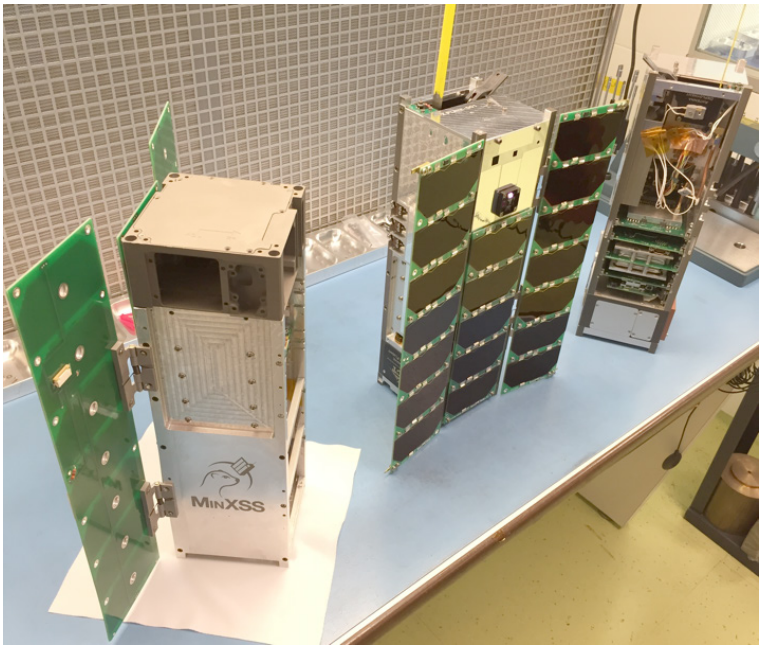

Figure 6.1: Photo of MinXSS family (left to right): prototype unit, flight model (FM)–1, FM–2.

6.2 Science Objectives

There is a rich history of solar SXR spectral observations over the past three decades, but with a significant gap of spectrally resolved measurements in the 0.46 nm range (see Figure 6.2). There were many new discoveries about solar flares during the 1980s using solar SXR spectral measurements from the Department of Defense P78–1, NASA Solar Maximum Mission (SMM), and Japan Aerospace Exploration Agency Hinotori satellites. For example, Doschek (1990) provides results about flare temperatures, electron densities, and elemental abundances for some flares during these missions. A review of flare observations from Yohkoh and the Compton Gamma Ray Observatory (CGRO), for the hard (higher energy) x–ray (HXR) range, is provided in Sterling and Hudson (1997). These earlier missions laid a solid foundation for studies of flare physics and flare

spectral variability that the Reuven Ramaty High–Energy Solar Spectroscopic Imager (RHESSI; Lin et al. 2002) and SDO continue today for the HXR and EUV ranges, respectively. Other missions that have contributed to our understanding of the solar x–ray spectrum, as listed in Figure 6.2, include the Solar and Heliospheric Observatory's (SOHO) Coronal Diagnostic Spectrometer (CDS), Hinode's EUV Imaging Spectrometer (EIS), GSAT–2's Solar X–ray Spectrometer (SOXS) Cadmium–Zinc–Telluride (CZT) and Si detectors, SMM's Bragg Crystal Spectrometer (BCS) and Flat Crystal Spectrometer (FCS), CGRO's Burst and Transient Source Experiment (BATSE), Hinotori's solar Flare Monitor (FLM) and solar Soft X–ray Monitor (HXM), and P78–1's Solar X–rays (SOLEX) and X–ray Monitor (MONEX). With solar flare spectral variability expected to peak near 2 nm (Rodgers et al. 2006), in a range not currently observed by any spectrometer, MinXSS measurements of the solar SXR irradiance will provide a more complete understanding of flare variability in conjunction with measurements from RHESSI and EVE.

There are also nearly four decades of broadband (510 nm wide) SXR measurements not shown in Figure 6.2 because they do not provide spectrally resolved measurements. The very limited spectral information from these broadband measurements cannot quantify the specific spectral energy distribution, nor directly quantify the varying contributions of emission lines (bound–bound) among the thermal radiative recombination (free–bound) and thermal and non–thermal bremsstrahlung (free–free) continua. These broadband measurements include, among others, the two geostationary operational environmental satellite (GOES) x–ray sensor (XRS) channels covering a combined band of 1.625 keV (0.05–0.8 nm) and the even broader band of 0.212 keV (0.1–7 nm) from several missions, including the Yohkoh soft x–ray telescope (1991–2001; Acton et al. 1999), Student Nitric Oxide Experiment (SNOE, 1998–2002; Bailey et al. 2000), Thermosphere–Ionosphere–Mesosphere Energetics and Dynamics (TIMED, 2002–present; Woods et al. 2005a), the Solar Radiation and Climate Experiment (SORCE, 2003–present; Woods et al. 2005b), and SDO (2010–present). Broadband measurements of solar SXRs have helped to resolve an outstanding difference between ionospheric models and measurements, such as the electron density from the Haystack Observatory incoherent scatter radar at Millstone Hill. In particular, the SNOE solar measurements were able to resolve

the factor–of–4 difference between models and measurements because the SNOE data indicated much more SXR irradiance than had been previously thought (Solomon et al. 2001). Additional broadband SXR measurements have been made since then; however, differences still remain in understanding solar SXR spectral distribution and atmospheric photoelectron flux. Although smaller, these discrepancies are still as large as a factor of 2 at some wavelengths, as shown in Figure 6.3; the lack of spectral resolution in the SXR range is thought to be the culprit for most of these disagreements. For example, Peterson et al. (2009) show that discrepancy between photoelectron measurements and models were significantly improved with new EUV spectral measurements down to 6 nm, and we anticipate further improvement with new solar SXR spectral measurements and atmospheric modeling with data from the MinXSS because of its ability to measure all wavelengths in its spectral range simultaneously and with the relatively high spectral resolution of 0.15 keV full–width at half–maximum (FWHM).

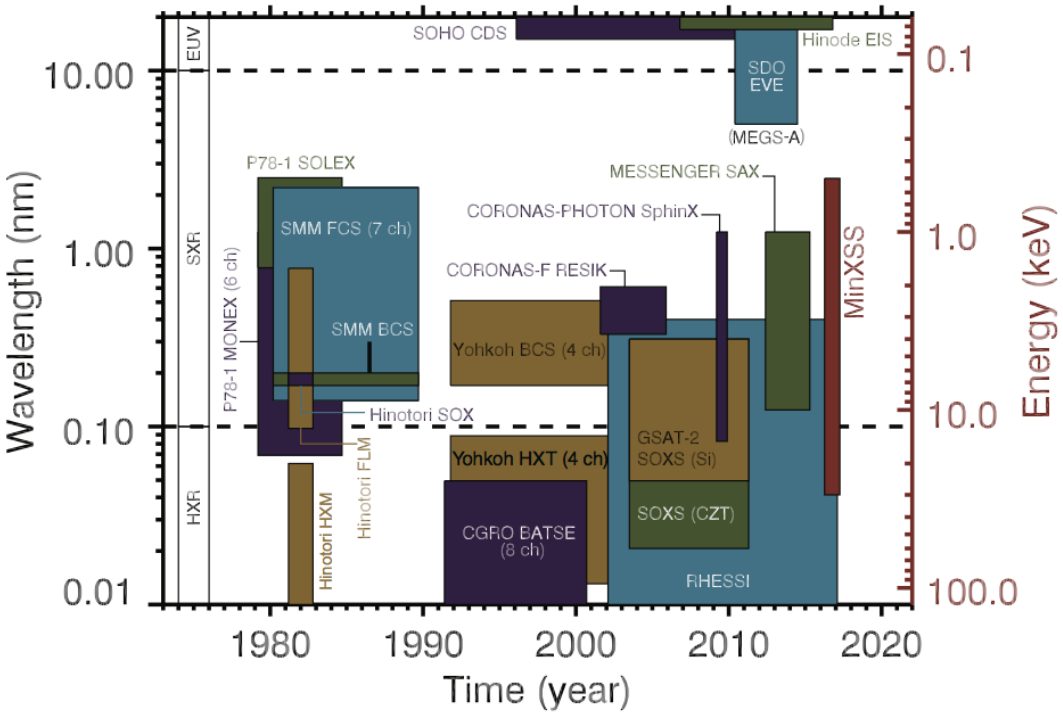

Figure 6.2: History of solar spectral measurements in and near soft x–ray 11 energies (not exhaustive). Figure courtesy of Amir Caspi and Tom Woods.

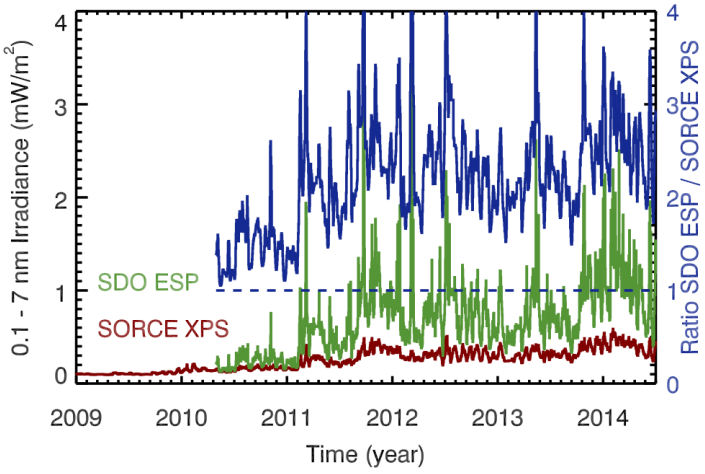

Figure 6.3: Solar 0.17 nm irradiance currently measured by broadband SXR photometers onboard NASA's SORCE and SDO satellites. Figure courtesy of Tom Woods.

6.2.1 Solar Flare Studies

Spectral models of the solar irradiance (e.g., CHIANTI; Dere et al. 1997; Landi et al. 2006) are needed to convert spectrally integrated broadband measurements into irradiance units. Detailed modeling to estimate the SXR spectrum during a flare in April 2002 using a set of broadband measurements from the TIMED Solar EUV Experiment (SEE) was performed by Rodgers et al. (2006). The CHIANTI spectral model is part of their analysis and is also routinely used for processing these broadband measurements (e.g., Woods et al. 2008). Although the CHIANTI spectra are scaled to match the broadband SXR irradiance in data processing, there are significant differences for individual emissions lines between the CHIANTI model and observations, often more than a factor of 2 (Woods and Chamberlin 2009; Caspi and Lin 2010). Furthermore, there are concerns that CHIANTI could be missing many of the very hot coronal emissions lines, especially in the SXR range where there are so few spectral measurements between 0.5 and 6 nm. Additionally, there are factor of 2 differences when comparing the irradiance results from different broadband instruments, which are worst during times of higher solar activity (Figure 6.3). These discrepancies can be partially explained by wavelength–dependent instrument calibrations, but the greater contribution

is likely the lack of knowledge of how this dynamic part of the solar spectrum changes as a function of wavelength and time.

The MinXSS spectrometer, an Amptek X123–SDD, flew on the EVE calibration rocket payload in June 2012, and that measurement had a difference of almost a factor of 8 below 2 nm as compared with the CHIANTI model prediction based on SORCE XPS broadband measurements (Caspi et al. 2015). This rocket result was a surprise considering that the SORCE–based CHIANTI model prediction agreed with SDO/EVE measurements down to 6 nm. Improvement of models of the solar SXR spectra, which is only possible with calibrated spectral measurements of the SXR emission, is critical to properly interpret these broadband measurements. Our goal with MinXSS observations is to reduce these SXR spectral differences from factors of 2 or more down to less than 30%. In addition, the MinXSS will measure solar SXR spectra with higher spectral resolution of 0.15 keV FWHM, as compared with the 0.6 keV FWHM resolution of the most recent analogous instrument, MESSENGER solar assembly for x rays (SAX; Schlemm et al. 2007). The MinXSS measurements will enable improvements to solar spectral models, such as CHIANTI and the Flare Irradiance Spectral Model (FISM; Chamberlin et al. 2007, 2008). By using the MinXSS to improve the FISM predictions in the SXR range, atmospheric studies over the past 30 years will be possible, such as those for the well–studied Halloween 2003 storm period, as well as future space weather events after the MinXSS mission is completed. Getting this spectral distribution of solar flare energy in the SXR range is critical as a driver for atmospheric variations and will be discussed briefly in the next section.

The MinXSS data will also help improve understanding of the physics of solar flares themselves. The 0.5–9 keV (0.13–2.4 nm) range observed by the MinXSS is rich with high–temperature spectral lines from coronal plasma with temperatures from 5 to 50 million K, which are greatly enhanced during even small solar flares. MinXSS will also observe the underlying free–free and free–bound continua, extending out to 20–30 keV, which can provide an independent diagnostic of the emitting plasma temperatures. Understanding how solar flares heat plasma, especially up to many tens of million Kelvin, is a pressing question in solar physics (e.g., Caspi and Lin 2010;

Fletcher et al. 2011; Caspi et al. 2014b), and the MinXSS observations will provide the best spectral measurements in this energy range to date. Observing the variations of spectral lines in comparison with the continuum will also provide insight into coronal elemental abundances, particularly for Mg, Si, Fe, S, and Ar, to help measure abundances and to understand how they may vary with solar activity and during flares.

6.2.2 Topics Beyond Solar Eruptive Events

Quiescent–Sun Studies Examples of data analysis and spectral modeling for two quiescent (non–flaring) solar measurements made with the X123 aboard the EVE calibration rocket flights in 2012 and 2013 are provided in Caspi et al. (2015). One of the tantalizing results from these two 5 min observations is that the coronal abundance of certain elements is different for the quieter SXR spectrum on 2012 June 23 than the more active (but not flaring) sun on 2013 October 21. These abundance differences suggest that different heating mechanisms occur in the quiet network versus active regions and support the concept that numerous small impulsive events ("nanoflares," e.g., Rodgers et al. 2006; Parker 1988) could be the source of the active region heating. Identifying the mechanism responsible for heating the quiet sun corona to millions of degrees, while the photosphere below it is only 6000 K, remains one of the fundamental outstanding problems in solar physics (Klimchuk 2006). We anticipate that one to three months of MinXSS measurements of the solar SXR spectrum will provide adequate data on active region evolution and several flares to more fully address these questions on nanoflare heating. The SXR variability is about a factor of 100–1000 over the solar cycle and can be as much as a factor of 10,000 for the largest X–class flares.

Improvements to Earth Atmospheric Models Energy from SXR radiation is deposited mostly in the ionospheric E region, from 80 to 150 km, but the altitude is strongly dependent on the incident solar SXR spectrum. This wavelength dependence is because of the steep slope and structure of the photoionization cross sections of atmospheric constituents in this wavelength range. The main reason that Earth's atmospheric cross section changes so dramatically in this range is

because of the K edges of O at 0.53 keV (2.3 nm) and of N at 0.4 keV (3.1 nm). The distribution of energy in solar SXRs, even while holding total energy constant, results in peak energy deposition in Earth's atmosphere to change in altitude. The peak energy is near the mesopause but can vary by more than 5 km. This separation is considered significant because it is approximately equal to the scale height at 100 km, it is critical to E–region electrodynamics, and the mesopause (the coldest region of the atmosphere) is a critical transition between the middle and upper atmosphere.

6.3 Mission Architecture

All standard satellite subsystems are present on the MinXSS CubeSat, except for propulsion. Each will be overviewed in the following sections. Figure 6.4 shows the requirements flowdown from the science objectives to the mission level requirements, along with the expected performance of the system on orbit. Figure 6.5 shows the mechanical block diagram, and Appendix B shows the resource break–down of the spacecraft subsystems. Volume is only approximate because many components have nonstandard geometries. The 4800 g mass limit is derived from the interface control document for the NanoRacks CubeSat Deployer. The measurement requirement for range corresponds to the ISO standard definition for SXRs, and MinXSS is only required to make measurements that fall somewhere within this range. The mission expectations listed are for FM–1 (ISS NanoRacks) only. The more conservative standard mass limit for a 3U CubeSat from the California Polytechnic State University CubeSat design specification is 4000 g and would result in a mass margin of 15% for the MinXSS.

6.3.1 Primary Instrument: Amptek X123–SDD

The purpose of the primary MinXSS science instrument is to measure solar spectra within the International Organization for Standardization (ISO) standard SXR range of 0.1–10 nm listed in the requirements flowdown (Figure 6.4). To function within a CubeSat, the instrument must be low mass, low power, and have a small volume. A commercial off–the–shelf solution perfectly met these design requirements. The Amptek X123–SDD weighs 324 g after custom modifications were

Science Objective
Understand solar SXR spectrum and its impact on ITM. Measure solar SXR spectrum and model ITM response.

Measurement Requirements	Predicted Performance
Range: 0.1 - 10 nm (0.12 - 12.4 keV)	0.04 - 3 nm (0.4 - 30 keV)
Resolution: < 1 nm (1.24 keV)	0.4 nm (0.15 keV)
Accuracy: Better than 30%	10%

Mission Level Requirements	Expectation
Altitude: ≤ 700 km	400 km
Inclination: ≥ 35°	52°
Pointing Accuracy: ≤ 2°	0.02°
Pointing Knowledge: ≤ 0.1°	0.02°
Lifetime: ≥ 1 month	5-12 months
Downlink: ≥ 360 kB/day	449 - 600 kB/day

Figure 6.4: High–level requirements flowdown for MinXSS.

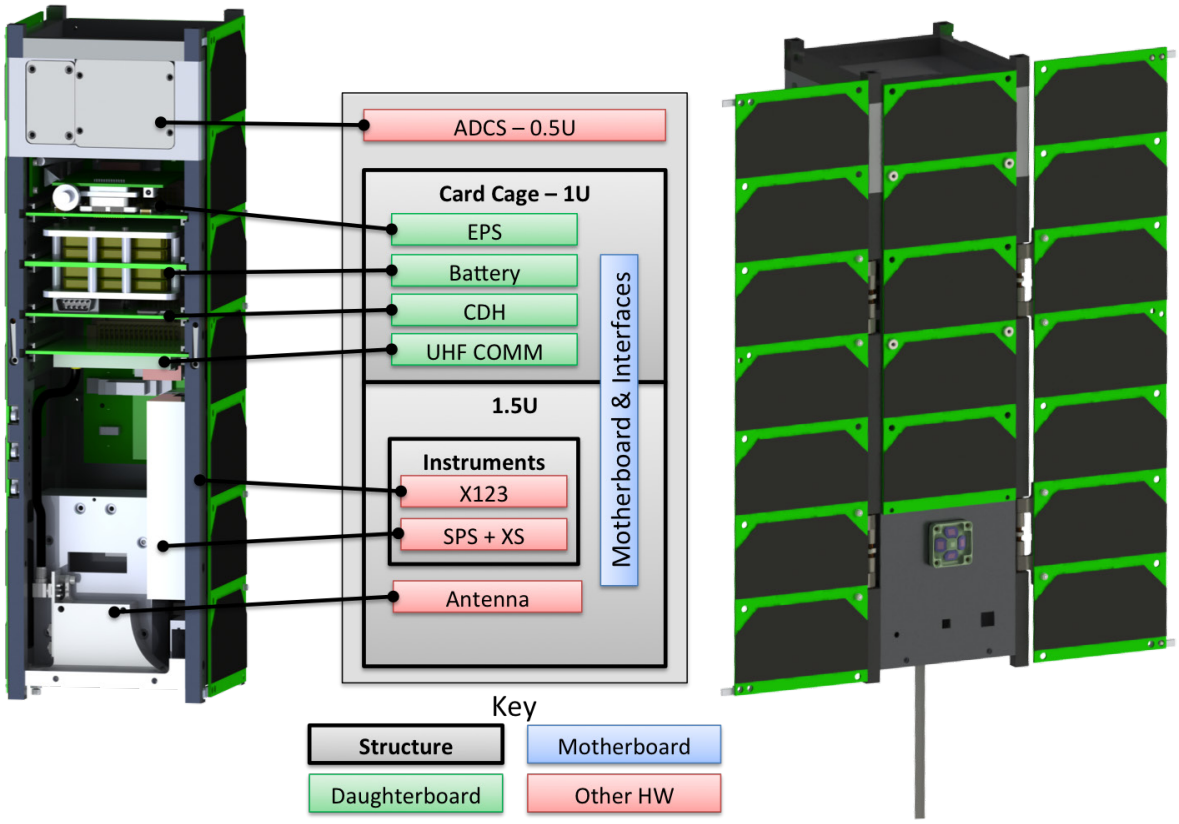

Figure 6.5: MinXSS CubeSat mechanical block diagram.

made for mounting to the CubeSat and thermal foam was added for cooling electrical components in vacuum. It consumes approximately 2.5 W of power nominally, and 5.0 W for approximately 1 min when first powered on. Much of the power draw (including the initial transient) results from the integrated thermoelectric cooler (TEC) reducing the temperature of the SDD to the user–defined set point (–50 °C for the MinXSS). The dimensions of the X123 are also sufficiently small to easily fit within a CubeSat because of the manufacturer's designed purpose as a handheld SXR measurement unit for geological fieldwork. The X123–SDD's 500 m active thickness and 16 m beryllium (Be) entrance window define a spectral range sensitivity of 0.430 keV (0.043 nm), which covers the primary range of interest for scientific studies of 0.52 nm. The instrument includes all the necessary processing electronics, including an integrated multichannel analyzer, to produce a spectrum that is output via an RS232 interface. It can also be commanded programmatically to change numerous parameters, such as integration time and energy thresholds. The custom modifications for spaceflight include staking the larger electronics components, adding a mounting plate for the electronics, adding a custom interface cable and 9–pin connector, adding a tungsten plate with pinhole aperture for the SDD, and providing stainless steel radiation shielding around the aluminum detector vacuum housing.

In October 2014, the MinXSS science instruments, including the X123, were calibrated at the National Institute of Standards and Technology (NIST) Synchrotron Ultraviolet Radiation Facility (SURF; Arp et al. 2011). The synchrotron radiation provides a calibrated continuum emission source, with a radiometric accuracy of 10% in the SXR range. The SURF electron storage ring beam energy is adjustable from 60 to 416 MeV; the synchrotron spectral distribution is dependent on the beam energy, and the MinXSS calibrations use the higher beam energies to maximize the incident SXR flux. The absolute radiometric calibration of the X123, as a function of wavelength, is then obtained by comparing the measured output spectra with the known incident photon flux from the SURF beam; an example, and further description, can be found in Caspi et al. (2015). The narrow spatial extent of the SURF beam in the x–ray range allows for a mechanical determination of the instrument optical axis ("bore–sight") relative to a reference frame, and the uniformity of

response over the instrument's field of view (FOV) is determined using a gimbal system to rotate the detector optical axis about the incident beam. The nonlinearity of the detector electronics is measured by adjusting the intensity of the incident synchrotron flux.

6.3.2 Secondary Instrument: Solar Position Sensor and X–Ray Sensor

The purpose of the secondary instrument is to provide support for scientific analysis of data from the primary instrument. Two sensors are needed to achieve this: one to provide independent high–precision attitude knowledge of the solar position and another to provide an in–flight SXR irradiance reference. Again, these instruments must be low mass, low power, and small volume to be accommodated within a CubeSat platform. MinXSS heavily leveraged instrument heritage from the larger GOES–R EUV x–ray irradiance sensor development at LASP, which already met all of these requirements. The custom–designed application specific integrated circuit (ASIC), in particular, provides the backbone of this exceptionally low–power, low–noise system. A custom mechanical design for the casing was necessary to integrate the subsystem with the MinXSS, which was manufactured for flight using aluminum sintering (3–D) printing.

Figure 6.6 shows an exploded mechanical view of this secondary instrument. The solar position sensor (SPS) is a quad–diode with effective neutral–density–7 filter and 2 mm^2 knife–edge aperture, with an FOV of 4°. The solar visible light falls on the four diodes such that the illumination on each diode depends on the incoming angle of the solar radiation. The resultant measurements are used to compute the sun's position to better than 1 arcmin (3σ) as described in Chamberlin et al. (2009). These data are sent to the attitude determination and control system (ADCS) for inclusion in the fine–attitude control solution and telemetered to the ground for use in science processing. The x–ray sensor (XS) is a single diode with two Be foil filters, whose total 16 μm thickness is matched to the X123 to define a response over the same 0.04–3 nm wavelength range. XS has a 5.0 mm diameter knife–edge aperture and an FOV of 4°. The diode operates in photocurrent mode, integrating the total SXR flux over its band–pass and integration period; this provides a measurement that can be compared with the integrated X123 spectrum, to within

measurement and calibration uncertainties. These data are also telemetered to the ground for use in science data processing.

The SPS and XS were also calibrated at SURF. The SPS optical axis and the transfer equation relating off–axis position to quad–diode output were determined using the gimbal system to rotate the optical axis around the incident SURF beam. The XS optical axis and uniformity of response over its FOV were similarly determined. The absolute radiometric response of the XS was determined similarly to the X123, comparing the known incident synchrotron photon flux with the output from the photodiode. (No absolute calibration was necessary for the SPS.) The SPS and XS system, including ASIC, had been previously measured to be highly linear through testing during GOES–R development, and so the MinXSS calibrations omitted nonlinearity testing.

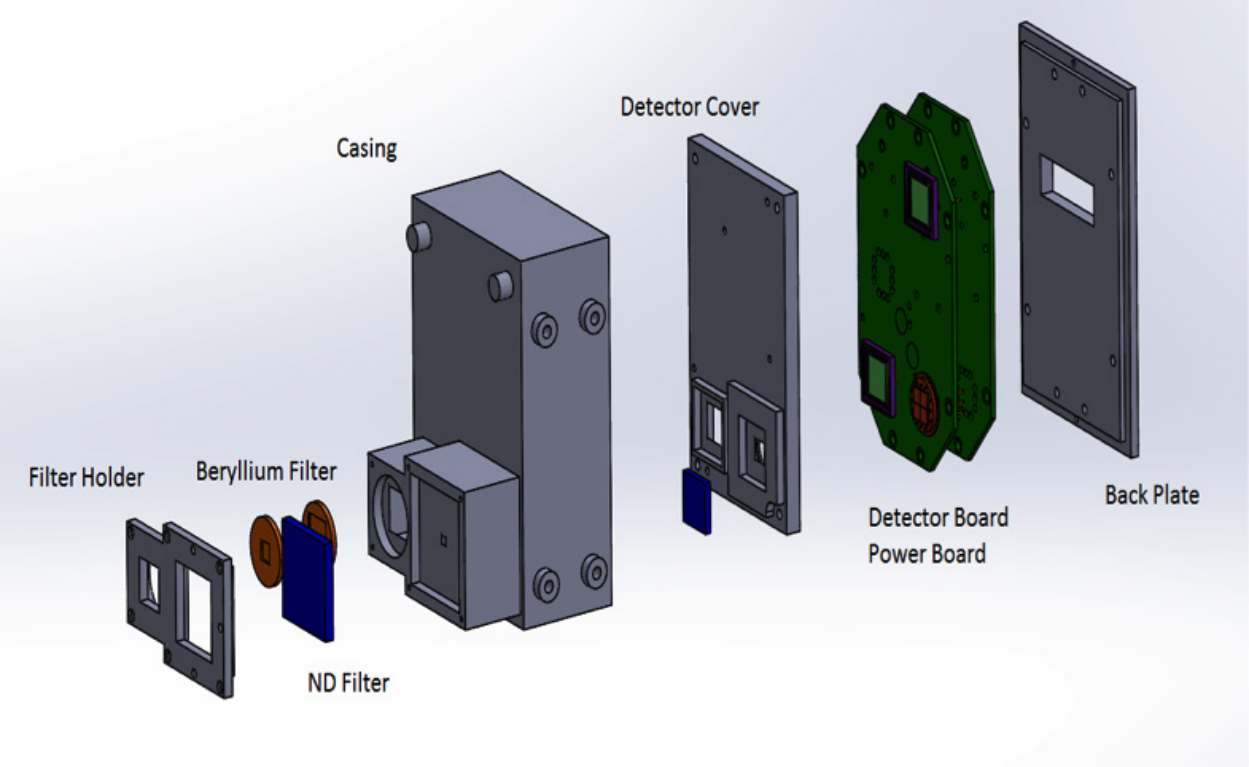

Figure 6.6: Solar position sensor and x–ray sensor (SPS and XS) exploded view. Figure courtesy of Siddhesh Naik.

6.3.3 CDH and Flight Software

The core of the MinXSS CDH subsystem is a low–power Microchip dsPIC33 Microcontroller Unit (MC dsPIC33EP512MU810). The CDH communicates with and controls the X123 instrument, UHF communications, and ADCS via RS232, monitors voltages, currents, and temperatures via I2C for the motherboard, CDH, communications, EPS, and SPS and XS, and reads detector data from the SPS and XS ASIC via digital input/output. Additionally, the CDH handles all incoming commands, housekeeping monitoring, data manipulation for downlinking data packets, power switching of subsystems, and configuration of the operation modes. Most of the CDH operation is configurable via uplinked command, and several of these CDH processes are autonomous for maintaining a safe power configuration. Data are stored on a 4 GB secure digital (SD) memory card, and each type of data packet has its own dedicated circular buffer on the SD card. This SD card can store more than 1400 days (3.8 years) of science, housekeeping, and log message data packets, and 48 h of ADCS high–rate data packets. The dsPIC33 internal real–time clock (RTC) and an external RTC integrated circuit (IC) provide precise time knowledge. The external RTC IC also has an electrically erasable programmable read–only memory for storing startup configuration parameters, which can be modified via uplinked commands. The dsPIC33 watchdog timer is used to initiate a reset of the system in case it becomes unresponsive, and a reset command can also be sent from the ground. The MinXSS FM–1 one year mission worst–case radiation dose estimate is 2.6 krad, with a minimum shielding of 2 mm of Al provided by the CubeSat structure. Two of the prototype CDH boards successfully passed radiation tests of 10 krad and 25 krad.

The embedded flight software is built on a Slot Real–Time Operating System (RTOS), written in C, as originally developed at LASP for the EVE rocket experiment. The key elements of the software design are robustness and simplicity, with the health and safety of the satellite as top priority. Because many of the tasks performed by the CDH are not time sensitive and can be handled at any time in the slot process, the real–time demands on the CDH and flight software are very low. The RTOS uses the dsPIC33 timer with 1 ms resolution for execution of tasks, but most

monitoring by the CDH has a cadence of 1 s or slower.

6.3.4 Electrical Power System, Battery, and Solar Panels

The MinXSS EPS is largely based on heritage from the successful CSSWE direct energy transfer (DET) design. The EPS uses high–efficiency buck converters for power regulation to 3.3 and 5.0 V and a simple battery charging logic for use with Li–polymer batteries. Minor design modifications were incorporated to accommodate the higher power generation and consumption on the MinXSS as compared with CSSWE, as well as more voltage and current monitors. Two additional major differences were implemented: pseudo–peak power tracking (see Section 6.4.4) and additional switches to prevent the system being powered before deployment to comply with NanoRacks ISS human safety standards.

The battery pack consists of four SparkFun 2–Ah Li–polymer batteries, configured as two parallel sets of two batteries in series to provide a 6–8.4 V unregulated 4–Ah bus; two temperature sensors, and two heaters, which are sandwiched between the batteries. Heat transfer tape was used between each layer of the battery pack to achieve a homogenous temperature distribution during flight. The PCB in the middle of the pack does not have a copper plane in its center as all other daughterboards do, the intent being to thermally isolate the batteries from the rest of the system. This was a part of the passive thermal design to create a battery–dedicated thermal zone, because the batteries have the narrowest operating temperature range of all components in the system. Finally, the pack was encapsulated with aluminum plates on standoffs, providing sufficient volume for the batteries to expand under vacuum and thermal cycling. Arathane 5753 with Cabosil glass beads was placed between the batteries and these encapsulation elements to act as a soft bumper to expanding batteries.

MinXSS uses 19 triple–junction GaAs, 30% efficient solar cells from Azur Space Solar Power, GmbH. One five–cell solar panel is fixed to the body of the CubeSat on the solar–oriented side, and two seven–cell solar panels will deploy by command to have the same solar orientation as the body–fixed panel. Because MinXSS is a sun–pointed spacecraft, these solar panels can nominally supply

22 W at end–of–life during the orbit insolation period. A 100 hour mission simulation test with the fully integrated spacecraft connected to a solar array simulator under various eclipse periods was performed to verify that there is adequate margin for operating all of the MinXSS subsystems and for charging the battery (see Section6.4.5). Additionally, flight software incorporated the ability to autonomously power off the X123 (the largest power consuming subsystem) and the other non–critical subsystems during eclipse if there are any battery power issues for eclipse operations. The power–cycling flags can be enabled via command, but we do not anticipate the need for their use.

6.3.5 Communications

MinXSS leveraged heritage from the CSSWE CubeSat by using the same radio and ground station for UHF communications. The ground station is located on the roof of the LASP Space Technology Research Building in Boulder. It consists of a pair of M2 436CP42 cross Yagi antennas, each with a gain of 17 dB_{dc} and a circular beamwidth of 21°. A Yaesu G5500 azimuth–elevation rotator controlled by SatPC32 points the antenna system. SatPC32 also accounts for Doppler shifts via its control of the ground radio, a Kenwood TS–200. The antennas and motors are mounted on an 2.4 m tower and are connected to the electronics in the control room below by 60 m low–loss cabling, which accrues 5.4 dBm of RF signal loss. The flight radio is an Astronautical Development, LLC Lithium–1 radio that operates in the UHF band at 437 MHz. Additionally, the antenna is nearly identical to that used on CSSWE, which is a deployable spring steel tape measure with a length of 47.6 cm. The gain pattern was measured using the MinXSS prototype in an anechoic chamber at First RF Corporation in Boulder, Colorado. The measurements were compared with a FEKO model and propagated through Satellite Tool Kit to estimate the expected daily average downlink data capacity: 600 $kB\ day^{--1}$ using the FEKO model or 449 $kB\ day^{--1}$ using the measurements. These estimates are not highly precise because of the limited fidelity of the model and the prototype structure, but provide an idea of what to expect. The requirement of at least 360 $kB\ day^{--1}$ appears to be easily satisfied.

6.3.6 Attitude Determination and Control System

To provide a stable view of the sun for the science observations and to maintain appropriate antenna orientation during ground contacts, MinXSS has an active ADCS. With the wide field of view of the X123 (4°), the pointing requirements for MinXSS are only $2°(3\sigma)$ accuracy and $0.1°(3\sigma)$ knowledge.

The commercial CubeSat ADCS onboard the MinXSS is a flexible ADCS CubeSat technology (XACT) from Blue Canyon Technologies (BCT). BCT has developed a 0.5 U–sized ADCS unit (0.85 kg) using miniature reaction wheels, torque rods, a star tracker, a coarse sun sensor, inertial measurement units, and magnetometers. The BCT XACT is expected to provide pointing accuracy and knowledge of better than $0.003°(1\sigma)$ in two axes, corresponding to the plane of sky of the star tracker, and $0.007°(1\sigma)$ in the third axis, parallel to the star tracker optical axis. The XACT interface uses 5 and 12 V power inputs (1.0 W nominal, 2.8 W peak) and serial communication (RS232 for the MinXSS, but other options are available). SPS provides two–axis (pitch/yaw) pointing knowledge on the sun to better than 1 arcmin (3σ), which can be sent to the XACT for closed–loop fine–sun pointing; however, the XACT system can easily meet the MinXSS pointing requirements without this additional knowledge.

After integration with MinXSS, multiple tests were performed to verify functionality and performance of the ADCS. A custom air–bearing table was built to provide a relatively torque–free environment for the ADCS to control the spacecraft. For example, we verified that the spacecraft can track the sun with a heliostat at LASP, that magnetometers reversed sign when the spacecraft was rotated 180° in each axis, that torque rods produced a measurable magnetic field, and that the star tracker took interpretable images and found matches to stars in its library when observing the night sky.

Figure 6.7: Prototype CubeSat card cage design. Figure courtesy of Tom Woods.

6.4 Advancing CubeSat Technologies and Lessons Learned

6.4.1 CubeSat Card Cage

Experience with the PC104 PCB interface on the CSSWE CubeSat led the MinXSS team away from the card stack design because of the difficulty in debugging boards once integrated. Instead, the CubeSat card cage design uses a motherboard/daughterboard architecture that allows any individual card to be easily removed, and an extender board optionally inserted to have access to the daughterboard for probing while still electrically connected (Figure 6.7). Additionally, the standard electrical interface allows boards to be swapped to any position. MinXSS uses a DIN 48–pin connector for the daughterboardmotherboard interface. This relatively large connector was chosen for ease of soldering for new engineering students and because it easily satisfied the requirements on the number of necessary pins and mechanical dimensions. In the future, a higher density connector with potentially more pins could be chosen to provide a lower mass and lower volume solution while still providing the flexibility of the card cage architecture.

6.4.2 3–D Printed Parts

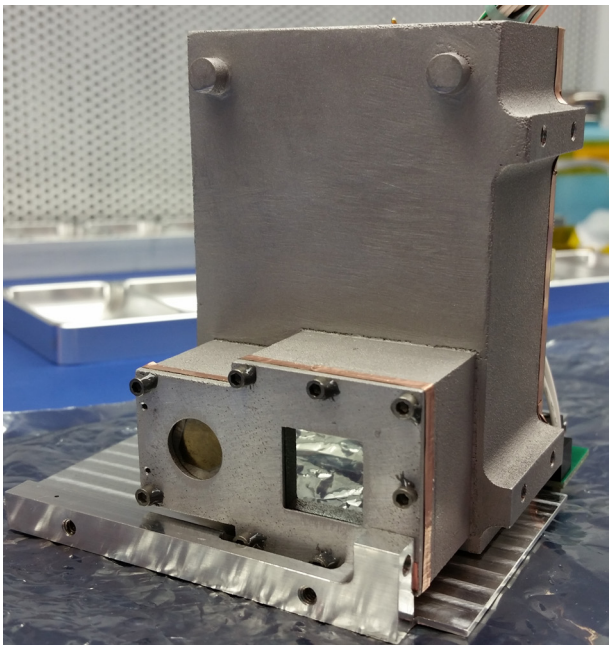

Figure 6.8: Aluminum 3–D printed SPS and XS housing after sanding and integration.

The MinXSS project used 3–D printed parts for both prototyping and flight components. For prototyping, the SPS and XS housing was 3–D printed in plastic twice as the design iterated, and the solar array hinges were printed in plastic once. This was done using CU's Objet 30 printer with VeroWhitePlus plastic. For flight, these same components were 3–D printed in metal using direct metal laser sintering at GPI Prototype. The SPS and XS housing is aluminum with a shot–blasted finish (Figure 6.8). This finish was very rough and required significant sanding to get an acceptable surface finish and clean edges. The solar array hinges are stainless steel with a shot–blasted finish (Figure 6.9). A minimal amount of sanding was required for these parts because the requirements were looser and the finish was slightly better than SPS and XS. The better finish was likely because of the hinges being a simpler part that required no filler material during the 3–D print (sintering) process.

As plastic 3–D printers become more pervasive, affordable, and precise, the draw toward using the resultant parts for flight is becoming stronger. A major risk that must be addressed

is the unknown properties of these materials, particularly in their response to vacuum and UV exposure. We would like to see an open database where specifications based on test results for common 3–D print materials, such as ABS and PLA, could be accessed.

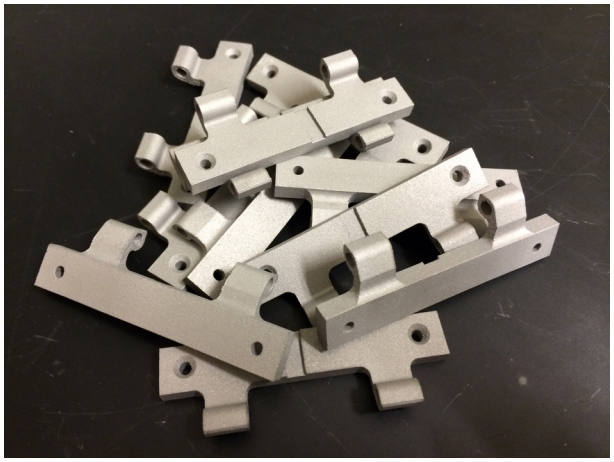

Figure 6.9: Stainless steel 3–D printed solar array hinges as delivered from vendor.

6.4.3 Simplification of Solar Panel Fabrication Process

CSSWE used epoxy (Arathane 5753) on the back of solar cells to adhere them to the solar panel PCBs. This technique is typical but requires significant assembly and curing time. MinXSS used double–sided Kapton tape with acrylic adhesive to adhere solar cells to the PCBs. We used a specialized rubber vacuum sealer to apply pressure to the cells uniformly and meet the manufacturer's recommended application pressure. This reduced the time to produce a solar panel from three days to one day. To get electrical conductivity from the back of the solar cell to the PCB, we applied silver epoxy in large vias behind each cell. We also tested a new–to–market tape: 3M Z–axis tape. This tape is electrically conductive between the adhesive and backside and could save the extra step of applying the silver epoxy or soldering/welding on tabs. For flight, Kapton tape was used because 1) the Z–axis tape adhesive was not rated for as wide a temperature range as the Kapton acrylic adhesive, 2) there was concern that the Z–axis tape could not sustain the high current of the solar cells for as long as solder or silver epoxy could, and 3) the Z–axis tape thermal

conductivity properties were not specified in the datasheet. In the future, we would like to see solar cell manufacturers adopt a standard form factor compatible with CubeSats. MinXSS uses 40 x 80 mm cells from Azur Space (Figure 6.10), which are a great fit within the rail boundaries of CubeSats (maximum of 83 mm wide and 340.5 mm long for 3U CubeSat). The 80 mm width for cells provides a 1.5 mm margin on each side from the rails. If the spacing between cells could be reduced to 4.5 mm or less, then there could be eight Azur Space solar cells instead of seven on a 3U panel. Alternatively, if the height of the cells were changed to be 50 mm instead of 40 mm, then they would be more modular for fitting one solar cell per 0.5U of the panel length. With six 50 x 80 mm cells instead of seven 40 x 80 mm cells, there could be 7% more power per 3U panel.

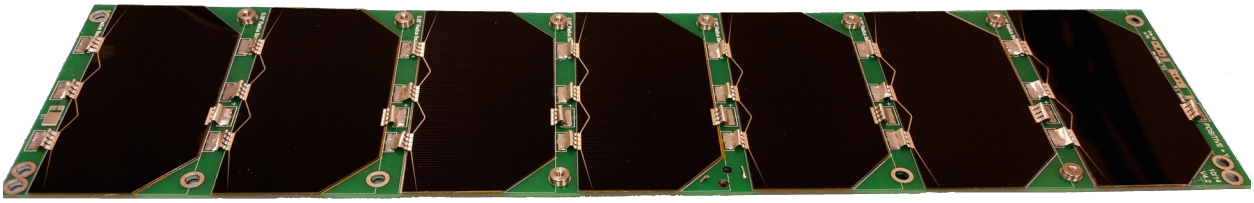

Figure 6.10: Populated seven–cell deployable solar array for MinXSS FM–1.

6.4.4 Pseudo–Peak Power Tracking

A modified DET EPS design was implemented on MinXSS that was inherited from the CSSWE CubeSat to include an additional specially selected resistor to create a pseudo–peak power tracking (PPPT) system. The extra resistor was chosen to prevent a rapid voltage drop from the solar cells when the battery attempts to draw a large current, namely, when the battery state of charge is relatively low right as the spacecraft exits the orbit eclipse.

In the CSSWE and MinXSS EPS design, the output of the solar panels power 8.6 V regulators that then provide regulated 8.5 V power directly to the battery and system. In this DET design, the batteries will charge up to 8.5 V, and there are no supporting electronics required to control the battery charging process. In reality, this simple approach only provides about 50% of the power intended from the solar panels when the battery capacity is low. In particular, when the battery

needs more power input (high current) for charging, the high current draw from the solar cells results in much lower voltage, following the standard solar cell current–voltage I–V curve. When the solar panel output voltage goes below the minimum input voltage level of the 8.6 V regulator, the regulator turns off. Consequently, the current drops and the solar panel output voltage increases, and the 8.6 V regulator turns back on. This results in a high–frequency on–off regulator oscillation that had the EPS 8.6 V regulators on for only about 50% of the time during the early part of the orbit dayside during mission simulations. The MinXSS solar panels were designed for 80% of peak efficiency at EOL, but the 50% decrease in power was an unacceptable power loss for the nominal power budget.

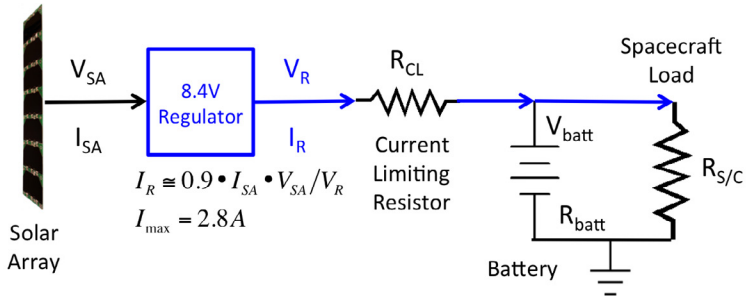

Figure 6.11: Simplified circuit diagram of PPPT for MinXSS EPS. Figure courtesy of Tom Woods.

The solution for MinXSS, without having to redesign or rebuild the EPS board, was to replace the sense resistor on the output of the solar panel regulator with a larger resistance so that the effective current draw out of the solar panel would be limited and thus would not cause the regulator to turn off. We refer to this current–limiting resistor for the solar panels as PPPT. Figure 6.11 shows a simplified version of the PPPT circuit for the MinXSS EPS. The value for this current–limiting resistor was estimated for the MinXSS power configuration using Equation 6.1.

$$I_{Reg} = \frac{V_{Reg} - -I_{max}R_{CL}}{R_{S/C}} + \frac{V_{Reg} - -I_{max}R_{CL} - -V_{Batt}}{R_{CL} + R_{Batt}} \tag{6.1}$$

where I_{Reg} is the current output from the regulating buck converter, V_{Reg} is the corresponding voltage, I_{max} is the maximum current from the solar panel, R_{CL} is the resistance of the current–

limiting resistor for pseudo–peak power tracking, $R_{S/C}$ is the spacecraft load, V_{Batt} is the voltage of the battery pack, and R_{Batt} is the resistance of the battery pack.

The first term on the right–hand side of Equation 6.1 is the current for the spacecraft load, and the second term is the current for charging the battery. The spacecraft load is assumed to be constant, but the battery charging current starts off high when the battery voltage is low and then ramps down to zero when the battery voltage is the same as the regulator voltage downstream of the current–limiting resistor. The ideal value for the current–limiting resistor R_{CL} is such that it limits the current out of the regulator I_{Reg} to be less than the maximum current I_{max} possible from the regulator (at the peak power part of the solar panel I–V curve) and when the battery voltage V_{batt} is at the lowest allowed level. For MinXSS design and configuration, the regulator voltage V_{Reg} is 8.5 V, the worst–case system load (largest power) has 7.0 Ω for R_{SC}, a battery impedance of 0.125 Ω, and a value of 2.8 A for I_{max}. The goal for MinXSS was to keep the battery voltage above 7.1 V at all times, and so an R_{CL} of 0.25 Ω is the desired value for the MinXSS configuration to satisfy Equation 6.1. That is, with this value of R_{CL}, I_{Reg} equals I_{max} when V_{batt} equals 7.1 V. After the current–limiting resistor was installed into the EPS, additional mission simulations were run. We verified that the prediction of the regulator current I_{Reg} and the measured battery voltage agreed with the measured regulator current.

One disadvantage to the PPPT implementation is that there is additional heating of the EPS board because of the larger resistance; however, this extra heating peaks right after exiting eclipse, the precise time when temperatures are cooler and heating is desired anyway. For example, the power loss (heating) in the PPPT current–limiting resistor is estimated to be 2.6 W when the battery voltage is at its lowest value of 7.1 V, decreasing to 0.93 W when the battery voltage is at 7.5 V, and reduces to less than 0.1 W once the battery voltage is above 8.0 V. The primary caveat in the PPPT design is that resistor tuning must be done a priori, and is fixed, whereas maximum PPT (MPPT) systems can tune resistance in real time to maintain the maximum power point on the solar cell I–V curve. The trade studies performed for CSSWE and MinXSS resulted in the selection of a custom DET EPS because of the simplicity of design. Both teams were unaware of

the consequential loss of power generation at the time of the original designs. The advantage of the PPPT circuit is that it is only minimally more complex than DET, adding little risk for a large benefit.

In the future, we would like to see a standard MPPT IC for interfacing to common CubeSat battery packs (e.g., 8.4 V Li–polymer battery packs). We found it difficult to identify a commercial MPPT IC or proven MPPT circuit that could be integrated with our system. We purchased the most promising MPPT IC, a Linear Technology LT3652, and spent significant time attempting to integrate it with the MinXSS EPS, but its intended use prevented proper functioning for our solar panel and battery configuration.

6.4.5 Importance of Flight Like Testing

Various tests were performed on MinXSS that were geared toward simulating the orbital environment and flight–like operations. These included low–external–torque tests of the ADCS, thermal vacuum with a long–duration mission simulation, early orbit end–to–end communication testing performed several miles away from the ground station, and detailed battery characterization of the actual batteries to be flown.

Using a custom–built air–bearing table, we tested the functionality and performance of the ADCS. This test simulated an orbital environment with reduced external torques present. Through this testing, we discovered that an operational amplifier (op–amp) was preventing the XACT coarse sun sensor from being properly read by its internal flight software, and this op–amp was replaced to resolve this issue. It is unlikely this would have been discovered otherwise and may have resulted in the spacecraft not being able to quickly find or accurately track the sun while on orbit. Significant effort in mission operations may have been able to salvage the mission in that situation, but only minor effort was required to replace the offending op–amp. Air–bearing testing requires very careful balancing of the system and as much reduction of external torques as possible (e.g., even airflow from building ventilation could limit the tracking duration while operating on the air–bearing table). It also requires the computation of moments of inertia specific to the air–bearing CubeSat

system to be provided to the ADCS for appropriate control to be implemented. Without such an update to the ADCS software, the ADCS response is too sluggish (slow) to confirm that the ADCS is tracking as expected.

Thermal vacuum tests are irreplaceable for determining if the CubeSat can function in vacuum and for measuring performance near the operational limits of components. Through such testing of MinXSS, we discovered a short in a battery heater that reset the entire system every few seconds, which only manifested under vacuum. This was caused by the battery expansion, which created an unintended electrical connection between the two nodes of the heater. Typically, CubeSats are only required to bake out, not perform a functional thermal vacuum test, but we highly recommend this test as a process to increase the success rate of CubeSats.

A 100 hour mission simulation test was performed on MinXSS during four of the eight hotcold cycles of the thermal vacuum testing. A solar array simulator, with an I–V curve programmed to model the Azur Space solar cells used on the MinXSS, was jumpered into the MinXSS EPS board. The jumper bypassed the two deployable solar panels. The output of the solar array simulator was programmatically cycled in intervals corresponding to ISS orbit insolation/eclipse periods at three different β angles. The total orbit period was 93 min and the three eclipse periods were 28 min (average β), 38 min ($\beta = 0°$), and 0 min ($\beta > 76°$). Power performance data were collected for the entire system throughout each of these scenarios and verified that the PPPT maintained a power positive state through many orbits. Additionally, this test was used to verify the functionality of a flight software commandable flag to disable power to the X123 during eclipse periods. This option was introduced into the flight software early in the project in anticipation of a marginal power balance. The X123 was chosen for power cycling because it is the largest consumer of power and because the primary science target (the sun) is not visible in eclipse. However, this is not the default state in the mission design because it introduces excessive power cycling on the primary science instrument; nominal operations leave the X123 powered on during the entire orbit. As the spacecraft performance degrades on orbit (e.g., solar cell efficiency loss), it may become necessary to enable the X123–eclipse–power–cycling flag. Finally, the 100 hour mission simulation test included

periodic stored–data downlinking with durations equivalent to the ground station contacts expected on orbit. The 100 hour mission simulation test was the most flight–like testing possible with the facilities available and greatly increased confidence in and understanding of the system as it will behave on orbit. It also ensured that the flight electronics are likely past the "infant mortality" phase.

End–to–end testing was also performed on the MinXSS to verify functionality of the full communication pipeline. The spacecraft was taken several miles away to a position in the line–of–sight of the ground station, and early orbit commissioning tests were performed. This boosted confidence in several areas: that we would meet the NanoRacks requirement of not deploying the MinXSS antenna or solar arrays in the first 30 min after deployment from the ISS, that those deployments would be successful, that communications could be established after antenna deployment, and that our ground software commissioning scripts could autonomously perform telemetry verification and commanding.

Significant battery testing was performed to comply with requirements flowed down from NASA Johnson Space Center through NanoRacks to all CubeSats going to the ISS. These requirements are in place to protect astronauts on the ISS and far exceed the standard CubeSat requirements in the California Polytechnic State University CubeSat Design Specification. Nevertheless, we recommend that all CubeSats perform several of these tests, if only to better understand the actual batteries to be flown (i.e., not just batteries from the same lot or of the same type). We found the following to be the most useful tests: visual inspection for dents or leaks, measuring the open circuit voltage of the fully configured battery pack, recording voltage, current, and temperature through three charge/discharge cycles; measuring the voltages at which overcharge and overdischarge protection activated and deactivated; and measuring mass before and after undergoing vacuum. Given availability of the equipment to perform these tests and measurements, it took approximately two weeks to complete this testing for each battery pack. Much of that time was dedicated to setup, waiting for charge cycles to complete, and interpretation of the results. Additional tests were required for astronaut safety on the ISS, but we would consider them to be

extraneous for non–ISS CubeSat missions. These include measuring of the physical dimensions of each battery, measuring the closed circuit voltage of the fully configured battery pack, measuring the time to trigger short–circuit protection and maintaining the short for 3 hours to verify the protection remains enabled; and doing a dedicated vibration test at five frequencies and strengths up to 9.65 g_{rms} on all three axes, with voltage measurements between each axis. These additional tests took several weeks of additional time and planning, particularly in the design, manufacturing, and modification of components to support vibration testing.

6.4.6 Importance of a Second CubeSat Unit

The fabrication of two identical sets of hardware in parallel is much less expensive than the same development in series, particularly if the start of the development for the second set is delayed by months or years. Small projects tend to have less stringent requirements on documentation, and so details can be forgotten and lost in the time between two sets of flight hardware developed in series. Having two sets of hardware enables the development and testing of flight software, while other activities proceed in parallel. It is important to note that parallel development also enables the replacement of a subsystem if a problem is found, which is critical when schedules are tight. This was the case for the MinXSS when the battery heater short was discovered in FM–1 at the initial pump down for its thermal vacuum test. We were delayed half a day to swap the battery pack out with FM–2, which did not have the same issue, as compared with the weeks of delay that would have been introduced if an entirely new battery pack had to be assembled and tested. Finally, having a second flight unit allows for debugging of hardware and software after delivery and launch of the first flight unit.

6.4.7 Low–Cost Mitigation of Radiation Issues for Electronics

The CubeSats developed at CU and LASP have generally used industrial–grade (automobile) electronic parts because those parts have wider operating temperature ranges. Typically, the automobile–grade ICs cost $ 10 as compared with $ 2 for standard commercial ICs, but this addi-

tional cost is outweighed by the significant benefits of the higher–grade components. For example, the number of uncorrupted SD card write cycles can be improved by a factor of 10100, and the operational temperature range can be expanded by purchasing a $ 70 4 GB hardened SD card instead of a $ 4 standard SD card. The total cost impact on the MinXSS for these industrial–grade electronics parts is only a few thousand dollars, a small fraction of the total budget, but it significantly improves the potential for a longer mission life. Although our intention was to have electronics that could operate over a wider temperature range, automobile–grade parts may also help with radiation tolerance of the electronics. Two MinXSS prototype CDH boards were radiation tested, one to 10 krad and another to 25 krad; both boards survived. It is not clear if industrial–grade parts made a difference or not for passing the harder radiation test; nonetheless, it is only a small cost increment to use the higher–grade parts.

6.5 Summary

CubeSat technologies and capabilities are now sufficiently mature to enable peer–review journal–quality science missions. This was clearly proven with the CSSWE CubeSat, which has 17 such articles to date (Li et al. 2012; Gerhardt et al. 2013; Li et al. 2013b,a, 2015; Baker et al. 2014; Jaynes et al. 2014; Schiller et al. 2014a,b; Blum et al. 2013; Blum and Schiller 2012; Kohnert et al. 2011; Palo et al. 2010; Schiller and Mahendrakumar 2010; Gerhardt 2010; Gerhardt and Palo 2016a,b). Leveraging that success and the recent development of a commercially available, precision three–axis ADCS, MinXSS will push the boundary of what science is possible with a CubeSat further still. The primary science objective of MinXSS is to fill a critical spectral gap in solar measurements currently made by large satellite missions at one hundredth their typical cost. All standard satellite subsystems are present in the MinXSS, except propulsion, packaged in a volume that can fit in a breadbox. Many of these subsystems were custom developed by CU and LASP (e.g., CDH, EPS, SPS, and XS, structure), primarily by graduate students with professional mentorship; and other subsystems were purchased from commercial vendors (e.g., flight radio, ADCS, primary science instrument).

Chapter 7

Detailed Thermal Modeling for a CubeSat

The purpose of thermal modeling for a spacecraft is to ensure that all components will stay within their operational and survival temperature limits while on orbit. That includes the science instruments, which often require very low temperatures and thermal stability. Thus, science instruments are often the drivers of thermal design when they are the most restrictive element. This was the case for the MinXSS CubeSat, whose primary science instrument, the X123, must keep its detector at -50 °C. The commercial X123 ships with an integrated thermal electric cooler (TEC) to achieve this, but its heat sink must be kept below +35 °C. This work is not direct modeling or analysis of solar eruptive events, but is instead in support of a mission that will do so. It is included here because it has been an important aspect of my training as an aerospace engineer, because the forward-modeling technique is applicable to science as well as engineering, and because it provides assurance that the solar eruptive events observed by the X123 onboard MinXSS won't be lost to noise.

Thermal modeling is ultimately an accounting of heat transfer throughout a system. As such, the first section of this chapter will describe the basic processes by which heat transfer occurs, namely, conduction, convection, and radiation. Radiation is of particular importance for spacecraft because it is the only means of heat escape from the system, so additional detail is provided. Section 7.2 covers the test environments and procedures for thermal vacuum and thermal balance testing. Section 7.3 goes into more mechanical detail of MinXSS than was provided in Chapter 6 because nuances such as material type, coatings, and mechanical interfaces are more pertinent

here. The model itself is then described in Section 7.4, including the constituents of the spacecraft model and the model environments it is placed in. Section 7.5 contains the critical comparison of model predictions to test measurements. Only the results after significant fine-tuning of the model are presented but the iterative, forward-modeling process is described. Finally, Section 7.6 makes predictions for the spacecraft on orbit. At the time of this writing, MinXSS Flight Model-1 (FM-1) has not yet been deployed from the International Space Station, so a comparison to actual temperatures cannot be done but will be compared at a later time, and those results should be published in a peer-review journal.

7.1 Fundamentals of Thermodynamics

The three basic ways for heat to propagate are conduction, convection, and radiation. Conduction occurs when there is physical contact between two objects such that the particles at the interface can interact with each other, resulting in an energy transfer. The temperature is a measure of an object's internal energy. The motion of particles within an object is limited in solid objects by either a lattice structure or the density of particles. Heat transfer occurs when there is a temperature gradient across the mechanical interface of two objects. In the warmer object, the particles have greater energy on average and they transfer some of that "excess" energy to the particles of the colder object. Thus, the warmer object cools and the vice versa. The efficiency of this heat transfer increases with greater temperature gradients.

Convection is the transfer of heat between objects through a fluid/gaseous[1] medium. The microscopic description is similar to conduction, only the particle energy exchange occurs between the object and the fluid medium. The fluid itself often has bulk motion that can then carry the newly absorbed heat away, sometimes to another interface where additional heat transfer can occur. Recall Chapter 2's description of the solar convection zone – the region of the sun where the dominant form of heat transfer is the absorption of heat from the top of the radiative zone where it

[1] The mathematics that describe fluid motion also apply to gases so physical descriptions often refer to both as fluid

is then carried by bulk plasma motion to the photosphere. Once launched to space, satellites exist in vacuum where there is insufficient fluid (air) to transfer heat, with the exception of pressure vessels that are often used to store propellants or coolants. The MinXSS CubeSat has no such chambers so convection can be safely ignored as a heat transfer mechanism for its thermal modeling.

Finally, radiation is heat transfer that requires no physical contact or transfer medium. Heat is instead propagated by photons emitted by one object and absorbed by another. In engineering modeling, radiation is inherently treated as a non-local thermodynamic equilibrium process (see the LTE/non-LTE discussion of Chapter 2), though it is simplified by not tracking remote heat sources/sinks. Two additional simplifications are typically made: the reduction of emissivity and absorptivity to single values from their spectral functions. Emissivity is related to spectral radiance, described by Planck's law (Equation 2.4). Recall that this equation describes the distribution of photons emitted by a source as a function wavelength and the source temperature. Sources with a temperature between 3 K and 3,600 K have spectral peaks in the infrared. Thus, most objects being modeled for aerospace engineering purposes have infrared peaks, which is where the emissivity value is taken. The emissivity is a dimensionless value between 0 and 1 that indicates how close to the blackbody peak radiance its emission comes, e.g., an emissivity of 1 means that the object emits the same amount of energy at its peak as a blackbody does at that peak. Emissivity provides a heat loss mechanism for spacecraft. Heat can be radiated away to space, where it no longer need be accounted for in a model, or absorbed by another component of the spacecraft. The absorptivity parameter is one of the three parameters that describes what happens to incident light: it can either be absorbed, reflected, or transmitted and the sum of these parameters must be 1 at each wavelength. Absorption often results in a temperature increase, which makes it critical for thermal modeling. While absorptivity is a function of wavelength just as emissivity is, it is typically taken at a single wavelength in the visible spectrum where sunlight intensity peaks. Excluding optics, transmission tends to be unimportant in thermal modeling as most objects are solid and have high opacity in the visible spectrum. Thus, by specifying emissivity and absorptivity for each spacecraft component, radiative heat transfer can be accounted for between the many different spacecraft

components, from remote sources (e.g., the sun), and to remote sinks (e.g., deep space).

7.2 Test Procedures

The purpose of environmental tests for a spacecraft in general are to ensure it can survive and operate in the harsh environments of launch and space. The dominant concern during launch is the strong vibration the spacecraft must endure. Vibration tests are performed on the spacecraft prior to launch to make sure that it will survive. On orbit, the most critical characteristic is the lack of air. In this environment, convection's role in heat transfer is negligible, which results in a very different temperature environment. This is tested on the ground using a thermal vacuum chamber. The thermal vacuum (TVAC) test brings the spacecraft temperatures to the hot and cold limits provided by the component specification sheets and ensures that the spacecraft can survive and operate across those ranges. In thermal balance (TBAL) testing, the chamber is reconfigured in such a way that simulates the orbital environment as much as possible. Additionally, special tests are performed to characterize heat propagation through the spacecraft, such as powering on particular subsystems to measure the heat propagation through the spacecraft. The purpose of TBAL is to provide measurements that a thermal model can then forward-fit.

The thermal vacuum chamber used for MinXSS testing was BEMCO-West at the Laboratory for Atmospheric and Space Physics (LASP). The chamber is a long cylinder with a 0.76 m diameter and 1.22 m length and has a base pressure of 1×10^{-7} Torr (particle density of 1.59×10^{-9} g cm^{-3} at 20 °C). Two independently controlled temperature surfaces are inside with ranges of about -75 °C to +80 °C: a large flat platen along the bottom and a curved shroud around the sides and top. Typically, some mechanical ground support equipment (GSE) will be used to clamp or bolt the test article to the platen and thus control of the platen temperature equates to temperature control of the spacecraft via conduction. The shroud is thermally isolated from the platen and serves as the primary means of radiative heating/cooling of the test article. Vacuum feedthroughs allow cabling for power and communications between the test article and GSE external to the tank.

The following two subsections describe the distinctions in setup between MinXSS thermal

vacuum cycle and thermal balance testing, as well as the test procedure for each.

7.2.1 Thermal Vacuum Cycle Test

TVAC purpose and setup The purpose of thermal vacuum cycle (TVAC) testing is to stress the system with extreme temepratures. Typically component specifications distinguish between operating and survival temperature ranges. The latter means that the component (typically electrical) will not be damaged within the limit but should not be operated, used, or powered. A spacecraft consists of many components, each of which has operating and survival limits (Table 7.1). In order to avoid breaking something, the component with the lowest upper limit and the component with the highest lower limit define the thermal vacuum test temperature range, unless the component has active temperature control. For the MinXSS testing, the hot survival temperature was +60 °C, cold survival was -30 °C (the batteries were thermally isolated from the rest of the system by design), hot operating temperature was initially +40 °C but the team decided to be more conservative and operate at +30 °C, and cold operating temperature would have been -20 °C but the control logic used a value of -25 °C because the internals of the spacecraft did not actually reach the -25 °C limit. Knowledge for temperature control of the chamber came from two thermocouples attached to opposite sides of the spacecraft exterior, which provided information about temperature gradients across the spacecraft from the side facing the platen to the side facing the top of the shroud (Figure 7.1).

Strong thermal conduction from the platen to the spacecraft was desired for TVAC in order to reach the temperature limits and do so relatively quickly[2] . This was achieved by 1) minimizing the number of mechanical interfaces between the two, because each interface introduces an inefficiency in heat transfer, and 2) using relatively high pressure at mechanical interfaces with bolts tightly torqued down. Figure 7.2 shows a picture of the test setup and a schematic of the mechanical interfaces. Additionally, a custom-built radio-frequency (RF) hat was placed around the antenna,

[2] It typically takes about 7 hours to make the transition between dwell temperatures, at a rate of about 7.5 °C per hour

Table 7.1: Component specified temperature ranges.

Component	Operating Range [°C]	Survival Range [°C]
ADCS	[-20, +60]	[-20, +60]
CDH, EPS, motherboard	[-30, +70]	[-40, +85]
Li-polymer batteries	[0, +40]	[-20, +70]
Radio	[-30, +70]	[-30, +70]
Solar panels	[-75, +100]	[-75, +100]
X123 detector heat sink	[-20, +35]	[-60, +60]
X123 electronics	[-20, +50]	[-40, +85]
Selected TVAC Range	[-25, +30]	[-30, +60]

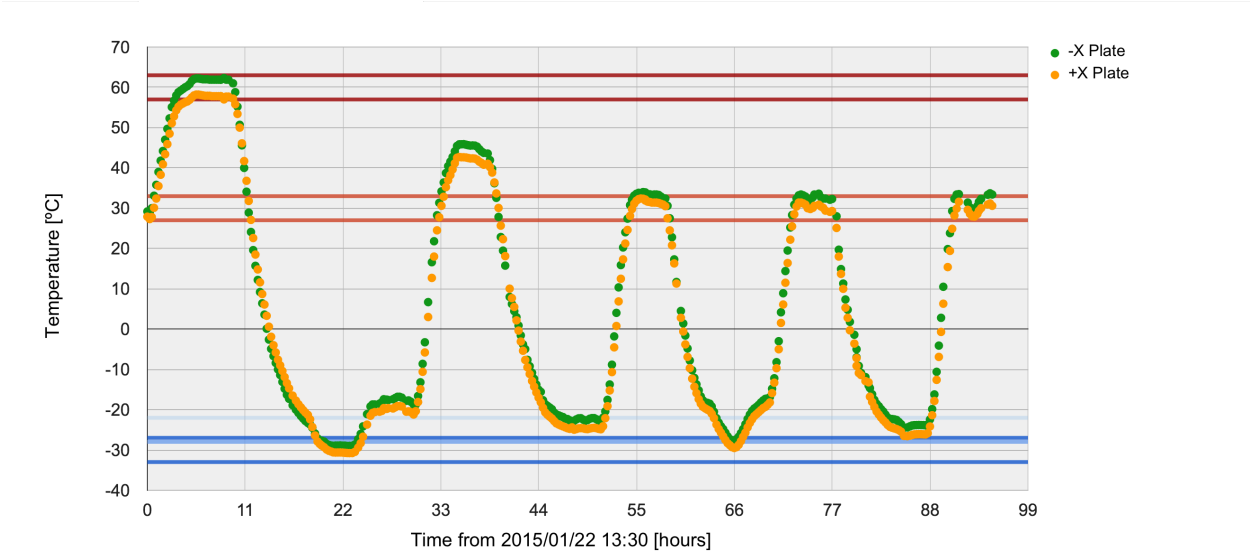

Figure 7.1: Measured temperatures from the first half of TVAC. The +X face of the spacecraft was down toward the platen. The dark red horizontal lines indicate the survival temperature, the dark blue lines indicate the cold survival temperature, the light red indicates the hot operating temperature, and the light blue indicates the cold operating temperature. Each of these values has a ±3 °C target range, as indicated on the plot. The first hot-cold cycle was for the survival temperature test and all others were for operational cycles. The first hot operational temperature test was done at +40 °C but the subsequent hot cycles targeted +30 °C.

which contained a small antenna with a coaxial cable through the vacuum feedthrough and to the ground station radio, as well as RF absorbent tiles to reduce reflections inside the chamber that could damage the flight radio. The RF link was the primary form of communication with

the spacecraft during testing. The direct cable connection to the CDH was only attached as a backup in case of issues with the RF link because it would take several hours to return to room temperature and backfill the chamber with air to regain access to the spacecraft in the event of an RF communications problem that could not be resolved. Fortunately, this backup did not need to be used during testing. Finally, a solar array simulator (SAS) was plugged into the EPS board where the ± Y solar panels would normally route their power. This required the use of some spare EPS baby boards to provide a conversion between circular GSE connectors and the flight-like ribbon cables. These pass-through boards were kapton taped down to the back side of the deployable solar panels. The solar arrays produce no power inside the dark chamber, but the simulator provided a means of inputting realistic voltage and current into the EPS for use in orbit simulations. Custom MATLAB software was written to autonomously cycle the simulator on or off with set time intervals. This feature was used to simulate the insolated and eclipse periods of orbit for several different orbital configurations. Note also that during testing, all of the remove-before-flight tags and covers were removed. These include plexi-glass covers for each of the three solar panels, a cover for the star tracker, a cover for the 3 instrument apertures and coarse sun sensor, and a pin to disconnect the battery from the bus.

TVAC procedure After the mechanical and electrical setup was complete, the chamber door was shut, ensuring a good O-ring seal. While the spacecraft was still powered off, the air was pulled out of the chamber. This was important because as air pressure decreases to about 1 Torr, the likelihood of an electric arc increases wherever there is a voltage. Below 1 Torr, this likelihood decreases again and it becomes safe to operate electronics. This behavior is characterized by the so called Paschen discharge curves. The spacecraft was powered and commanded into safe mode and manual measurements of pressure and many temperatures throughout the system were taken periodically from that point forward. The platen and shroud temperatures were then set to high values with the goal of getting the ± X spacecraft plates to the hot survival temperature. Once this temperature was reached, a 4 hour dwell was maintained. Then the platen and shroud were set to cold values with the goal of getting the ± X spacecraft plates to the cold survival temperature.

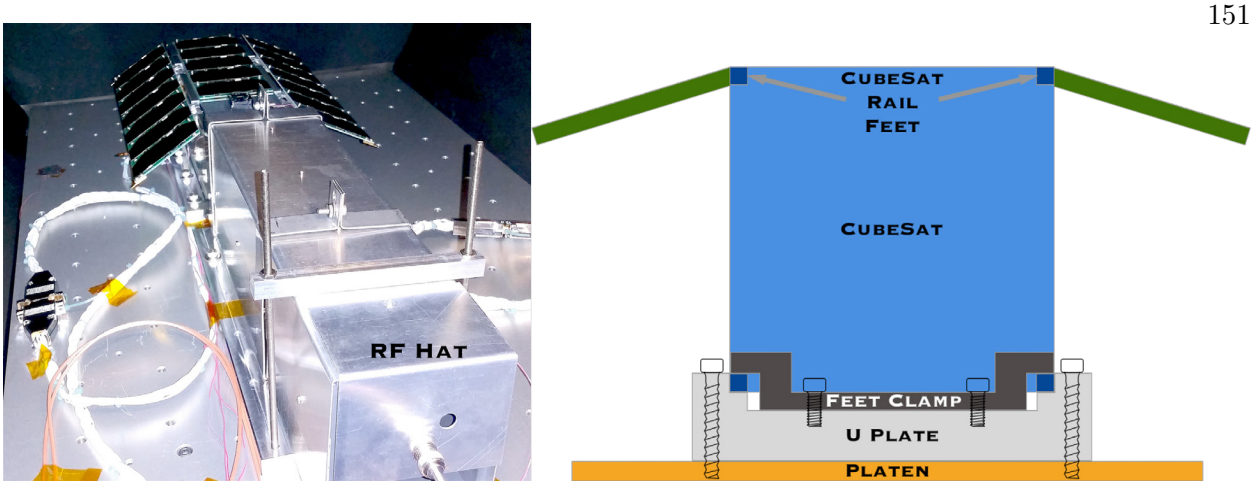

Figure 7.2: (Left) Picture of the TVAC test setup. The platen is the large flat surface with many bolt holes. The U plate can be seen just on top of the platen with several bolts attaching it to the platen along its length. The feet clamps are not visible in the image because the RF hat blocks its view. White cables can be seen running to the spacecraft to provide power and backup communications in case the RF link fails. The red cables lead to thermocouples placed on the platen, shroud, and spacecraft. (Right) Schematic of the mechanical interfaces between the chamber's platen and the spacecraft in thermal vacuum testing.

Once reached, a 4 hour dwell was maintained. In this way, hot and cold operating limits were then cycled with a 4 hour dwell at each. This was repeated four times and then temperatures were brought back to ~20 °C and the chamber backfilled. Herein, this testing will be referred to as TVAC-1. The spacecraft was removed and several improvements to software and hardware were made. About two months later, the operating temperature cycles were continued for another 4 cycles (TVAC-2, Figure 7.3).

Throughout TVAC-1, the spacecraft was power cycled to ensure that the system could successfully come up at any number of temperatures and temperature transitions. In TVAC-2, the spacecraft was powered on for the duration (~100 hours) to ensure smooth long-duration operation of the spacecraft to simulate spaceflight. Additionally, comprehensive performance tests (CPTs) were completed at the start and end of both TVAC runs, as well as at several points during TVAC-1. The CPT consists of telemetry checks, commanding checks, and numerous subsystem checks, e.g., reaction wheel response, heater response, and instrument response. Also, in TVAC-1, the SAS

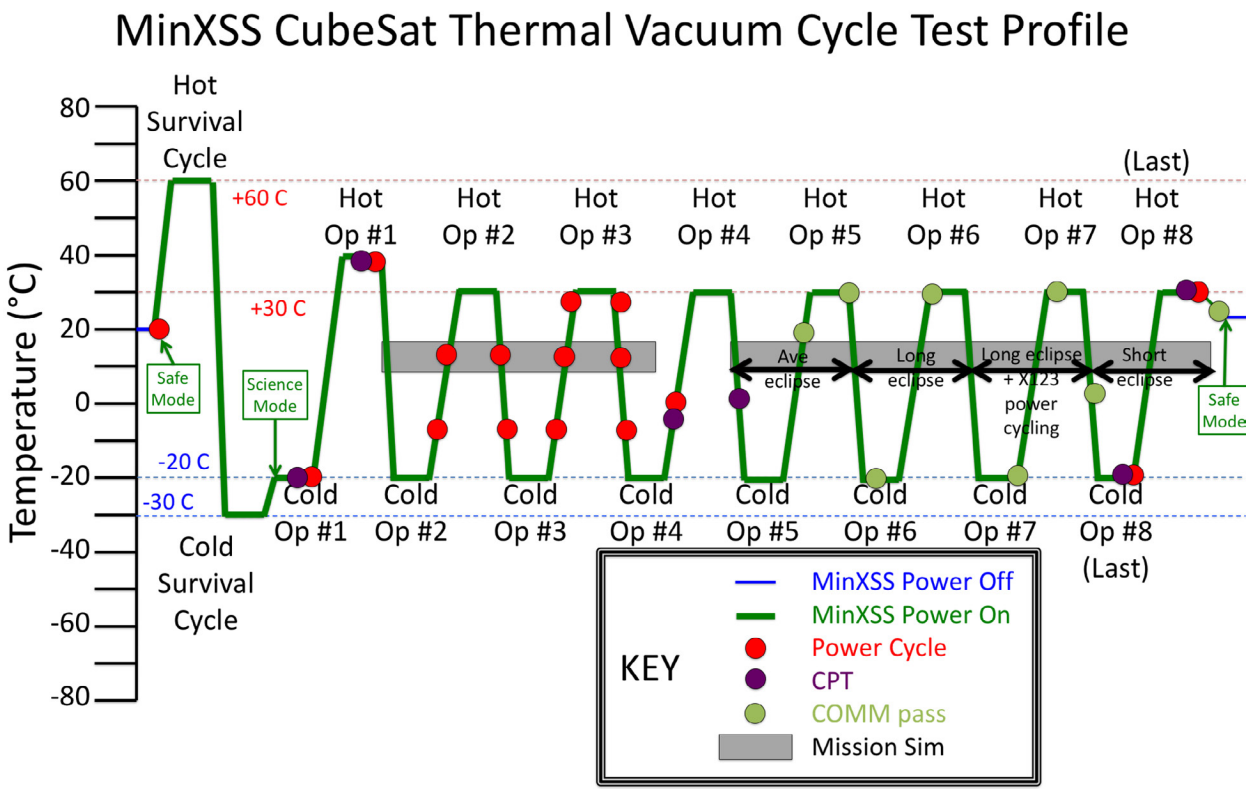

Figure 7.3: The operations plan for thermal vacuum testing. Figure courtesy of Tom Woods.

was programmed to provide constant power, as is the case when the β angle of an ISS orbit is greater than 70.2°. β in this context refers to the angle between the orbital plane and the vector to the sun, which is defined such that $\beta = 0°$ corresponds to the maximum eclipse period. $\beta = 90°$ means the orbital plane is perpendicular, which usually means the spacecraft is always in sunlight. In TVAC-2, average, long, and short eclipse periods were programmed into the MATLAB script to test system performance in these orbit scenarios. Finally, during TVAC-2, radio communication passes were simulated several times per day by dumping stored data determined to take about 6 minutes to complete playback, as will be the case on orbit. This resulted in significant heat generation by the flight radio but provided confidence that the radio will not exceed its operating temperature limit even in the hottest environments.

7.2.2 Thermal Balance

TBAL purpose and setup The purpose of thermal balance (TBAL) testing is to provide measurements for thermal model validation. Additionally, making the chamber resemble an orbital scenario as much as possible provides testing that is unique from TVAC and boosts confidence in the thermal performance of the spacecraft. To this end, the shroud is made cold to resemble deep space while the platen is made hot to resemble the sun. On orbit, MinXSS will actively point one face (+X) toward the sun, so that face was pointed toward the hot platen. Distinctly from TVAC, high conductivity is not desired between the platen and spacecraft. On orbit, the only heat exchange between the environment and the spacecraft is through radiation, so TBAL seeks to emulate this by mounting the CubeSat in the chamber with thick blocks of thermally isolating Delrin, minimizing the surface area contact between the block and the spacecraft, and maximizing the unobstructed view between the platen and spacecraft (Figures 7.4, 7.5). In order to validate the thermal model, it is useful to reach an equilibrium point in the test where nothing is changing and then to initiate heat load pulses by switching on high-power-consuming electronics (e.g., heaters and the radio) for brief periods of times. This results in a temperature propagation through the spacecraft that is measured at several points and can be forward-fit with the model. This aides in determining conductivity across mechanical interfaces for the model.

There were several other differences in setup between TVAC and TBAL. Between the Delrin blocks and the platen, we placed a thin sheet of metal coated with Krylon flat black paint, which has an emissivity greater than 0.95. This improved the radiative coupling between the platen and the spacecraft, bringing it closer to the expectation on orbit while also reducing the time to reach equilibrium temperature. At the start of TBAL, a flight antenna deployment was done to prove the functionality of the release mechanism in vacuum. This meant that the RF hat could not be used. The radio amplification level was set to 115, corresponding to a measured output of about 0.7 W, rather than its full power setting of 175 (4.7 W output) because the built-in protection on the radio is not at risk of damaging itself at these levels. Despite having no ground antenna inside

the chamber, there was still sufficient signal coming through the coaxial feedthrough to use the RF link for communications. Additionally, many more thermocouples were used on the outside of the spacecraft. Where TVAC only had two sensors, one each on the ± X faces, TBAL had 15 total; Table 7.2 lists the locations of each. There were also thermocouples placed at several locations on the shroud and one on the platen near the spacecraft.

Table 7.2: Thermocouple locations on spacecraft for TBAL. "Top" refers to the +Z direction. As an example, the thermocouples on the -X, -Z, and -Y faces can be seen in Figure 7.5, identifiable by the strips of kapton tape.

Face	Approximate location
-Y	Bottom Middle Top
+Y	Bottom Middle Top
-X	Bottom Middle Top
+X	Bottom Under solar array On solar array Top
-Z	Center
+Z	Center

TBAL procedure After the mechanical and electrical interfaces were established, the chamber door was shut and vacuum pulled, while the spacecraft remained off. Once the safe point of the Paschen discharge curve was reached, the spacecraft was powered on. No commands were sent to bypass its default startup mode. In this mode, the spacecraft believes it has just been ejected so a 30 minute timer starts before deployments are executed autonomously after the timer expires. This is a requirement built into CubeSat standards. Through the small viewport into the chamber, 240 frames-per-second video was captured of the antenna deployment. The solar

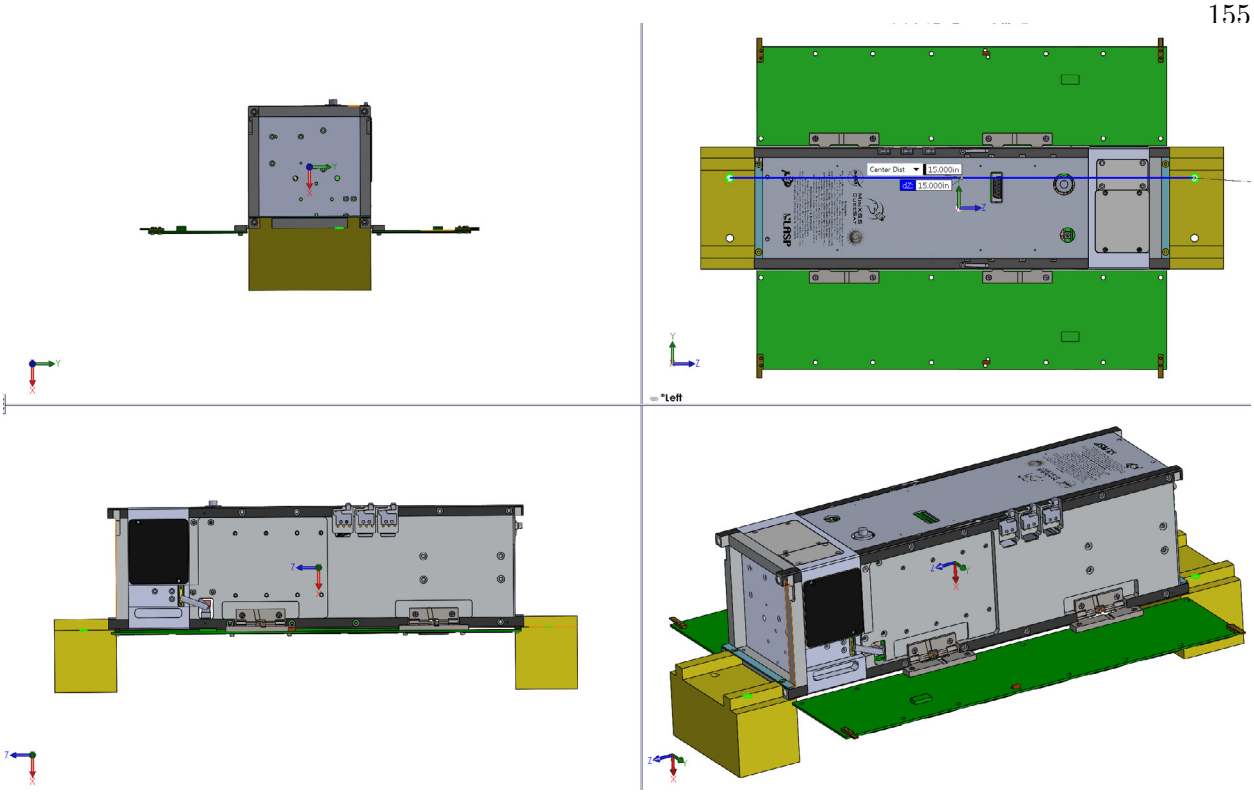

Figure 7.4: SolidWorks images of the spacecraft on the custom mechanical GSE for thermal balance mounting. The yellow blocks are made of Delrin (white color in reality but yellow here for clarity) with a small aluminum bar across the top of the CubeSat feet (highlighted in blue) to lock the spacecraft in place.

arrays were already in a deployed configuration because deploying them with the abundance of cables present was deemed too risky. The antenna successfully deployed and the spacecraft auto-promoted to safe mode, where it began to beacon every 9 seconds. Just as in TVAC, pressures and temperatures were recorded periodically from this time until the end of the test. The chamber temperatures were then configured – first to the cold thermal balance condition.

In cold balance, the platen temperature was set such that the thermocouple on it (near the spacecraft) reached roughly +34 °C and the shroud was set so that the shroud thermocouple closest to the spacecraft ("top rear") reached approximately -32 °C (Figure 7.6). It was discovered that the shroud had a significant temperature gradient across its length (Figure 7.6), which has since been fixed in the chamber. This temperature gradient existed within the field-of-view of the spacecraft

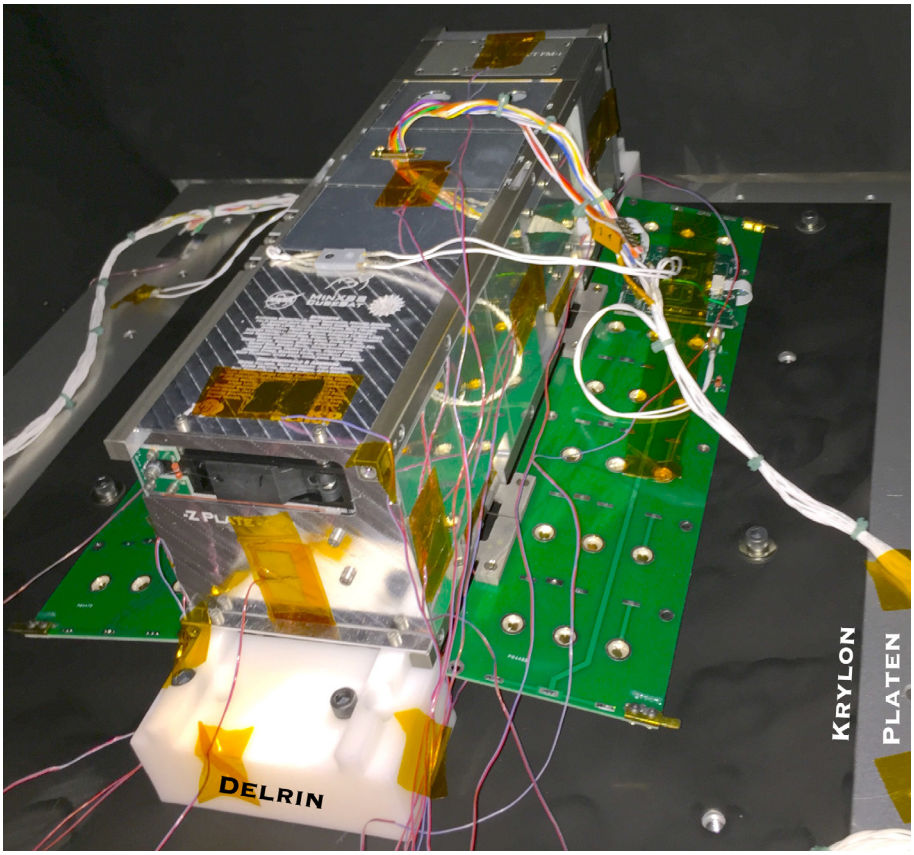

Figure 7.5: Picture of the thermal balance setup. The large grey surface is the platen, the black metal sheet has been spray painted with Krylon flat black paint to increase emissivity from the hot platen. The white delrin blocks provide the mechanical mounting of the spacecraft to the chamber, with minimized thermal conduction and maximized radiative field-of-view. The antenna deployment module can be seen in the foreground on the -Z face of the spacecraft. The antenna remained stowed until vacuum was established. Many more thermocouples (red cables) can be seen here than were in TVAC, which provided more temperature points for model correlation.

and resulted in an overall warmer environment than was targeted. This was accounted for in the thermal model configuration (see Section 7.4). Additionally in cold balance, orbit simulations of power were performed using the solar array simulator, similarly to TVAC. Only the average eclipse period of 36.6 minutes was used. This provided a periodic and realistic heat load to the EPS that could then be used for further tuning of the model. Other power cycling was also done. The reaction wheels were generally idled during all thermal testing to minimize the number of stressful cycles placed on them, but they were powered on for three minutes toward the end of an insolated

power period in order to determine if there would be an impact to temperatures. The CDH board sent beacons for the radio to transmit every 9 seconds but these packets only take ∼0.5 seconds to transmit, so the transmitter was switched off ∼95% of the time. Near the end of another insolated power period, the CDH was commanded to transmit sufficient stored data to keep the transmitter on for ∼6 minutes, a period of time similar to the expectations for on-orbit operations. As described earlier, the radio amplification level here was set lower than it will be on orbit, so the dissipated heat was less than what should be expected on orbit. Radio efficiency, which is a function of power setting, also plays a role in heat dissipation. At the power setting of 115 used in TBAL, the expected heat dissipation in the radio's power amplifier is about 0.6 W; the full power setting of 175 used on-orbit should result in a heat dissipation of ∼3.3 W. However, the intent of this test was to fine-tune the conductivities of the mechanical interfaces between the radio and the ± Y radiator surfaces, most of which are used for the other daughterboards in the system as well. The difference between the test and orbit radio heat dissipations is not germane to this objective.

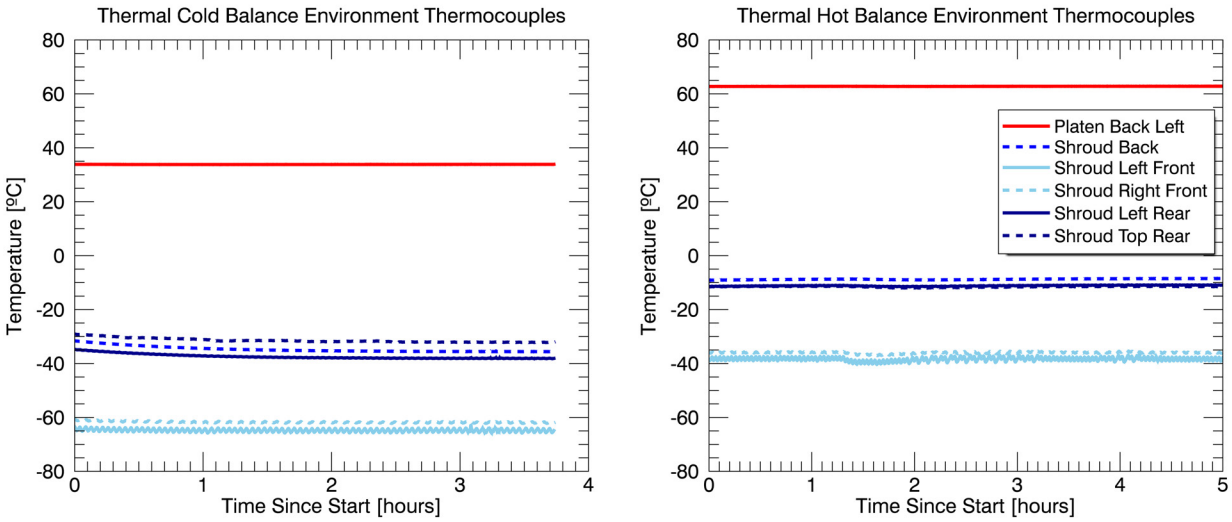

Figure 7.6: Temperature measurements from the TCs placed inside the chamber environment during (left) cold and (right) hot balance. The multiple shroud TCs (blue) show a ∼30 °C gradient across the length of the chamber.

In hot balance, the platen thermocouple (TC) reached +62 °C and the shroud TC nearest

MinXSS reached -11 °C (Figure 7.6). The SAS output was on for the duration of this test, simulating a fully sunlit period of the orbit. This allowed the system to reach a very stable temperature equilibrium, which provided an excellent baseline for the same power-pulse testing of the reaction wheels and the radio described for cold balance.

7.3 Mechanical Description of MinXSS Relevant to Thermal Properties

Chapter 6 provided a brief overview of the MinXSS CubeSat but in this section, more details of the mechanical design relevant to the thermal model are described. The structure itself consists of six custom-machined aluminum 6061 plates and the XACT ADCS bolted together with #4-40 A286 screws. Most of the outside surfaces have been covered with silver-coated Teflon tape to increase emissivity and serve as radiators for the spacecraft. The system mechanical block diagram (Figure 6.5) hints at where additional mechanical interfaces exist. Inside, a motherboard runs most of the length of the CubeSat on the sun-facing (+X) side. Each daughterboard slots into two Unitrack Kooler-Guide rails on the ± Y sides and plugs into a large 48-pin connector on the motherboard. The card rails were specifically chosen for their improved heat conduction through copper-beryllium springs that contact the board. Each daughterboard, except the battery board, has an internal copper layer to improve conductivity from the electrical components to the card rails. The XACT ADCS bolts to the top of the structure with #4-40 bolts. The instruments are bolted to the side walls with #2-56 bolts. The X123 electronics board was discovered to have two locations that got much hotter than their surroundings when in operation. High-conductivity thermal foam was placed in those locations to provide a path for heat flow between the hot electrical components and the wall of the box containing them – particularly crucial when no air is present to convect heat away. Figure 7.7 shows a system thermal block diagram to indicate the different zones of the spacecraft.

Most of the spacecraft is thermally passive. The two exceptions are the batteries and the X123 detector. The batteries have been intentionally thermally isolated from the rest of the system because their lower-operating temperature limit is much higher than anything else (0 °C) and they

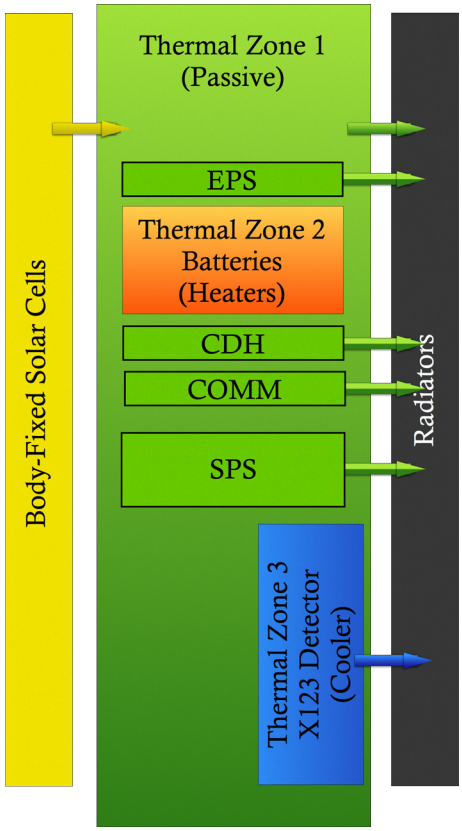

Figure 7.7: Thermal zone block diagram for MinXSS. The primary zone is passively managed. Zone 2 is isolated and dedicated to the batteries and contains two heaters for active management. Zone 3 is the X123 detector head, which has an embedded thermal electric cooler to maintain its temperature set point. It shares the -Y radiator plate with the full system.

are critical to the operation of the spacecraft. A heater is sandwiched between the top two batteries and between the bottom two batteries along with temperature sensors so that flight software can keep the batteries safely above their lower-operating limit. The X123 detector is responsible for the primary science measurement and has an active thermal electric cooler (TEC) to keep the small silicon detector at -50 °C, which reduces thermal noise in the measurement. The TEC requires a heat sink below +35 °C in order to maintain the detector temperature. There are several mechanical interfaces between the heat sink and the radiative surface on the outside of the spacecraft, each of which introduces an inefficiency in heat transfer. Accounting for conduction across mechanical interfaces is one of the primary methods of thermal modeling.

7.4 Model Overview

The thermal model is implemented in C & R Tech's Thermal Desktop (TD) – a massive plugin for AutoCAD[3] . This provides the benefit of a graphical user interface with 3D modeling and visualization to the advanced and well-developed thermal modeling on the backend. The software also has the capability to model orbits.

7.4.1 Model Constituents

The TD model for MinXSS consists of 38 physical objects with 319 nodes (points where the model computes temperature), 11 heat loads, 24 contactors (surface-surface conductors), 22 node-node conductors, and 2 heaters (Figure 7.8, left). Each physical object has density, conductivity, specific heat, absorptivity, and emissivity properties. Because the CAD has appropriate physical dimensions, the density of each component can be scaled to match measurements such that the total mass of the model is near the total measured mass. The measured mass for FM-1 is 3.52 kg and the model mass is 3.65 kg. Numerous other model checks can be performed in TD, including such sanity checks as "painting" the model with emissivity or other model properties (Figure 7.8, right).

Physical objects in the MinXSS TD model are represented by "rects" and "bricks". Rects are 2-dimensional rectangles while bricks are rectangular prisms. More complex geometries are possible in TD but not necessary for MinXSS, with three exceptions. The instrument apertures allow light to enter directly inside the spacecraft and these are modeled as small circles that share their central node with nodes corresponding to the front of the instruments. In this way, light directly impacts the instruments where it would otherwise be shielded by the aluminum structure. TD also allows for many physical properties of rects and bricks to be specified beyond density, specific heat, and conductivity, but these are the only ones necessary for the relatively simple MinXSS CubeSat. Similarly for optical properties, many more can be specified beyond absorptivity and emissivity,

[3] CAD is short for Computed Aided Drawing

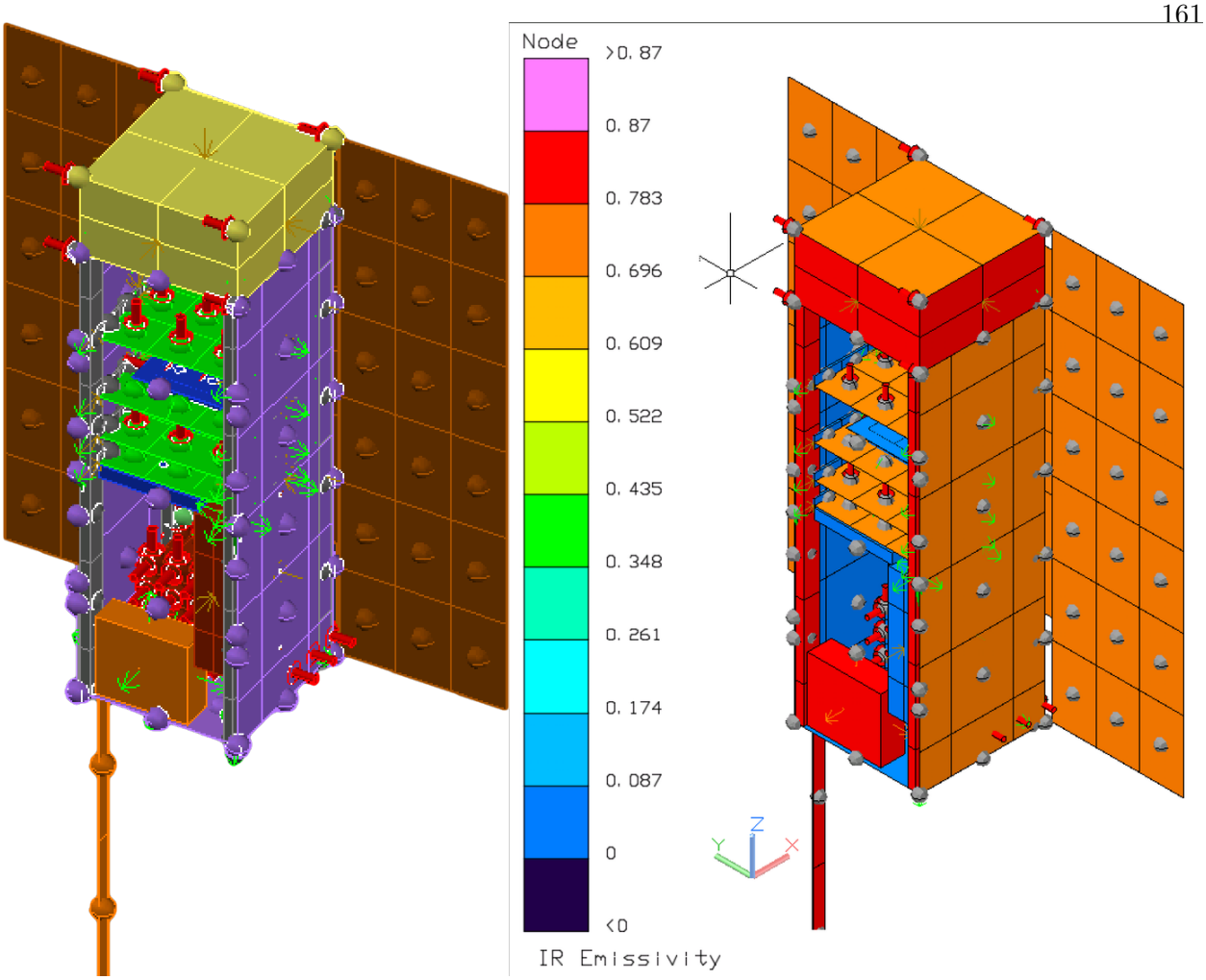

Figure 7.8: (Left) Image of the Thermal Desktop model for MinXSS. The colors of the surfaces simply provide contrast for clarity. The small spheres at the center of each rectangle are the nodes where temperatures are computed. The red arrows indicate heat loads. Green arrows indicate contactors while colored lines between nodes (none visible) indicate conductors. (Right) Thermal Desktop model check for emissivity. The model surfaces are "painted" by colors corresponding to their infrared (IR) emissivity. In this way, it is possible to verify that coatings have been applied properly to the inside and outside of surfaces.

and more detail within these properties can be specified (e.g., making them functions of angle and/or temperature). But again, none of this functionality is required for obtaining an adequately accurate model of MinXSS.

TD can handle heat propagation by all of the means described in Section 7.1, but convection is not modeled here because TVAC, TBAL, and orbit are all in vacuum environments and because

MinXSS contains no pressure vessels. Radiation is handled by the backend simulator and the only user input required are the optical properties of all physical objects, including the environmental ones. Conduction is also handled on the backend given the user-specified conductors and contactors. Power dissipation by electronics are modeled as heat loads specified by wattage. It is possible to make heat loads a function of time or temperature. More advanced techniques can also be applied to make a heat load dependent on the temperature of a node not directly associated with the physical object it is being applied to. This was done for MinXSS in order to model the behavior of the X123 TEC, which draws more power when its heat sink temperature rises. This results in a positive feedback loop because as the X123 draws more power, it dissipates more heat and raises the temperature of the heat sink, which causes the TEC to require yet more power. Either an equilibrium is reached or the X123 power reaches its maximum and the detector temperature begins to rise. Fortunately, this latter situation does not seem likely to occur based on the testing and modeling. TD can also model heaters, which require the user to specify the node or surface to apply them to, as well as the wattage. The power can be constant or proportional to temperature. Two temperatures are specified: the points at which the heater should power on and off. The MinXSS model only includes the two battery heaters because the instrument heater on the inside of the -X face of the spacecraft has been tested with no measured temperature increase observed at other subsystems. This plate simply closes up the box and its conductive coupling to the rest of the structure is simply too weak to measurably impact the system at any location that temperature sensors are present. Neither is it critical for system operation, so it can be safely ignored for modeling purposes, and the instrument heater will probably not be used in flight.

All of the user-defined points described above are essentially variables – tunable knobs – for the modeler to adjust in order to achieve correlation of predicted temperatures to measured ones. Most of these have reasonable starting values based on specification sheets, industry standards, calculations, or measurements in the lab. Appendix C provides a listing of all of these variables and their final values. Some values were not modified from their initial estimates while others were tuned to reach correlation between modeled and measured temperatures.

7.4.2 Model Environments

Vacuum chamber The thermal vacuum chamber model was provided by Bret Lamprecht, a senior LASP thermal engineer, who uses this model frequently for other projects. The critical components for MinXSS are the platen, shroud, Krylon (high-emissivity) plate, and back wall. The platen and shroud have "boundary nodes" that accept user-input constant temperatures, from where heat is propagated across surfaces accordingly. This creates the proper radiative environment for comparison to the measurements. Each element is modeled in CAD with dimensions corresponding to the actual test chamber. The one modification made for MinXSS was the addition of two more boundary nodes on the shroud to account for the measured temperature gradient (Figure 7.9).

Orbit scenarios Two orbital scenarios are pertinent to the following sections: ISS hot and cold. These correspond to the orbit FM-1 has at different points in the precession of its orbit. Table 7.3 details the orbital parameters for these scenarios.

Table 7.3: Orbital scenario parameters

	ISS Cold	ISS Hot
Altitude [km]	350	420
β [°]	0	90
Sunlight [W m^{-2}]	1361	
Albedo	0.3 below 70° latitude 0.8 above 70° latitude	
Planetshine [°C]	-23.15	

7.5 Comparison of Model Predictions to Test Measurements

There are no strict criteria for the agreement between all predicted temperatures and their measured counterparts. Generally, agreement to within 10 °C is good enough, within 5 °C is desirable, and within 3 °C is exceptional. Components with stricter temperature requirements, e.g.,

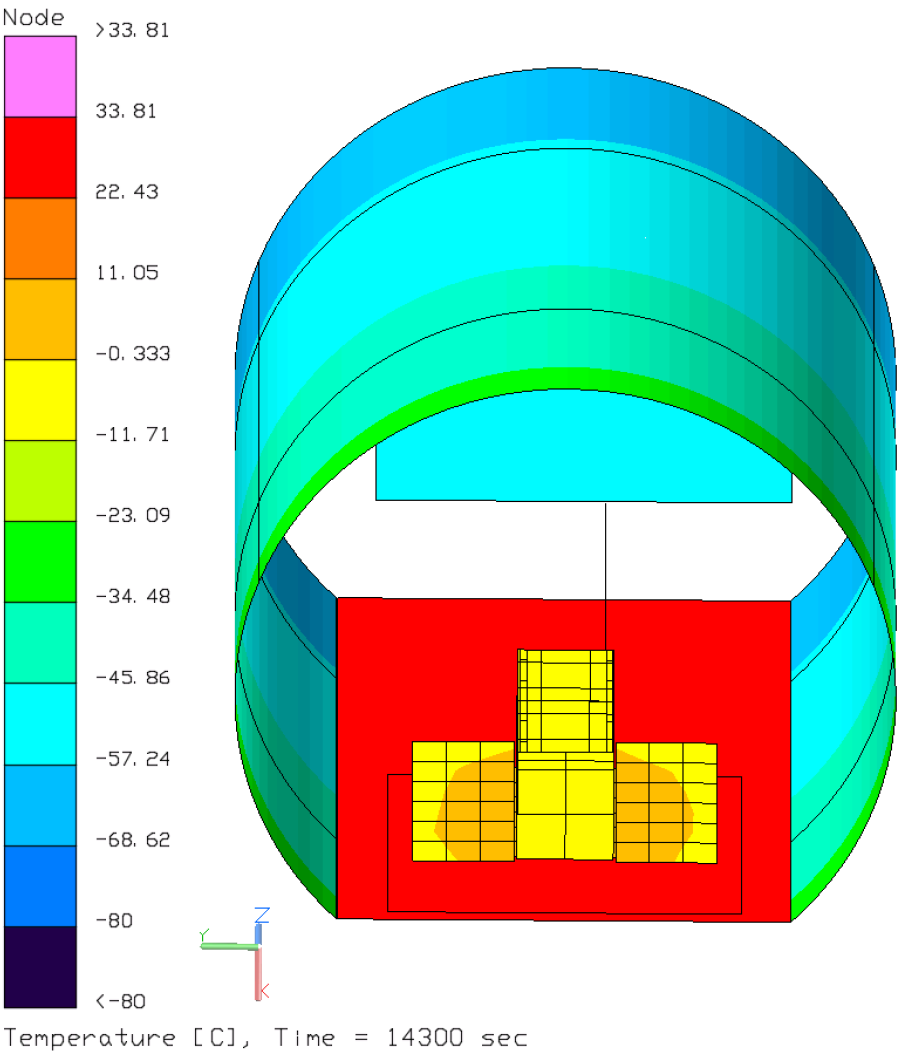

Figure 7.9: The MinXSS TD model inside the modeled BEMCO-west vacuum chamber. The color coding corresponds to temperatures at a specific point in time during cold balance. The gradient across the shroud can be seen.

the battery's lower limit of 0 °C, should be more carefully matched if any predictions indicate they are nearing their temperature limits. This section will first describe bulk temperature comparisons and then numerous comparisons between single temperature measurements and the corresponding model prediction.

First, to get a sense of the bulk agreement between measurement and model, Figure 7.10 shows all of the sensors internal to MinXSS, thermocouples on the exterior of MinXSS, and the

corresponding model values. Rather than plot individual nodes in the model, the TD temperature "measure" tool was used to interpolate temperature near the actual locations of measured temperatures.

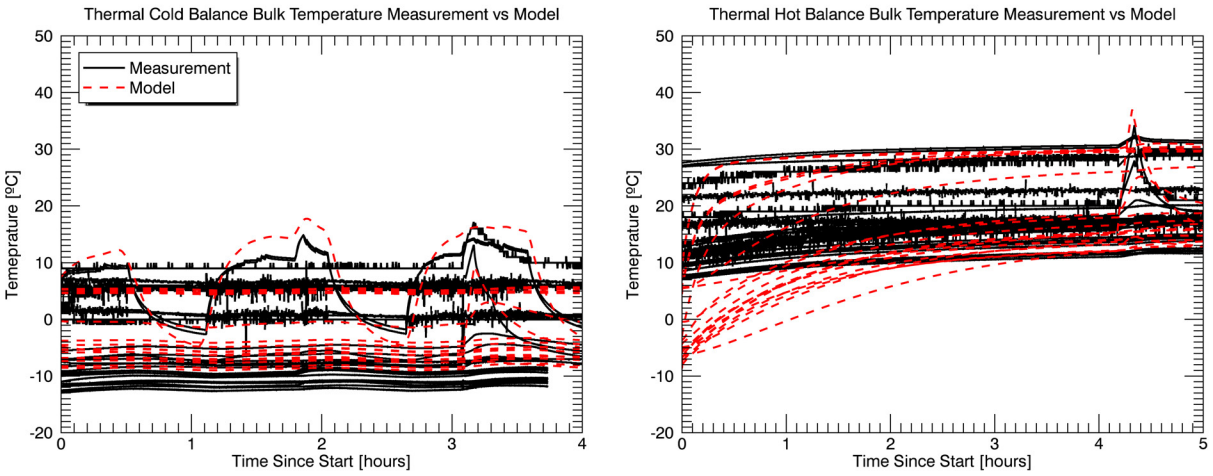

Figure 7.10: Bulk temperature comparison between measurements and model predictions for (left) cold balance run as a steady-state model prior to transients and (right) hot balance run as the full transient option using the temperatures at the end of the cold balance model run as starting points.

In general, Figure 7.10 shows that the bulk temperatures between measurement and model match to within a few degrees. The cold balance was run with the "steady state before transient" option selected. In a purely transient run, each node starts with an initial temperature of +20 °C, unless overridden by the user. The nodes then begin interacting with the environment via heat transfer and applying heat loads and heaters. This entire process appears in the plotted data. If run with the steady state prior to transient option selected, the model establishes equilibrium before providing temperatures to be plotted. Variability in this case is due to time-varying heat loads and heaters, such as the periodic ~hour-long temperature increases are due to the orbit simulation power cycling. The sharp peak around 3.25 hours in the cold balance test is from the 6-minute radio transmission. The peak-on-a-peak around 2 hours is due to the reaction wheels being powered on, which manifests as additional power draw through the EPS board.

The hot balance was not run with the steady state option. Its starting point temperatures were overridden with the temperatures at the end of the cold balance run. In other words, the right-most point for each of the red curves in the cold balance plot is the same as the left-most point of the red curves in the hot balance plot. The red lines essentially move from one plot to the other. Contrast this with the discontinuity in the measured values (black curves) between the two plots. This is simply due to the fact that the transition period of the measurements is not plotted. The transition took ~10 hours as the chamber temperatures themselves slowly changed and the test article slowly responded. Plotting this transition would diminish the clarity of the period of interest where correlation is sought. Once at equilibrium, the hot balance case was exceptionally stable because there was no power cycling of the SAS, which is why the black curves are more or less flat until the extended radio transmission at ~4.25 hours. Running the model as a transient shows how the model converges to the environment and that when it does so, it converges to the measured values.

In the cold case, the measured temperatures on the exterior of the spacecraft are systematically colder than the model prediction. These are the black lines below -10 °C. The discrepancy is likely due to radiative coupling of the actual sensors with the environment that was not modeled. Specifically, each thermocouple was covered with a small piece of aluminum tape, all of which was then covered with a slightly larger piece of kapton tape (some of which are visible in Figure 7.5).

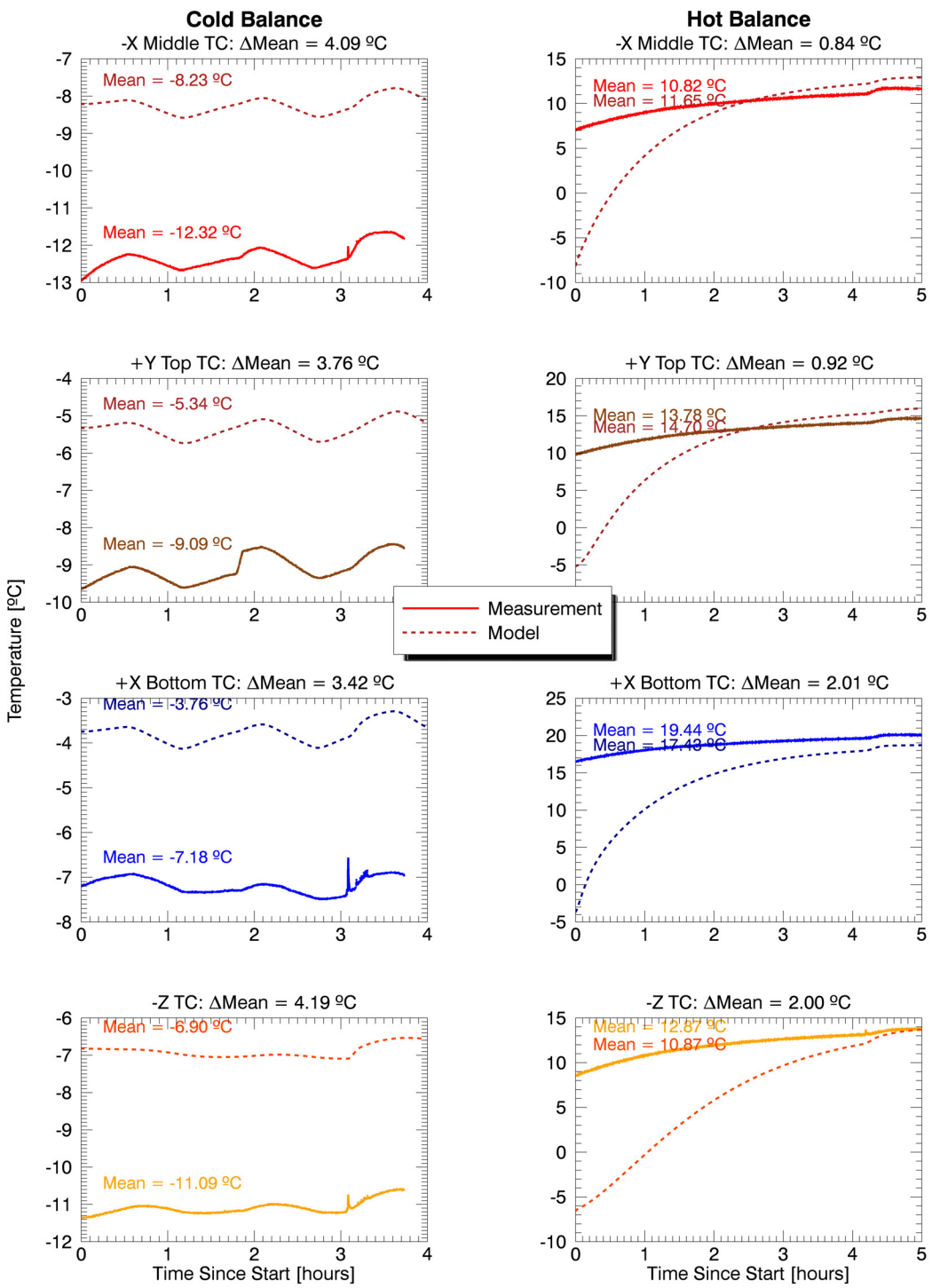

Figure 7.11: Temperature comparison between measurements and model for several representative TCs on the exterior of the spacecraft. The left column is for cold thermal balance and the right column is for hot thermal balance. The colors are used simply for differentiation and easier identification. Solid lines are measurements and dashed lines are model predictions at the approximate corresponding physical location. The mean values in the left column (cold balance) are taken across the entire time series. The mean values in the right column (hot balance) are taken only across hours 3-4 because the temperature convergence of the model is not representative of how well the model predictions match the measurements and it also excludes the power pulse from the extended radio transmission at ~4.25 hours. Data cadence for both the measurements and model is 9 seconds. Note that the vertical axis is autoscaled for every plot.

Figure 7.11 shows the temperature measurements versus model predictions for the external TCs in both cold and hot cases. All deltas are within the 5 °C desirable limit, with all of the hot balance deltas reaching the exceptional threshold of 3 °C. The power cycling behavior can be seen in the cold balance plots (left column), which provide evidence that the passive cooling system is working. In particular, the SAS provides power via cables plugged directly into the EPS board. The EPS board routes power to all subsystems but is only ∼90% efficient, so 10% of that power is converted to heat inside components of the board, primarily in the buck converters that step voltage down from raw, unregulated solar panel voltage to the 8.4 V, 5 V, and 3.3 V levels used in the system. The electrical components conduct heat into the PCB, which contains a copper layer that conducts heat from a localized position to the area of the entire board. At the edge of the board, the Unitrack Kooler-Guide rails have copper-beryllium springs pressing tightly against the edges of the board, where conduction allows heat a path outside the board. The card rails are bolted to the aluminum 6061 ± Y structure with two #2-56 bolts. There is also direct surface-to-surface contact between the ± Y walls and the card rails. Thus, conduction allows heat to travel to the ± Y walls, whose outer surfaces are covered with silver coated teflon tape. This tape has relatively high emissivity ($\epsilon = 0.84$) that is the final step in heat release that was generated by the EPS electrical components. Clearly, there are many mechanical interfaces between the buck converters and the radiative surfaces. Each interface results in a small inefficiency in heat transfer because contact between two objects is never as seamless as a single continuous object. Modeling every interface including every electrical component on a board is simply not feasible: it would introduce significant complexity to be managed, generally require more information than could be obtained in a reasonable amount of time, increase model processing time enormously, and increase the number of small uncertainties that could stack on each other to result in poor predictions. Instead, the heat load is modeled as a direct input to the board, the board has edge contactors defined to the card rails, and the card rails have face contactors to the ± Y walls. Each of these have tunable parameters: the heat load can be made to time vary and the amount of power, and the conductors/contactors conductance in W C^{-1} can be altered. Forward modeling is used

to match the temperature measurements. A reasonable guess is initially input for each of these variables based on calculations, measurements, or a specification sheet. For example, the Kooler-Guide rails specification sheet provides a plot of temperature rise versus power, as measured at various positions on the rail with a PCB in it. That information can be used to determine the W C^{-1} but is dependent on many factors such as pressure of the copper-beryllium springs (which is itself dependent on PCB thickness), spatial distribution of heat generation, and the temperature of the heat sink for the rail. Rather than try to determine all of this *a priori*, the model is run and temperatures plotted against those measured. If the prediction shows temperatures on the board are too low, then it can be reasonably assumed the conductivity to the rail needs to be decreased. The model is run again and the predictions compared to the measurements, in an iterative process. Additionally, the power consumption of the system during testing is a known quantity and estimates of subsystem efficiency can be made (Figure 7.12). Here too, forward modeling is applied to achieve agreement between model predictions and measured values.

All of the power coming from the SAS goes into the EPS board. The EPS board also has measures of voltage and current in several locations, which can then be compared to the SAS output power to estimate the EPS efficiency. The mean EPS power consumption during this period was 9.28 W. Comparing that to the 10.61 W mean from the SAS, the EPS appears to be ~87.5% efficient. Multiplying the 10.61 W input by the EPS inefficiency (12.5%), we obtain 1.32 W dissipated as heat on average in the EPS board. This calculation can instead be performed as a function of time. This was done and used as input into the thermal model by converting the EPS heat load from a constant value to a time varying one with the estimated heat dissipation. Because hot balance had a different power profile than cold balance, the same calculations were done on those data and input in the thermal model to replace the cold balance EPS heat load. The result of these computations is that the modeled temperature profile of the EPS board closely matches the measured values (Figure 7.13, top left).

Figure 7.13 shows that the temperature agreement between the model and the measurements is again quite good. All are within the desired 5 °C, and all but the COMM board in hot balance

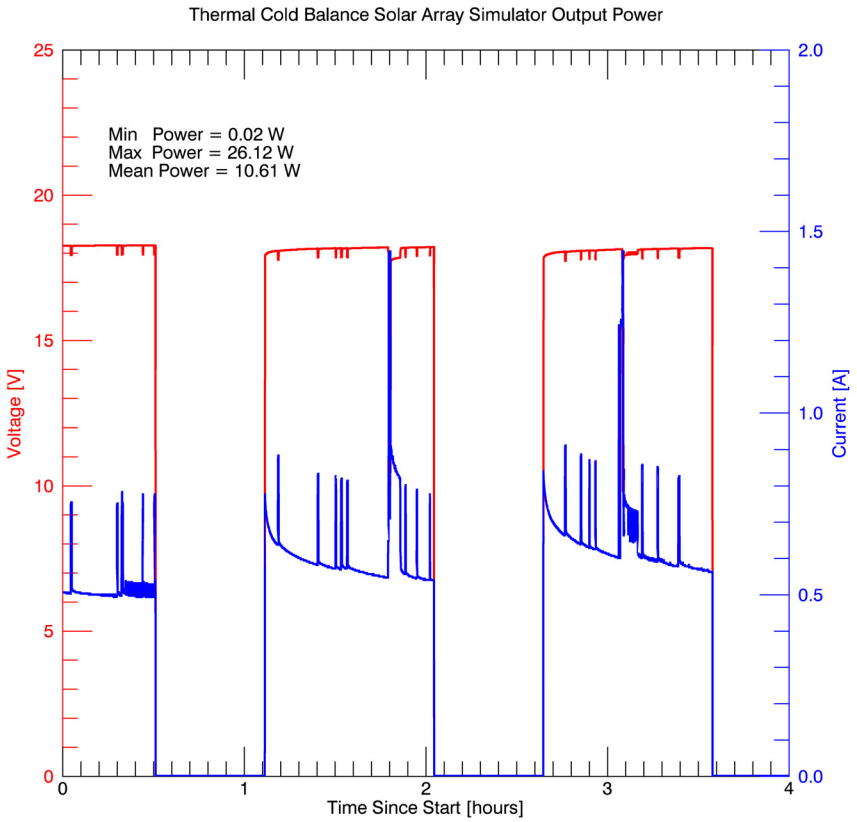

Figure 7.12: Output voltage and current from the SAS during cold thermal balance. This is the only external source of power for the spacecraft so it accounts for the total system power consumption. The orbit-simulation power cycling can be seen. The two large spikes in current around 2 hours and 3.25 hours are due to reaction wheels being powered on and the radio transmitting for several minutes, respectively. The other spikes are likely related to when the radio beacons every 9 seconds, which is asynchronously sampled in current.

are within the exceptional 3 °C threshold. The EPS and COMM board have time-varying heat loads while the battery board has two heaters. The battery heaters do not trigger in reality or in the model until the battery temperature falls below +5 °C. The measured battery temperature has the additional constraint that at least 2 samples must be below the temperature threshold before flight software will enable the heaters. As can be seen in the measured battery temperature during cold balance, when power is being provided by the solar arrays, the noise on the battery temperature sensor greatly increases. The persistence criteria was never met though, so the heaters

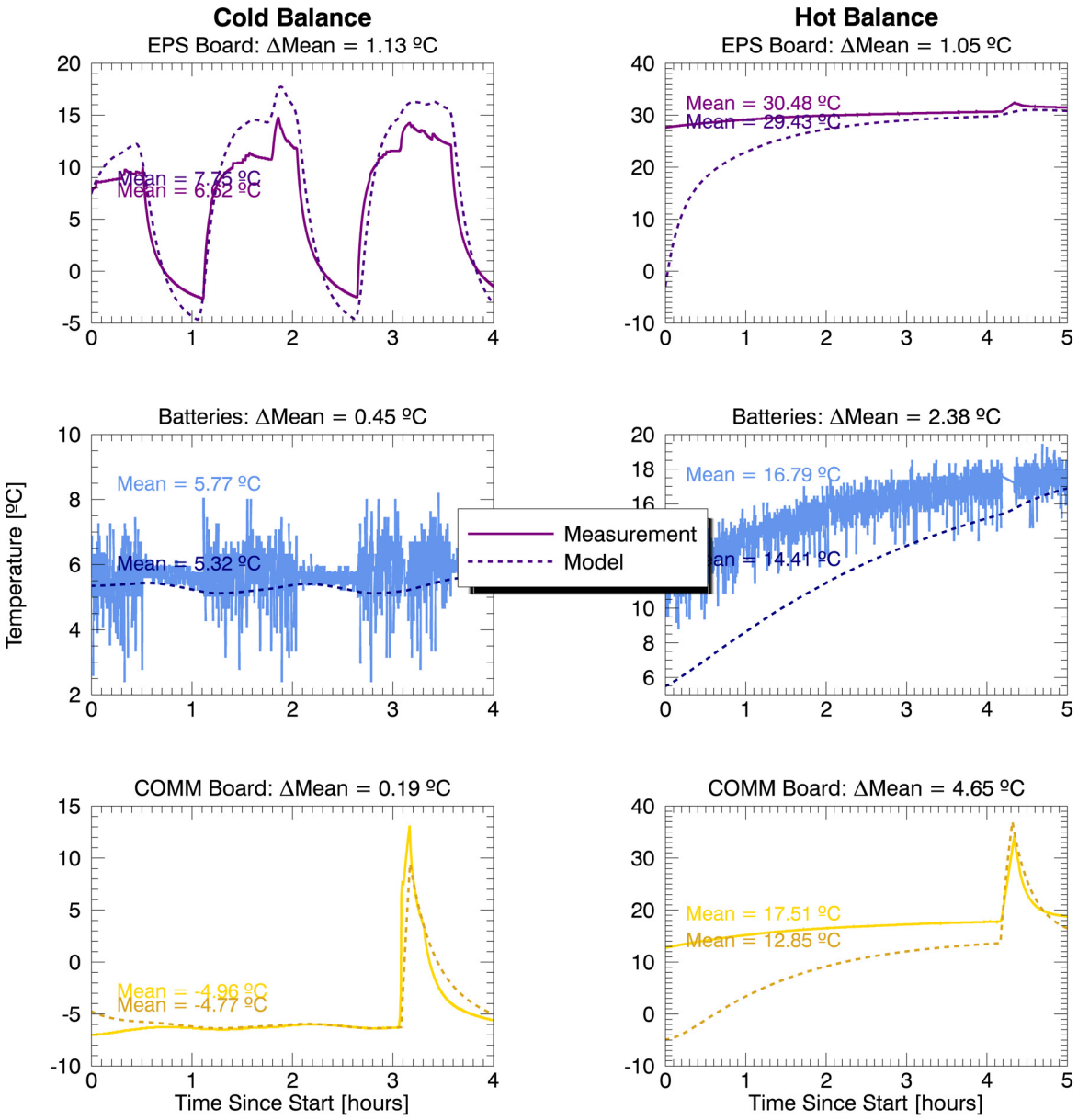

Figure 7.13: Same as Figure 7.11 but for PCBs with time-varying heat loads or heaters.

were never triggered during cold balance. Note that the heaters were triggered during TVAC cold survival and cold operational cycles, which provided assurance that they will work as intended on orbit. As mentioned at the start of this chapter, agreement between model and measurement should be greater when near critical temperature thresholds. In the cold case for the battery, the measurements and model indicated that the battery was less than a degree above the threshold to

trigger the heater. Here, agreement between the two is better than half a degree. Note that the really critical temperature for the batteries is their lower-operating limit of 0 °C but the heater set point is +5 °C to account for thermal inertia and uncertainty in the measurement. Also note that there are two battery heaters and two battery temperature sensors in a fully redundant configuration. Only one temperature sensor is shown – the other data are essentially identical.

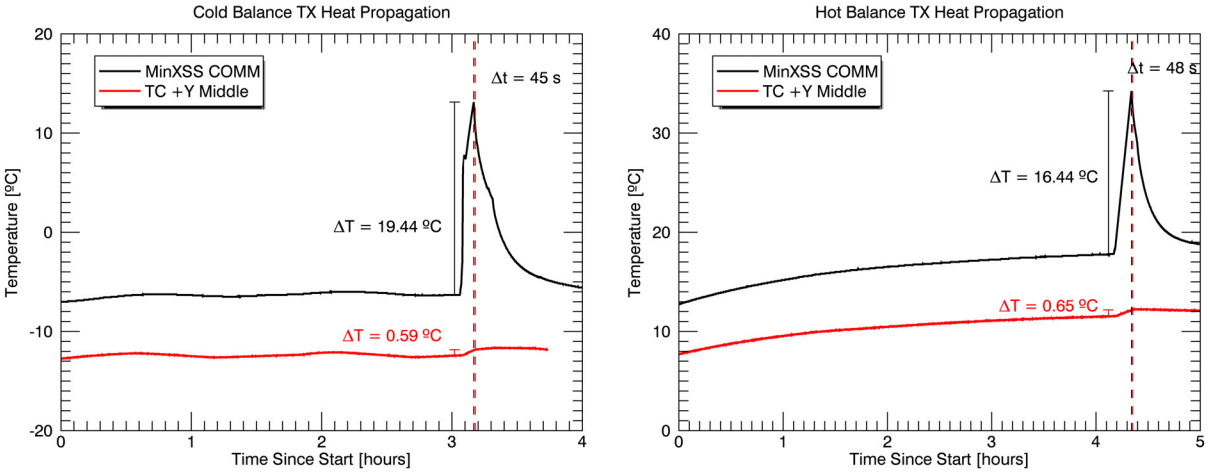

Figure 7.14: Heat propagates from the radio to the radiators. The black curve shows the measured COMM board temperature, which is near the power amplifier of the radio – the primary source of its heat. A corresponding, though delayed and diminished, increase is observed in the radiator plates.

The model performance for the COMM board (bottom row of Figure 7.13) is the best of all comparisons in the cold case and the worst in the hot case, but still within the desirable range. The peak around 3 hours is better matched in the hot balance case. These differences are most likely due to heat load modeling versus actual heat dissipation in the radio. Power measurements of the radio were taken (see Section 7.2.2) and those data used for the time varying heat load in the model. Even without any forward modeling of the heat load, the agreement is good. This heat pulse was used to fine-tune the conductance values for the Kooler-Guide rails, however. Figure 7.14 shows the two relevant temperature measurements.

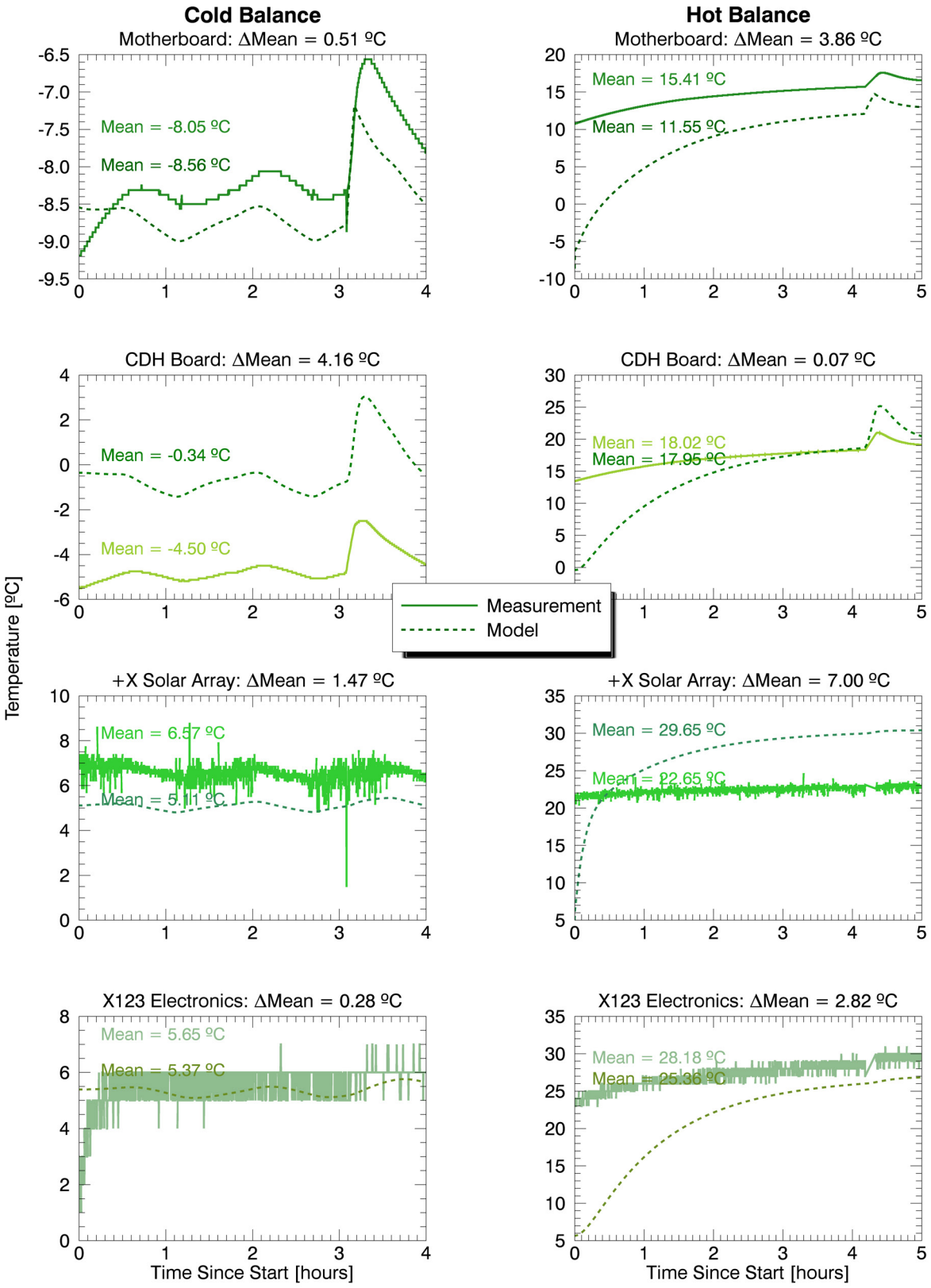

Figure 7.15: Same as Figure 7.13 but for PCBs without time-varying heat loads or heaters.

Figure 7.15 shows the agreement between measurement and model temperatures for the passive PCBs in the system. Passive in this sense simply means that their heat loads are constant but the boards still respond to heat input via conduction and radiation. Here, all 8 modeled temperature means are within the "good enough" 10 °C range of the measured values, 7 of which are within the 5 °desired limit, and 5 of which are within the exceptional limit of 3 °C. The strong temperature response of daughterboards other than the COMM board to the transmission period is primarily due to conduction through the motherboard, rather than through the ± Y walls. As was seen in Figure 7.14, the temperature increase in the ± Y walls was extremely small while the temperature response of the motherboard shown in Figure 7.15 is much stronger; the ∼2 °C increase in motherboard temperature is mirrored in the CDH temperature. This is likely because the daughterboards are connected to the motherboard with 48 pin connectors that have large copper pins soldered to the daughterboard PCB – the conductive path from the copper planes in the daughterboards through the connector is probably stronger than the path through the 8 small copper-beryllium springs in the Kooler-Guide rails.

The body-fixed (+X) solar array has 0.94 mm thick delrin washers on each of the 6 bolts separating it from the +X structural wall. These were intended to provide some thermal isolation between the array and the rest of the system. Solar arrays on orbit can swing to extremely high temperatures – a heat load which is not desired inside the spacecraft where most electronics, especially the X123 TEC, operate better at colder temperatures. The trade off here is that less conduction into the spacecraft means the array itself gets hotter and solar cells become less efficient with increasing temperature. There is adequate power margin in the MinXSS system to account for such inefficiencies in the solar cells, however. In order to determine the actual conductance between the solar array and the +X structural wall, TCs were placed on each in the same Y-Z position. If the junction were 100% conductively efficient, the two temperatures should be equal and if it were 0% efficient, there should be a large difference in temperature. Figure 7.16 shows the measured and modeled temperatures for cold and hot balance in the same format as prior plots.

The difference between the measured temperature on the SA and on the structure just below

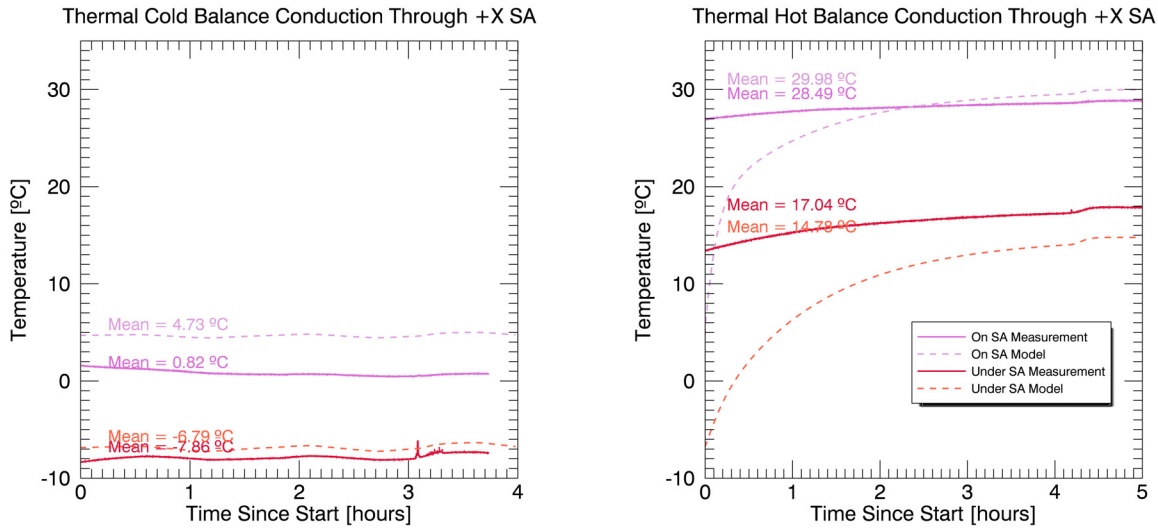

Figure 7.16: Same format as Figure 7.13 but for the body-fixed solar array (SA) and the body it is fixed to.

it for the cold case is 8.68 °C on average, compared to 11.79 °C in the model. In the hot case the measured difference is 11.45 °C and the model difference is 15.2 °C. Differences like these were used to alter the conductivity between the two surfaces in the model until the above result was obtained. The final conductivity value was 0.2 W C^{-1}. All such final conductances can be found in Appendix C.

Figure 7.17 shows the measured temperatures for the X123 detector, the TC on the nearest radiator surface (-Y bottom), and the total power consumed by the X123. For the cold condition, the mean power was computed across the entire time series. For hot balance, the mean power corresponds to hours 3-4, as has been the case for prior analysis. Note that lab measurements indicated that the X123 electronics box itself accounted for about 0.42 W of the total power. The TEC accounts for the difference between the total power and this constant consumption. The X123 detector temperature value corresponds to the detector itself, which is regulated by the TEC so does not vary from its set point. What is crucial for modeling is the heat sink side of the TEC and the radiator it is attached to – the -Y plate.

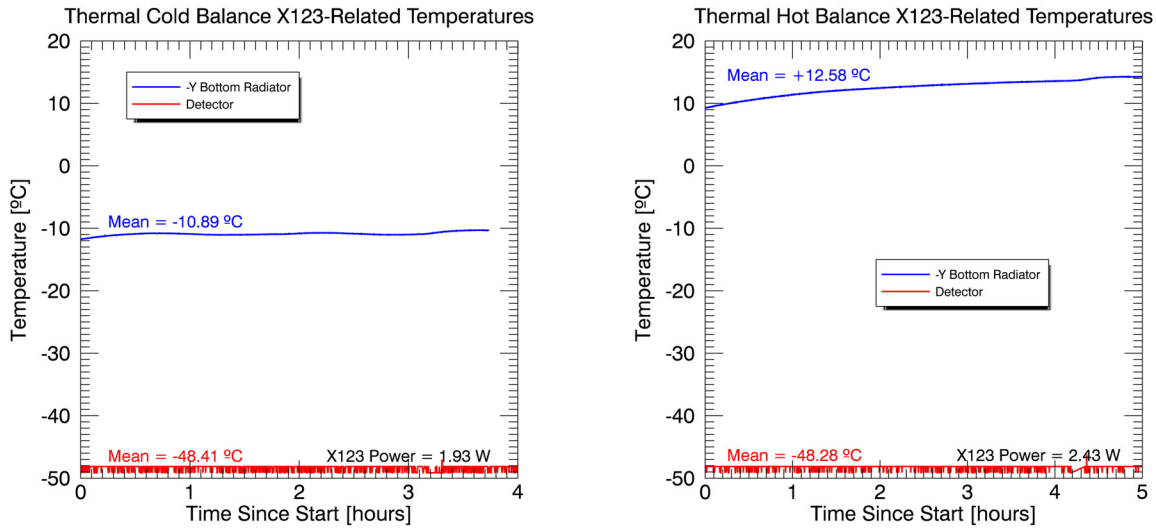

Figure 7.17: Similar format as Figure 7.13 but for measured values only of the X123 detector and the -Y bottom TC – the nearest TC to the X123 detector.

These data were used to create a specialized heat load for the X123 detector in the model. The cold-regulated detector itself is not modeled, instead the brick is used to determine the heat sink environment that the X123 detector head exists within. A logic object was created inside TD that accepts temperature input from a bottom -Y plate node and applies a linear relationship to power based on the power data provided above. The power output from that logic object was used for the heat load of the X123 detector head in the model. In this way, the behavior of the TEC was captured and the positive-feedback loop of the system modeled. This behavior is then easily retained when the MinXSS thermal model is placed in orbit, which is what we turn to next.

7.6 Predicted Orbital Performance

At the time of writing, delays in the deployment of MinXSS FM-1 from the ISS have prevented the possibility of comparing these model predictions to on-orbit measurements. A peer-review paper including these comparisons will be published at a later time. Nevertheless, the predictions are shared here.

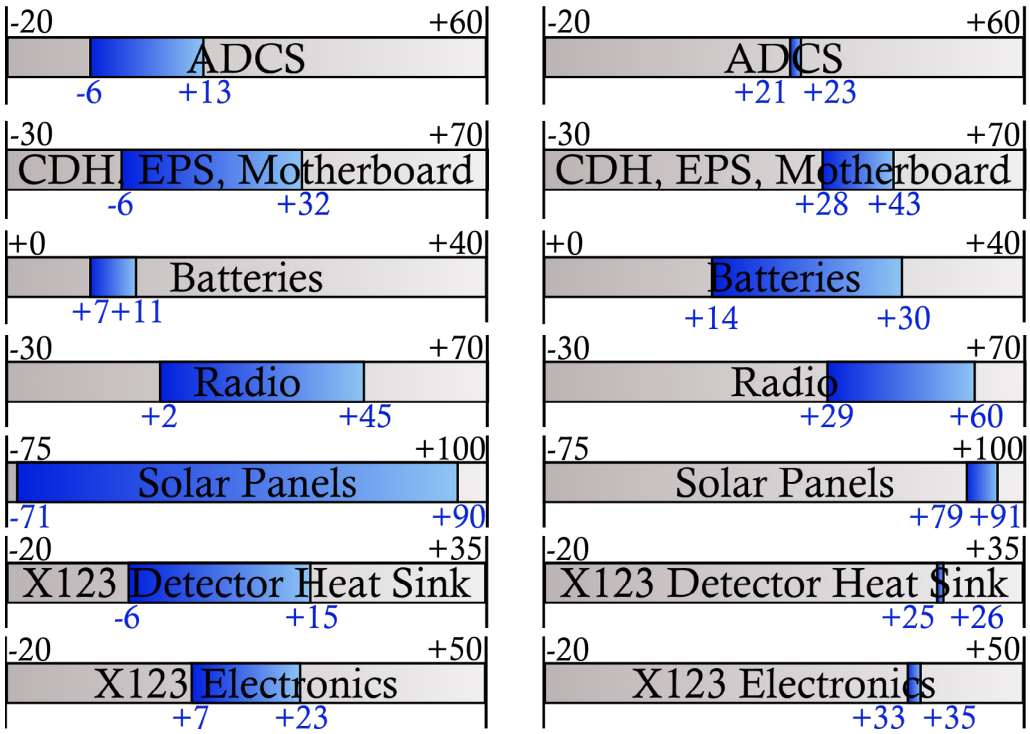

Figure 7.18: The range of temperatures predicted (blue) versus the temperature requirements (grey) for the (left) cold case and (right) hot case. The greatest temperature range is used in all cases. For example, the deployable solar panels swing to greater cold and hot values, so those define the blue range in the figure.

Model Changes to Accommodate Orbital Predictions Two heat loads were altered from thermal balance for orbit predictions: the EPS and radio heat loads. In the thermal balance model, measured power data from the cold and hot cases were used to estimate the amount of heat dissipation in the EPS and those time-dependent heat loads were run in the corresponding model. Similarly for the radio, the time-variation in the model was a direct result of measurements from the test. For orbit predictions, the EPS heat load was set to 1.2 W when the spacecraft is in sunlight and 0 when in eclipse. These values were the mean power values from cold thermal balance, which simulated orbital power cycling with the SAS. This was done with the *hrIllum* parameter automatically generated by TD, which is an eclipse flag. The radio transmit power was increased to the expected flight heat dissipation and a realistic periodicity for orbit introduced: every orbit for 5 orbits in a row, the transmission is enabled for 6 minutes. The vacuum chamber structure

was also removed from the model.

Predicted Temperatures on Orbit Figure 7.18 shows how the predicted temperature ranges compare to the requirements specified in Table 7.1. All are within their requirements in both the cold and hot case for the ISS orbit.

Figure 7.19 shows several of the external spacecraft temperatures in the same fashion as previous figures. The increase in temperature from approximately 5-10 hours is due to the radio transmissions during those orbits. It is only clearly visible in the hot case because the orbit-induced variations are small. It is most clearly identified in the -Z plate because this is where the antenna is bolted and heat readily propagates down the semi-rigid copper cable between the radio and the antenna. The X123 TEC can create a temperature difference between the detector and the heat sink of 85 °C. The heat sink is bolted to the -Y radiator plate, and the temperature at the position closest is the -Y bottom (row 2 of Figure 7.19). With the desired detector temperature of -50 °C, this means the heat sink should be no more than +35 °C. The conduction between the heat sink and the radiator plate is not perfect, however, due to multiple mechanical interfaces. Thus, a radiator plate temperature well below +35 °C is desired. This condition is easily met in the cold case, and is likely to be sufficiently met in the hot case. Only on-orbit performance will provide the clear answer to this question.

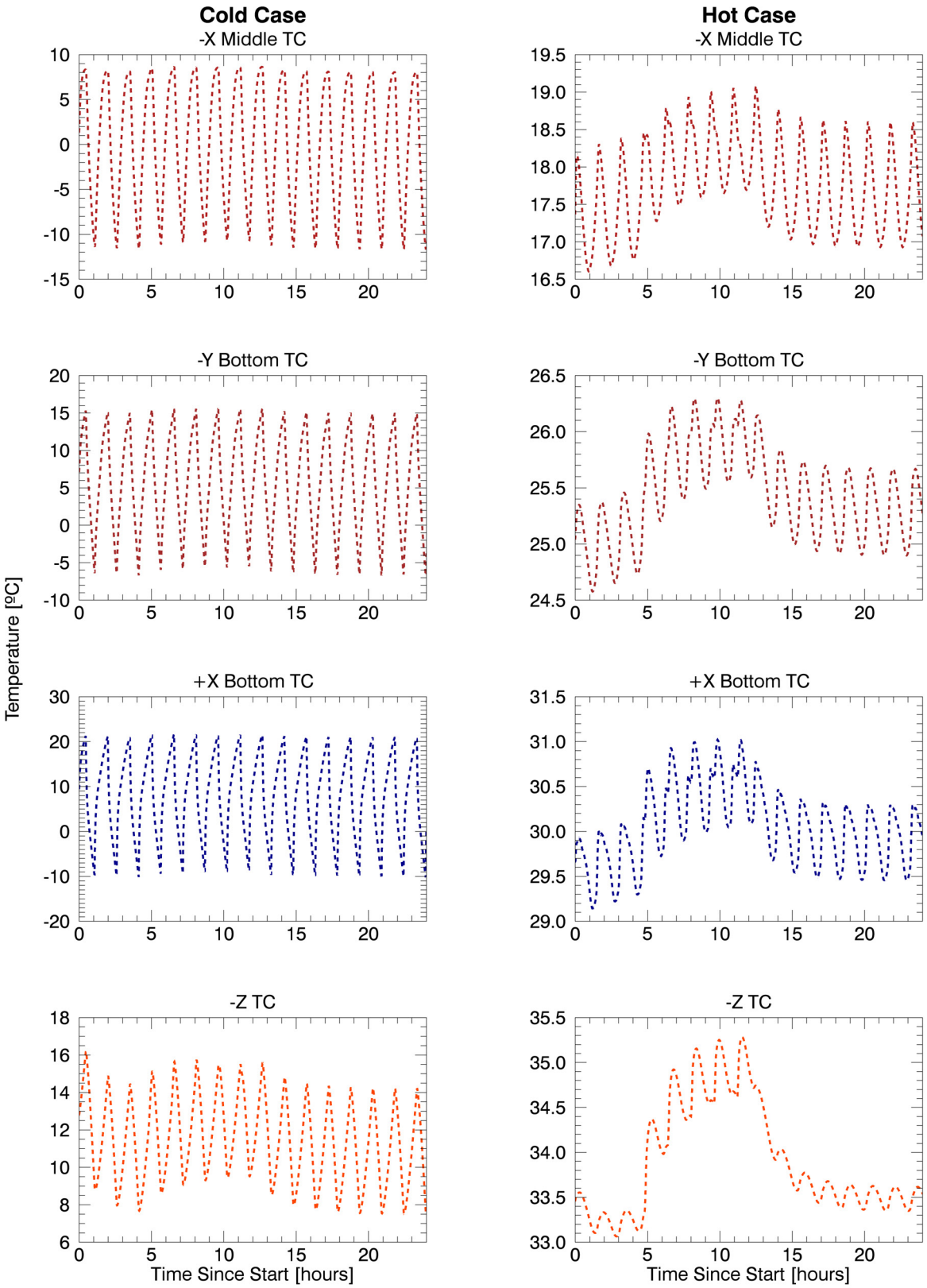

Figure 7.19: Same as Figure 7.11 but for predictions only of the cold ($\beta = 0°$) and hot ($\beta = 75°$) cases. The color schemes, plot ordering, and dashed lines have been maintained for easy comparison. Also, the -Y bottom TC is now plotted in place of +Y top as it is the most important for the X123. The actual time series is nearly identical for both, however.

Figure 7.20 shows the boards with strong time variation in temperature. As expected based on thermal vacuum and thermal balance testing, the EPS board runs 10-15 °C hotter than other daughterboards, such as the CDH. This is a direct consequence of its greater power inefficiency and more power being run through it. Nevertheless, it easily falls between its operating temperature limits of [-30, +70] °C in both cases. The batteries temperature suggests that the heaters will never be needed on orbit when running nominal operations. They will only be powered on if the battery temperature falls below +5 °C for several samples. In the hot case, that is certainly unlikely as the prediction indicates the batteries will be at roughly +30 °C, which is 10 °C lower than their upper-operating limit. The lowest point in the cold case is about 7.5 °C. The model heat loads are representative of science-mode operations, with all subsystems powered on and regular data downlink periods to the ground. The worst case cold condition would be $\beta = 0$ while the spacecraft is in phoenix mode. In this mode, the ADCS, X123, and SPS are all powered off and the radio does not even beacon every 9 seconds as it does in safe mode. The intent of phoenix mode is to bring battery charge level up because it has sunk dangerously low. The heaters will be required in this situation, which is unfortunate because it will be an additional power draw. However, the period of time the heaters are required is inversely proportional to β angle, so this worst case scenario is only representative of a brief period. Additionally, the power draw of the heaters is only ∼3 W, compared to the ∼5 W of normal load from the other subsystems, and ∼10 W of the transmitter. Comprehensive performance tests have established that the time to increase the battery temperature by 2 °C is ∼1 minute. The time for them to fall back 2 °C has not been measured, but it's reasonable to assume that it would be of the same order. A ∼50% duty-cycle on the heaters would result in an average power draw of ∼1.5 W.

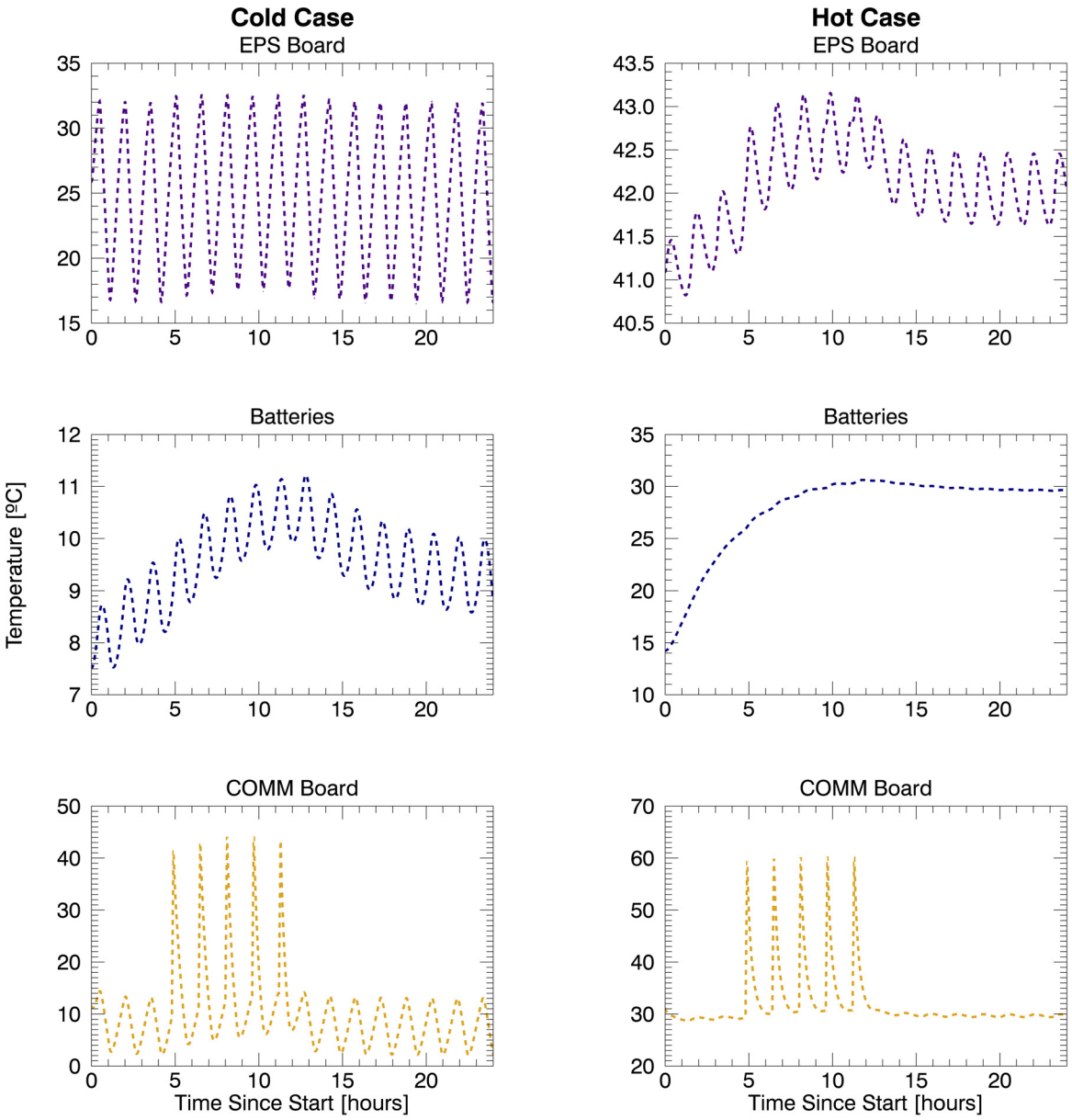

Figure 7.20: Same as Figure 7.19 but for the boards corresponding to Figure 7.13.

The COMM board temperature is one that should be monitored closely on orbit. It is a strong function of the power setting of the radio. Figure 7.20 is the result of a radio power setting of 140, which corresponds to a calculated heat load of 6.31 W. Table 7.4 contains measurements of the actual Li-1 radio in MinXSS FM-1. If the model instead uses the maximum power setting and the input power directly, the COMM board temperature reaches 100 °C. Experience with the CSSWE CubeSat, which ran for 2.5 years with the same radio, indicates that the COMM board temperature

should be expected to reach about 50 °C. There is uncertainty in that number, however, because CSSWE only had the internal radio temperature on its processor, not an independent temperature sensor closer to the power amplifier of the radio (where most of the heat is dissipated). Comparisons between this internal radio temperature and the COMM board temperature during thermal balance indicate that there's a 5-10 °C difference between the two, where the COMM board is colder when not transmitting and hotter when it is. Based on these predictions, it would be prudent to closely monitor the COMM board temperature on orbit and consider reducing the radio power setting if temperatures are approaching or exceeding the +70 °C operating limit. This is not a decision without risk. The radio has been known to lock up when this command is sent, which causes it to stop transmitting intelligible packets and it begins to rapidly heat. Flight software was written to mitigate this; the CDH will automatically power cycle the radio if the radio fails to send the CDH its 10-second status packet for more than 5 minutes. This functionality has been verified on the ground. There is also an additional risk that the radio power level could be reduced to a point where there is insufficient link margin for receipt of spacecraft transmissions. No autonomous software would undo this, but commands could still be used to set the radio power level higher again with no difficulty.

Figure 7.21 shows the ISS orbit predictions for the same PCBs that were shown in Figure 7.15. Again, the $\beta = 0°$orbit (cold case) with significant periods of eclipse results in wide temperature variation. The impact of the radio transmissions is apparent in the cold case for the motherboard and CDH board but is quite obvious in all of the boards in hot balance. The motherboard and CDH are well within their operating temperature limits of [-30, +70] °C in both cases. The X123 electronics temperature also falls within the operating temperature limits of [-20, +50] °C in both cases. The solar arrays have the largest temperature variation of any component, as expected. They swing between -20 °C and +80 °C in the cold case and run at a nearly constant 81 °C in the hot case. Not shown are the deployable solar panels, which swing between -71 °C and +90 °C in the cold case and are nearly constant at +85 °C in the hot case. This approaches their upper operating temperature limit of +100 °C. That limit is not a hard one; rather, it is a "desirement"

Table 7.4: MinXSS FM-1 power measurements with an input voltage of 8.48 V and a 40 dBm attenuator. Measurements courtesy of Bena Mero.

Power Setting	Input Current [A]	Input Power [W]	Output Power [dBm] (w/ attenuation)	Output Power [dBm] (w/o attenuation)	Output Power [W]	Efficiency [%]	Heat load [W]
100	0.155	0.57	-33.48	6.52	0.00449	0.8	0.56
110	0.300	1.80	-18.93	21.07	0.128	7.1	1.67
120	0.570	4.09	-11.12	28.88	0.773	18.9	3.31
125	0.770	5.78	-8.22	31.78	1.51	26.1	4.28
130	0.910	6.97	-6.92	33.08	2.03	29.2	4.94
135	0.108	8.37	-5.49	34.51	2.82	33.8	5.54
140	0.121	9.51	-4.94	35.06	3.21	33.7	6.31
145	0.132	10.45	-4.33	35.67	3.69	35.3	6.76
150	0.143	11.38	-4.07	35.93	3.92	34.4	7.46
155	0.152	12.14	-3.75	36.25	4.22	34.7	7.93
160	0.161	12.91	-3.56	36.44	4.41	34.1	8.50
165	0.170	13.63	-3.41	36.59	4.56	33.5	9.07
170	0.179	14.43	-3.33	36.67	4.65	32.2	9.79
175	0.188	15.20	-3.25	36.75	4.73	31.1	10.46

to avoid falling too far down the efficiency curve of the solar cells. The +X body-fixed solar arrays were intentionally partially isolated from the structure of the spacecraft with delrin washers to reduce the impact of the wide temperature variation on the rest of the system. The trade-off in this context is that the solar panel itself gets hotter. However, these predictions indicate that the solar array should stay within the range of acceptability.

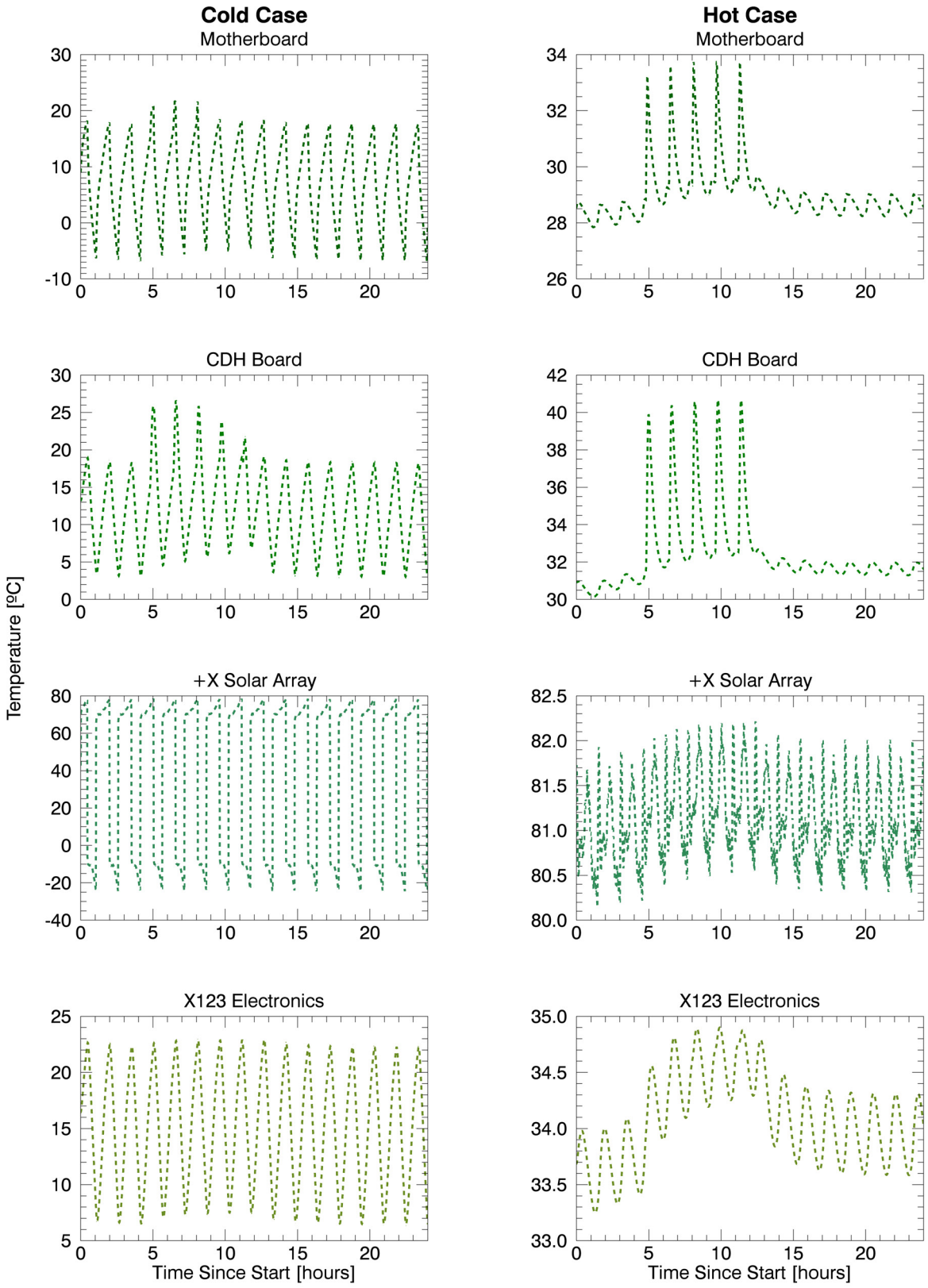

Figure 7.21: Same as Figure 7.19 but for the boards corresponding to Figure 7.15.

7.7 Summary

Thermal balance analysis has been performed for hot and cold environments in order to tune the thermal model for more accurate orbit predictions. All 22 measurement and model temperatures were found to agree within 10 °C. 21 of those agreed to better than 5 °C, 14 of which agreed to better than 3 °C. Predictions were made for the ISS-orbit at high and low β (i.e., short and long eclipse), and all 22 temperatures were within operating temperature limits. The radio is the sole source of concern; its heat load is uncertain and should be monitored closely on orbit to determine if its temperature reaches its upper limit. In such a case, the option to reduce the radio power setting should be considered. Realistic duration transmissions were performed during thermal vacuum testing, including at the hot operational cycle dwells, and radio temperatures did not exceed limits. However, this was not done at the maximum power setting so there remains some risk of reaching the temperature limit on orbit.

The details of mechanical implementation for MinXSS abound, but the CubeSat standard itself ensures that there are more similarities than differences with other CubeSats. Furthermore, the fidelity of thermal modeling washes out many of the nuances in such a way that the model and corresponding results of this work should have value for other CubeSat projects. In particular, the concern for the radio hot temperature during data downlink is a concern for MinXSS and possibly for other CubeSats. It is prudent to have a heater for the batteries to keep them above 0 °C, but it appears that the battery heater will be inactive for most of the MinXSS mission, due in part to the passive thermal design of conductively isolating the batteries.

Chapter 8

Summary and Future Work

The unifying element of the work contained within this dissertation is the study of solar eruptive events – primarily coronal mass ejections (CMEs) and solar flares. These two types of events represent about the same amount of energy, upwards of 10^{25} J, placing them among the most energetic events in the solar system. The energy storage typically takes tens of days but its release occurs over a few minutes to a few hours. That energy powers numerous physical processes in plasma regimes that push the limits of theory, instrumentation, data analysis, and laboratory experiments. Furthermore, these explosions occur about once daily, on average. Thus, solar eruptions are fertile ground for scientific study. Chapter 2 provided background information on the scientific consensus for this field of study. This includes a tracing of energy propagation from the solar core to the heliosphere, the mechanisms by which energy is slowly stored and explosively released in the corona; and descriptions of the instruments capable of observing this process that were used in subsequent chapters.

There are practical motivations driving this research as well. When the harsh electromagnetic (EM) radiation from solar flares interacts with the earth's atmosphere and when the plasma from coronal mass ejections interacts with the earth's magnetic field, the consequences are felt. For example, radio communications can be disrupted, forcing airlines to reroute. Havoc can be wreaked by geomagnetic storms with degraded or even loss of GPS navigation, which impacts agricultural and oil drilling technologies that now depend on precise position knowledge via GPS receivers. As a final example, power grids can be overloaded, causing cities to be without electricity for hours or

weeks. These and other impacts indicate that the sun has dramatic interactions with Earth that go far beyond the light and warmth it also provides. The true test of any science is its ability to make predictions, and there is a strong push from the space weather community to improve our ability to predict when and where solar eruptive events will occur as well as their magnitude. Much research is being done to improve our prediction capabilities for solar flares, but to date, the best we can do is provide a likelihood forecast. Since the impact of a flare results from its EM emission, the light we receive indicating its occurrence arrives at the same time as the light that does the damage. Coronal mass ejections, on the other hand, take several hours to a few days to reach Earth, so "nowcasting" is possible.

Chapter 1 laid out the questions that this dissertation sought to address, which all related to the physics of solar eruptive events, how observations of one component of them might be useful proxies for other parts (e.g., dimmings relationship to CMEs), and what is needed to develop new instruments to observe them. In Chapters 3 - 5 we addressed the Introduction's questions related to dimming and CMEs. The research followed a basic flow: from the physics driving the observations, to detailed case studies, to analysis of many events in a semi-statistical approach. It was made clear that coronal dimming can be detected in EUV irradiance, which was shown with the SDO/EVE data that have a spectral resolution of 1 Å. The precision of EVE was computed for the various extracted emission lines used in this study: the average precision for dimming lines is 0.23% and the average for non-dimming lines is 0.66%, as compared to typical dimming depths of about 2%. Thus, the signal exists but is not very strong. This is the ideal scenario for superposed epoch analysis. In this type of analysis, time series data from numerous events that have a common critical time (e.g., time of flare peak) and aligned at that "key" time, stacked "on top" of each other and then the statistical moments at each point in time computed to come up with the average behavioral response to the event. This statistical method is a good one for pulling a weak signal out of noise. This type of analysis was performed in Mason and Hoeksema (2010) with magnetic field complexity proxies and solar flare key times. Future work will do the same with the coronal dimming irradiance light curves. Nevertheless, we've shown here that spatial resolution

is not required to observe dimming. It only requires sufficient spectral resolution and instrument precision. To date, we have only considered events that do not have overlap in time. It may be possible to characterize the onset of dimming even if another event occurs during the hours-long depressed period, but this is left to future work.

By first segregating the various mechanisms that can cause an apparent emission decrease as measured by imperfect instruments, it was possible to identify their unique observational characteristics. This was done initially from first principles – what are all the ways plasma's light could dim? Instruments have finite wavelength sensitivity but typically sample several wavelengths, which can then be used to determine if dimming in one wavelength corresponds to a brightening in another. Such a situation is quite common and is indicative of temperature variation in the source plasma – it is well established that the temperature distribution in the corona is wide and time-varying. By using instruments that complement each other's strengths, it is possible to identify the dimming signatures, even when they occur simultaneously or co-spatially. This is possible because of the third critical parameter: temperature. Spectral information translates into temperature information, which can be fairly precise when prominent emission lines are present. Temperature and space are linked in the coronal plasma and it was shown that the temperature evolution of the plasma could be isolated spatially with AIA or with temperature information from EVE. Thus, ample time, space, and temperature resolution provide a means of deconvolving dimming signatures in order to isolate the one we care about most: mass-loss dimming, which correlates to the CME. The development of this deconvolution strategy is the main result of Chapter 4. It used SDO/EVE measurements of coronal emission lines in the 171 Å - 304 Å range.

We also found that EUV irradiance dimmings have a characteristic shape, as expected based on the image analysis from numerous other studies. Just like the image data, the irradiance during a dimming event begins with a sudden decrease in emission that lasts a few tens of minutes followed by several hours of depressed emission before recovery. Raw irradiance light curves often also have large intensity peaks due to the temperature evolution induced by the flare, which we found could be removed using warmer emission lines. The new "corrected" dimming light curve

could then be parameterized in terms of slope and depth. It is also possible to characterize the duration of dimming, both in terms of how long it takes to reach a particular intensity and how long until the emission recovers to its pre-event level. In practice, however, dynamics in the corona mean that something is always changing on timescales of many hours. For example, active regions anywhere on the disk evolve or eruptions on the far-side can propagate to the front size and cause sympathetic eruptions. Thus, duration is likely not a particularly useful parameterization. One major limitation here is that filament eruptions likely cannot be parameterized with irradiance. Filaments tend to exist for hours or days prior to the eruptive event and are dark at the pre-event point used to normalize the irradiance and remain dark as they erupt. Filaments also contain a considerable fraction of the mass of CMEs when they are present. If the filament happens to cause an obscuration, it may be possible to estimate its density. Imaging data are required to estimate its volume. Hence, irradiance-based CME masses are lower limits in the case of filament-eruption (as opposed to "plain" plasma pileup) CMEs.

We proposed two hypotheses about the relationship between coronal dimming light curves and CME kinetic energy. The more massive a CME, the more emitting plasma it steals away with it, so the darkness in the coronal void should be deeper. In other words, dimming magnitude should be proportional to CME mass. We derived a physical relationship between these two and found that the CME mass should go as the $\sqrt{\text{depth}}$. Secondly, the faster a CME departs, the faster the dimming light curve should reach its minimum value. In the limiting case, if a volume of plasma were to suddenly blink out in the corona, there would be an instantaneous drop in emission. Thus, the slope of a dimming light curve should also be directly proportional to the speed of a CME. Space weather forecasters care about CME mass because it is an indicator of its geoeffectiness, i.e., a more massive CME tends to cause more problems if it impacts Earth. We derived a physical relationship here too, that the CME speed should go as the slope/depth. However, several assumptions were made during the derivation and we may need to test these assumptions in future work. For example, we assumed that the size of CME initiation in the corona is the same for all events. We also assumed that the midpoint of the slope should correspond to the average CME velocity in its acceleration

profile. That may be true but we only had coronagraph data that can only observe down to about 2 $R_\odot$, by which point the CME has usually stopped accelerating. Furthermore, for space weather we care more about the terminal velocity than the velocity at the midpoint of acceleration. Because we know the distance between the sun and earth, knowledge of the interplanetary CME speed can be translated into an earth-arrival time, which is the most important number to space weather forecasters. We did however find an empirical relationship directly between CME speed and dimming slope. The Pearson correlation coefficient was high, though there was appreciable scatter in the data. Analysis of more events should determine whether this relationship holds true in general. If a new instrument could provide dimming irradiance measurements between about 150 and 350 Å for characterizing dimming and obtain an estimate of CME initiation position (e.g., by using an observed flare location as a reasonable proxy), the estimated CME kinetic parameters could be input into the existing WSA-ENLIL model (Parsons et al. 2011) to propagate the disturbance through interplanetary space and output predicted arrival time and impact. The best results of the CME-dimming correlations are summarized by the equations

$$\begin{aligned} v_{CME}\left[\frac{km}{s}\right] &\approx 2.36\times10^{6}\left[\frac{km}{\%}\right]\times s_{dim}\left[\frac{\%}{s}\right] \\ m_{CME}\,[g] &\approx 2.59\times10^{15}\left[\frac{g}{\%}\right]\times\sqrt{d_{dim}}\,[\%] \end{aligned} \tag{8.1}$$

where v_{CME} is the speed of the CME, s_{dim} is the slope of dimming, m_{CME} is the mass of the CME, and d_{dim} is the depth of dimming.

The next logical step in this series of studies is to apply the methods already developed to a truly statistically-sized sample. The Extreme Ultraviolet (EUV) Variability Experiment (EVE) Multiple EUV Grating Spectrographs-A (MEGS-A) is the primary source of data herein, so searching and characterizing its entire 4-year history of observations for dimming will be the means by which a large statistical sample is acquired. Already, preliminary results indicate that hundreds of dimmings should be expected (recall Figure 3.4). In order to characterize this number of dimming events, automated routines will have to be further developed, refined, and validated. The publicly available Coordinated Data Analysis Workshops (CDAW) CME Catalog now provides CME masses

and speeds that span this 4 year period and beyond. By combining these data, the correlations developed in Chapter 5 can be bolstered and new insights gained.

Additionally, automated methods of dimming spatial identification are now available. Larisza Krista at the High Altitude Observatory is a collaborator and has developed one such method using direct imaging from the Atmospheric Imaging Assembly (AIA). A group at the Royal Observatory of Belgium has developed a similar algorithm that uses difference images for identification. Comparison of the results of these methods and those from the automated EVE dimming characterization should present new questions and discoveries.

Not included in any of the prior discussion is the magnetic field. Chapter 2 established that the coronal magnetic field is the source of solar eruptions. As such, it cannot be ignored and analysis of it promises to result in a deeper understanding of dimming. To date, measurements of the coronal magnetic field have been prohibitively difficult and sparse. Models have been developed to propagate the measured photospheric magnetic field into the corona, which have been useful but a lack of coronal measurements has still been debilitating. That is now changing with the forthcoming opening of the Daniel K. Inouye Solar Telescope (DKIST), which will provide routine measurements of coronal magnetic field.

Another avenue of future research is to use data from the PROBA2 spacecraft, which is operated at the Royal Observatory of Belgium. It contains the Large Yield Radiometer (LYRA), an instrument similar to EVE, and the Sun Watcher using APS and Image Processing (SWAP), similar to AIA. One of the exciting advantages of SWAP is that it has a much wider field of view than AIA, extending almost all the way to the inner boundary of coronagraph images. These data can be used to observe CME propagation in the low corona, which should correlate more strongly with the dimming irradiance light curve.

Finally, the findings of Chapters 3 - 5 can be applied in the development of new instruments that specifically target dimming irradiance. Those studies have shown that spatial resolution is not required to isolate mass-loss dimming. Therefore, an EUV spectrograph, much like the EVE MEGS-A instrument but equipped with a telescope, could be pointed toward stars other than

the sun. These stellar data would provide a novel measurement of extrasolar CME kinetic energy for the astrophysics community. The exoplanet community, in particular, is interested in such measurements because the flux of stellar plasma particles has major implications for the habitability of exoplanets. Such an instrument can be quite small in volume and mass and requires little power so could be easily added to solar missions or turned into a dedicated astrophysics mission, such as a NASA Small Explorer (SMEX) or CubeSat, by adding a telescope to the front of the instrument. Proposals for both of these are presently in the works at LASP. Clearly, there is no shortage of work to be done in the field of coronal dimming and its relationship to coronal mass ejections.

The remaining chapters of this dissertation, 6 and 7, focus on the development of a new mission to study solar flares, the active sun, and the impact on Earth's upper atmosphere. One of the surprising lingering questions in solar physics is how energy is spectrally distributed in solar flares. No two solar flares are identical, but the first step in fledgling sciences is typically classification of observations. To date, the dominant classification of solar flares has been done with a single wavelength band in the X-rays, as measured by the long history of Geostationary Operational Environmental Satellites (GOES). Because solar flares are so energetic, they initiate numerous physical processes that have emissions spanning the spectrum from gamma to radio. And therein lies the explanation for why we have not yet answered how energy is distributed in a solar flare: there is no single instrument that can spectrally resolve all wavelengths. Instead, data from multiple instruments with concurrent observations must be combined. Also surprising is that the region of a flare spectrum expected to have the greatest enhancement, the soft x-rays (SXRs), has had very few spectral measurements. The Miniature X-ray Solar Spectrometer (MinXSS) CubeSat will provide spectral measurements across the majority of the SXR band for the first time. More details of the science motivation and system design for the MinXSS mission are the subject of Chapter 6. All of the science questions posed in the Introduction have yet to be addressed because MinXSS has yet to deploy from the International Space Station. However, the engineering questions have largely been addressed.

The MinXSS measurement is made possible with a relatively new technology: a silicon drift

detector. The detector must be kept cooled to prevent thermal noise from drowning out the signal. This is achieved with a thermoelectric cooler – an active thermal management system that can create a ΔT of 85 °C. Because the desired temperature of the detector is -50 °C, this means that the heat sink on the detector must be kept below +35 °C. This driving requirement led to the need for a detailed thermal model for the MinXSS CubeSat. Chapter 7 describes the thermal design of the system, the thermal model developed of it, the thermal vacuum cycle and thermal balance testing performed, the forward modeling used to match thermal balance test measurements, and the temperature predictions for different orbit configurations. At the time of this writing, MinXSS Flight Model 1 (FM-1) is onboard the International Space Station (ISS) awaiting deployment and FM-2 has yet to be delivered. As such, comparisons between model predictions and on-orbit measurements are not yet possible. This comparison is the obvious next step for the thermal modeling effort. With sufficient time between the deployment of FM-1 and the delivery of FM-2, modifications to the thermal design could be made to improve performance in any high-thermal-risk areas. However, this is not expected to be necessary as the thermal balance testing was a test dedicated to tuning the thermal model to within a few °C, and the subsequent orbital predictions indicate that nothing should be at risk in a way that could not be managed by changing software defaults and/or commanding. Forward modeling in this application was the tuning of heat loads, conductivities, absorptivities, and emissivities of the various subsystems. Many of these tuned parameters could be applied to other CubeSat projects that may not have the resources for a dedicated thermal balance test and modeling effort. The procedure and results can be found in Chapter 7 and the model parameters in Appendix C.

In summary, this dissertation on solar eruptive events presents a new theoretical and observational framework for coronal dimming; establishes a method of flare and dimming deconvolution for irradiance measurements; establishes correlations between dimming irradiance light curve parameters and coronal mass ejection kinetic energy; outlines the development of a new, low-cost CubeSat mission to address important outstanding questions in solar physics; and describes spacecraft thermal testing and modeling that ensure the adequate performance of the science instruments and

supporting subsystems for the CubeSat.

Bibliography

Acton, L. W., Weston, D. C., and Bruner, M. E. (1999). Deriving solar X ray irradiance from Yohkoh observations. Journal of Geophysical Research, 104(A7):14827.

American Society for Testing and Materials (2000). Solar Spectra: Air Mass Zero.

Andretta, V., Del Zanna, G., and Jordan, S. D. (2003). The EUV helium spectrum in the quiet Sun: A by-product of coronal emission? Astronomy and Astrophysics, 400(2):737–752.

Arp, U., Clark, C., Deng, L., Faradzhev, N., Farrell, A., Furst, M., Grantham, S., Hagley, E., Hill, S., Lucatorto, T., Shaw, P.-S., Tarrio, C., and Vest, R. (2011). SURF III: A flexible synchrotron radiation source for radiometry and research. Nuclear Instruments and Methods in Physics Research Section A: Accelerators, Spectrometers, Detectors and Associated Equipment, 649(1):12–14.

Aschwanden, M. J. (2004). Physics of the Solar Corona. An Introduction.

Aschwanden, M. J. (2009). 4-D modeling of CME expansion and EUV dimming observed with STEREO/EUVI. Annales Geophysicae, 27(8):3275–3286.

Aschwanden, M. J., Nitta, N. V., Wuelser, J.-P., Lemen, J. R., Sandman, A., Vourlidas, A., and Colaninno, R. C. (2009a). First Measurements of the Mass of Coronal Mass Ejections From the EUV Dimming Observed With Stereo EUVI A + B Spacecraft. The Astrophysical Journal, 706(1):376–392.

Aschwanden, M. J., Wuelser, J. P., Nitta, N. V., and Lemen, J. R. (2009b). Solar Flare and CME Observations with STEREO/EUVI. Solar Physics, 256(1-2):3–40.

Attrill, G. D. R., Harra, L. K., van Driel-Gesztelyi, L., and Wills-Davey, M. J. (2010). Revealing the Fine Structure of Coronal Dimmings andAssociated Flows withHinode/EIS. Solar Physics, 264(1):119–147.

Bailey, S. M., Woods, T. N., Barth, C. A., Solomon, S. C., Canfield, L. R., and Korde, R. (2000). Measurements of the solar soft X-ray irradiance by the Student Nitric Oxide Explorer : First analysis and underflight calibrations. Journal of Geophysical Research, 105:27179–193.

Baker, D. N., Jaynes, A. N., Hoxie, V. C., Thorne, R. M., Foster, J. C., Li, X., Fennell, J. F., Wygant, J. R., Kanekal, S. G., Erickson, P. J., Kurth, W., Li, W., Ma, Q., Schiller, Q., Blum, L., Malaspina, D. M., Gerrard, A., and Lanzerotti, L. J. (2014). An impenetrable barrier to ultrarelativistic electrons in the Van Allen radiation belts. Nature, 515(7528):531–4.

Basu, . and Antia, . (1995). Helium abundance in the solar envelope. Monthly Notices of the Royal Astronomical Society, 276(4):1402–1408.

Bein, B. M., Temmer, M., Vourlidas, A., Veronig, A. M., and Utz, D. (2013). THE HEIGHT EVOLUTION OF THE TRUE CORONAL MASS EJECTION MASS DERIVED FROM STEREO COR1 AND COR2 OBSERVATIONS. 31.

Bevington, P. (2003). Data reduction and error analysis for the physical sciences. McGraw-Hill, Boston.

Bewsher, D., Harrison, R. A., and Brown, D. S. (2008). The relationship between EUV dimming and coronal mass ejections I. Statistical study and probability model. Astronomy & Astrophysics, 478:897–906.

Blum, L. and Schiller, Q. (2012). Characterization and Testing of an Energetic Particle Telescope for a CubeSat Platform.

Blum, L. W., Schiller, Q., Li, X., Millan, R., Halford, A., and Woodger, L. (2013). New conjunctive CubeSat and balloon measurements to quantify rapid energetic electron precipitation. Geophysical Research Letters, 40(22):5833–5837.

Brueckner, G. E., Howard, R. A., Koomen, M. J., Korendyke, C. M., Michels, D. J., Moses, J. D., Socker, D. G., Dere, K. P., Lamy, P. L., Llebaria, A., Bout, M. V., Schwenn, R., Simnett, G. M., Bedford, D. K., and Eyles, C. J. (1995). The Large Angle Spectroscopic Coronagraph. Solar Physics, 162:357–402.

Caspi, A., Krucker, S., and Lin, R. P. (2014a). STATISTICAL PROPERTIES OF SUPER-HOT SOLAR FLARES. The Astrophysical Journal, 781(1):43.

Caspi, A. and Lin, R. P. (2010). RHESSI Line and Continuum Observations of Super-hot Flare Plasma. The Astrophysical Journal, 725:L161–166.

Caspi, A., McTiernan, J. M., and Warren, H. P. (2014b). CONSTRAINING SOLAR FLARE DIFFERENTIAL EMISSION MEASURES WITH EVE AND RHESSI. The Astrophysical Journal, 788(2):L31.

Caspi, A., Woods, T. N., and Warren, H. P. (2015). New Observations of the Solar 0.55 Kev Soft X-Ray Spectrum. The Astrophysical Journal, 802(1):L2.

Chaisson, E. and McMillan, S. (1999). Astronomy Today. Prentice-Hall, 3rd editio edition.

Chamberlin, P. C., Woods, T. N., and Eparvier, F. G. (2007). Flare Irradiance Spectral Model (FISM): Daily component algorithms and results. Space Weather, 5(7):n/a–n/a.

Chamberlin, P. C., Woods, T. N., and Eparvier, F. G. (2008). Flare Irradiance Spectral Model (FISM): Flare component algorithms and results. Space Weather, 6(5):n/a–n/a.

Chamberlin, P. C., Woods, T. N., Eparvier, F. G., and Jones, A. R. (2009). <title>Next generation x-ray sensor (XRS) for the NOAA GOES-R satellite series</title>. In Fineschi, S. and Fennelly, J. A., editors, SPIE Optical Engineering + Applications, pages 743802–743802–10. International Society for Optics and Photonics.

Chandrasekhar, S. (1939). An introduction to the study of stellar structure. The University of Chicago Press.

Chen, P. F., Fang, C., and Shibata, K. (2005). A Full View of EIT Waves. The Astrophysical Journal, 622(2):1202–1210.

Chen, P. F., Wu, S. T., Shibata, K., and Fang, C. (2002). Evidence of EIT and Moreton Waves in Numerical Simulations. The Astrophysical Journal, 572(1):L99–L102.

Christensen-Dalsgaard, J., Dappen, W., Ajukov, S. V., Anderson, E. R., Antia, H. M., Basu, S., Baturin, V. A., Berthomieu, G., Chaboyer, B., Chitre, S. M., Cox, A. N., Demarque, P., Donatowicz, J., Dziembowski, W. A., Gabriel, M., Gough, D. O., Guenther, D. B., Guzik, J. A., Harvey, J. W., Hill, F., Houdek, G., Iglesias, C. A., Kosovichev, A. G., Leibacher, J. W., Morel, P., Proffitt, C. R., Provost, J., Reiter, J., Rhodes, E. J., Rogers, F. J., Roxburgh, I. W., Thompson, M. J., and Ulrich, R. K. (1996). The Current State of Solar Modeling. Science, 272(5266):1286–1292.

Christensen-Dalsgaard, J., Gough, D. O., and Thompson, M. J. (1991). The depth of the solar convection zone. The Astrophysical Journal, 378:413.

Colaninno, R. C. and Vourlidas, A. (2009). First Determination of the True Mass of Coronal Mass Ejections: A Novel Approach To Using the Two Stereo Viewpoints. The Astrophysical Journal, 698:852–858.

Colaninno, R. C., Vourlidas, A., and Wu, C. C. (2013). Quantitative comparison of methods for predicting the arrival ofcoronal mass ejections at Earth based on multiview imaging. Journal of Geophysical Research: Space Physics, 118(11):6866–6879.

DeForest, C. E., Howard, T. A., and McComas, D. J. (2014). Inbound Waves in the Solar Corona: A Direct Indicator of Alfvén Surface Location. The Astrophysical Journal, 787(2):124.

Dere, K. P., Landi, E., Mason, H. E., Monsignori Fossi, B. C., and Young, P. R. (1997). CHIANTI - an atomic database for emission lines. Astronomy and Astrophysics Supplement Series, 125:149–173.

Domingo, V., Fleck, B., and Poland, A. I. (1995). The SOHO mission: An overview. Solar Physics, 162(1-2):1–37.

Doschek, G. A. (1990). Soft X-ray spectroscopy of solar flares - an overview. The Astrophysical Journal Supplement Series, 73:117.

Eddy, J. A. (1979). A New Sun: The Solar Results from Skylab. National Aeronautics and Space Administration, Washington, D. C.

Eddy, J. A. (2009). The Sun, the Earth, and Near-Earth Space. NASA.

Emslie, A. G., Dennis, B. R., Shih, A. Y., Chamberlin, P. C., Mewaldt, R. A., Moore, C. S., Share, G. H., Vourlidas, A., and Welsch, B. T. (2012). Global Energetics of Thirty-Eight Large Solar Eruptive Events. The Astrophysical Journal, 759(1):71.

Fletcher, L., Dennis, B. R., Hudson, H. S., Krucker, S., Phillips, K., Veronig, A. M., Battaglia, M., Bone, L., Caspi, A., Chen, Q., Gallagher, P. T., Grigis, P. T., Ji, H., Liu, W., Milligan, R. O., and Temmer, M. (2011). An Observational Overview of Solar Flares. Space Science Reviews, 159(1-4):19–106.

Forbes, T. G. (2000). A review on the genesis of coronal mass ejections. Journal of Geophysical Research: Space Physics, 105(A10):23153–23165.

Gary, G. A. (2001). Plasma Beta above a Solar Active Region: Rethinking the Paradigm. Solar Physics, 203(1):71–86.

Gerhardt, D. (2010). Passive Magnetic Attitude Control for CubeSat Spacecraft.

Gerhardt, D. and Palo, S. (2016a). Volume Magnetization for System-Level Testing of Magnetic Materials within Small Satellites.

Gerhardt, D. and Palo, S. E. (2016b). Passive Magnetic Attitude Control Settling Prediction with On-Orbit Verification using the Colorado Student Space Weather Experiment CubeSat.

Gerhardt, D., Palo, S. E., Schiller, Q., Blum, L., Li, X., and Kohnert, R. (2013). The Colorado Student Space Weather Experiment (CSSWE) On-Orbit Performance. Journal of Small Satellites, 3(1):265–281.

Gilbert, H. R., Inglis, a. R., Mays, M. L., Ofman, L., Thompson, B. J., and Young, C. a. (2013). Energy Release From Impacting Prominence Material Following the 2011 June 7 Eruption. The Astrophysical Journal, 776(1):L12.

Giordano, S., Antonucci, E., and Dodero, M. (2000). OXYGEN VELOCITIES IN A POLAR CORONAL. Advances in Space Research, 25(9):1927–1930.

Gopalswamy, N., Yashiro, S., Michalek, G., Stenborg, G., Vourlidas, A., L, F. S., and Howard, R. A. (2009). The SOHO / LASCO CME Catalog. Earth Moon Planet, 104:295–313.

Gough, D. O. and Kosovichev, A. G. (1990). Inside the Sun: Proceedings of the 121st Colloquium of the Internatio pages 327–340. Springer Netherlands, Dordrecht.

Greenstein, J. L. (1958). High-Resolution Spectra of Comet MRKOS. The Astrophysical Journal, 128:106.

Guenther, D. B. (1989). Age of the sun. The Astrophysical Journal, 339:1156.

Harra, L. K., Mandrini, C. H., Dasso, S., Gulisano, A. M., Steed, K., and Imada, S. (2010). Determining the Solar Source of a Magnetic Cloud Using a Velocity Difference Technique. Solar Physics, 268(1):213–230.

Harra, L. K. and Sterling, A. C. (2001). Material Outflows from Coronal Intensity "Dimming Regions" During Coronal Mass Ejection Onset. The Astrophysical Journal Letters, 561:215–218.

Harrison, R. A., Bryans, P., Simnett, G. M., and Lyons, M. (2003). Coronal dimming and the coronal mass ejection onset. Astronomy & Astrophysics, 400:1071–1083.

Harrison, R. A. and Lyons, M. (2000). A spectroscopic study of coronal dimming associated with a coronal mass ejection. Astronomy & Astrophysics, 1108:1097–1108.

Holman, G. (2008). Overview of Solar Flares.

Howard, R. A., Moses, J. D., Vourlidas, A., Newmark, J. S., Socker, D. G., Plunkett, S. P., Korendyke, C. M., Cook, J. W., Hurley, A., Davila, J. M., Thompson, W. T., St. Cyr, O. C., Mentzell, E., Mehalick, K., Lemen, J. R., Wuelser, J. P., Duncan, D. W., Tarbell, T. D., Wolfson, C. J., Moore, A., Harrison, R. A., Waltham, N., Lang, J., Davis, C. J., Eyles, C. J., Mapson-Menard, H., Simnett, G. M., Halain, J. P., Defise, J. M., Mazy, E., Rochus, P., Mercier, R., Ravet, M. F., Delmotte, F., Auchere, F., Delaboudiniere, J. P., Bothmer, V., Deutsch, W., Wang, D., Rich, N., Cooper, S., Stephens, V., Maahs, G., Baugh, R., McMullin, D., and Carter, T. (2008). Sun Earth Connection Coronal and Heliospheric Investigation (SECCHI). Space Science Reviews, 136(1-4):67–115.

Hudson, H. S., Acton, L. W., and Freeland, S. L. (1996). A Long-Duration Solar Flare with Mass Ejection and Global Consequences. The Astrophysical Journal, 470:629–635.

Hudson, H. S., Lemen, J. R., St. Cyr, O. C., Sterling, A. C., and Webb, D. F. (1998). X-ray coronal changes during halo CMEs. Geophysical Research Letters, 25(14):2481–2484.

Hudson, H. S., Woods, T. N., Chamberlin, P. C., Fletcher, L., Zanna, G. D., Didkovsky, L., Labrosse, N., and Graham, D. (2011). The EVE Doppler Sensitivity and Flare Observations. Solar Physics, 273:69–80.

Hyder, C. L. and Lites, B. W. (1970). H-alpha Doppler Brightening and Lyman-alpha Doppler Dimming in Moving H-alpha Prominences. Solar Physics, 14(1):147–156.

Imada, S., Hara, H., Watanabe, T., Kamio, S., Asai, A., Matsuzaki, K., Harra, L. K., and Mariska, J. T. (2007). Discovery of a Temperature-Dependent Upflow in the Plage Region during a Gradual Phase of the X-Class Flare. Publications of the Astronomical Society of Japan, 59(sp3):S793–S799.

International Energy Agency (2015). 2015 Key World Energy Statistics. Technical report, International Energy Agency.

Jaynes, A. N., Li, X., Schiller, Q. G., Blum, L. W., Tu, W., Turner, D. L., Ni, B., Bortnik, J., Baker, D. N., Kanekal, S. G., Blake, J. B., and Wygant, J. (2014). Evolution of relativistic outer belt electrons during an extended quiescent period. Journal of Geophysical Research: Space Physics, 119(12):9558–9566.

Jin, M., Ding, M. D., Chen, P. F., Fang, C., and Imada, S. (2009). CORONAL MASS EJECTION INDUCED OUTFLOWS OBSERVED WITH HINODE /EIS. The Astrophysical Journal, 702(1):27–38.

Kahler, S. (1992). Solar Flares and Coronal Mass Ejections. Annual Review of Astronomy and Astrophysics, 30:113–141.

Kahler, S. W. (1982). The role of the big flare syndrome in correlations of solar energetic proton fluxes and associated microwave burst parameters. Journal of Geophysical Research, 87(A5):3439.

Kaiser, M. L., Kucera, T. A., Davila, J. M., St. Cyr, O. C., Guhathakurta, M., and Christian, E. (2007). The STEREO Mission: An Introduction. Space Science Reviews, 136(1-4):5–16.

Kippenhahn, R., Weigert, A., and Weiss, A. (2012). Stellar Structure and Evolution. Astronomy and Astrophysics Library. Springer Berlin Heidelberg, Berlin, Heidelberg.

Klimchuk, J. A. (2006). On Solving the Coronal Heating Problem. Solar Physics, 234(1):41–77.

Klimchuk, J. A. (2015). Key aspects of coronal heating. Philosophical transactions. Series A, Mathematical, physical, and engineering sciences, 373(2042):20140256.

Kohnert, R., Palo, S., and Li, X. (2011). Small Space Weather Research Mission Designed Fully by Students. Space Weather, 9(4):n/a–n/a.

Kontar, E. P., Brown, J. C., Emslie, A. G., Hajdas, W., Holman, G. D., Hurford, G. J., Kašparová, J., Mallik, P. C. V., Massone, A. M., McConnell, M. L., Piana, M., Prato, M., Schmahl, E. J., and Suarez-Garcia, E. (2011). Deducing Electron Properties from Hard X-ray Observations. Space Science Reviews, 159(1-4):301–355.

Krista, L. D. and Reinard, A. (2013). STUDY OF THE RECURRING DIMMING REGION DETECTED AT AR 11305 USING THE CORONAL DIMMING TRACKER (CoDiT). The Astrophysical Journal, 762(2):91.

Labrosse, N. and Mcglinchey, K. (2012). Plasma diagnostic in eruptive prominences from SDO / AIA observations at 304 Å. Astronomy & Astrophysics, 537:A100.

Landi, E., Del Zanna, G., Young, P. R., Dere, K. P., Mason, H. E., and Landini, M. (2006). CHIANTIAn Atomic Database for Emission Lines. VII. New Data for XRays and Other Improvements. The Astrophysical Journal Supplement Series, 162:261–280.

Lang, K. R. (2001). The Cambridge Encyclopedia of the Sun. The Cambridge Encyclopedia of the Sun.

Lemen, J. R., Title, A. M., Akin, D. J., Boerner, P. F., Chou, C., Drake, J. F., Duncan, D. W., Edwards, C. G., Friedlaender, F. M., Heyman, G. F., Hurlburt, N. E., Katz, N. L., Kushner, G. D., Levay, M., Lindgren, R. W., Mathur, D. P., Mcfeaters, E. L., Mitchell, S., Rehse, R. A., Schrijver, C. J., Springer, L. A., Stern, R. A., Tarbell, T. D., Wolfson, C. J., Yanari, C., Bookbinder, J. A., Cheimets, P. N., Caldwell, D., Deluca, E. E., Gates, R., Golub, L., Park, S., Podgorski, W. A., Bush, R. I., Scherrer, P. H., Gummin, M. A., Smith, P., Auker, G., Jerram, P., Pool, P., Soufli, R., Windt, D. L., Beardsley, S., Clapp, M., Lang, J., and Waltham, N. (2012). The Atmospheric Imaging Assembly (AIA) on the Solar Dynamics Observatory (SDO). Solar Physics, 275:17–40.

Li, X., Palo, S., Kohnert, R., Blum, L., Gerhardt, D., Schiller, Q., and Califf, S. (2013a). Small Mission Accomplished by Students-Big Impact on Space Weather Research. Space Weather, 11(2):55–56.

Li, X., Palo, S., Kohnert, R., Gerhardt, D., Blum, L., Schiller, Q., Turner, D., Tu, W., Sheiko, N., and Cooper, C. S. (2012). Colorado Student Space Weather Experiment: Differential Flux Measurements of Energetic Particles in a Highly Inclined Low Earth Orbit. In Summers, D., Mann, I. R., Baker, D. N., and Schulz, M., editors, Dynamics of the Earth's Radiation Belts and Inner Magnetosphere, Geophysical Monograph Series, pages 385–411, Washington, D. C. American Geophysical Union.

Li, X., Schiller, Q., Blum, L., Califf, S., Zhao, H., Tu, W., Turner, D. L., Gerhardt, D., Palo, S., Kanekal, S., Baker, D. N., Fennell, J., Blake, J. B., Looper, M., Reeves, G. D., and Spence, H. (2013b). First results from CSSWE CubeSat: Characteristics of relativistic electrons in the near-Earth environment during the October 2012 magnetic storms. Journal of Geophysical Research: Space Physics, 118(10):6489–6499.

Li, X., Selesnick, R. S., Baker, D. N., Jaynes, A. N., Kanekal, S. G., Schiller, Q., Blum, L., Fennell, J., and Blake, J. B. (2015). Upper limit on the inner radiation belt MeV electron intensity. Journal of geophysical research. Space physics, 120(2):1215–1228.

Lin, R. P., Dennis, B. R., Hurford, G. J., Smith, D. M., Zehnder, A., Harvey, P. R., Curtis, D. W., Pankow, D., Turin, P., Bester, M., Csillaghy, A., Lewis, M., Madden, N., Beek, H. F., Appleby, M., Raudorf, T., Mctiernan, J., Ramaty, R., Schmahl, E., Schwartz, R., Krucker, S., Abiad, R., Quinn, T., Berg, P., Hashii, M., Sterling, R., Jackson, R., Pratt, R., Campbell, R. D., Malone, D., Landis, D., Cork, C., Tolbert, A. K., Zarro, D. M., Snow, F., Thomsen, K., and Henneck, R. (2002). The Reuven Ramaty High-Energy Solar Spectroscopic Imager (RHESSI). Solar Physics, 210:3–32.

Liu, W. and Ofman, L. (2014). Advances in Observing Various Coronal EUV Waves in the SDO Era and Their Seismological Applications (Invited Review). Solar Physics, 289(9):3233–3277.

Mariska, J. T. (1993). The Solar Transition Region. Cambridge University Press.

Mason, J. P. and Hoeksema, J. T. (2010). Testing Automated Solar Flare Forecasting With 13 Years of Michelson Doppler Imager Magnetograms. The Astrophysical Journal, 723:634–640.

Mason, J. P., Woods, T. N., Caspi, A., Thompson, B. J., and Hock, R. A. (2014). MECHANISMS AND OBSERVATIONS OF CORONAL DIMMING FOR THE 2010 AUGUST 7 EVENT. The Astrophysical Journal, 789(1):61.

Mazzotta, P., Mazzitelli, G., Colafrancesco, S., and Vittorio, N. (1998). Ionization balance for optically thin plasmas: Rate coefficients for all atoms and ions of the elements H to Ni. Astronomy and Astrophysics Supplement Series, 133(3):403–409.

Mihalas, D. M. (1970). No Title. W. H. Freeman and Company.

Muhr, N., Veronig, A. M., Kienreich, I. W., and Temmer, M. (2011). Analysis of Characteristic Parameters of Large-Scale Coronal Waves Observed by the Solar-Terrestrial Relations Observatory/Extreme Ultraviolet Imager. The Astrophysical Journal, 89:89.

National Research Council (2008). Severe Space Weather Events - Understanding Societal and Economic Impacts. page 131.

Palo, S., Li, X., Gerhardt, D., Turner, D., Kohnert, R., Hoxie, V., and Batiste, S. (2010). Conducting Science with a CubeSat: The Colorado Student Space Weather Experiment.

Parker, E. N. (1988). Nanoflares and the solar X-ray corona. The Astrophysical Journal, 330:474.

Parsons, A., Biesecker, D., Odstrcil, D., Millward, G., Hill, S., and Pizzo, V. (2011). Wang-Sheeley-Arge-Enlil Cone Model Transitions to Operations. Space Weather, 9(3):n/a–n/a.

Pearson, K. (1895). Note on Regression and Inheritance in the Case of Two Parents. Proceedings of the Royal Society of London, 58:240–242.

Pesnell, W. D., Thompson, B. J., and Chamberlin, P. C. (2012). The Solar Dynamics Observatory (SDO). Solar Physics, 275:3–15.

Peterson, W. K., Stavros, E. N., Richards, P. G., Chamberlin, P. C., Woods, T. N., Bailey, S. M., and Solomon, S. C. (2009). Photoelectrons as a tool to evaluate spectral variations in solar EUV irradiance over solar cycle timescales. Journal of Geophysical Research, 114:A10304.

Pohjolainen, S., Vilmer, N., Khan, J. I., and Hillaris, A. E. (2005). Early signatures of large-scale field line opening Multi-wavelength analysis of features connected with a halo CME event. Astronomy & Astrophysics, 434:329–341.

Reinard, A. A. and Biesecker, D. A. (2008). Coronal Mass Ejection-Associated Coronal Dimmings. The Astrophysical Journal, 674:576–585.

Reinard, A. A. and Biesecker, D. A. (2009). The Relationship Between Coronal Dimming and Coronal Mass Ejection Properties. The Astrophysical Journal, 705(1):914–919.

Robbrecht, E. and Wang, Y.-M. (2010). The Temperature-Dependent Nature of Coronal Dimmings. The Astrophysical Journal Letters, 720:88–92.

Rodgers, E. M., Bailey, S. M., Warren, H. P., Woods, T. N., and Eparvier, F. G. (2006). Soft X-ray irradiances during solar flares observed by TIMED-SEE. Journal of Geophysical Research, 111(A10):A10S13.

Rompolt, . (1967). The Hα Radiation Field in the Solar Corona for Moving Prominences. Acta Astronomica, 17.

Rust, D. M. and Hildner, E. (1976). Expansion of an X-ray Coronal Arch into the Outer Corona. Solar Physics, 48:381–387.

Schiller, Q., Gerhardt, D., Blum, L., Li, X., and Palo, S. (2014a). Design and scientific return of a miniaturized particle telescope onboard the Colorado Student Space Weather Experiment (CSSWE) CubeSat. In 2014 IEEE Aerospace Conference, pages 1–14. IEEE.

Schiller, Q., Li, X., Blum, L., Tu, W., Turner, D. L., and Blake, J. B. (2014b). A nonstorm time enhancement of relativistic electrons in the outer radiation belt. Geophysical Research Letters, 41(1):7–12.

Schiller, Q. and Mahendrakumar, A. (2010). REPTile: A Miniaturized Detector for a CubeSat Mission to Measure Relativistic Particles in Near-Earth Space.

Schlemm, C. E., Starr, R. D., Ho, G. C., Bechtold, K. E., Hamilton, S. A., Boldt, J. D., Boynton, W. V., Bradley, W., Fraeman, M. E., Gold, R. E., Goldsten, J. O., Hayes, J. R., Jaskulek, S. E., Rossano, E., Rumpf, R. A., Schaefer, E. D., Strohbehn, K., Shelton, R. G., Thompson, R. E., Trombka, J. I., and Williams, B. D. (2007). The X-Ray Spectrometer on the MESSENGER Spacecraft. Space Science Reviews, 131(1-4):393–415.

Schrijver, C. J. and Higgins, P. A. (2015). A Statistical Study of Distant Consequences of Large Solar Energetic Events. Solar Physics, 290(10):2943–2950.

Schrijver, C. J. and Title, A. M. (2011). Long-range magnetic couplings between solar flares and coronal mass ejections observed by SDO and STEREO. Journal of Geophysical Research, 116(A4):69–80.

Solomon, S. C., Bailey, S. M., and Woods, T. N. (2001). Effect of solar soft X-rays on the lower ionosphere. Geophysical Research Letters, 28(11):2149–2152.

Sterling, A. C. and Hudson, H. S. (1997). YOHKOH SXT OBSERVATIONS OF X-RAY DIMMING ASSOCIATED WITH A HALO CORONAL MASS EJECTION. The Astrophysical Journal, 491:L55–L58.

Swings, P. (1941). Complex Structure of Cometary bands Tentatively Ascribed to the Contour of the Solar Spectrum. Lick Observatory Bulletin, 508.

Temmer, M. (2016). Kinematical properties of coronal mass ejections. Astronomische Nachrichten, accepted.

Thompson, B. J., Cliver, E. W., Nitta, N. V., Delannée, C., and Delaboudiniere, J. P. (2000). Coronal Dimmings and Energetic CMEs in April-May 1998. Geophysical Research Letters, 27(10):1431–1434.

Tian, H., McIntosh, S. W., Xia, L., He, J., and Wang, X. (2012). What Can We Learn About Solar Coronal Mass Ejections, Coronal Dimmings, and Extreme-Ultraviolet Jets Through Spectroscopic Observations? The Astrophysical Journal, 748(2):106.

Vourlidas, A., Howard, R. A., Esfandiari, E., Patsourakos, S., Yashiro, S., and Michalek, G. (2010). COMPREHENSIVE ANALYSIS OF CORONAL MASS EJECTION MASS AND ENERGY PROPERTIES OVER A FULL SOLAR CYCLE. The Astrophysical Journal, 722(2):1522–1538.

Vourlidas, A., Howard, R. A., Esfandiari, E., Patsourakos, S., Yashiro, S., and Michalek, G. (2011). ERRATUM: COMPREHENSIVE ANALYSIS OF CORONAL MASS EJECTION MASS AND ENERGY PROPERTIES OVER A FULL SOLAR CYCLE (2010, ApJ, 722, 1522). The Astrophysical Journal, 730(1):59.

Vourlidas, A., Subramanian, P., Dere, K. P., and Howard, R. A. (2000). LargeAngle Spectrometric Coronagraph Measurements of the Energetics of Coronal Mass Ejections. The Astrophysical Journal, 534(1):456–467.

Wang, Y. and Zhang, J. (2007). A Comparative Study between Eruptive XClass Flares Associated with Coronal Mass Ejections and Confined XClass Flares. The Astrophysical Journal, 665(2):1428–1438.

Wang, Y. and Zhang, J. (2008). A Statistical Study of Solar Active Regions That Produce Extremely Fast Coronal Mass Ejections. The Astrophysical Journal, 680(2):1516–1522.

Woods, T. N. and Chamberlin, P. C. (2009). Comparison of solar soft X-ray irradiance from broadband photometers to a high spectral resolution rocket observation. Advances in Space Research, 43:349–354.

Woods, T. N., Chamberlin, P. C., Peterson, W. K., Meier, R. R., Richards, P. G., Strickland, D. J., Lu, G., Qian, L., Solomon, S. C., Iijima, B. A., Mannucci, A. J., and Tsurutani, B. T. (2008). XUV Photometer System (XPS): Improved Solar Irradiance Algorithm Using CHIANTI Spectral Models. Solar Physics, 250(2):235–267.

Woods, T. N., Eparvier, F. G., Bailey, S. M., Chamberlin, P. C., Lean, J., Rottman, G. J., Solomon, S. C., Tobiska, W. K., and Woodraska, D. L. (2005a). Solar EUV Experiment (SEE): Mission overview and first results. Journal of Geophysical Research, 110:A01312.

Woods, T. N., Eparvier, F. G., Hock, R. A., Jones, A. R., Woodraska, D. L., Judge, D., Didkovsky, L., Lean, J., Mariska, J. T., Warren, H., McMullin, D., Chamberlin, P. C., Berthiaume, G., Bailey, S. M., Fuller-Rowell, T., Sojka, J., Tobiska, W. K., and Viereck, R. (2012). Extreme Ultraviolet Variability Experiment (EVE) on the Solar Dynamics Observatory (SDO): Overview of Science Objectives, Instrument Design, Data Products, and Model Developments. Solar Physics, 275:115–143.

Woods, T. N., Hock, R. A., Eparvier, F. G., Jones, A. R., Chamberlin, P. C., Klimchuk, J. A., Didkovsky, L., Judge, D., Mariska, J. T., Warren, H. P., Schrijver, C. J., Webb, D. F., Bailey, S. M., and Tobiska, W. K. (2011). New Solar Extreme-Ultraviolet irradiance Observations During Flares. The Astrophysical Journal, 739:59.

Woods, T. N., Kopp, G., and Chamberlin, P. C. (2006). Contributions of the solar ultraviolet irradiance to the total solar irradiance during large flares. Journal of Geophysical Research, 111(A10):A10S14.

Woods, T. N., Rottman, G., and Vest, R. (2005b). XUV Photometer System (XPS): Overview and Calibrations. Solar Physics, 230(1-2):345–374.

Yashiro, S., Gopalswamy, N., Akiyama, S., Michalek, G., and Howard, R. A. (2005). Visibility of coronal mass ejections as a function of flare location and intensity. Journal of Geophysical Research, 110(A12):A12S05.

Zharkova, V. V., Arzner, K., Benz, A. O., Browning, P., Dauphin, C., Emslie, A. G., Fletcher, L., Kontar, E. P., Mann, G., Onofri, M., Petrosian, V., Turkmani, R., Vilmer, N., and Vlahos, L. (2011). Recent Advances in Understanding Particle Acceleration Processes in Solar Flares. Space Science Reviews, 159(1-4):357–420.

Zhukov, A. N. and Auchère, F. (2004). On the nature of EIT waves, EUV dimmings and their link to CMEs. Astronomy & Astrophysics, 427:705–716.

Zirker, J. B. (2004). Journey from the Center of the Sun. Princeton Science Library.

Appendix A

Coronal Dimming Event List and Ancillary Data

Table A.1

#	Date	Time (UTC)	AIA Location	GOES Class	Peak Time (UTC)	Flare Location	Flare Energy [J]	CME Onset (UTC)	PA [°]	Speed [km s^{-1}]	Mass [g]	CME Kinetic Energy [J]	Dimming Depth [%] (±)	Dimming Slope [% s^{-1}] (±)
1	2011/02/10	07:40	N20 WL	–	–	–	–	–	–	–	–	–	0.68 (0.06)	2.38E-4 (4.97E-5)
2	2011/02/10	13:36	N20 WL	–	–	–	–	14:24	280	338	3.40E14	1.94E22	0.21 (0.15)	4.22E-4 (3.96E-4)
3	2011/02/11	07:46	N20 WL	B9.0	08:13	N15 WL	3.93E22	08:38	280	175	1.40E14	2.14E21	1.66 (0.11)	3.83E-4 (1.24E-4)
4	2011/02/11	13:21	N60 00	–	–	–	–	–	–	–	–	–	0.81 (0.12)	1.44E-4 (1.36E-4)
5	2011/02/11	21:43	N10 EL	–	–	–	–	22:12	100	469	2.60E15	2.86E23	1.30 (0.17)	1.89E-4 (1.22E-4)
6	2011/02/12	06:05	N30 E10	–	–	–	–	–	–	–	–	–	1.06 (0.28)	9.08E-4 (3.60E-4)
7	2011/02/13	17:52	S10 E10	M6.6	17:38	S20 E04	1.41E24	18:24	80	349	3.42E15	2.08E23	2.94 (0.11)	5.92E-4 (1.18E-4)
8	2011/02/14	07:00	S10 00	C6.6	06:58	–	1.17E23	08:12	288	303	1.20E13	5.51E20	1.42 (0.06)	2.22E-4 (2.85E-5)
9	2011/02/14	17:36	N30 E20	M2.2	17:26	N56 W18	4.14E23	18:09	80	396	4.62E15	3.62E23	–	–
10	2011/02/15	02:07	00 00	X2.2	01:56	00 00	5.48E24	02:09	100	897	5.09E15	2.05E24	4.41 (0.10)	5.07E-4 (8.84E-5)
11	2011/02/16	14:40	S20 W20	M1.6	14:25	S20 W32	1.61E23	–	–	–	–	–	1.95 (0.09)	4.15E-4 (8.25E-5)
12	2011/02/17	00:47	N00 E40	–	–	–	–	–	–	–	–	–	2.68 (0.09)	4.60E-4 (1.04E-4)
13	2011/02/18	11:15	S10 W50	–	–	–	–	12:12	281	350	6.60E13	4.04E21	1.23 (0.09)	4.22E-4 (9.44E-5)
14	2011/02/18	19:20	N30 00	C7.1	19:18	–	–	–	–	–	–	–	4.28 (0.13)	2.12E-4 (4.89E-5)
15	2011/02/24	07:40	N10 EL	M3.5	07:35	00 EL	2.79E22	–	–	–	–	–	3.71 (0.07)	5.22E-4 (5.89E-5)
16	2011/02/25	07:00	N45 E60	–	–	–	–	08:00	349	370	6.50E14	4.45E22	1.33 (0.16)	3.38E-4 (2.13E-4)
17	2011/08/02	05:10	N05 W23	M1.4	06:19	N14 W15	1.18E24	06:36	288	1110	7.10E15	4.37E24	4.77 (0.08)	2.83E-4 (4.57E-5)
18	2011/08/02	13:00	N00 EL	–	–	–	–	–	–	–	–	–	0.47 (0.13)	6.20E-4 (1.89E-4)
19	2011/08/03	13:43	N05 W47	M6.0	13:48	N16 W30	3.57E24	14:00	Halo	1100	7.80E15	4.72E24	2.68 (0.08)	8.00E-4 (9.40E-5)

Table A.2: Table continued...

#	Date	Time (UTC)	AIA Location	GOES Class	Peak Time (UTC)	Flare Location	Flare Energy [J]	CME Onset (UTC)	PA [°]	Speed [km s^{-1}]	Mass [g]	CME Kinetic Energy [J]	Dimming Depth [%] (±)	Dimming Slope [% s^{-1}] (±)
20	2011/08/04	04:12	N05 W57	M9.3	03:57	N19 W36	2.29E24	04:12	Halo	2080	5.70E15	1.23E25	5.22 (0.06)	9.86E-4 (5.32E-5)
21	2011/08/04	04:41	N80 00	–	–	–	–	06:24	20	338	–	–	–	–
22	2011/08/05	07:25	S20 E30	–	–	–	–	07:12	101	110	–	–	–	–
23	2011/08/06	11:50	S15 E10	C1.3	11:44	S17 E20	1.85E22	–	–	–	–	–	1.67 (0.07)	3.32E-4 (7.53E-5)
24	2011/08/06	18:25	N05 W25	–	–	–	–	–	–	–	–	–	–	–
25	2011/08/06	17:35	N30 WL	C1.4	18:07	–	8.40E22	17:24	289	176	5.10E14	7.90E21	–	–
26	2011/08/06	22:40	N10 W25	–	22:51	N16 W35	3.18E22	–	–	–	–	–	1.00 (0.11)	1.20E-4 (9.27E-5)
27	2011/08/07	04:00	N10 W55	–	–	–	–	05:48	259	459	7.00E13	7.37E21	0.61 (0.11)	3.16E-4 (1.77E-4)
28	2011/08/08	01:15	N80 E05	–	–	–	–	–	–	–	–	–	–	–
29	2011/08/08	11:00	N15 W70	C1.3	03:10	N18 W58	9.75E21	–	–	–	–	–	–	–
30	2011/08/08	17:42	N05 W05	–	–	–	–	–	–	–	–	–	2.61 (0.09)	7.46E-4 (1.18E-4)
31	2011/08/08	18:42	N05 W75	M3.5	18:10	N16 W61	6.60E23	18:24	305	1248	2.09E15	1.63E24	–	–
32	2011/08/09	08:10	00 W60	X6.9	08:05	N17 W69	5.74E24	08:24	Halo	1474	3.84E15	4.17E24	1.73 (0.14)	9.72E-4 (2.92E-4)
33	2011/08/09	09:12	S30 EL	–	–	–	–	–	–	–	–	–	–	–
34	2011/08/09	11:26	N05 00	–	–	–	–	14:00	291	428	–	–	2.79 (0.06)	3.96E-4 (5.40E-5)
35	2011/08/11	10:23	00 WL	C6.2	10:23	–	3.51E23	10:54	Halo	1144	2.29E15	1.50E24	1.08 (0.12)	4.88E-4 (1.65E-4)
36	2011/08/12	00:09	N45 E80	–	–	–	–	03:47	30	346	5.10E14	3.05E22	1.92 (0.07)	2.28E-4 (4.71E-5)
37	2011/08/12	11:13	N50 E70	–	–	–	–	–	–	–	–	–	1.23 (0.14)	1.84E-4 (4.98E-5)
38	2010/08/04	18:05	N05 E60	M1.0	18:24	–	5.94E23	18:36	Halo	850	6.40E15	2.31E24	2.20 (0.06)	4.37E-4 (4.54E-5)

Appendix B

MinXSS CubeSat Mass/Power Tables

Table B.1: The two mass limits correspond to the NanoRacks and Cal Poly requirements, respectively.

Component	Mass [g]	Peak Power [W]	Nominal Power [W]
ADCS	870.1	1.94	1.19
CDH	46.3	0.70	0.22
COMM	124.6	9.50	9.50
EPS	901.5	–	–
SPS/XP	386.5	0.25	0.25
Structure	780.0	–	–
Thermal	2.6	3.30 (Heaters)	–
X123	323.6	5.00	2.79
Total	3435.2	20.69	13.95
Limits	4800/4000	–	–
Margin [%]	28.4/14.1	–	–

Appendix C

MinXSS Thermal Model Parameter Tables

Table C.1: Thermal Desktop node-node conductors in MinXSS model.

Object A	Object B	Conductance [W $^{\circ}C^{-1}$]
+X structure plate	Y structure plates	4.00
-X structure plate	Y structure plates	0.26
Antenna	Antenna deployment module	0.05
CDH, COMM, EPS boards	Motherboard	0.011
Radio	Antenna	0.03
Y structure plates	-Z structure plate	0.02
X123 board	X123 electronics box	0.038

Table C.2: Thermal Desktop contactors in MinXSS model.

Object A	Object B	Conductance [W °C^{-1}]
Daughter boards	Kooler-Guide rails	0.02
Antenna deployment module	-Z structure plate	0.105
Batteries	Battery board	0.03
Body-fixed solar panel	+X structure plate	0.2
+X structure plate	Motherboard	0.05
Kooler-Guide rails	Y structure plates	0.105
Radio	COMM board	31.62
SPS/XP	-Z structure plate	0.105
Structure	ADCS	0.21
X123 detector head	-Y structure plate	1.07
X123 electronics box	-Y structure plate	0.105

Table C.3: Thermal Desktop heat loads in MinXSS model.

Name	Applied To	Heat Load [W]
ADCS	ADCS brick	1.94 (orbit) 1.19 (testing)
Battery	Battery brick	0.122 (charging) 0.001-0.016 (discharging)
CDH	CDH rect	0.224
EPS	EPS rect	0 (eclipse), 1.2 (insolated), time varying (testing)
Radio receive	Radio brick	0.09
Radio transmit	Radio brick	0-6.3 (orbit), 0-3.2 (testing)
SPS/XP	SPS/XP brick	0.25
X123 detector head	X123 detector brick	1.5-2.0 (Temperature dependent)
X123 electronics	X123 board rect	0.42

Table C.4: Thermal Desktop heaters in MinXSS model.

Name	Power [W]	On Temp [°C]	Off Temp [°C]
Battery Heater 1	1.59	5	6
Battery Heater 2	1.59	5	6

Table C.5: Thermal Desktop optical properties in MinXSS model.

Name	Applied to	Absorptivity	Emissivity
Aperture passthrough	SPS/XP and X123 apertures	1	0
Delrin	Antenna deployment module	0.96	0.87
5mil silver coated teflon	ADCS +Z, +X plate, ±Y plate, half of -X plate	0.09	0.78
Al 6061 bare	Battery encapsulation plates, Kooler-Guide rails, Radio, Structure, SPS/XP, X123	0.031	0.039
Yellow tape measure	Antenna	0.38	0.8
Battery foil	Batteries	0.5	0.04
Black anodize	ADCS, structure rails	0.73	0.86
Circuit board	PCBs	0.6	0.7
Emcore solar cells	Solar cells	0.9	0.87

Table C.6: Thermal Desktop thermophysical properties in MinXSS model.

Name	Applied To	Conductivity [W in $^{-1}$ C^{-1}]	Specific Heat [J kg^{-1} C^{-1}]	Density [kg in^{-3}]
Aluminum 6061	ADCS, battery encapsulation plates, Kooler-Guide rails, structure, SPS/XP, X123	0-4.5 (Temperature dependent)	100-1100 (Temperature dependent)	0.044
Aluminum 6061 (2)	X123 and structure	4.26	963	0.045
Copper	CDH, COMM, EPS boards	8.6-10.8 (Temperature dependent)	0-450 (Temperature dependent)	0.146
Delrin	Antenna deployment module	0.009	0.35	0.023
Lithium polymer batteries	Batteries	0.0051	1011.8	0.035
PCB - FR4	Motherboard, battery board, solar panels	0.01	1	0.03
Stainless steel 300 series	Antenna	0.25-0.65 (Temperature dependent)	300-640 (Temperature dependent)	0.13